U.S. Department of Energy
Energy Efficiency
and Renewable Energy
Bringing you a prosperous future where energy
is clean, abundant, reliable, and affordable

HEAVY VEHICLE SYSTEMS OPTIMIZATION

Less dependence on foreign oil, and eventual transition to an emissions-free, petroleum-free vehicle

FreedomCAR and Vehicle Technologies Program

2004 ANNUAL PROGRESS REPORT

21ST CENTURY TRUCK PARTNERSHIP

FreedomCAR & Fuel Partnership

U.S. Department of Energy
FreedomCAR and Vehicle Technologies Program
1000 Independence Avenue, S.W.
Washington, D.C. 20585-0121

FY 2004

Annual Progress Report for Heavy Vehicle Systems Optimization

Energy Efficiency and Renewable Energy
FreedomCAR and Vehicle Technologies Program

Approved by Dr. Sidney Diamond **Technology Area Development Specialist**

February 2005

Contents

Contents (Cont.)

Contents (Cont.)

Foreword

The U.S. Department of Energy (DOE) effort on Heavy Vehicle Systems Optimization addresses the very important area of non-engine losses that account for a significant amount of fuel consumption. These losses are usually referred to as Parasitic Energy Losses. For example, aerodynamic drag accounts for about 53% of the non-engine losses of a fully loaded class 8 tractor-trailer traveling at 65 mph on a level highway; rolling resistance, 32%; drivetrain, 6%; and auxiliary losses, 9%. As aerodynamic drag is reduced, brakes that already operate at capacity can be seriously compromised. Therefore, the program also includes a safety line item that concentrates on improving brake systems. Funds in FY 2004 were approximately $10.8 M. Projects are selected on the basis of (1) proposals addressing open solicitations issued by the FreedomCAR and Vehicle Technologies (FCVT) Program or (2) proposals from national laboratories. Contracts with our industrial partners are cost-shared at least 50%.

The primary goal of this technology development area is to develop cost-effective technologies that will vastly improve the fuel efficiency of heavy vehicles and will eventually devolve into all vehicles. The ultimate goals are consistent with those of the 21st Century Truck Partnership: a 10-mph, fully loaded class 8 tractor/trailer traveling at highway speeds. Note that a 1% increase in fuel efficiency for long-haul trucks will result in a yearly fuel savings of 100 million gallons of fuel.

Individual goals are to reduce the aerodynamic drag coefficient by 25%, resulting in approximately a 12.5% increase in fuel efficiency at 65 mph (and increasing at higher speeds); a 40% decrease in rolling resistance; a 30% decrease in drivetrain losses; a 50% decrease in auxiliary loads; and an 8% decrease in the size of the radiator, despite the higher cooling demands of higher-power engines and exhaust gas recirculation.

Steady and significant progress on achieving these goals has been made in FY 2004:

- On-track tests of a tractor-trailer combination with flat boat tails have demonstrated a 4.2% increase in fuel efficiency at 60 mph. Furthermore, rounding the leading edge of the trailer results in further increases in fuel efficiency. Computations indicate that rounded boat tails and side skirts will reduce the drag coefficient by 20%.

- A recently signed contract with the Truck Manufacturers Association with four OEMs as subcontractors will fleet-test some of the near-commercial devices that are available for reduction of aerodynamic drag.

- Road tests of the “More Electric Truck” have demonstrated a 2% increase in fuel economy obtained by electrification of several of the belt-driven components. Furthermore, the on-board auxiliary power unit will increase fuel economy by another 6% by reduction of engine idling time. The idle reduction campaign of FCVT, which consisted of analysis and publicity, has captured the interest of the U.S. Environmental Protection Agency (EPA), U.S. Department of Defense (DOD), U.S. Department of Transportation (DOT), and several state energy agencies, all of which have now taken a lead role in implementation.

- Tests under realistic conditions on a laser-glazed rail have shown that a reduction in friction of up to 40% can be achieved. A consist management program was demonstrated to save about 2.5% fuel in a 100-car train running between Kansas City and Los Angeles. Further savings will be achieved when the locomotives are fully hybridized.

- Wind tunnel tests have shown that the drag coefficient of empty coal cars is between 35 and 42% higher than that of loaded coal cars. Computations indicate that simple devices can reduce the drag coefficient in empty coal cars by 10%.

- Superhard coatings have achieved friction coefficients of less than 0.03 under boundary-layer-lubrication conditions with virtually no wear that could contribute significantly to the increased energy efficiency of reciprocating and rotating vehicular components.

- West Virginia University has devised and analyzed alternative structural arrangements for the floor of a heavy van trailer, leading to the conclusion that significant weight reduction is possible.

- Argonne National Laboratory has developed a model of heat transfer in nanofluids and found that a key mechanism of temperature- and size-dependent thermal conductivity is the dynamic interactions between nanoparticles and liquid molecules. This finding could lead to a substantial downsizing of truck cooling systems and a reduction of the parasitic energy loss of the systems.

Finally, four new industrial contracts have been initiated: Truck Manufacturer Association — fleet demonstration of near-commercial drag reduction technologies; Eaton Corp — reduction of friction and wear of gears; Caterpillar — demonstration of a 5–11% improvement in the fuel efficiency of medium-duty trucks through the use of electrically driven components and the use of intelligent engine idling control and energy storage technologies; and Caterpillar — demonstration of increased fuel efficiency through improvements in cooling system performance, air system management, and advanced power management.

The accomplishments mentioned above reflect only some of the progress achieved in FY 2004 in the area of parasitic energy loss. A review of all of the sections of the annual report indicates that the progress toward the stated goals of the HV Systems Optimization Technology Development Area is significant and that they can be met by continuing the same vigorous R&D that currently is contained within the research portfolio.

Finally, it is my pleasure to thank the dedicated scientists and engineers who work with the FCVT Program. It is their expertise, drive, and initiative that have made great strides in their technologies. Their innovations will continue to contribute to advances in reduction of parasitic energy losses for heavy vehicles and to the significant reduction of U.S. dependence on petroleum fuels.

Dr. Sidney Diamond, Technology Area Development Specialist
Heavy Vehicle Systems Optimization
FreedomCAR and Vehicle Technologies Program
Energy Efficiency and Renewable Energy
U.S. Department of Energy

I. Aerodynamic Drag Reduction

A. DOE Project on Heavy Vehicle Aerodynamic Drag

Project Principal Investigator: R.C. McCallen
Lawrence Livermore National Laboratory
P.O. Box 808, Livermore, CA 94551-0808
(925) 423-0958, e-mail: mccallen1@llnl.gov

Principal Investigator: K. Salari
Co-Investigators: J. Ortega, P. Castellucci, C. Eastwood, K. Whittaker
Lawrence Livermore National Laboratory
P.O. Box 808, Livermore, CA 94551-0808
(925) 424-4635, e-mail: salari1@llnl.gov

Principal Investigators: L.J. DeChant
Co-Investigators: C.J. Roy, J.L. Payne, B. Hassan
Sandia National Laboratories
P.O. Box 5800, MS 0825, Albuquerque, NM 87185-0825
(505) 844-4250, e-mail: ljdecha@sandia.gov

Principal Investigator: W.D. Pointer
Argonne National Laboratory
9700 S. Cass Avenue, NE-208, Argonne, IL 60439
(630) 252-1052, e-mail: dpointer@anl.gov

Principal Investigator: F. Browand
Co-Investigators: M. Hammache, T.-Y. Hsu
Aerospace & Mechanical Engineering, University of Southern California
RRB 203, Los Angeles CA 90089-1191
(213) 740-5359, e-mail: browand@spock.usc.edu

Principal Investigator: J. Ross
Co-Investigators: D. Satran, J.T. Heineck, S. Walker, D. Yaste
NASA Ames Research Center
MS 260-1, Moffett Field, CA 94035
(650) 604-6722, e-mail: jcross@mail.arc.nasa.gov

Principal Investigator: R. Englar
Georgia Tech Research Institute
ATASL, CCRF, Atlanta, GA 30332-0844
(770) 528-3222, e-mail: bob.englar@gtri.gatech.edu

Principal Investigator: A. Leonard
Co-Investigators: M. Rubel, P. Chatelain
California Institute of Technology
1200 East California Blvd. MC 301-46, Pasadena, CA 91125
(626) 395-4465, e-mail: tony@galcit.caltech.edu

Technology Development Manager: Sid Diamond
(202) 586-8032, e-mail: sid.diamond@ee.doe.gov
Technical Program Manager: Jules Routbort
(630) 252-5065, e-mail: routbort@anl.gov

Contractors: Lawrence Livermore National Laboratory, Sandia National Laboratories, Argonne National Laboratory, NASA Ames Research Center, Georgia Tech Research Institute, University of Southern California, California Institute of Technology
Contract No.: W-7405-ENG-48, DE-AC04-94AL85000, W-31-109-ENG-38, DE-AI01-99EE50559, DE-AC03-02EE5069, DE-AC03-98EE50512, DE-AC03-98EE50506

Consortium members road-testing base flaps at Crows Landing, California.
Charles Radovich, USC
Fred Browand, USC *Scott Johnston, PATH*
Mathieu Boivin, Norcan Aluminum

Objectives

- Provide guidance to industry in the reduction of aerodynamic drag of heavy truck vehicles.
- Establish a database of experimental, computational, and conceptual design information and demonstrate potential of new drag-reduction devices.

Approach

- Develop and demonstrate the ability to simulate and analyze aerodynamic flow around heavy truck vehicles by using existing and advanced computational fluid dynamics (CFD) tools.
- Through an extensive experimental effort, generate an experimental database for code validation.
- By using experimental database, validate computations.
- Provide industry with design guidance and insight into flow phenomena from experiments and computations.

- Investigate aero devices (e.g., base flaps, tractor-trailer gap stabilizer, underbody skirts and wedges, blowing and acoustic devices), provide industry with conceptual designs of drag reducing devices, and demonstrate the full-scale fuel economy potential of these devices.

Accomplishments

- The Program has demonstrated several concepts and devices that meet the 25% drag reduction goal.
- Insight from experiments and experimental database has provided clear guidance to industry on reliable, predictable experimental techniques.
- Computational results provide clear guidance and caution warnings on the use of steady Reynolds-averaged Navier Stokes (RANS) models for CFD simulations.
- Investigated aerodynamics of filled and empty rail coal cars and designed devices predicted to produce drag reductions of 10% for empty cars.

Future Direction

- Continue to develop and evaluate drag-reducing conceptual designs and encourage and work with industry to road-test the most promising drag-reducing devices.
- Continue experimental data reduction and analysis for the generic conventional model (GCM).
- Continue computations of flow around GCM, compare to experimental data, perform analyses, and provide guidance to industry on use of unsteady RANS and hybrid RANS/Large-Eddy Simulation (LES) methods.
- Develop and use an apparatus for studying wheel and tire splash and spray, pursuing ways to minimize this road safety hazard.
- Investigate airflow around rotating tires for improved brake cooling, as well as drag reduction.
- Collaborate with DOE Industrial Consortium, which will be conducting fleet tests of advanced aerodynamic drag reduction devices. Schedule industry site visits and meetings to share findings and encourage consideration of effective design concepts for road testing.
- Leverage Program work and seek funding from other agencies.

Introduction

A modern Class 8 tractor-trailer can weigh up to 80,000 pounds and has a wind-averaged drag coefficient around $C_D = 0.6$. The drag coefficient is defined as the drag/(dynamic pressure x projected area). The higher the speed the more energy is consumed in overcoming aerodynamic drag. At 70 miles per hour, a common highway speed today, overcoming aerodynamic drag represents about 65% of the total energy expenditure for a typical heavy truck vehicle. Reduced fuel consumption for heavy vehicles can be achieved by altering truck shapes to decrease the aerodynamic resistance (drag). It is conceivable that present-day truck drag coefficients might be reduced by as much as 50%. This reduction in drag would represent approximately a 25% reduction in fuel use at highway speeds. An estimated total savings of $1.5 billion per year (pre-2004 fuel prices) can be recognized in the United States alone for just a 6% reduction in fuel use. This reduction represents 1% of all fuel use in the United States.

The project goal is to develop and demonstrate the ability to simulate and analyze aerodynamic flow around heavy truck vehicles by using existing and advanced computational fluid dynamics (CFD) tools. Activities also include an extensive experimental effort to generate data for code validation and a design effort for developing drag-reducing devices. The final products are specific device concepts that can significantly reduce aerodynamic drag (and thus improve fuel efficiency) in addition to an experimental database and validated CFD tools. The objective is to provide industry with clear guidance on methods of computational simulation and experimental modeling techniques that work for predicting the flow phenomena around a heavy vehicle and add-on drag-reducing devices. Development of effective drag-reducing devices is also a major goal.

The following reports on the findings and accomplishments for fiscal year 2004 in the project's three focus areas:

- Drag-reduction devices,
- Experimental testing, and
- Computational modeling.

A summary is given in the introduction portion of this report, and detailed reports from each participating organization are provided in the appendices. Included are experimental results and plans by NASA, USC, GTRI, and LLNL in Appendices A through D. The computational results from LLNL and SNL for the integrated tractor-trailer benchmark geometry called the Ground Transportation System (GTS) model and trailer wake flow investigations are in Appendices D and E, from ANL for the Generic Conventional Model (GCM) in Appendix F, by LLNL for the tractor-trailer gap flow investigations in Appendix D, and turbulence model development and benchmark simulations being investigated by LLNL and Caltech in Appendices D and G. USC also provides field test results for the base flap device (Appendix B), GTRI continues its investigation of a blowing device (Appendix C), and LLNL presents results for base skirts and wedges (Appendix D).

Drag-Reduction Devices

There are three areas identified for aero drag reduction, and several drag reduction devices have been investigated

- **Tractor-Trailer Gap**
  Stabilizing devices, cab extenders
- **Wheels/Underbody**
  Skirts/lowboy trailer ($\Delta C_D \sim 0.05$), splitter plate
- **Trailer Base**
  Boattail plates ($\Delta C_D \sim 0.05$), base flaps ($\Delta C_D \sim 0.08$), rounded edges, and pneumatics

Overview of Accomplishments

The Program has demonstrated several concepts and devices that meet the 25% drag reduction goal. Specific devices have addressed base, gap, and underbody drag reduction. Use of a simple base flap at the trailing edge of the trailer, side extenders or splitter plate at the tractor-trailer gap, and a skirt or a simple short underbody wedge should provide drag reduction exceeding 25%. At highway speeds, fuel savings around 12% should be recognized for a 25% reduction in drag. This would represent a savings of $3 billion/year in the United States (pre-2004 fuel prices).

The highly successful testing program has provided detailed data for computational validation, resulted in guidance on device concepts, and established wind-tunnel testing guidelines. The detailed data exceed what is typically available for careful code validation in a relatively complex flow and is thus of interest to the general fluid dynamics/aerodynamics research and development community. The state-of-the-art in Particle Image Velocimetry (PIV) was significantly advanced in the efforts at the NASA wind tunnels. With the Ground Transportations System (GTS) model in the 7-ft × 10-ft wind tunnel, NASA succeeded in being one of the first to use a three-dimensional (3D) PIV system in a production wind tunnel. To use PIV in the 12-ft pressure wind tunnel with the Generic Conventional Model (GCM), a new and innovative approach that provided remote control of the PIV system was developed. With this remote system, the tunnel was not opened — a costly and time-consuming procedure — to re-position cameras.

The computational flow modeling has provided guidance in model definition, mesh refinement, and choice of turbulence model for heavy vehicles. Computations have been used for both the evaluation of flow physics and to guide the conceptual design of devices. For example, it was demonstrated computationally that a splitter plate that *partially* closes the tractor-trailer gap is adequate to maintain the desired reduced drag, maintain symmetric flow condition, and avoid gap blow through. Previous designs assumed that *full* gap closure from the tractor to the trailer was necessary.

The Program has successfully established industry contacts and collaborations and international recognition in the academic community. The *1st International Conference on the Aerodynamics of Heavy Vehicles: Trucks, Busses and Trains,* which was led by the DOE Aero Team, attracted world-renowned researchers and developers from academia, as well as significant industry interest and participation. It should also be emphasized that by combining the best of academia and government lab capabilities, technical developments have been leveraged across programs within DOE Labs, NASA, and university programs and DOE's Heavy Vehicle Program milestones have been delivered. Examples are the progress in the state-of-the-art in 3D PIV, advances in turbulence modeling with the use of hybrid RANS and LES models for efficient and accurate flow modeling, and the use of broadcast fuel rates during real-time, full-scale testing. The Program's achievements also include the Team's many publications and record-of-inventions or patents that have resulted from the DOE Heavy Vehicle Program work.

Future Plans

Future new areas being investigated are wheel and wheel well aerodynamics related to brake cooling and tire splash and spray, as well as an entirely new related area of investigation involving the evaluation of coal car aerodynamics with the objective of identifying drag reduction devices for filled and empty cars.

The Team will continue with its computational effort while enhancing its full-scale testing effort in collaboration with fleet owners and manufacturers. Substantial efforts to establish contacts with the fleets are planned. For example, the Team representative, Jim Ross, was invited to participate in a panel at the TMA meeting in Nashville Tennessee this September. The focus topic of the panel is the recognized increase in fuel use during the cold weather season. Jim used this opportunity to share the Team's findings with fleet owners and operators and seek their feedback on ways to get aero device technology on the road.

To successfully get aerodynamic devices on the road, full-scale testing in collaboration with fleet owners and operators is needed. Testing locations that have been thus far utilized by the Team are the TRC in Ohio and Crow's Landing in California. Both controlled and long road tests are needed at speeds at or exceeding 65 miles per hour.

Computations of rotating wheels and investigations into the influence of underbody flow are planned and are recognized areas of interest to industry. This effort is in addition to moving forward on full-vehicle simulations with advanced models. Unsteady RANS and hybrid LES/RANS modeling of the full GCM vehicle with comparison and analysis of the 12-ft NASA Pressure Wind Tunnel data is planned. It is important to determine if unsteady RANS and hybrid RANS/LES turbulence modeling can capture primary flow features. Guidelines for *steady* RANS have been openly shared and are available to industry. *Unsteady* RANS and hybrid models need to be assessed for grid sensitivity and boundary conditions. This assessment will provide specific guidelines for computations with advanced models and will assist in the further conceptual design of drag-reduction devices and an integrated vehicle.

Tractor manufacturers are also interested in computational results for specific commercial tools, but it should be noted that guidelines for use of specific turbulence modeling approaches is not dependent on choice of computational tool. Currently, the National Lab participants are utilizing commercial and NASA codes, as well as their own in-house tools. There are advantages to each. For the addition of new models and for response to R&D issues, especially on large parallel machines for investigating model performance, the NASA and in-house tools provide the quickest and most flexible approach. However, for geometry and mesh generation, the commercial tools tend to provide some desirable options.

It is recognized that further fuel savings are possible and vehicle safety can be enhanced by leveraging the accomplishments of the DOE Aero Team to investigate an integrated heavy vehicle system. The effect of aerodynamics on brake cooling and engine cooling will be considered. Air control for improved braking and engine performance is currently a high priority for industry. Also, the initiated efforts in wheel, tire, and vehicle splash and spray will continue. This splash and spray investigation will provide an understanding of this multiphase flow phenomena, thus leading to conceptual designs for mitigation of splash and spray for improved vehicle and highway safety. Published research and development in the open literature appears to lack information in this area of interest.

The Team is also planning to continue its pursuit to improve aerodynamics and reduce fuel use areas with flow regimes similar to those of heavy vehicles. This year's experiments and computations of railway coal cars have demonstrated the substantial increase in drag from full to empty railcars. The aerodynamic drag of an empty railcar in the wind tunnel is 32% and 42% at 0 and 10° yaw, respectively, compared with that for a full railcar. We plan to continue working with our contact, Jim Hart, of Johnstown America Corporation (Johnstown, Pennsylvania) for guidance in conceptual designs that are automatic and durable for the 20-plus-year life of a coal car. Experiments and computations have been used for the smart design of drag mitigating devices. These conceptual designs will condition the flow so that the empty car will mimic the flow of a full car, providing substantial fuel savings.

B. A Study of Reynolds Number Effects and Drag-Reduction Concepts on a Generic Tractor-Trailer

Principal Investigator: Bruce L. Storms
AerospaceComputing, Inc.
M/S/260-1
NASA Ames Research Center
Moffett Field, CA 94035
(650) 604-1356, fax: (650) 604-4511, e-mail: bstorms@mail.arc.nasa.gov

Field Project Manager: James C. Ross
NASA Ames Research Center
M/S/260-1
Moffett Field, CA 94035
(650) 604-1356, fax: (650) 604-4511, e-mail: james.c.ross@nasa.gov

Technology Development Area Specialist: Sidney Diamond
(202) 586-8032, fax: (202) 586-1600, e-mail: sid.diamond@ee.doe.gov
Technical Program Manager: Jules Routbort
(630) 252-5065, fax: (630) 252-4289, e-mail: routbort@anl.gov

Participants
Dale R. Satran, James T. Heineck, Stephen M. Walker
NASA Ames Research Center

Contractor: NASA Ames Research Center
Contract No.: DE-AI01-99EE50559

NASA's effort consists of two experimental focus areas:

- A Study of Reynolds Number Effects and Drag-Reduction Concepts on a Generic Tractor-Trailer Objective
- An Experimental Study of Aerodynamic Drag of Empty and Full Coal Cars

The following describes the objectives, approach, accomplishments, and future direction for each of these focus areas.

Objectives

- To investigate Reynolds-number effects on the flow field and resulting aerodynamic forces generated by a 1:8-scale model of a class-8 tractor-trailer configuration.
- To provide quality experimental data on a simplified tractor-trailer geometry for CFD validation.

Approach

- Vary the total pressure of the wind tunnel, thereby varying the Reynolds number from 500,000 to full-scale values over 6 million, on the basis of trailer width.
- Measure the forces and momentum surface, pressure distribution, and off-body flow. Measurements were made at various yaw angles to study the influence of crosswind and to calculate wind-averaged drag coefficients.
- Several drag-reduction concepts were studied to document their potential benefit as well as their Reynolds-number sensitivity.

Accomplishments

- CFD validation data are now available for use by interested industry and government researchers.
- Reynolds number effects were found to be relatively small above a value of ~1 million. Care should be taken in interpreting smaller-scale data.
- The results of the study were presented at the 34th AIAA Fluid Dynamics Conference and Exhibit in Portland, Oregon, on July 1, 2004 (paper number AIAA-2004-2251).

Future Direction

- Additional drag-reduction devices will be examined for under-body flow control/drag reduction.
- Results from this study will be made more widely available via CD/DVD distribution to interested parties.

Introduction

For a typical heavy vehicle at a highway speed of 70 mph, the energy required to overcome aerodynamic drag is about 65% of the total expenditure (which also includes rolling friction, transmission losses, and accessories). By altering the vehicle shape, it has been estimated that modern truck drag coefficients may be reduced by up to 50%, resulting in an annual national fuel savings of three billion gallons. This large potential savings, coupled with increasing fuel costs, has spurred renewed interest in heavy-vehicle aerodynamics.

Recently, a series of experimental and computational studies has been funded by the Department of Energy. With the goal of CFD validation, the experimental efforts have focused on simplified geometries at 1:8-scale and below. Early experiments focused on the simplified geometry of the Ground Transportation System (GTS) model representative of a class-8 tractor-trailer with a cab-over-engine design. A 1:8-scale GTS model with no tractor-trailer gap and no wheels was first studied with the addition of several ogival boattails and slants to the base of the trailer. The largest overall drag reduction of 10% was obtained by an 8-ft ogive configuration (full scale). The addition of boattail plates to the same model resulted in a 19% drag reduction, and particle image velocimetry (PIV) measurements behind the trailer document a significant reduction in the wake size due to the flow turning provided by the plates. Variation of the tractor-trailer gap on a 1:15-scale model at zero yaw revealed relatively constant drag on the tractor while the trailer drag increases by a factor of three as the gap increases from zero to $1.55*\sqrt{A}$. Reynolds-averaged Navier-Stokes computations of this geometry include both grid-size and turbulence-model studies.

The Generic Conventional Model of the current study was previously investigated at a Reynolds number of 1.1 million in the NASA-Army 7-ft × 10-ft wind tunnel. The results include forces and moments, surface pressures, and 3-D particle-image velocimetry. Measurements of two tractor-trailer gaps (40 and 80 inches full scale) indicated significantly greater drag for the larger gap at low yaw angles (between ±4°) and reduced drag at higher angles. Several drag-reduction concepts were investigated, including tractor side extenders, boattail plates, and a trailer belly box. Comparisons of PIV data were presented in the tractor-trailer gap with and without side extenders and in the trailer wake with and without boattail plates.

Experimental Setup

The investigation was conducted in the 12-Foot Pressure Wind Tunnel located at the NASA Ames Research Center. This facility can be pressurized from 0.25 to 6 atmospheres at Mach numbers from 0.1 to 0.5. The test section has a circular cross section 12 ft in diameter with four 4-ft-wide flat surfaces centered about the horizontal and vertical centerlines. A ground plane was installed 21 in. above the tunnel floor, providing a flat surface 10 ft wide and 18 ft long. Pressure taps were located on both the ground plane (2 rows of 64 taps) and the test-section walls (8 rows of 30 taps). A fairing was installed to isolate the model-support hardware from the air stream, and speed-correction probes were used to correct the facility speed as a result of the blockage of the ground plane and fairing. There was also an additional pitot-static probe installed on the upper-left ceiling to measure the free-stream conditions in the test section. All of the data presented are referenced to the Mach number based on a wall tap at location 6.17 ft forward of the center of rotation at an azimuth of 60° from vertical (two o'clock looking downstream).

A photograph of the GCM baseline configuration installed in the wind-tunnel test section is shown in Figure 1. This 1:8-scale model is representative of a generic class-8 tractor-trailer with the engine in front of the cab. Designed for CFD validation, the model includes a number of geometry simplifications in order to facilitate grid generation and avoid the associated flow complexities. In particular, no effort was made to duplicate the complex geometry of the undercarriage of either the tractor or trailer (both were approximated by flat surfaces). Similarly, the wheel wells of the tractor were not modeled, and only the portion of the wheels below the tractor lower surface was included. Also, the tractor geometry (designed by the Calmar Research Corp.) is a streamlined shape representative of a modern tractor design while omitting most small-scale surface details and flow-through components. The trailer measures 45 ft in length (full scale) with

Figure 1. The Generic Conventional Model installed in the 12-Ft Pressure Wind Tunnel.

rounded front vertical edges (8-in. full-scale radius). The tractor-trailer gap for this study was held constant at the full-scale equivalent (40 in.). The GCM was attached to the model-support hardware by using four vertical posts that were 1.75 in. in diameter. The four posts were non-metric, with 0.030 in. of clearance as they passed through the trailer floor. The model was mounted with its wheels 0.15 in. above the ground plane and centered laterally in the tunnel. The center of rotation of the model was located 54.36 in. aft of the tractor front bumper. The model frontal area of 1.6623 ft^2 gives a solid blockage of 1.5%.

The overall model loads were measured by using a six-component internal balance that was mounted inside the trailer. The manufacturer-specified accuracy of the internal balance in the axial (drag) direction was ±1 lb, but repeat runs indicated the experimental uncertainty to be on the order of ±0.5 lb. The tractor was suspended from the trailer through a set of flexures and two load cells that measure the drag and yawing moment of the tractor alone. The specified accuracy of the load cells was ±0.45 lb. The model was instrumented with 200 pressure taps on the tractor and 276 taps on the trailer. There were also 12 unsteady pressure transducers mounted on the tractor rear surface, trailer front surface, and the trailer rear surface. A three-component PIV system was used to obtain horizontal-plane velocity measurements in the tractor-trailer gap. Details of the PIV system installation are presented in Ref. 12. Pressure measurements will be documented in a future report.

The model was yawed through a range of angles between ±14°. Except where noted, all data were acquired at a Mach number of 0.15, which allowed for Reynolds number studies with no Mach-number effects. With the tunnel pressurized to six atmospheres, the Reynolds number was over 6 million, on the basis of the trailer width, which is comparable to a full-scale truck driving at 75 mph. At one atmosphere, the Reynolds number was 1 million, based on the trailer width, which is comparable to a full-scale truck driving at 15 mph.

Various add-on drag-reduction devices were tested on the bases of both tractor and trailer, as well as on the trailer under-carriage. In this report, results will be presented for tractor side and roof extenders, trailer boattail and base flaps, and trailer belly box and skirts. Details of each device will accompany the discussion of the associated results.

Results and Discussion

The results presented below detail the body-axis axial force (drag) coefficient for the tractor-trailer combination and its components. This drag coefficient represents the force along the axis of the vehicle in the direction of travel. The internal balance also provided lift, side force, and moment measurements, which will not be discussed. With the objective of CFD validation, no wall corrections were applied to the data, and all coefficients were calculated on the basis of the static pressure at a known point in the test section (as detailed above). Without wall corrections, the computed drag coefficients will differ from those of the equivalent model in free air. However, the measured differences between configurations should be representative of the effects of the associated geometric modifications.

The drag data presented herein were acquired for increasing yaw angle, unless otherwise noted. Using the variation of drag with yaw angle, wind-averaged drag coefficients were computed by using the SAE Recommended Practice of Ref. 13. This practice assumes that the mean wind speed in the United States of 7 mph has an equal probability of approaching the vehicle from any direction. This mean wind speed and the vehicle velocity were used to calculate a weighted average of the drag coefficient at various yaw angles. The wind-averaged drag coefficients reported in this paper were computed for a highway speed of 55 mph.

A. Baseline Configuration

The baseline geometry for this study is representative of a modern tractor design with the standard aero package less the side or roof extenders. Yaw angle sweeps for increasing and decreasing angle revealed significant hysteresis in the resulting drag measurements (Figure 2). Since the drag curve of a simplified geometry with no gap is relatively continuous, the discontinuities at high yaw angles are likely due to changes of the flow structures within the tractor-trailer gap. The effect of Reynolds number is most evident at the yaw angles

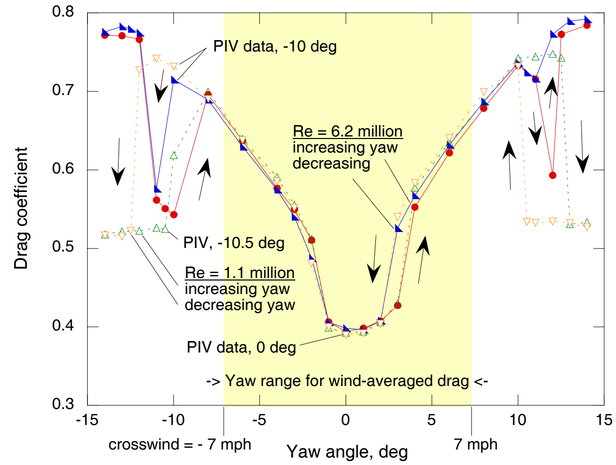

Figure 2. Baseline hysteresis of drag coefficient for two Reynolds numbers.

greater than 8° where the peak drag and hysteresis are notably different. At lower yaw angles, however, the differences are relatively small and the hysteresis paths are nearly duplicated. For a mean crosswind of 7 mph ($-7.2 < \psi < 7.2$) as shown in Figure 2, the wind-averaged drag coefficients at Reynolds numbers of 1 and 6 million (0.582 and 0.578, respectively) differed by less than 1%.

A three-component PIV system was employed for velocity measurements in the tractor-trailer gap. The velocity vector maps (Figures 3–5) are averages of 100 discrete measurements acquired at 2 Hz in intermittent bursts (due to computer limitations) over a period of three minutes. Although data were acquired at 1/4, 1/2, and 3/4 trailer heights, the results presented in this report are limited to the topmost location. In these figures, the direction and magnitude of the vectors indicate the in-plane velocities, while the color map indicates the out-of-plane (vertical) velocity. The velocity vector maps for zero yaw (Figure 3) reveal two counter-rotating recirculation regions in the gap and suggest minimal sensitivity to Reynolds number. The yaw angle of –10° (Figure 4), however, is in the hysteresis region of the drag curves where there are significant differences between two Reynolds numbers. Both measurements were obtained for decreasing yaw angle that correspond to the upper curves, as indicated in Figure 2. Similar to the zero-yaw case, the flowfield at Re = 5 million exhibits two recirculation regions, but they are strongly

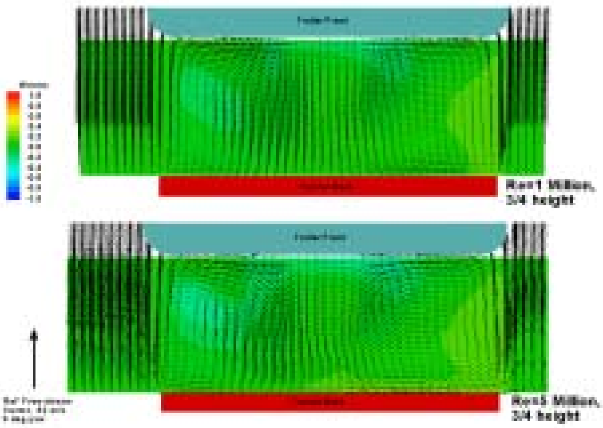

Figure 3. PIV measurements in the tractor-trailer gap at yaw = 0°. Top view of horizontal PIV data plane at 0.75 h.

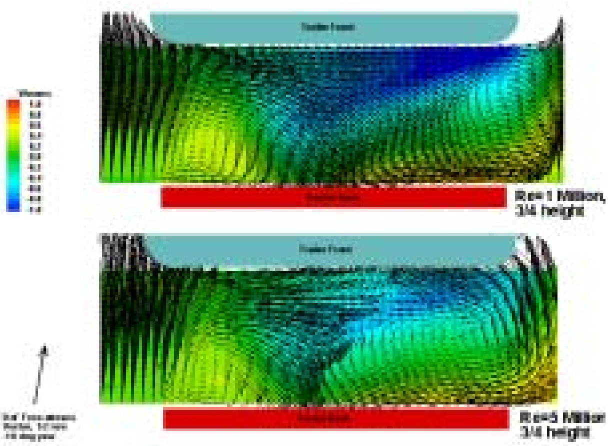

Figure 4. PIV measurements in the tractor-trailer gap at yaw = -10°.

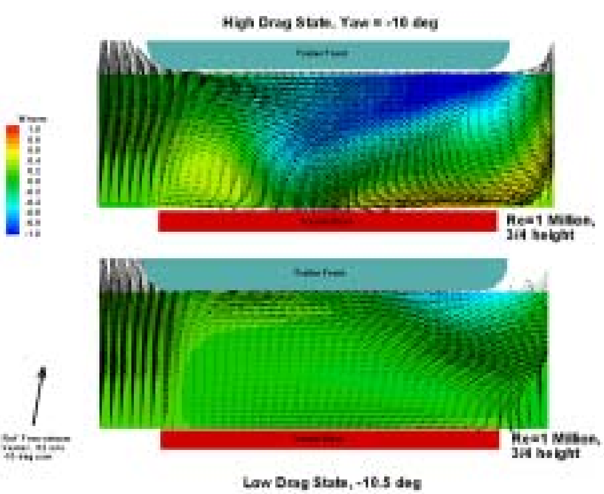

Figure 5. PIV measurements in the tractor-trailer gap for high- and low-drag states near -10°. Top view of horizontal PIV data plane at 0.75 h.

asymmetric and with much higher velocities. At Re = 1 million, only the tight recirculation on the windward (left) side is present, and there are significantly greater crossflow and downward velocities compared to the higher Reynolds number. The corresponding drag coefficient for Re = 1 million is 2% higher than that for Re = 5 million. The lower measurement locations revealed similar flow structures to the topmost height, but with reduced Reynolds-number sensitivity.

The PIV data also provide insight into the drag-curve hysteresis. A look at two neighboring yaw angles near –10° reveal drastically different flowfields at one Reynolds number (Figure 5). As indicated on the drag curves (Figure 2), these two measurements correspond to yaw angles of –10° (decreasing) and –10.5° (increasing) at Re = 1 million. For the yaw angle of –10.5°, the windward recirculation region is absent, and the velocities in the gap are significantly lower than the –10° case. It is hypothesized that lower gap velocities yield higher pressures on the back of the cab (less drag) and a smaller separation region on the leeward (right) side of the truck (not visible in PIV images). As a result, the drag of the –10.5° case is 28% lower than that of the –10° case.

B. Side and Roof Extenders

Similar to the components of a modern tractor aero package, side and roof extenders were attached to the rear of the tractor, as shown in Figure 6. The extenders were 1/8-in. thick (model scale), with four different lengths ranging from 30% to 60% of the tractor-trailer gap. For a length of 60% gap (as shown), the total drag coefficient as a function of yaw angle (Figure 7) illustrates the dramatic effect of the extenders. At yaw angles less than 2°, the drag reduction is minimal, while at higher angles, the reduction increases dramatically to 35% at 10°. At a Reynolds number of 6 million, the wind-averaged drag coefficient of 0.422 for the 0.6 g extenders was 27% lower than that of the baseline without extenders. The low Reynolds-number measurements were marginally higher than those of the full-scale Reynolds number until about 10° yaw, at which point the curves cross and the low-Re drag drops off at the highest yaw angle of 14°. PIV data for this model with extenders were acquired previously in the NASA Ames 7- × 10-ft wind tunnel at a

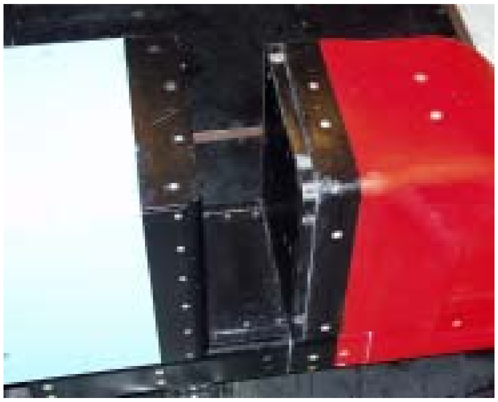

a) Baseline configuration

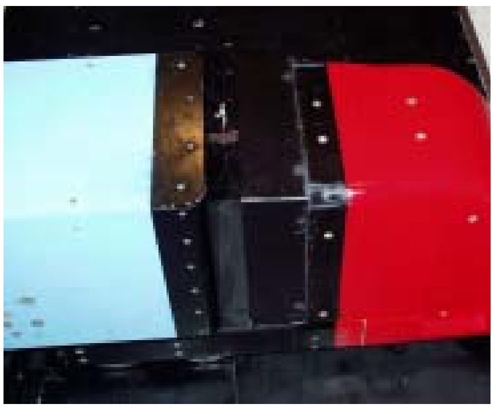

b) Side and roof extenders (0.6 g)

Figure 6. Close-up of tractor-trailer gap with and without side and roof extenders.

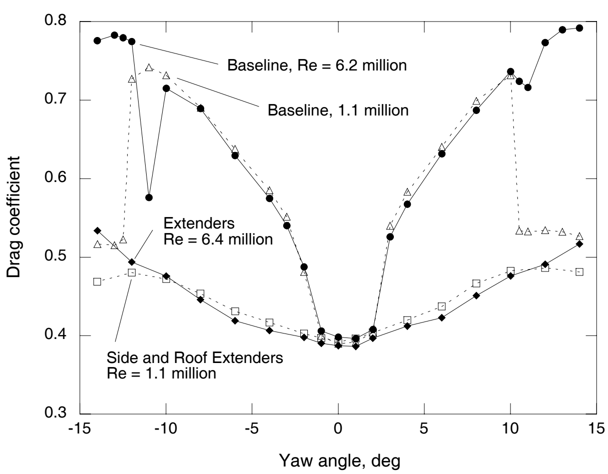

Figure 7. Effect of tractor side and roof extenders (0.6 g) on total drag coefficient.

Reynolds number of 1 million. The results indicate a significant reduction in the gap cross flow due to the presence of the side and roof extenders.

The wind-averaged drag reduction provided by the extenders is plotted as a function of extender length in Figure 8. For the four extender lengths tested between 30% and 60% gap width, there is a consistent trend of increasing drag reduction with increasing extender length. More specifically, the drag reduction increases from 25% to 27% for an increase in extender length from 30% gap to 60% gap. Although greater extender lengths may be impractical from an operational standpoint, these data suggest that additional drag reduction may be obtained by completely blocking the gap crossflow. As demonstrated in Ref. 2, a centerline gap seal can be more effective than the side extenders of a standard tractor aero package.

To determine the effect of Reynolds number, the facility total pressure was varied while the Mach number was held constant. The change in wind-averaged drag coefficient with Reynolds number (Figure 9) reveals differing sensitivities for the baseline and extender configurations. In this figure, the error bars on the baseline data points show the magnitude of experimental uncertainty due to both measurement resolution and repeatability. Error bars were of the same magnitude for the extender configuration, but they were omitted from the figure for clarity. For the baseline, the drag coefficient is observed to increase by an average of 0.006 (1%) for Reynolds numbers less than 4 million. The extender configuration, however, does not indicate a significant increase until below 3 million, with a

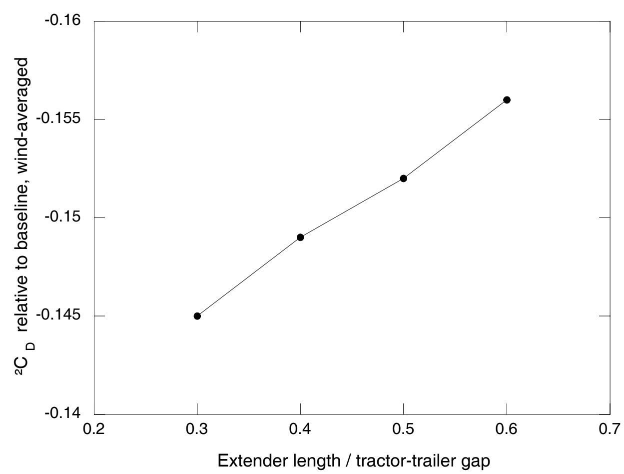

Figure 8. Wind-averaged drag reduction due to side and roof extenders at Re = 6 million.

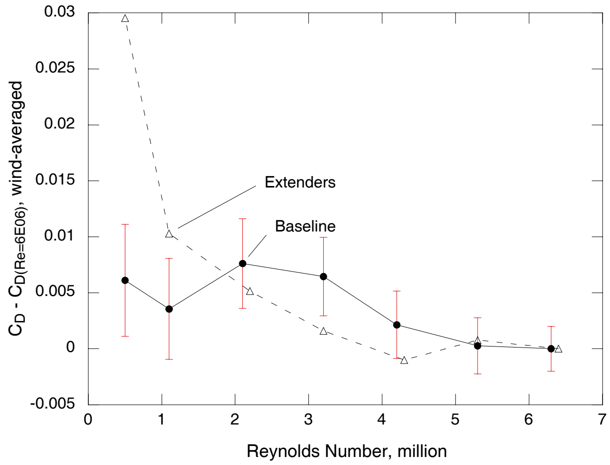

Figure 9. Reynolds-number sensitivity of wind-averaged drag for baseline and side extenders.

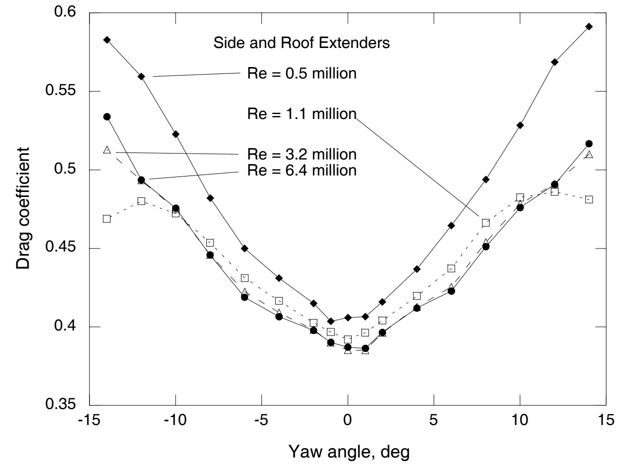

Figure 10. Reynolds-number sensitivity of side and roof extenders on drag curves.

dramatic increase, close to 0.03 (6.9%), at Re = 500,000. The drag curves for the extender configuration at several Reynolds numbers (Figure 10) illustrate a significant increase in drag that increases with crossflow at Re = 500,000. This increase is likely due to flow variations in the vicinity of the trailer leading-edge curvature, which is more sensitive to Reynolds number than to sharp corners.

C. Aerodynamic Boattail Plates

Since the side and roof extenders are first-generation drag-reduction devices common to most modern tractor aero packages, the effect of the boattail plates (and all subsequent devices) will be measured relative to the extender configuration. Aerodynamic boat-tailing devices have several different variations, but boattail plates typically refer to panels mounted perpendicular to the trailer base and inset from the edges of the trailer. In this case, the same boattail plates that were studied on the simplified GTS model[5] were applied to the rear of the GCM trailer, as shown in Figure 11. The plates extended 3.75 in. from the end of the trailer and were inset 0.625 in. from the sides and top of the trailer. The bottom plate was mounted flush with the bottom of the trailer.

Figure 11. Aerodynamic boattail plates installed on the base of the trailer.

Relative to the side and roof extenders, the boattail plates significantly reduced the drag by a relatively constant margin between ±10° (Figure 12). At Re = 6 million, the wind-averaged drag coefficient

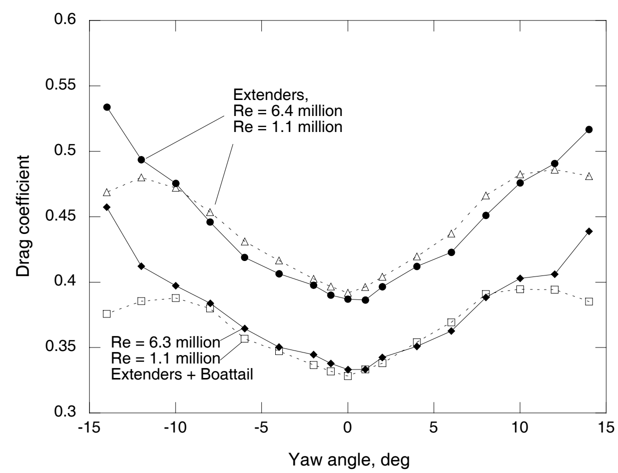

Figure 12. Effect of boattail plates on total drag coefficient.

was 0.364, which is 13.7% less than the extenders-only configuration. Relative to the high-Reynolds-number case, the drag curve for the boattail plates at Re = 1.1 million exhibited the same roll off at high yaw angles as that of the side extenders alone. The results were mixed at lower angles, with the low-Re curve lower than the high-Re curve at negative yaw angles and higher at some positive yaw angles. These mixed results are evident in the resulting wind-averaged drag coefficients, which differ by only 0.6%.

D. Trailer Base Flaps

Another method of aerodynamic boat-tailing is what will be referred to as base flaps. In this embodiment, the panels are attached to the edges of the trailer base and angled inward. In the current study, measurements were made for a base-flap length of 3.125 in. (25 in. full scale) at angles ranging from 0 to 28°. The installation photo (Figure 13) shows the base flaps with a 20° deflection mounted on the rear of the trailer. Note that the linkages connecting the flaps to the base were designed for easy angle change and are not representative of the full-scale hardware.

The effect of the base flaps on the total drag coefficient is presented in Figure 14 for a flap angle of 16°. Relative to the side and roof extenders alone, the addition of the base flaps provides significant drag reduction that marginally increases with yaw angle. The Reynolds-number sensitivity of the base flaps is minimal for most yaw angles between ±10°. As in the previous configurations, the drag for Re = 1.1 million rolls off at the higher yaw angles, while the drag at full-scale Reynolds number continues to increase.

The effect of base-flap angle on wind-averaged drag reduction is presented in Figure 15. Different symbols are used to indicate the data from two separate wind-tunnel entries (four months apart) of the same model in the NASA Ames 12-Ft Pressure Wind Tunnel. The lower Reynolds number on the second entry was due to limitations of the coincident PIV measurements. Although there is an unexplained offset in the two curves (marginally larger than the experimental uncertainty), the trends indicate that the optimum base-flap angle is around

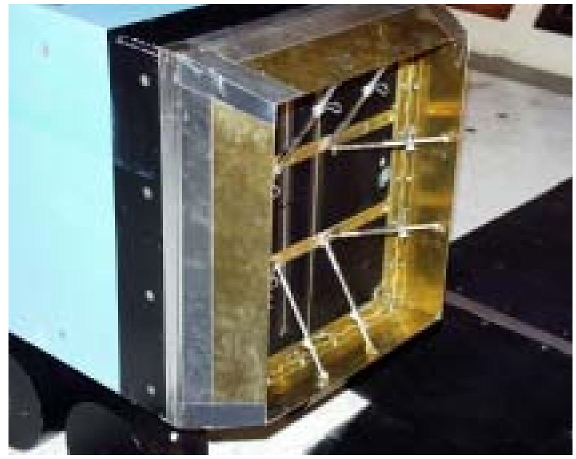

Figure 13. Base flaps installed on trailer base (flap angle = 20°).

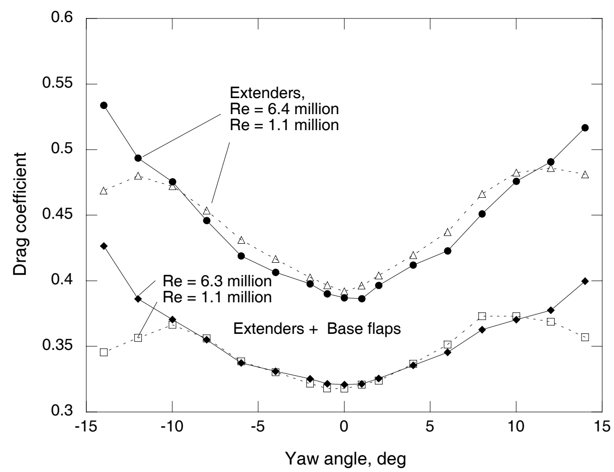

Figure 14. Effect of 16° base flaps of total drag coefficient.

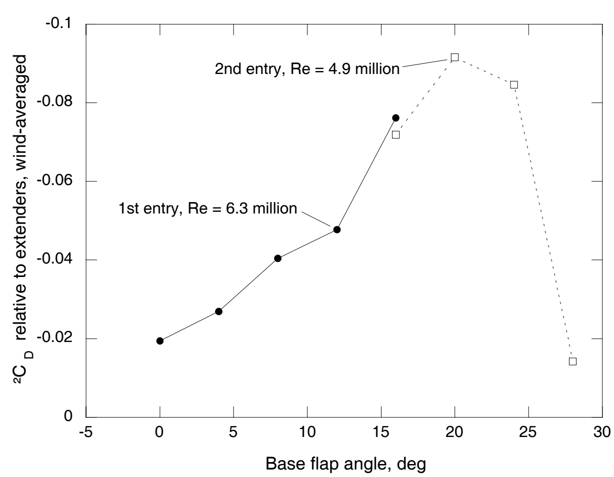

Figure 15. Effect of base-flap angle on wind-averaged drag reduction.

20°. The wind-averaged drag coefficient with 20° base flaps is 0.340, which is 19.4% less than the extender configuration and 6.6% less than the boattail-plate configuration. Previous small-scale experiments[2] at a Reynolds number of 1.25 million yielded an optimum base-flap configuration with an angle of 15° and a full-scale panel length of 20 inches. The difference between these two experiments is likely due to the differences in the base-flap lengths since the Reynolds-number effects were observed to be minimal. However, the effect of Reynolds number might be more significant at higher flap angles where the flow reattachment on the base flaps is more sensitive.

E. Trailer Belly Box and Skirts

Several drag-reduction concepts were studied, with the goal of reducing the lateral flow under the trailer. As in previous studies, trailer side skirts consisted of flat panels extending downward from the sides of the trailer between the end of the tractor bed and the front of the trailer wheels. The full-skirt configuration extended to the rear of the trailer covering the trailer wheels and included lateral panels at the trailer base and behind the tractor bed. The trailer belly box (Figure 16), so named because of its resemblance to the design of moving trailers, was identical to the full-skirt configuration, with the addition of a horizontal surface at the bottom of the skirt to form a box on the undercarriage of the trailer. All of these configurations had full-scale (11.8 in.) ground clearance.

The varying effect of the trailer belly box and skirts on the overall drag is presented in Figure 17 for Re = 6.3 million. Relative to the extender-only case, the trailer belly box was the most effective, with a wind-averaged drag reduction of 11.8%. The side skirts were somewhat less effective, with a drag reduction of 6.2%, while the full-skirt configuration increased the wind-averaged drag by 3.8%. The increase in drag of the full-skirt configuration is likely due to the cavity flow that forms inside the skirt. The wind-averaged drag coefficients for these three cases were 0.372, 0.396, and 0.438, respectively. Because of time limitations, a Reynolds-number sensitivity study was not performed for these configurations.

a) Baseline (no belly box)

b) Trailer with belly box

Figure 16. Rear view of trailer with and without belly box.

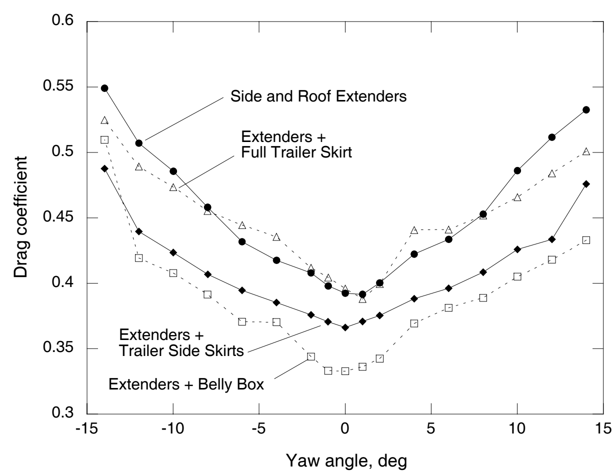

Figure 17. Effect of trailer belly box and skirts on total drag coefficient (Re = 6.3 million).

Conclusions

For all configurations, the effect of Reynolds number was most evident at high yaw angles ($y > 8°$ and $y < -8°$) where there was a significant reduction in drag at lower Reynolds numbers. However, this difference did not significantly affect the computation of the wind-averaged drag coefficients at 55 mph, which uses data at lower yaw angles. As a result, the variation of Reynolds number for the baseline revealed an increase in the wind-averaged drag on the order of 1% for Re ≤ 3 million. The Reynolds-number sensitivity for side and roof extenders was more dramatic with an increase in wind-averaged drag of over 7% for Re = 500,000. Limited data for the boat-tail devices suggest that the Reynolds-number sensitivity is similar to that of the baseline. No Reynolds-number study was performed for the undercarriage flow barriers.

The PIV measurements in the tractor-trailer gap document significant crossflow velocities and recirculation regions at yaw angles near 10°. Baseline measurements with reduced drag exhibited significantly reduced crossflow and less-coherent recirculation regions. Since the tractor side and roof extenders function to reduce the gap crossflow and increase the tractor back pressure, the addition of the extenders to the baseline reduced the measured drag at all yaw angles. This reduction was dramatic at high yaw angles (35% at 10°) and minimal at low angles (2% at 0°). Of the four extender lengths tested (0.3–0.6 gap), the longest extenders were most effective yielding a 27% reduction in the wind-averaged drag coefficient. Since extenders are a standard component of a modern tractor aero package, the effectiveness of the remaining drag-reduction concepts were measured relative to this extender configuration. Note that no wall corrections were applied to the experimental measurements in order to facilitate comparison with CFD simulations. However, the influence of the tunnel walls was minimized by calculating the tunnel speed on the basis of the static pressure at a location adjacent to the model.

Of the boat-tailing concepts (boattail plates and base flaps), the base flaps were found to be most effective. Base-flap angles from 0 to 28° were studied, resulting in an optimum angle of 20°. This result is higher than a previous low-Reynolds-number study and may suggest some Reynolds-number sensitivity of the base-flap angle. The trailer belly box was the most effective trailer-undercarriage concept, with almost double the drag reduction of simple side skirts. The belly box and full skirt configurations were identical except for the lower-surface enclosure of the belly box. The drag of the full-skirt configuration, however, was increased while that of the belly-box configuration was significantly reduced. This result stresses the importance of eliminating cavity flows to minimize drag.

For more details and a list of references, please see the associated technical paper (AIAA-2004-2251).

C. An Experimental Study of Aerodynamic Drag of Empty and Full Coal Cars

Objective

- To investigate the additional aerodynamic drag experienced by empty coal cars relative to cars full of coal and methods to reduce the empty-car drag.

Approach

- Small-scale wind-tunnel tests of empty and full coal cars and associated drag-reduction devices. 1:87th scale models were used — drag measured by using a miniature 2-lb linear load cell.

Accomplishments

- The drag penalty of empty coal cars relative to full cars varies from 35% to 42%, depending on the direction of the prevailing wind (0–10°).
- Initial tests of vertical plates in the empty car showed a ~50% reduction in the drag penalty for empty cars.

Future Direction

- Additional drag-reduction devices will be examined in collaboration with a coal car manufacturer and Lawrence Livermore National Laboratory researchers.

As part of a DOE-sponsored study, the aerodynamic drag of 1/87th-scale coal cars was measured in a wind tunnel. The goal of the experiment was to measure the difference in drag between full and empty cars to determine if drag mitigation efforts are warranted.

The measurements were made in the NASA-Ames 15-in. × 15-in. low-speed wind tunnel. This is an open-circuit, suction-type tunnel with at square test section measuring 60 in. in length. Five coal cars were mounted on a scale train track (Figure 1), with the middle car connected to the upwind car by a 2-lb load cell (Figure 2) and disconnected from the downwind car. All cars (except the middle car) were glued to the track to prevent motion along the track. This configuration was tested at a freestream velocity of 65 m/s (145 mph) with and without simulated coal. The tunnel speed was chosen to maximize the measured drag and minimize measurement uncertainty. The five-car combination was tested at yaw angles of zero and 10° to determine the effects of crosswind. The blockage of the coal cars at zero yaw was 0.9%.

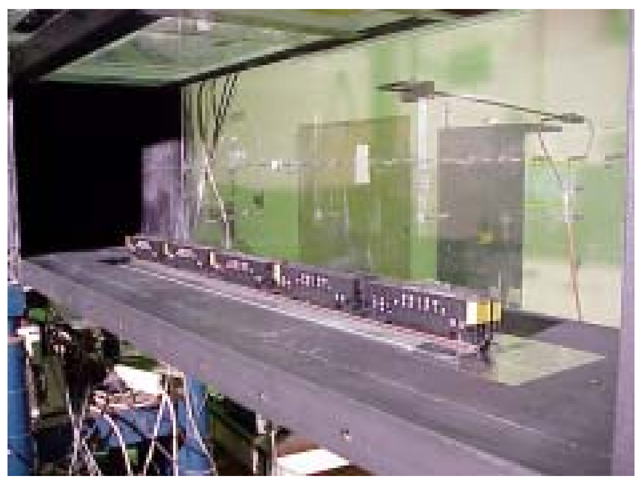

Figure 1. Five coal cars mounted in wind-tunnel test section. Pitot-static probe used for tunnel speed measurement is visible above first car near the top of the photo.

The small- and full-scale Reynolds numbers of the coal cars (assuming full-scale velocity of 60 mph) are 0.16 and 5.8 million, respectively. Because of the nature of bluff-body flow fields, this difference in Reynolds number is not expected to significantly affect the experimental results. The drag coefficient for each configuration (Table 1) was calculated on the basis of the square root of the zero-yaw frontal area. The uncertainty based on measurement resolution and repeatability was 1.2–2.5%,

Figure 2. Load cell connecting metric car (at left) to upwind car (at right). The load cell is the thin vertical strip at the center of the photo. Instrumentation wiring enters upwind car in the white cable. Simulated coal is visible in both cars.

Table 1. Drag coefficients for full and empty coal cars at 0 and 10° yaw (empty car is reference at each yaw angle).

Yaw (°)	Cd empty	Cd full	%diff
0	0.315	0.216	31
10	0.519	0.300	42

depending on the magnitude of the drag measurement. As indicated below, the drag on the full coal car was significantly less than that of the empty car (32%). This difference was even greater (42%) for the 10° yaw condition in which the drag was significantly increased relative to the zero-yaw case. These results suggest that significant fuel savings could be obtained by reducing the drag of the empty coal cars.

Vertical dividers were installed to manipulate the flow inside the cars, with the goal of making the external flow more like it is when the car is loaded with coal (Figure 3). The dividers had a significant effect on the drag. The single divider reduced the empty-car drag by 15% at zero yaw. The three dividers reduced the empty-car drag by 21%. More work is needed to identify the overall best approach to drag reduction. This effort will be considerably helped by the concurrent CFD being performed at Lawrence Livermore National Laboratory.

Figure 3. Vertical plates installed in model cars. Note single and three evenly spaced vertical dividers.

D. Experimental Measurement of the Flow-Field of Heavy Trucks

Principal Investigator: Fred Browand
Aerospace & Mechanical Engineering, University of Southern California
RRB 203, Los Angeles CA 90089-1191
(213) 740-5359, fax: (213) 740-7774, e-mail: browand@spock.usc.edu

Technology Development Area Specialist: Sidney Diamond
(202) 586-8032, fax: (202) 586-1600, e-mail: sid.diamond@ee.doe.gov
Technical Program Manager: Jules Routbort
(630) 252-5065, fax: (630) 252-4289, e-mail: routbort@anl.gov

Contractor: National Energy Technology Laboratory, Pittsburgh, PA 15236-0940
Contract No.: DE-AC03-98EE50512

Objective

- Improve the performance of heavy trucks by reducing aerodynamic drag and by increasing safety.

Approach

- Identify areas where improved use of aerodynamic design could decrease truck drag and consequently improve fuel economy. These include:
  – Gap between tractor and trailer — We have identified the importance of cross-gap flow as a source of drag increase.
  – Trailer base — We have performed wind tunnel testing to evaluate the performance of various flapped devices to close the trailer-base wake more efficiently.

Accomplishments

I. Minimizing drag due to cross-gap flow

- Wind tunnel flow field studies document the appearance of violent cross-gap flows under certain conditions.
- The cross-gap flow has been studied by means of a special analysis procedure entitled Proper Orthogonal Decomposition.
- Suggestions are made to minimize this unwanted cross-gap flow by means of a simple splitter plate attached to the front of the trailer and partially covering the gap.

II. Field measurement of fuel savings using a trailer-base add-on

- Field tests directly measure fuel consumption of a Class-8 tractor and trailer with and without flaps attached to the sides and top of the trailer. The most promising flap geometry for field test was chosen on the basis of wind tunnel tests.
- The field test documents fuel savings of about 4%; to our knowledge, these savings are the best that have been achieved for a simple, passive, trailer-base add-on.

Future Direction

- Initiate a program and a new testing apparatus to study wheel/tire splash and spray.

This report describes the progress we have made on two separate aerodynamic problems (I) describing the sensitivity of the drag to the geometry of the gap between tractor and trailer and (II) providing field test results of high quality to demonstrate the fuel savings to be realized for flaps attached to the base of a trailer.

I. Minimizing Drag due to Cross-Gap Flow

Certain aspects of the tractor-trailer gap flow-field have been described in a paper ("Flow Structure in the Gap Between Two Bluff-Bodies," D. Arcas, F. Browand, & M. Hammache, AIAA Paper No. 2004-2250) prepared for the AIAA meeting in Portland June 28–July 1, 2004. The gap data are presented in the mathematical format of a Proper Orthogonal Decomposition, which will facilitate comparisons between the experimental results and the ongoing numerical computations at LLNL.

This work and earlier studies describing the gap flow ("On the Aerodynamics of Tractor-Trailers," M. Hammache & F. Browand, *Proceedings of the UEF Conference on: The Aerodynamics of Heavy Vehicles: Trucks, Buses and Trains*, Lecture Notes in Applied and Computational Mechanics, Springer-Verlag, Heidelberg, September 2004) have provided a clear and quantitatively correct picture of the flow field within the gap for a variety of flow conditions. An example of the gap flow for an angle of yaw of 6° is shown in Figure 1.

The velocity field within the gap is determined from Digital Particle Image Velocimetry (DPIV) measurements. Accurate mean-flow streamlines are superimposed upon several field quantities plotted in color in the upper left of Figure 1. On the upper right of Figure 1 is the mean velocity magnitude; to the lower left is mean, or average, vorticity; and to the lower right is the root-mean-square amplitude of the unsteady fluctuation. The flow crossing the gap can be seen to be quite large — especially in the vicinity of the front of the trailer. The flow picture suggests that a short fin, or plate, protruding from the front of the trailer might serve to substantially or entirely disrupt the cross-gap flow.

Splitter-Plate Gap Stabilization

A follow-on experiment, performed by Eric Liu at USC, shows the effect upon trailer drag of a splitter plate of various lengths placed at the nose of the trailer in the center-plane. The geometry is shown in

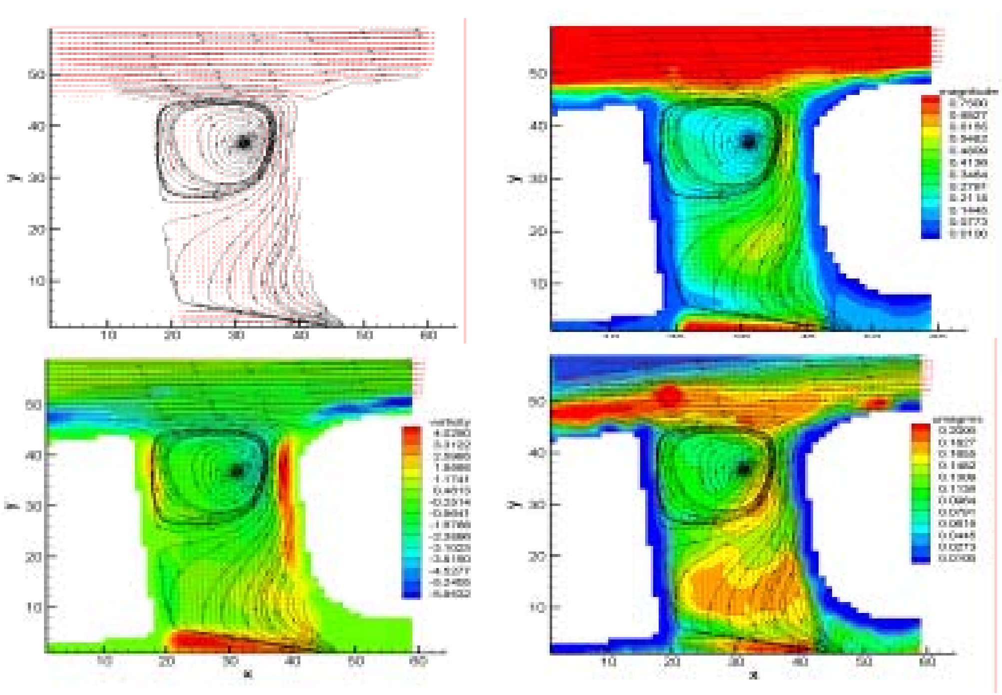

Figure 1. Wind tunnel model of simple tractor-trailer gap flow at a gap of ½ trailer width. The cab outline to the left and the trailer outline to the right are yawed 6° to simulated a side-wind.

Figure 2, and photographs of the model in the USC wind tunnel are shown in Figures 3 and 4. The gap, G, is normalized by the square root of the cross-sectional area, √A = 181 mm.

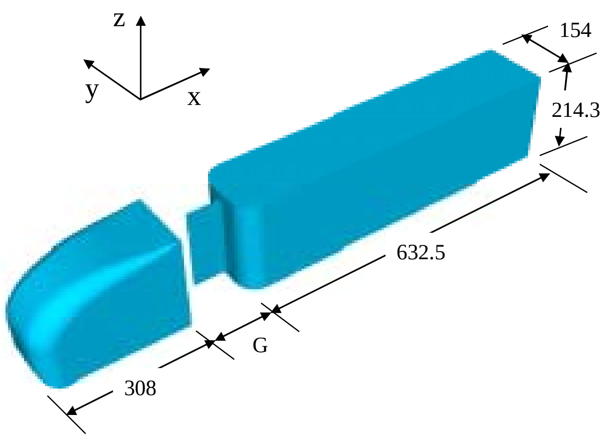

Figure 2. Geometry of wind tunnel model (dimensions in mm).

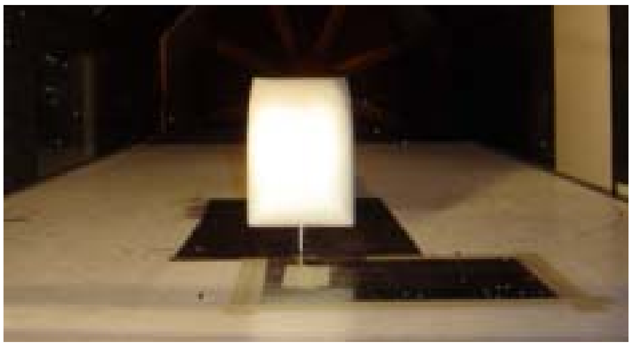

Figure 3. Head-on view of model in wind tunnel.

Figure 4. Detail of splitter plate installation.

The results of the test are given in Figure 5, which shows the drag coefficient for the trailer as a function of yaw angle for various lengths of splitter plate. There is little change in drag at small yaw angles, but as yaw angle increases, the splitter plat becomes more effective. All three splitter plate lengths have about the same performance at this gap length, but at larger gaps (not shown), the longer plates show less improvement and can actually lead to drag increases. For this reason, the shorter plate would seem to be the desirable choice. Figure 6 gives drag for the 1/3 gap length splitter plate for three separate gap lengths with yaw angle as a parameter. The results are quite consistent in producing a drag saving. We suggest that such simple fin geometries be given wind tunnel testing at full-scale or be subjected to over-the-road testing where operation can be evaluated under actual field conditions.

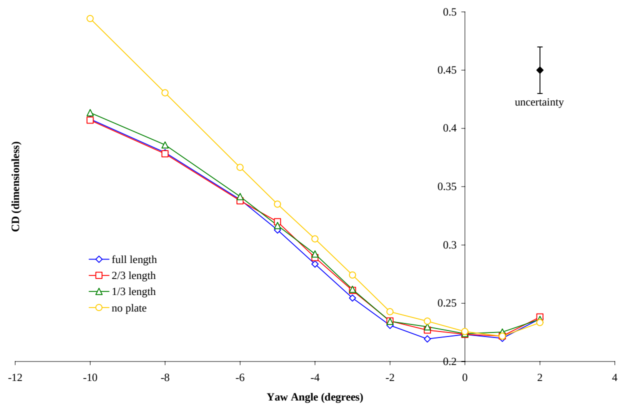

Figure 5. C_D for three splitter plate lengths versus yaw angle at G = 0.5 (G = gap/√A).

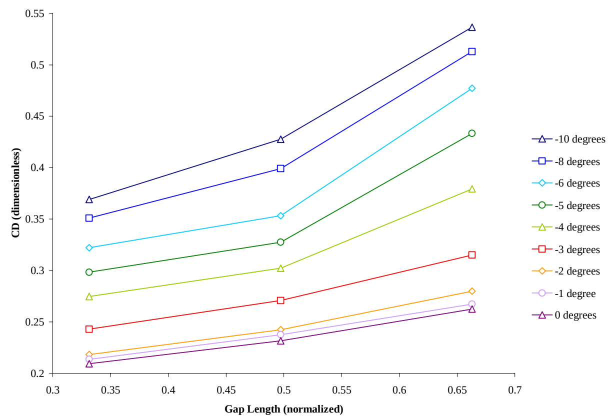

Figure 6. C_D for 1/3 gap length splitter plate as a function of normalized gap length.

II. Field Measurement of Fuel Savings Using a Trailer-Base Add-On

A very successful field test was performed at the NASA Crows Landing Flight Facility on May 17–22 to evaluate the anticipated fuel savings associated with base-flap add-ons. USC organized and participated in the tests. The base flaps and the trailer were provided by Norcan Aluminum Incorporated, and the tests were conducted with trucks and personnel from California PATH at UC Berkeley. The data acquired were of high quality for a field test. Testing showed an optimum fuel consumption saving of about 4% at an optimum flap angle of about 13°, although the entire flap-angle range from 10° to 16° would provide nearly the same savings. The modification to the trailer base is simple and relatively inexpensive to implement. The test results, and the unique experimental procedure for the tests, are documented for presentation at the SAE World Congress, April 2005 (paper # 05-B83, "Fuel Savings by Means of Flaps Attached to the Base of a Trailer: Field Test Results," F. Browand, C. Radovich, & M. Boivin).

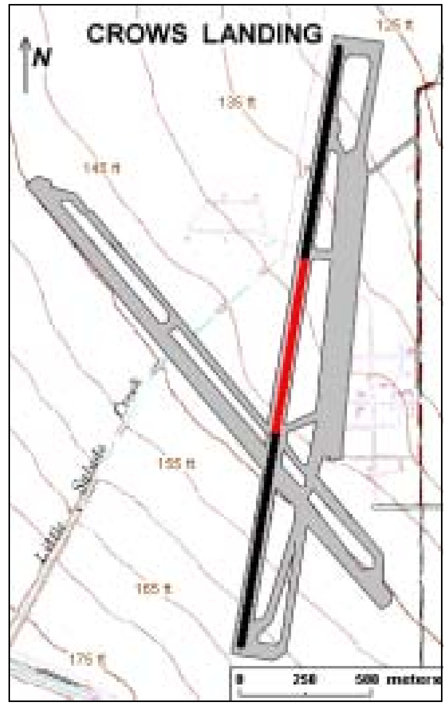

Figure 7. Plan view of the NASA Crows Landing Flight Facility. Red bar marks measurement interval on runway.

The Site at Crows Landing

The present tests are performed at the NASA Crows Landing Flight Facility at the northern end of the San Joaquin valley. The main runway is approximately 2400 m in length and is oriented roughly north-south, as shown in Figure 7.

Truck and Trailer

A single Freightliner 2001 Century Class truck is used for the tests. The truck is powered by Cummins N14 Celect engine developing a maximum of 350 HP. The truck has an automatic transmission, Allison HD 4060 (six forward gears), and a rear axle ratio of 4.63. In operation, the truck executes multiple runs up and down the runway. A run consists of an acceleration phase to a predetermined speed, a uniform speed phase, and a deceleration phase. First, an achievable speed trajectory is established for the truck on the runway. This desired speed trajectory is then programmed into an on-board computer that controls the truck and ensures that all runs are executed in identical fashion.

The Base Flaps

Base flaps are attached to the sides and top of the rear of the trailer. The flaps are constructed from a fiberglass-epoxy-resin material and are one-quarter of the base width in length (about 61 cm, or 2 ft). Figure 8 presents several of the flaps used for the test. The side-flaps swing on piano hinges that are bolted directly to the rear side-edges of the trailer to produce a sealed joint. This installation detail is dictated by the need to quickly remove the flaps for the "no-flaps" control runs.

The flap angle is adjusted by means of two aluminum supports. Holes are pre-drilled to allow the five flap angles to be set quickly. In commercial application, the flaps are attached along the rear door hinge lines, so that no gap appears at the joint between the flap and the side of the trailer. Also in commercial application, the flaps are constrained only by a short length of cable attached to the rear door. Higher pressures on the trailer base and on the inside of the flap, compared to the stream side of the flap, are sufficient to keep the flap extended at highway speeds.

Figure 8. Views of flap installation.

The flap at the top of the rear door is split so the doors can be opened. The two flap-halves are mounted by means of hinges and are kept in place by means of adjustable turnbuckles (Figure 8, upper right). The split in the top flap is sealed with duct tape. The “no-flaps” control is obtained by completely removing flaps from the sides and taping the top flaps against the rear door.

Test Procedure

A typical run sequence starts at a fixed point at one end of the runway. Computer control is initiated, data acquisition begins, and the truck accelerates. When the programmed acceleration ramp terminates, the truck continues along the runway at the preset cruise speed of 26.8 m/s (60.0 mph). Distance along the track is determined by integration of the forward speed. At a pre-determined distance, the braking sequence is initiated, and the truck slows to a stop at the far end of the runway. Data acquisition stops, and the run file is logged in the computer. The truck is turned and made ready for the return from a second fixed point on the track. Typically, a run and the return run are accomplished within about 6 min. A total of 16 runs, or 8 run-pairs, are accumulated for each flap angle setting (about 45 min of test time) and constitute one data set. When a data set is completed, the truck is returned to the garage area, and a new flap angle is positioned. Setting a new flap angle usually takes 20–30 min. Four flap angles — corresponding to four data sets — are accumulated each day during the 6:00–10:30 AM period, when wind and temperature are most favorable. The total database over five testing days, May 17–21, consists of 304 runs (152 run-pairs) — or 19 data sets — at the flap angles 10°, 13°, 16°, 19°, and 22°, as well as the no-flaps condition that serves as the control.

A total of 10 variables are recorded for each data set. The variables include time, integrated distance, engine torque, engine rpm, vehicle speed, and instantaneous fuel consumption (broadcast fuel rate). All of these signals are commonly available on the J1939 bus.

Results

Plotted as the solid symbols in Figure 9 are the averaged results — excluding the four data sets showing the least internal consistency (data set rms > 1.5%). In addition, the dashed bars give the estimated 99% confidence interval for each flap angle. The confidence interval is determined from the standard deviation estimate at each flap angle. A 99% confidence interval suggests that if the tests are repeated under the same conditions, the averaged values will lay within the bounds of the confidence bars 99% of the time. While our repeated sampling over the week-long period does not alter the variability inherent in the data, repeated sampling does provide a much more accurate estimate of the mean (averaged) values.

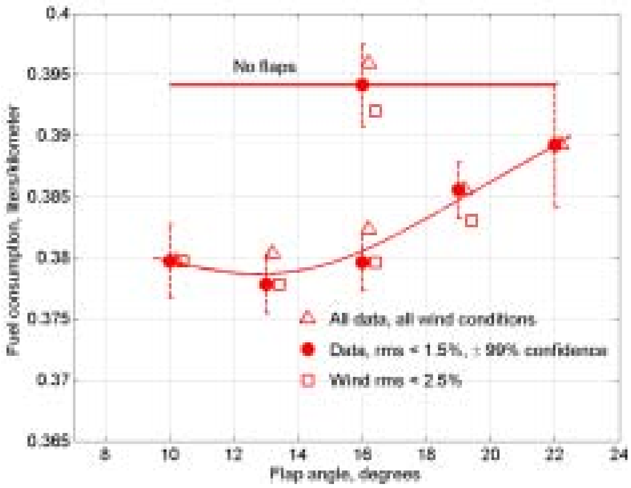

Figure 9. Fuel consumption savings versus flap angle, various data reduction strategies.

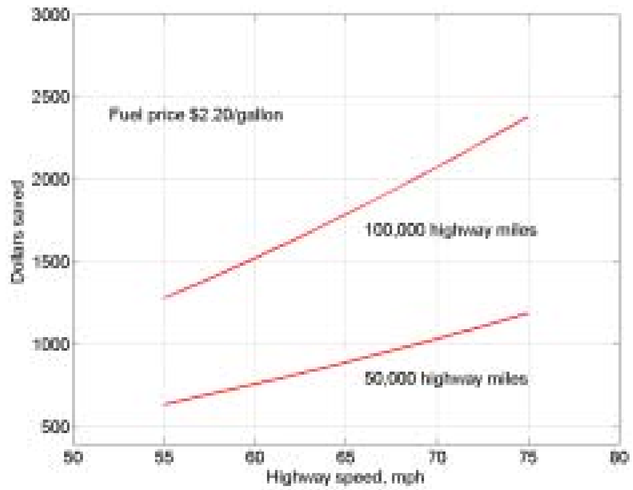

Figure 10. Potential dollar-savings from use of base flaps on a single trailer.

Also shown are the two other data reduction choices — triangles indicate the result when all the data are utilized, and squares indicate the result when only runs at low wind intensity are kept. These three results are not substantially different — they all lie within the 99% confidence bounds. Expressed as a fraction of the fuel consumption without flaps, the averaged values are accurate to about ±0.6%.

Implications for Fleet Operation

There is minimum fuel consumption at a flap angle of about 13°, but the minimum is broad — the fuel consumed at 10° and 16° is only marginally greater. It would be advantageous from an operations standpoint to have such a broad minimum.

The savings in fuel consumption arising from the use of base flaps at a 13º flap angle is 1.63 L/100 km, or in gallons and miles, 0.693 gal/100 mi. A dollar value can be placed on the accumulated savings by assuming a price for fuel. Figure 10 shows the results for a fuel price of $2.20/gal for distances of 50,000 and 100,000 highway miles traveled.

These savings represent the increment associated only with the change in drag due to the presence or absence of flaps. The result will hold for any truck of similar size and shape and engine performance regardless of the loading of the truck or the rolling resistance.

The horizontal axis in Figure 10 is highway speed. Although the tests presented here are performed at 60 mph, the results are easily extrapolated to other speeds because the fuel needed to travel a given distance is quadratic in speed. Dollar savings from the use of flaps is greater at higher speeds, because aerodynamic drag is a larger fraction of the total resistance. However, total fuel consumption will increase with increasing speed.

E. Continued Development and Improvement of Pneumatic Heavy Vehicles

Principal Investigator: Robert J. Englar
Georgia Tech Research Institute (GTRI)
Atlanta, GA 30332-0844
(770) 528-3222, fax: (770) 528-7077,
e-mail: bob.englar@gtri.gatech.edu

Technology Development Manager: Sid Diamond
(202) 586-8032, e-mail: sid.diamond@ee.doe.gov

Technical Program Manager: Jules Routbort
(630) 252-5065, e-mail: routbort@anl.gov

Contractor: Dept. of Energy – National Energy Technology Laboratory, Morgantown, WV
Contract No.: DE-AC26-02EE50691

Objectives

- Previous smaller-scale model wind-tunnel evaluations at GTRI had demonstrated up to 15% reduction in aerodynamic drag coefficient due to blowing and 10–12% due to the device's corner rounding for a combined drag reduction of 25–27%, not accounting for the fuel use by the blower. However, these tunnel results had translated into less-than-expected fuel economy increases during full-scale on-track testing. Reasons for this difference need to be determined and improved aerodynamic characteristics identified.
- Continue this pneumatic heavy vehicle (PHV) technology development by employing new wind-tunnel results to modify the PHV test trailer. Conduct additional fuel economy evaluations of the blown test vehicle to confirm improved drag reduction for parasitic energy loss reduction, fuel economy improvement, reduced emissions, and increased safety of operations for Heavy Vehicles.

Approach

- Conduct additional experimental evaluations of modified wind-tunnel models to enhance the pneumatic aerodynamic capabilities of the PHV configurations.
- Use these results to modify the DOE full-scale pneumatic test vehicle.
- Conduct preliminary on-road testing followed by on-track SAE Type-II fuel economy tests of the PHV test vehicle to verify and improve the drag-reduction and fuel-economy-increasing properties.
- Identify pneumatic aerodynamic and geometry improvements to increase fuel economy by an additional factor of 2 to 3 over that exhibited during our earlier Phase I SAE Type-II fuel-economy tests.

Accomplishments

- Wind-tunnel tests of our modified smaller-scale PHV model have shown improved drag reductions for the more-realistic current configuration with real-world components, such as axles, springs, under-ride bar, and jack stands. These tests confirmed that this new blown PHV model could reduce drag coefficient by 31% below that of the baseline HV configuration, with major geometry modification and not accounting for fuel use for blowing. New tests also demonstrated that active blowing control can reduce side-wind effects, and that the device has the potential to assist in braking and safety of operation for PHVs.
- Improvements thus needed for the Phase II full-scale PHV track test were identified, and the new test trailer design and modifications were completed. Primary here were improved fairings leading into the blown surfaces, improved blowing surfaces, and improved cab gap extenders.

- On-road and on-track SAE Type-II testing were completed. Results show increased improvement in fuel economy due to both blowing and the physical geometry of the new PHV truck. Results also show Fuel Economy Increase (%FEI) of up to 4.5 % at 65 mph due to blowing only, not accounting for fuel used by the blower.

Future Direction

- Conduct additional development and demonstrations of pneumatic aerodynamic drag-reduction, braking, fuel-economy, and safety of operation techniques to provide a confirming database allowing application of this technology to operational PHVs. Interact with DOE and Truck Manufacturers Association's test and evaluation of these devices on their operational rigs.

Introduction

Since aerodynamic drag is the major component of Heavy Vehicle (HV) resistance at highway speed and thus strongly impacts related fuel economy, GTRI has been applying advanced aircraft aerodynamic technology whereby blowing is used to reduce that drag generated by these bluff-based high-drag vehicles. Using the pneumatic aerodynamic technology known as Circulation Control [Ref. 1] and certain geometry changes, we have been able to reduce the drag coefficient (C_D) in HV models due to blowing by up to 15% and to reduce the C_D due to the device's corner rounding in HV models by 10–12% for a total reduction of 25–27%, not accounting for fuel use by the blower (see Figure 1), during a 5-yr tunnel test program for DOE [2, 3, 4]. We could also increase drag as needed for braking during downhill operation without any moving aerodynamic parts by blowing only select trailing-edge surfaces on the trailer. We could potentially reduce the huge drag increase and loss of stability that occur when an HV experiences side winds or gusts. This multi-function potential of the blown configurations is seen in the wind tunnel data of Figure 1. Possible compressed air sources are an HV tractor's turbocharger or an auxiliary engine similar to a refrigeration unit.

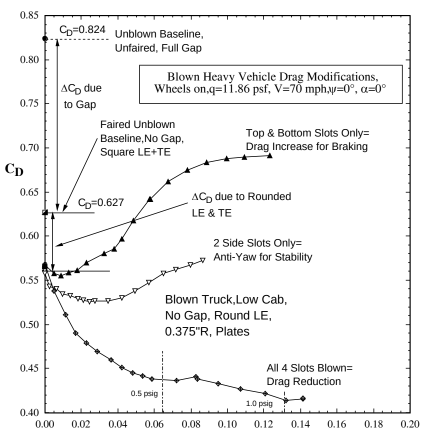

Figure 1. Drag reduction or drag increase demonstrated by earlier GTRI GTS generic model PHV, depending on blowing slot activated.

Full-scale fuel economy tests were conducted [3, 4] during our previous DOE program. These SAE Type-II official test-track results on a Pneumatic HV (PHV) configuration were somewhat different from the tunnel models, which showed a measured %FEI of only 4–5%, not accounting for energy use for blowing. Since that first SAE test, the current program has thus concentrated on determining the difference between wind-tunnel results and the less-than-expected full-scale performance, correcting the blown configuration problem areas, and preparing for a second fuel-economy evaluation with the improved PHV vehicle.

Experimental Details and Results for Updated Wind-Tunnel Model

Experimental wind-tunnel developments of this technology conducted on a smaller-scale PHV model under previous DOE funding [2, 3, 4, 5] had led to two full-scale on-road Tuning Tests plus an SAE Type-II Fuel Economy Test conducted at the 7.5-mi test track at the Transportation Research Center in Ohio, with the results reported above. However, the wind-tunnel model employed here (the very generic Ground Transportation System, GTS, configuration modified with our blowing systems [2, 3]) was geometrically quite different from the actual on-road and on-track test PHV configuration. This simple model had generated drag reductions of up to 84% relative to a stock trailer configuration

[5]. Since the fuel economy increases from these drag reductions were found to be less for the track-test PHV vehicle than those predicted by the tunnel data, we returned to the tunnel this past year to determine the reasons and possible corrections on a model modified to be very similar to the full-scale blown test truck. These results were reported in references 6 and 7 and are summarized here to demonstrate the significance of certain aerodynamic components and features.

The new PHV model fabricated and tested is shown in Figure 2, where many of the new components are noted. At DOE's request, we replaced the earlier generic GTS tractor with the more current Generic Conventional Model (GCM) tractor shown in Figure 2. Note that while this tractor model is representative of current on-road vehicles, it is not specific to any one brand. The new trailer has blowing surface components similar to those of the previews trailer but covering less vertical length (the trailer floor is raised to the conventional level, not "low-boy" height). The model has many new components typical of the real test vehicle:

- Trailer suspension, springs, brakes, axles, support feet (jack stand), and I-beam floor rails;
- Tractor differentials and suspension;
- Mirrors;
- Cab gap extenders (full or 60% coverage);
- Trailer rear under-ride bar and mud flaps; and
- Stock wheels spaced 4 per axle, plus other wheel options.

Figure 2. New GCM tractor model with full cab extender (CE3"), 4 stock wheels per axle, jack stands, and differentials.

Details of some 325 new wind-tunnel runs conducted over ranges of tunnel speed, blowing rate, yaw (side wind) angle, and model configuration variations are presented in references 6 and 7, and the most significant findings are presented below.

The importance of cab extenders in counteracting the adverse effects of asymmetric vortex shedding in the gap between tractor and trailer is shown in Figure 3 for the unblown tractor/trailer configuration. Clearly, a gap fairing is needed here (see "Full Open Gap" curves), but since 100% full-coverage gap ex-tenders (CE3") are not practical during real vehicle turning, we decided on a 60% gap closure (CE1.5"), which produces nearly the same aerodynamic drag results as the 100% full closure but is functionally feasible (it leaves a 16" gap on the real vehicle).

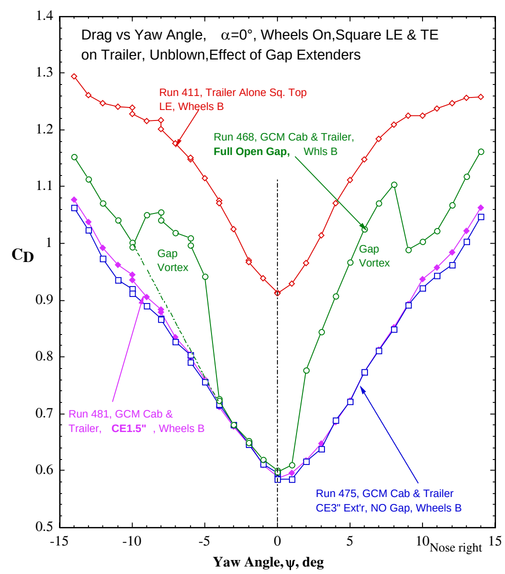

Figure 3. Measured drag of the new trailer and the tractor/trailer combo at yaw angle for various gaps.

Figure 4 shows the results of blowing and the effects of various components on drag reduction as compared to the conventional GCM model with square leading and trailing edges on the trailer and a full open gap. Run 171 is the best blown configuration of the GTS "unrealistic" generic model from the previous tests.

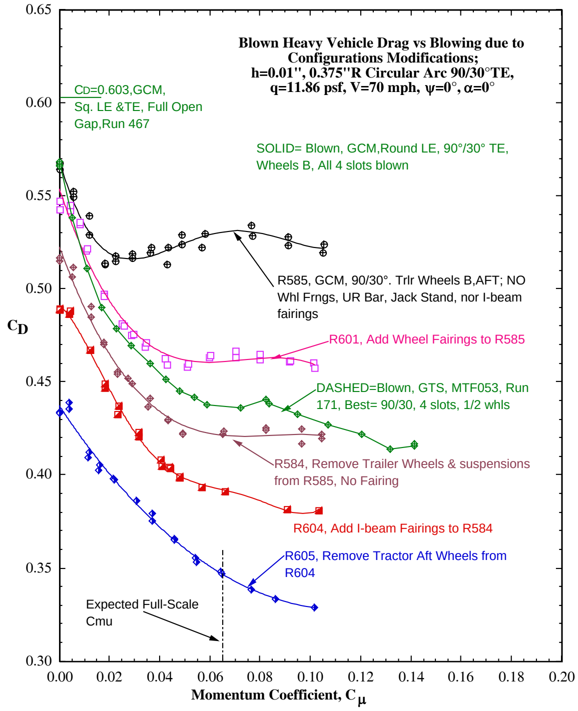

Figure 4. Measured drag reduction due to blowing all 4 slots of various configurations.

The top curve (Run 585) of Figure 4 represents the corresponding blown trailing edge geometry with the representative 4-per-axle wheels and suspension installed on the GCM PHV model. Initial drag reduction due to Cμ flattens out and then rises slightly as the wake from the wheels interferes with the jet turning, much as it did on the full-scale PHV described in reference 4. As we faired the wheels (Run 601), the conditions improved until the new blown truck was very close to the dashed target curve from the previous generic tests (Run 171). This new configuration without the under-floor disturbance yields a drag reduction of 24% below the unblown baseline (Run 467) at the expected full-scale blowing coefficient of Cμ=0.065. Note, however, that if the trailer-wheel wake effects were eliminated entirely (Run 584), and if the floor I-beams were faired over (Run 604), considerably better C_D reduction will occur. In the extreme, if the aft tractor wheel effects were eliminated as well (Run 605), a drag coefficient of C_D=0.33 is possible for this PHV configuration — this is on the order of current sports car coupes. This result further emphasizes the strong influence of the vehicle undercarriage. These results need be considered by other researchers conducting drag reduction efforts on current HVs: it is very important to account for the underbody and wheels of the entire vehicle.

Fairings covering the trailer suspension, axles, and wheels were tested, thus eliminating many of the undercarriage problems from Figure 4. Figure 5 shows the drag reductions of the faired configuration compared to the “baseline” HV, which has a drag coefficient C_D=0.702. The blown results, which are due to several variations in slot height, are seen here. While all configurations have the same slot height on the top and sides, the bottom surface slot height is varied here to determine any gains from improving the disturbed lower surface flow by adding more mass flow there. Indeed, it is seen that increasing the lower slot height does reduce C_D at the same Cμ. In the extreme, too large a bottom slot can reverse this trend. For the best arrangement, C_D is reduced by 31% at Cμ=0.04–0.05 relative to the stock baseline configuration (C_D=0.702), with major geometry modification and no accounting for fuel use for blowing. Thus, this latest wind-tunnel evaluation has provided a “real-world” configuration that should be capable of about a 15–16% fuel economy increase at highway speeds. These tests

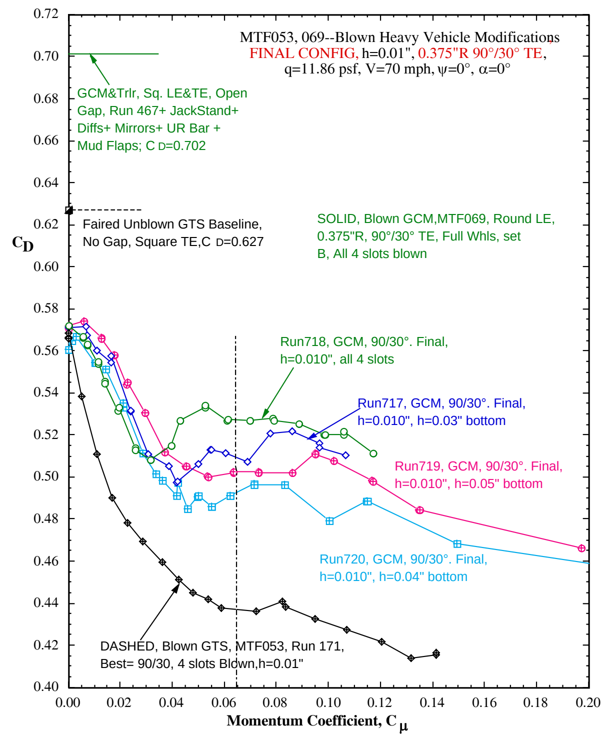

Figure 5. Drag reduction due to blowing and geometry on the final PHV configuration.

also confirmed the ability of blowing to provide yawing moment to counteract side winds and thus provide directional stability to these large-sided vehicles [7]. A valuable lesson learned from these tests was the considerable interference (separated and reversed flow) effects produced by all of the mechanical components and the wheels on the trailer underside.

One last item of interest from these tests is the additional drag and incremental horsepower required to overcome the protrusions into the flow of the components shown in Table 1.

Table 1. Drag increments and corresponding required HP due to external components.

Component	ΔC_D	ΔHP @ 70 mph
Rear View Mirrors	+0.043	+10.51
Under-ride bar	+0.049	+11.97
Mud flaps	+0.005	+1.22
Jack stands (feet)	+0.002	+0.49
Tractor Different'l	+0.001	+0.24

Figure 5 thus represents the drag of the full-scale PHV test vehicle configuration, which eliminates the major Table 1 component items (under-ride bar and flaps are now enclosed) but still is hampered by the presence of the required rear-view mirrors.

Full-Scale Trailer Modifications

As a result of the above series of tunnel evaluations and developments, a final blown PHV configuration to undergo fuel economy testing was determined and includes the following:

- Ninety-degree (vertical side corners) and 30-degree (top & bottom) blowing surfaces with variable slot heights;
- 60% cab extender, 16-in. gap exposed;
- Wheel and axle fairings on trailer and no exposed trailer mud flaps;
- Forward trailer wheel location;
- Aerodynamic under-ride bar (airfoil fairing);
- Stock wheels, four per axle on trailer;
- Stock differentials, axles, and springs on tractor; and
- Side mirrors on tractor, as required.

The trailer modification was completed by GTRI and our teammate prototype shop Novatek, Inc., in early summer 2004. It is shown at the test track in Figure 6. Not shown are the internal blowers connected by ducting to the trailing edge blowing surfaces and the internal diesel drive motor powering these blowers. Air was entrained into these blowers through the NACA inlets on the trailer sidewalls shown in Figure 6. Preliminary checkout testing was conducted at GTRI to measure internal and jet pressures, temperatures, and flow rates; degree of trailing edge jet turning; and data systems operation. When all systems where confirmed, the PHV trailer was picked up by teammate Volvo Technology of America (VTA) and transported to Volvo's facility in North Carolina.

Preliminary Tuning Test 3 (TT3)

After arrival at the Volvo facility, the test truck was again evaluated to assure blowing jet turning, which proved quite satisfactory, especially on the 90-degree vertical surfaces. Tuning Test 3 (TT3) was then conducted on a four-lane highway to confirm that all blowing and data systems were operating successfully on-road and to generate preliminary fuel consumption data before the upcoming SAE Type-II test. On-road flow field attachment due to jet turning was very similar to that shown in Figure 6 with blowing ON. With blowing

Figure 6. Tuft flow visualization showing flow turning with blowing ON.

OFF, the tufts pointed aft and fluttered. This photo gives a graphic demonstration of the blowing effectiveness in preventing aft-surface flow separation on the trailer aft corners.

Although not considered as truly indicative of fuel economy determination, these on-road tuning tests we conducted yielded significant and informative trends. To eliminate any side wind or elevation effects, they were run in both north/south directions on a 2.9-mi length of four-lane highway using an on-board digital fuel readout based on recorded pulses of the Volvo diesel engine's fuel-injection system. Speed was set and maintained by the Volvo cruise control at 65 mph between preset road signposts once the vehicle had achieved test speed, so no accelerations/ decelerations were included. On-board laptop computers recorded truck engine parameters and fuel consumption plus blowing parameters. The data were averaged over the N/S runs to yield each test point, and then each test condition was repeated at least once for consistency (29 runs were conducted in three days in August 2004).

Fuel economy was determined by using several methods, with results shown in Figure 7 as functions of blowing momentum coefficient, Cμ. (Data are plotted as percent miles/gallon change from the mpg of the baseline stock trailer, which was also tested with the same tractor.) The engine parameters were recorded digitally and integrated to give time-averaged mpg. The data shown in Figure 7, labeled "full distance," were integrated over the entire 2.9-mi run, averaged in each direction. These time-averaged data (striped bars) are compared here with the trends of the wind-tunnel data "MTF069" (this tunnel data has been converted to %mpg increase by assuming that $\%C_D$ reduction is roughly twice the %fuel economy increase [2, 3, 4]). These "on-road" integrated data thus show the %Fuel Economy Increase to range from 4-5% ±1%.

This preliminary TT3 was thus completed, and although it was not considered an official fuel economy test, it confirmed that the PHV blown test rig was yielding appropriate drag reduction characteristics due to blowing and was thus ready for SAE Type-II fuel economy testing.

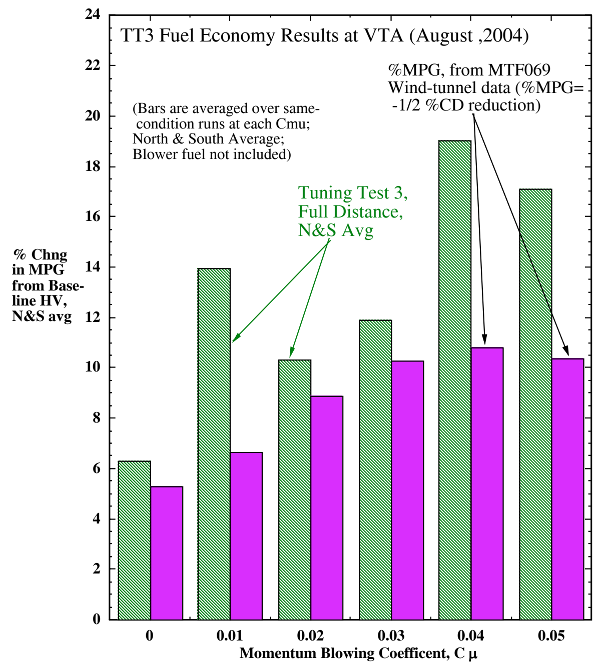

Figure 7. Tuning Test 3 Fuel economy results and wind-tunnel comparisons.

Phase II SAE Type-II Tests

The pneumatic test truck and a stock reference (control) tractor/trailer were transported by Volvo to the Transportation Research Center (TRC) 7.5-mi test track in East Liberty, OH, for our Phase II SAE Type-II fuel economy evaluations. These tests were conducted by TRC drivers and personnel in strict accordance with SAE J1321 procedures [8]. For each valid test point of fuel consumed, these require that three successive runs of six laps each (45 mi around the TRC test oval), at a constant speed and constant blowing parameters or test configuration, be made by the test (T) truck and by the control (C) truck at the same time within certain allowable departure times and displacement distances. Fuel economy is measured by weighing removable fuel tanks and then comparing the test truck's fuel burned with the control truck's. This eliminates variations in temperature, side winds, an other parameters. When the test/control fuel-burned ratio is within a required consistency of each other for three measured runs, that data point is considered valid. A view of the entire PHV test vehicle, including the added 60% cab extenders and wheel fairings, is seen in Figure 8. The control tractor-trailer was a second Volvo/Great Dane combo with stock geometry, also shown in Figure 8.

Figure 8. PHV test trailer (top) at TRC with rebuilt cab extenders and control trailer (bottom).

For these test runs, our target data points based on TT3 and Figure 7 were Cμ=0.0. 0.02 and 0.04 at 65 mph and Cμ=0.0, 0.02, and 0.035 at 75 mph. Plus, for comparison as a baseline vehicle, the PHV test truck had to be disassembled on-site and returned to the baseline (stock) configuration and then run at 65 and 75 mph. This test program was conducted at TRC in September 2004.

The %Fuel Economy Increase ratios (%FEI, same as %MPG increase) come from comparing the T/C fuel-burned ratios for each test condition to the T/C of the stock baseline truck at the same speed [8]. These TRC fuel economy increases are seen for the two test vehicle speeds in Figure 9 ("PHV Total," top solid curves), and are compared with the GTRI wind-tunnel-based data from Figure 7. The TRC data have a very similar trend to the tunnel data in terms of increased %FEI with blowing Cμ. The lower solid curves show %FEI due to blowing only, where up to 4.5%FEI is seen, not accounting for fuel use by compression. Higher blowing than 0.03 seems to cause a slight drop in fuel economy, just as it did in the tunnel data at higher Cμ, probably because of the lack of flow disturbance underneath the trailer and degradation of the effects of higher blowing (see Figure 5 as well). However, relative to our previous SAE test on the first generation of this PHV test truck [3, 4, 5], these results are more than 2.2 times those earlier %FEI results. To put the findings in perspective, a 1% increase in FEI

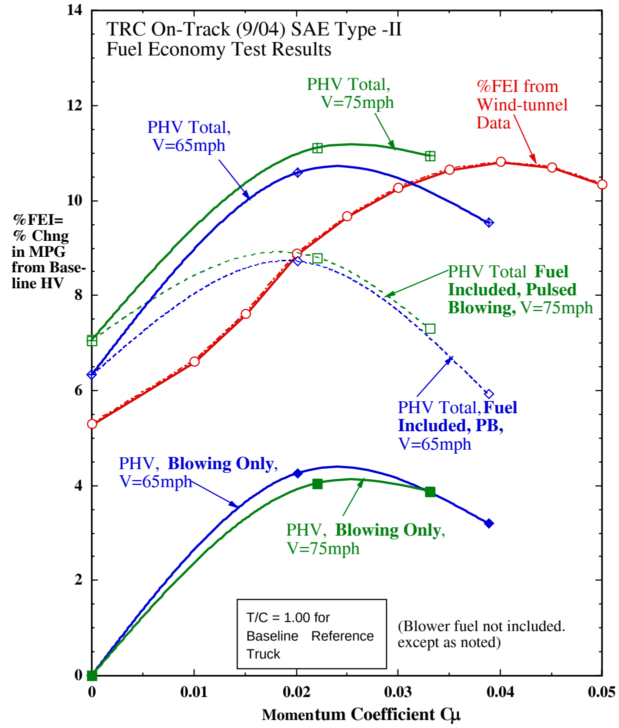

Figure 9. TRC SAE Type-II fuel economy results for the pneumatic system components.

represents approximately 220–240 million gal of diesel fuel saved by the U.S. heavy vehicle fleet each year.

In the above sets of data, fuel used to power the blower engine has yet to be included. In the middle (dashed) curves of Figure 9, we have included blower fuel burned, in which we have also added the use of pulsed (cyclic) blowing to reduce the blowing mass flow required to achieve these drag reductions (see reference 9 for details of this technology, which GTRI developed with NASA). Results including this not-yet-optimized system still show approximately 8–9%FEI for these blown configurations, including blower fuel. Note also in Figure 9 that the data at the higher speed (75 mph) show greater improvement from blowing than at 65 mph since drag there is the more dominant term over rolling resistance. As noted, the raw TRC data have been equalized to ensure that the T/C ratios for the baseline reference configurations (from which the test vehicle fuel economy increasaes were derived) were the same (1.0) at both speeds.

Conclusions

To advance the state of development of pneumatic aerodynamics for heavy vehicle drag reduction, fuel economy, braking, stability, and safety of operation, GTRI and its team members have continued in 2004 our previous program for DOE EERE. We have conducted new model-scale wind-tunnel investigations to identify and correct aerodynamic problem areas from our first fuel-economy test. We have also completed new full-scale on-road and test-track fuel economy validations of these advanced capabilities on a full-scale PHV. Results of this recent effort include:

- We have identified aero problem areas existing after our first PHV road test and how to correct these; current wind tunnel data indicate that drag reductions of up to 31% result from the new "real-world" PHV configuration, from which fuel economy increases of about 15–16% due to blowing and associated geometry improvements should result at highway speeds. On the basis of this wind-tunnel data, a new blown test vehicle modification was fabricated and assembled.

- SAE Type-II fuel economy runs of this new PHV vehicle on the TRC test track showed an improvement of up to 4.5% at 65 mph as a result of blowing only, not accounting for fuel used by the blower.

- The PHV concept has now been verified both by smaller-scale wind tunnel evaluations and by full-scale on-road and on-track SAE testing to be a promising means to reduce drag and increase fuel economy of HVs. We must still address and resolve the problems caused by undercarriage and wheel component disturbances that seem to cause lesser blowing effectiveness at higher blowing.

References

1. Englar, R.J., "Circulation Control Pneumatic Aerodynamics: Blown Force and Moment Augmentation and Modification; Past, Present and Future," AIAA Paper 2000-2541, June 2000.
2. Englar, R.J., "Advanced Aerodynamic Devices to Improve the Performance, Economics, Handling and Safety of Heavy Vehicles," SAE Paper 2001-01-2072, May 14–16, 2001.
3. Englar, R.J., "Pneumatic Heavy Vehicle Aerodynamic Drag Reduction, Safety Enhancement, and Performance Improvement," Proceedings of the UEF Conference "The Aerodynamics of Heavy Vehicles: Trucks, Buses, and Trains," Dec. 2002.
4. Englar, R.J., "Drag Reduction, Safety Enhancement and Performance Improvement for Heavy Vehicles and SUVs Using Advanced Pneumatic Aerodynamic Technology," SAE Paper 2003-01-3378, Nov. 2003.
5. Diamond, S., "FY2003 Annual Progress Report for Heavy Vehicle Systems Optimization, FreedomCAR and Vehicle Technologies Program," Feb. 2004.
6. Englar, R.J., "Continued Development & Improvement of Pneumatic Heavy Vehicles, Phase VI, DOE Quarterly Report 7," April 15, 2004.
7. Englar, R.J., "Continued Development & Improvement of Pneumatic Heavy Vehicles, Phase VI, DOE Quarterly Report. 8," July 15, 2004.
8. "Joint TMC/SAE Fuel Consumption Test Procedure-Type-II," SAE J1321, Oct. 1986.
9. Jones, G.S., and R.J. Englar, "Advances in Pneumatic High-Lift Systems through Pulsed Blowing," AIAA Paper 2003-3411, June 2003.

F. Heavy Vehicle Aerodynamic Drag: Experiments, Computations, and Design

Kambiz Salari, Jason Ortega, Paul Castellucci, Craig Eastwood, Rose McCallen, Kipp Whittaker
Lawrence Livermore National Laboratory
7000 East Ave, L-098, Livermore, CA 94551
(925) 423-0958, fax: (925) 422-3389, e-mail: mccallen1@llnl.gov

Technology Development Area Specialist: Sidney Diamond
(202) 586-8032, fax: (202) 586-1600, e-mail: sid.diamond@ee.doe.gov
Technical Program Manager: Jules Routbort
(630) 252-5065, fax: (630) 252-4289, e-mail: routbort@anl.gov

Contractor: Lawrence Livermore National Laboratory
Contract No.: EEW0046

LLNL's effort consists of four experimental, computational, and design focus areas:

- An Experimental Study of Drag Reduction Devices for a trailer Underbody and Base
- Investigation of Predictive Capability of RANS to Model Bluff Body Aerodynamics
- Splash and Spray Suppression
- Computational Investigation of Aerodynamics of Rail Coal Cars and Drag Reducing Add-On Devices

The following describes the objectives, approach, accomplishments, and future directions for each of these focus areas.

A. An Experimental Study of Drag Reduction Devices for a Trailer Underbody and Base

Objective

- This wind tunnel study investigates optimization of trailer base flaps and alternative forms of trailer skirts in an effort to reduce the aerodynamic drag of heavy vehicles, thereby improving their fuel efficiency.

Approach

- Low-speed wind tunnel measurements are made on a $1/16^{th}$-scale generic tractor-trailer model at a width-based Reynolds number of 325,000.
- The model is fixed to a turntable, allowing the yaw angle to be varied between $\pm 14^o$ in 2^o increments.
- Various add-on drag reduction devices are mounted to the model underbody and base.
- The wind-averaged drag coefficient at 65 mph is computed for each configuration, allowing the effectiveness of the add-on devices to be assessed.

Accomplishments

- The most effective add-on drag reduction device for the trailer underbody is a wedge-shaped skirt, which reduces the wind-averaged drag coefficient by 2.0%.
- For the trailer base, the most effective add-on drag reduction device is a set of curved base flaps having a radius of curvature of 0.91 times the trailer width. These curved base flaps reduce the wind-averaged drag coefficient by 18.8%, providing the greatest drag reduction of any of the devices tested.
- Maximum drag reduction for the angled base flaps occurs when the top and side flaps have deflection angles of 11.1° and 10.1°, respectively.

- When the wedge-shaped skirt and curved base flaps are used in conjunction with one another, the wind-averaged drag coefficient is reduced by 20%.

Future Direction

- CFD simulations will be performed on a heavy vehicle with a wedge-shaped skirt to gain additional insight into the performance characteristics of the wedge-shaped skirts.
- When future track tests are performed by using the angled base flaps, a recommendation will be made to test unequal deflection angles for the side and top base flaps.

Introduction

In an effort to improve the fuel efficiency of heavy vehicles, this wind tunnel study investigates the optimization of trailer base flaps and alternative forms of trailer underbody skirt designs. Previous research [1, 2] on angled base flaps has demonstrated that this concept is capable of reducing the drag by as much as 10% on a heavy vehicle when the flaps are deployed at equal angular deflections. However, it is quite possible that an optimum configuration may be one in which the top and side base flaps have slightly different angular deflections. In the subsequent sections, we explore this possibility. Additionally, we investigate the drag-reducing capability of curved base flaps, which have previously shown to perform about as well as straight base flaps [2]. To circumvent the shortcomings of straight side skirts, which limit access to the trailer underside, we investigate three variations of a wedge trailer skirt concept that may provide the drag-reduction benefits of straight side skirts.

Experimental Setup

The effectiveness of trailer underbody and base drag reduction devices is assessed by making axial force measurements in a wind tunnel on a 1/16th-scale generic tractor-trailer model (Figure 1), which is a simple representation of a near-future tractor/trailer. The wind tunnel measurements are made in the NASA Ames Fluid Mechanics Laboratory open-circuit wind tunnel, which has a contraction ratio of 9:1, a test section size of 813 mm × 1219 mm, and freestream turbulence level of 0.15%. The model measures 162 mm × 225 mm × 1238 m, giving a nominal width-based Reynolds number of $\mathrm{Re}_w = Vw/\nu$ = 325,000, where w is the model width = 162 mm, ν is the kinematic viscosity of air,

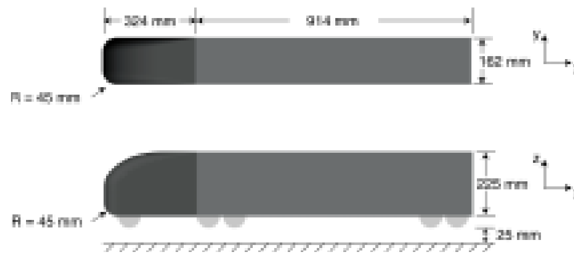

Figure 1. Model of the cab-over engine tractor-trailer used in the wind tunnel study.

and V is the freestream velocity. For each model configuration, the axial force measurements are made at yaw angles, ψ, ranging from ±14° in 2° increments.

Four skirt designs (Figure 2) are tested on the trailer underside: a long wedge skirt (Figure 2a), which has an apex angle of 10°; a short wedge skirt (Figure 2b), which has an apex angle of 22°; a short wedge skirt with an upstream center skirt (Figure 2c); and two conventional straight side skirts (Figure 2d), which are used as a reference for making performance comparisons with the other three skirt designs. A set of angled flaps is tested as a means of reducing the base drag of the model (Figure 3a). The four curved base flap devices are constructed by using a rapid prototyping technique (selective laser sintering), which forms a single-pieced design. The curved base flaps extend a distance of 48 mm from the trailer base and have radii of curvature, R, of 52, 79, 148, and 288 mm. In units of the trailer width, the radii of curvature are 0.32w, 0.49w, 0.91w, and 1.78w.

Results

The wind-averaged drag coefficients [3], C_{dwa}, for the four trailer skirts are listed in Table 1. It should be noted that the trailer skirts Cooper [1] tested yielded reductions in the wind-averaged drag

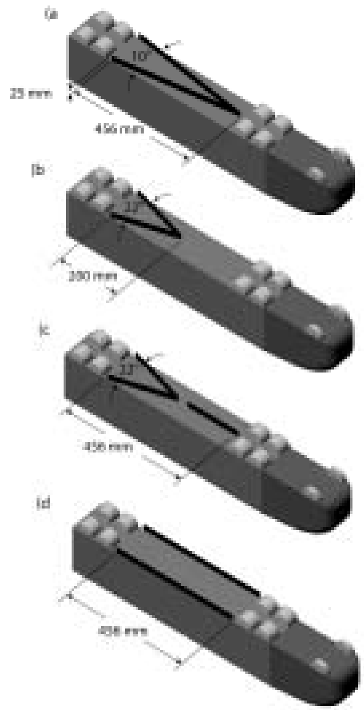

Figure 2. Skirt designs used to reduce the trailer underbody aerodynamic drag: (a) long wedge skirt, (b) short wedge skirt, (c) short wedge skirt with center skirt, (d) straight side skirts. (Note that the gap between the center skirt and short wedge skirt in [c] is to allow clearance for the sting mount.)

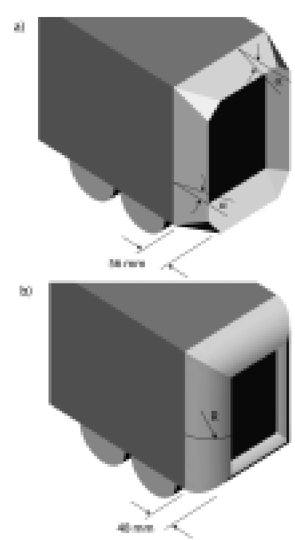

Figure 3. Base flap designs: (a) angled base flaps; (b) curved base flap.

coefficient that are much larger than those shown presently. The reason for this difference may be because the models Cooper used had complete axles and wheels on the trailer, which would likely contribute a much greater portion to the overall vehicle drag than simple half-cylinder wheels. Hence, the installation of the skirts on the more realistic models could result in a greater drag reduction. Both short wedge skirts provide negligible reduction of the wind-averaged drag coefficient. On the other hand, it can be seen that the long wedge skirt provides the greatest drag reduction of the four trailer skirt designs. *This suggests that the long wedge skirt is a design that can improve upon that of the traditional straight side skirts by not only yielding a greater reduction in the wind-averaged drag coefficient, but also by allowing easier access to the trailer underside.* However, additional testing of the long wedge skirt with a more realistic trailer underbody and a moving ground plane is needed before a definite conclusion can be drawn.

The angled base flaps on the sides and top of the trailer are tested at independent angular deflections of 5°, 10°, 15°, and 20°, while the bottom flap is maintained at a deflection angle of 0°. It is seen in the data that there is a combination of α_{side} and α_{top} that yields a minimum in the wind-averaged drag coefficient in the vicinity of $\alpha_{side} \approx 10°$ and $\alpha_{top} \approx 10°$. The wind-averaged drag coefficients in the range of $5° \leq \alpha_{side} \leq 15°$, $5° \leq \alpha_{top} \leq 15°$ are fit with a second-order polynomial surface to estimate the angular deflections that yield a minimum value of the wind-averaged drag coefficient. Doing so gives a minimum in the polynomial surface at $\alpha_{side} = 10.1°$ and $\alpha_{top} = 11.1°$, at which location the wind-averaged drag coefficient is 0.493±0.004. Table 1 shows that this value is 16.4±0.8% less than that of the baseline configuration.

As a comparison to the base flaps made of straight plates, four curved base flap configurations are tested. The minimum measured wind-averaged drag coefficient occurs for the curved base flaps that have a dimensionless radius of curvature of $R/w = 0.91$. As shown in Table 1, the wind-averaged drag coefficient for this configuration is 18.8±0.8% less than that of the baseline case. *This reduction in the drag coefficient is the largest for any single add-on device tested in this study.*

Having analyzed the performance of the trailer skirts and base flaps on an individual basis, we now assess the effectiveness of combinations of these devices and determine the configuration that results in the greatest drag reduction. Of all the devices tested, the combination of the curved base flaps (R/w = 0.91) with the long wedge skirt gives the greatest reduction in the wind-averaged drag coefficient. This combination results in a 20.0±0.8% reduction in the wind-averaged drag coefficient, the majority of which is due to the contribution of the curved base flaps. The wind-averaged drag coefficients for this configuration and that of the combination of the long wedge skirt and the straight base flaps at $\alpha_{side} = \alpha_{top} = 10°$ are shown in Table 1.

A comparison of the wind-averaged drag coefficients of the model with trailer skirts and the model with base flaps indicates that the base flaps provide a substantially larger drag reduction than do the skirts. Assuming that the trends in the wind-averaged drag coefficients are applicable to full-sale heavy vehicles, these results could have important implications for the current day trucking industry.

Table 1. Wind-averaged drag coefficient, C_{dwa}, and the percent reduction in the wind-averaged drag coefficient relative to the baseline case for various model configurations.

Configuration	C_{dwa} (±0.004)	% Reduction in C_{dwa} (±0.8%)
Baseline	0.590	—
Baseline w/long wedge skirt	0.578	2.0
Baseline w/short wedge skirt	0.587	0.1
Baseline w/short wedge skirt and center skirt	0.587	0.1
Baseline w/straight side skirts	0.582	1.4
Baseline w/angled base flaps (α_{top} = 11.1°, α_{side} = 10.1°)	0.493	16.4
Baseline w/curved base flaps (R/w = 0.91)	0.479	18.8
Baseline w/angled base flaps (α_{top} = 10°, α_{side} = 10°) and long wedge skirt	0.484	18.0
Baseline w/curved base flaps (R/w = 0.91) and long wedge skirt	0.472	20.0

Clearly, if a trucking fleet decided to purchase a single add-on drag device to obtain the greatest drag reduction, the choice of curved base flaps would be the best alternative. However, the angled base flaps may be more attractive from an investment point of view since their rather simple design would be less to manufacture and, thus, require a smaller initial investment.

Conclusions

Through this study, we have investigated several add-on drag-reduction devices. The wind-averaged drag coefficient is used as a means of comparing the performance of trailer skirts and base flaps. Of the trailer skirts that are tested, the long wedge skirt provides the greatest drag reduction. The angled and curved base flap devices yield reductions in the wind-averaged drag coefficient approximately eight to nine times greater than that of the long wedge skirt. It should be noted that the results of this wind tunnel study are valid for the low Reynolds number regime that was tested. Future tests will be conducted on actual heavy vehicles to determine the influence of Reynolds number and the moving ground plane beneath the vehicle.

What is needed to get these devices onto operating heavy vehicles is a committed effort between the government, the tractor/trailer manufacturers, and the trucking fleets. The government has seen the opportunity to improve the fuel economy of heavy vehicles and has taken the initiative to support research and development in heavy vehicle aerodynamics. The involvement of tractor/trailer manufacturers can provide expertise in both road testing and design issues of these devices. The trucking fleets can give practical insight into how these devices impact the operational capability of their fleets and foresee any potential concerns. Only until this collaboration is established will the nation be able to benefit from the significant cost savings that these second-generation drag reduction devices can provide.

References

1. Cooper, K.R., “Truck Aerodynamics Reborn — Lessons from the Past,” SAE Paper No. 2003-01-3376, 2003.
2. Cooper, K.R., “The Effect of Front-Edge Rounding and Rear-Edge Shaping on the

Aerodynamic Drag of Bluff Vehicles in Ground Proximity," Paper No. 850288, *SAE International Congress*, Detroit, MI, February 25–March 1, 1985.

3. Ingram, K.C., "The Wind-Averaged Drag Coefficient Applied to Heavy Goods Vehicles," Transport and Road Research Laboratory Supplementary Report 392, 1978.

B. Investigation of Predictive Capability of RANS to Model Bluff Body Aerodynamics

Objectives

- Investigate the applicability of state-of-the-art computational modeling and simulations to predict the flow field around bluff bodies as related to the DOE Heavy Vehicle aerodynamics project. Specifically, determine the predictive capability of several commonly used, steady, Reynolds Averaged Navier-Stokes (RANS) turbulence models.
- Provide tractor and trailer manufacturers with a knowledge base that describes the advantages and disadvantages of each turbulence model when selected for use within a commercial code.

Approach

- Perform simulations of a simplified tractor/trailer geometry for validating the drag prediction capabilities of selected RANS turbulence models.
- Compare the force coefficients, as well as the surface pressures and flow features, to experimental data [1] of the Ground Transportation System (GTS) at 0° and 10° yaw conducted in conjunction with NASA Ames Research Center in their 7' 10' wind tunnel.

Accomplishments

- Compared the experimentally obtained floor boundary layer profile at the wind tunnel test-section entrance with those predicted by each of the turbulence models.
- Compared computed aerodynamic force coefficients for the selected turbulence models to the experimental data at yaw angles of 0° and 10°. Menter's two-equation BSL RANS model shows the closest agreement to the experimental data, generally predicting drag within 5%. However, all of the models fail to capture the structure of the wake flow near the trailer base. Consequently, all of the selected models fail to reproduce the experimental base pressure coefficients.

Future Direction

- Investigate the applicability of unsteady RANS, large-eddy simulation (LES), and combinations of the two, for the prediction of these massively separated base flows.

Introduction

The objective is to investigate the applicability of state-of-the-art computational modeling and simulations to predict the flow field around bluff bodies as related to the DOE Heavy Vehicle aerodynamics project. Specifically, the goal is to determine the predictive capability of several commonly used, steady, Reynolds Averaged Navier-Stokes (RANS) turbulence models. This information will provide tractor and trailer manufacturers with a knowledge base that describes the advantages and disadvantages of each turbulence model choice.

Computation Approach and Results

Simulations are performed on a 1/8th-scale simplified tractor/trailer geometry for validating the drag prediction capabilities of selected RANS turbulence models. These models include the one-equation Spalart-Allmaras (SA) [2] and the two-equation Wilcox (KW) [3] and Menter (BSL) [4] k-ε models. The force coefficients, as well as the surface pressures and flow features, are compared to experimental data [1] of the Ground Transportation System (GTS) at 0° and 10° yaw. The data were acquired from an experiment conducted in conjunction with NASA Ames Research Center in its 7-ft × 10-ft wind tunnel.

Simulations of the GTS are run by using NASA's OVERFLOW code. OVERFLOW is a fully compressible, 3-D, finite volume code employing overset grids. In all simulations, the flow is assumed to be fully turbulent and no attempt is made to model transition. Additionally, no wall functions are used, as all turbulence equations are integrated to the wall.

As the GTS model is exposed to the floor boundary layer of the 7-ft × 10-ft wind tunnel, the accuracy of a validation simulation depends on how well the upstream boundary layer is represented. Thus, a portion of the wind tunnel geometry is modeled, where careful attention is paid to matching the simulation boundary conditions to the actual wind tunnel conditions. Figure 1 presents a comparison between the experimentally obtained floor boundary layer profile at the wind tunnel test-section entrance and those predicted by each of the turbulence models.

Corresponding to the NASA experiment[1] run 7, points 9 and 5, the GTS baseline configuration at 0° and 10° yaw are selected for simulation. Using the SA, KW, and BSL models, 0° yaw simulations are conducted on a 14-million-element grid. In addition, the BSL model is chosen to ensure grid convergence of the solution on a coarser 11-million-element grid. In a similar fashion, 10° yaw simulations are run on 19 and 14 million element meshes.

Tables 1 and 2 show the computed aerodynamic force coefficients for the selected turbulence models and the experimental data at yaw angles of 0° and 10° respectively. Among these models, Menter's two-equation BSL shows the closest agreement to the experimental data, generally predicting drag within 5%.

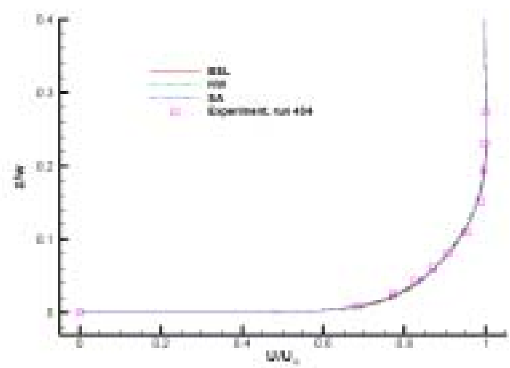

Figure 1. Floor boundary layer velocity profile.

Table 1. Aerodynamic force coefficients at 0° yaw.

	CD	CL	CS
SA, 14 million elements	0.3173	-0.1317	5.1E-06
KW, 14 million elements	0.2377	-0.1070	-4.3E-04
BSL, 14 million elements	0.2638	-0.1214	-1.4E-05
BSL, 11 million elements	0.2684	-0.1220	-3.0E-06
NASA experiment	0.263 ± 0.01	-0.152 ± 0.01	0.007 ± 0.01

Table 2. Aerodynamic force coefficients at 10° yaw.

	CD	CL	CS
SA, 19 million elements	0.6361	-0.1162	1.1451
KW, 19 million elements	0.5708	-0.0236	1.1431
BSL, 19 million elements	0.5626	-0.0320	1.1376
BSL, 14 million elements	0.5701	-0.0252	1.1329
NASA experiment	0.542 ± 0.01	0.026 ± 0.01	1.200 ± 0.01

Differences among the turbulence models in the computed force coefficients are found to be primarily due to contribution of the predicted pressure field around the GTS model. The computed pressure coefficients for each model are in close agreement with the experimental data, except for the area near the base of the trailer. Figures 2 and 3 illustrate the agreement between the predicted pressure coefficients and those obtained along the centerline of the top surface of GTS at 0° and 10° yaw. It is clear, however, that none of the turbulence models capture either the pressure field magnitude or trend at the base of the trailer. Figures 4 and 5 display the discrepancy between the computed pressure coefficients along the base centerline and the experimental data for each yaw angle.

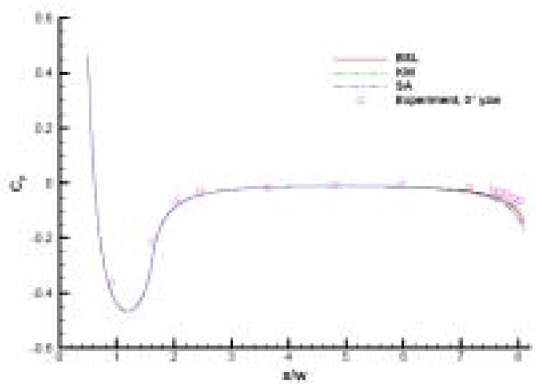

Figure 2. GTS top surface centerline pressure coefficients at 0° yaw.

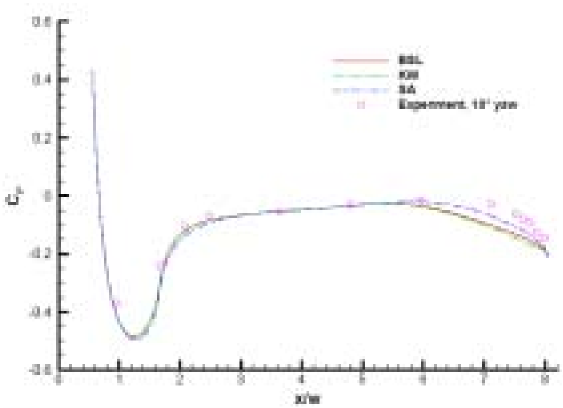

Figure 3. GTS top surface centerline pressure coefficients for 10° yaw.

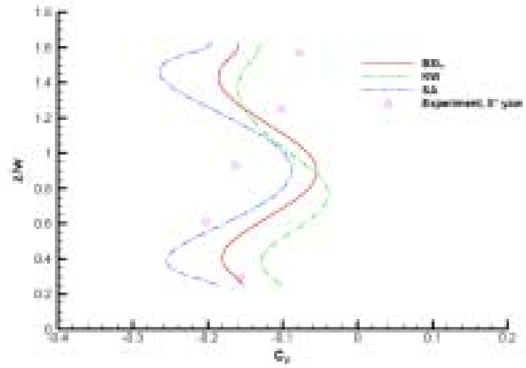

Figure 4. GTS base centerline pressure coefficients at 0° yaw.

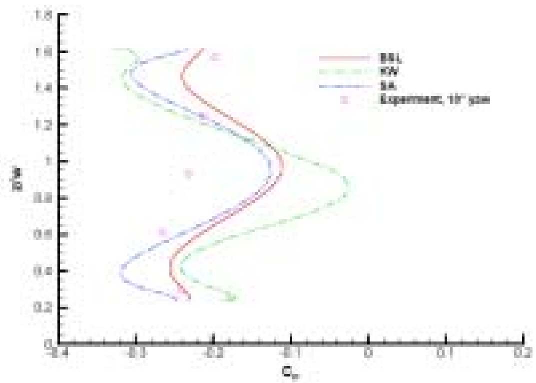

Figure 5. GTS base centerline pressure coefficients at 10° yaw.

The accuracy of the base flow predicted by the selected turbulence models is further illustrated by examining the time-averaged PIV data available in the wake of the trailer. Although hidden by the similarity in force coefficients, the selected turbulence models predict very different separated wakes, particularly in the low-velocity area very near the base of the trailer. As expected from the computed pressure coefficients, none of the models fully capture the separated flow structure indicated by the time-averaged PIV data. For example, along the model centerline, Figure 6 shows the BSL wake at 0° yaw. For comparison, particle traces of the time-averaged PIV data are provided in Figure 7.

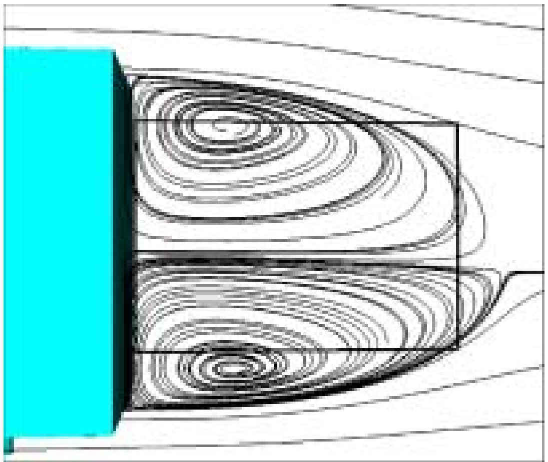

Figure 6. BSL model centerline wake flow particle traces.

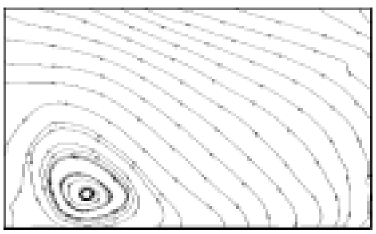

Figure 7. Particle traces of time-averaged PIV data within the frame in Figure 6.

Conclusions

Overall, the Menter BSL RANS model simulation is closer to the experiment than either the KW or SA simulations; however, all of the models fail to capture the structure of the wake flow near the base. Consequently, all of the selected models fail to reproduce the experimental base pressure coefficients. Although the drag force coefficients appear to be somewhat insensitive to the details of the flow near the base, to assess the efficacy of drag-reducing devices in the wake, steady RANS models are likely to prove to be inadequate. To consistently achieve drag values to within the incremental values produced by trailer base treatments, unsteady simulations may be required to fully represent the wake flow. Future plans call for investigation of the applicability of unsteady RANS, large-eddy simulation (LES), and combinations of the two, for the prediction of these massively separated base flows.

References

1. Storms, B., et al., “An Experimental Study of the Ground Transportation System (GTS) Model in the NASA Ames 7- by 10-Ft Wind Tunnel,” NASA/TM-2001-209621, Feb. 2001.
2. Spalart, P.R., and Allmaras, S.R., A One-Equation Turbulence Model for Aerodynamic Flows, AIAA Paper 92-439, Reno, NV, 1992.
3. Wilcox, D.C., Turbulence Modeling for CFD, 2nd Edition, DCW Industries, 1998.
4. Menter, F.R., Two-Equation Eddy-Viscosity Turbulence Models for Engineering Applications, AIAA J., 32 (8), 1994, 1598-1605.

C. Splash and Spray Suppression

Objectives

- Analyze the formation and spread of spray clouds generated around and behind heavy vehicles by using both laboratory experiments and validated computational models.
- Develop a collection of predictive computational tools available to tire and truck manufacturers that will allow the effects of add-on splash and spray suppression devices on vehicle aerodynamics and potential synergies between add-on aerodynamic devices and spray mitigation to be thoroughly explored.

Approach

- The droplet size, space, and velocity distributions determined as a function of tire speed and tread pattern from our experimental investigation will be used as an initial condition for our computational simulations.
- Commercially available computational fluid dynamics (CFD) codes will be used to predict the aerodynamic atomization of these droplets. User-defined atomization subroutines will be added to the commercial packages as necessary.
- Detailed computational investigations of the aerodynamics of rotating tires and wheel-wells and their effect on splash and spray will be performed.
- The effects of splash and spray suppression devices on brake cooling will be investigated, and possible enhancements to brake cooling resulting from well-designed add-on aerodynamic devices will be explored.
- Validated state-of-the-art large-eddy simulation (LES) models capable of capturing the spatial evolution of fine droplets in a turbulent flow will be developed and used to simulate the dispersion of mist around and behind heavy trucks.

Accomplishments

- Reviewed the literature to determine both the existence and outcome of prior efforts toward splash and spray suppression and to delineate the pertinent physics governing the problem.
- Coordinated experimental research plan with team at USC.
- By working with USC, developed an experimental test rig.
- Began investigating STAR-CD's ability to track free fluid surfaces via its implementation of the volume of fluid (VOF) method and to predict ensuing droplet formation.
- Began studying STAR-CD's ability to accurately simulate the flow around a rotating tire, including both aerodynamic and free-surface phenomena.
- Began investigating STAR-CD's ability to capture aerodynamic droplet breakup (secondary atomization) and turbulent transport of sub-Kolmogorov scale particles.

Future Direction

- This project is in its very nascent stages. All aspects of the project discussed above are under continuing development.

Introduction

The spray clouds generated around and behind heavy trucks traveling on highways during adverse weather conditions lead to reduced visibility and increased anxiety for motorists traveling nearby and pose a significant public safety concern. Our objective is to analyze the formation and spread of these clouds by using both laboratory experiments and validated computational models.

Experiments

Fred Browand and co-workers at the University of Southern California have developed a unique test rig to investigate water pick-up by tire treads and the primary formation of droplets in the wake of a rotating tire. The test rig consists of a tubular aluminum frame supporting two spinning wheels mounted pendulum-style upon swinging rigid arms. Commercially available, thirteen-inch-diameter wheels are used. Michelin of North America is providing custom tires with specified tread designs. The two wheels are pressed together with a lateral spring-damper to form a well-defined, accurately controllable tire patch. The wheels are rolled in contact with one another by using a sprocket and chain drive. The plane of symmetry of the experimental facility replaces the road surface. Water is introduced from a solenoid-actuated injector placed just ahead of the tire patch and is injected at a velocity matching the peripheral speed of the tires, as would be the case for a rolling tire on a wet road.

The formation of water droplets just downstream of the contact patch is studied by using a digital camera, pulsed laser light, and numerical algorithms similar to those developed for digital particle image velocimetry (DPIV). High-speed (4,000–16,000 fps) digital images of ligament formation and droplet ejection from the tire surface are also feasible. This facility allows the investigation of various tread geometries to understand their function in water uptake and primary droplet formation in a much more controlled manner than has been possible.

Computations

The droplet size, space, and velocity distributions determined as a function of tire speed and tread pattern from our experimental investigation will be used as an initial condition for our computational simulations. Commercially available computational fluid dynamics (CFD) codes will be used to predict the aerodynamic atomization of these droplets. User-defined atomization subroutines will be added to the commercial packages as necessary. The aerodynamics of rotating tires and wheel-wells are of paramount importance to the secondary atomization process. Detailed computational investigations of these effects will be performed in conjunction with the atomization study. This will allow us to simultaneously investigate the effects of splash and spray suppression devices on brake cooling and to explore possible enhancements to brake cooling resulting from well-designed add-on aerodynamic devices.

Validated state-of-the-art large-eddy simulation (LES) models capable of capturing the spatial evolution of fine droplets in a turbulent flow will be developed and used to simulate the dispersion of mist around and behind heavy trucks. Ultimately, we wish to develop a collection of predictive computational tools available to tire and truck manufacturers. It is desired, therefore, to implement the specialized models developed in this phase of the study as user subroutines in widely available CFD codes. The result will be a package that allows the effects of add-on splash-and-spray-suppression devices on vehicle aerodynamics and potential synergies between add-on aerodynamic devices and spray mitigation to be thoroughly explored.

Accomplishments and Conclusions

We began this study with an extensive review of the literature to determine both the existence and outcome of prior efforts toward splash and spray suppression and to delineate the pertinent physics governing the problem. We helped to coordinate the experimental research plan with the team at USC and develop the experimental test rig. We began studying the suitability of commercial CFD codes to (1) simulate both primary and secondary formation of droplets and (2) simulate water entrainment and ejection by rotating tires. In particular, we have begun investigating STAR-CD's ability to track free fluid surfaces via its implementation of the volume of fluid (VOF) method and to predict droplet formation. We have also begun studying STAR-CD's ability to accurately simulate the flow around a rotating tire, including both aerodynamic and free-surface phenomena. We have also begun investigating STAR-CD's ability to capture aerodynamic droplet breakup (secondary atomization) and turbulent transport of sub-Kolmogorov-scale particles.

Future Direction

This project is in its very nascent stages. All aspects of the project discussed above are under continuing development.

D. Computational Investigation of Aerodynamics of Rail Coal Cars and Drag-Reducing Add-On Devices

Objective

- To reduce the aerodynamic drag of an empty rail coal car through use of drag-reducing add-on devices.

Approach

- The turbulent time-averaged flow field around a generic coal car at realistic Reynolds number is simulated by using a RANS computational approach.
- Design drag-reducing add-on devices and test by using the same computational modeling technique.

Accomplishments

- The turbulent flow field around the coal car was computed by Star-CD using a standard high Reynolds number k-ε turbulence model with a wall function. A large recirculation area within the interior of the car that extends over almost the entire length of the car is largely responsible for producing the high aerodynamic drag for an empty coal car.
- Designed a new add-on device to manipulate the interior flow structure of the car. Computations indicate a 10% drag reduction over the base empty coal car with this new device.

Future Direction

- Further investigate the potential of LLNL drag-reducing add-on device by optimizing the number, location, and height of the plates.
- Collaborate with NASA Ames on its experimental study of coal car aerodynamics and drag reducing add-on devices

---

Introduction

The objective of this work is to reduce the aerodynamic drag of an empty rail coal car through the use of drag-reducing add-on devices. Constraints are imposed on the design of these devices, such as no interference with loading and unloading, no alteration of car internal volume, and no or minimum maintenance.

The turbulent time-averaged flow field around a generic coal car at realistic Reynolds number is simulated by using the RANS computational approach. The predicated flow field is carefully investigated for possible flow structures that are susceptible to manipulation by add-on devices. Then, drag-reducing add-on devices are designed and tested by using the same computational modeling technique.

Computations and Results

To perform modeling and simulation on an empty coal car, a generic model was needed. A CAD definition of such a model was provided by Jim Ross at NASA Ames for this investigation. NASA is currently studying the aerodynamics of loaded and unloaded coal cars through a series of experiments. As the NASA experimental data become available, the computational results can be validated. The geometry of the generic coal car is shown in Figure 1; the car's dimensions are 6.84 m × 1.45 m × 1.80 m.

The turbulent flow field around the coal car was computed by Star-CD using a standard high Reynolds number k-ε turbulence model with a wall function. The flow is assumed to be incompressible and fully turbulent. A realistic flow Reynolds

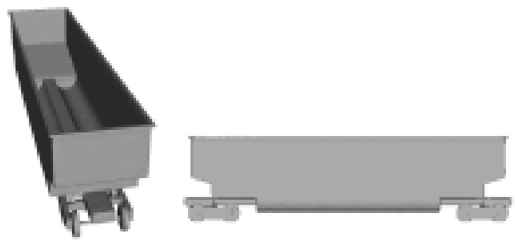

Figure 1. Generic coal car geometry.

number of 4 million, which was based on the car width and a flow velocity of 70 km/h (43.6 mi/h), was used for all computations. Figure 2 presents the flow field around the empty coal car using particle traces. The stagnation area in front and flow over the car are clearly visible. Figure 3 shows a large recirculation area within the interior of the car that extends over almost the entire length of the car. This flow structure is largely responsible for producing the high aerodynamic drag for an empty coal car. The computed drag coefficient for this case is 1.28, and the lift coefficient is -0.1 (downward force).

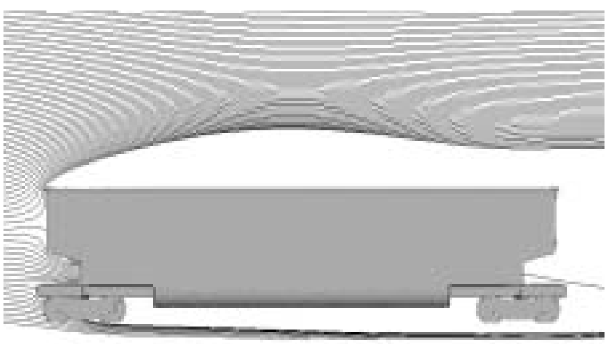

Figure 2. Particle traces showing the flow field around the coal car.

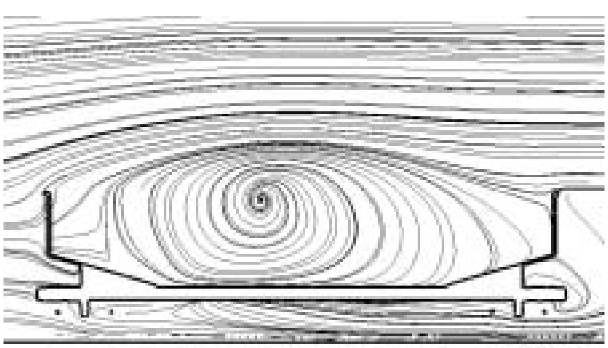

Figure 3. Particle traces on a symmetry plane including the interior space.

To reduce the aerodynamic drag of this generic coal car, the flow recirculation within the car needs to be modified. Figure 4 presents a new LLNL add-on device designed to manipulate the interior flow structure of the car. Presently, the device consists of two thin plates that split the car into three equal-length sections, and they extend half way up as shown in Figure 4. The number of plates could range from 1 to 10, and the height of each plate could vary from a one-third up to the full height of the car. The device is extremely simple and should not require any maintenance. Because of utilization of thin plates, the coal car capacity and loading and unloading are not affected. This is our first attempt to evaluate the performance of an LLNL drag-reducing device.

Figures 5 and 6 present the computed flow field around the coal car caused by the presence of the aerodynamic add-on devices. Figure 5 shows a flow pattern similar to that in Figure 2, except that particle traces show lower flow deflection on top of the car. The reason for this is shown in Figure 6 where the flow recirculation is confined to a region between the two thin plates. For this geometry, the drag and lift coefficients are 1.16 and -0.15, respectively. This represents a 10% drag reduction

Figure 4. Generic coal car with the aerodynamic add-on device.

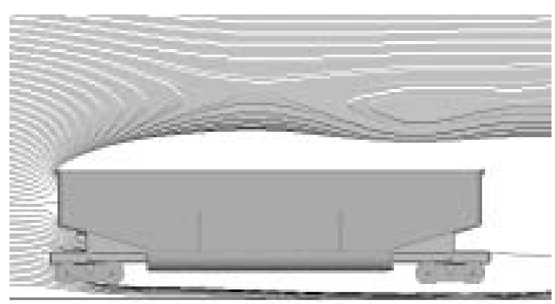

Figure 5. Particle trace showing the flow field about the coal car with the add-on device.

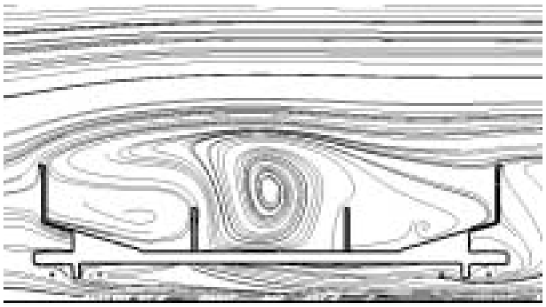

Figure 6. Particle traces on a symmetry plane, including the interior space with the add-on device.

over the base empty coal car. Because of the limited scope of this effort, no attempt has been made to optimize the number, spacing, and the height of the plates for maximum possible drag reduction.

Conclusions

The potential of an LLNL drag-reducing add-on device will be further investigated by optimizing the number, the location, and the height of the plates. Another objective is to collaborate with NASA Ames researchers on their experimental study of coal car aerodynamics and drag-reducing add-on devices.

G. Computational and Analytical Simulation of Simplified GTS Geometries/Bluff Bodies

Principal Investigator: Lawrence J. DeChant (PI), Basil Hassan, Jeff Payne, Matt Barone, Chris Roy (Contractor: Auburn U.)
Affiliation: Sandia National Laboratories
Address: P.O. Box 5800, Albuquerque, NM 87185-0825
(505) 844-4250, fax: (505) 844-4523, e-mail: ljdecha@sandia.gov

Technology Development Area Specialist: Sidney Diamond
(202) 586-8032, fax: (202) 586-1600, e-mail: sid.diamond@ee.doe.gov
Technical Program Manager: Jules Routbort
(630) 252-5065, fax: (630) 252-4289, e-mail: routbort@anl.gov

Contractor: Sandia National Laboratories
Contract No.: DE-AC04-94AL85000

Objectives

- Examine the effectiveness of the Detached Eddy Simulation (DES) approach for predicting tractor/trailer wakes.
- Explore potential for reduced order drag coefficient model based upon combined Green's function and Gram-Charlier series method.

Approach

- Sandia's SACCARA code was used to conduct DES simulations of a truncated version of the Ground Transportation System (GTS) without boattail plates.
- Preliminary computations were run on a coarse (4 million cell) mesh.
- The DES simulations were compared to steady-state Reynold's-Averaged Navier-Stokes (RANS) computations and experimental data.
- A reduced-order model was developed by using self-similar, far-field, turbulent wake concepts to estimate the 2-d drag coefficient for a range of bluff body problems.

Accomplishments

- Statistically converged unsteady DES solutions were obtained for the truncated GTS model on the coarse mesh at a Reynolds number of 2 million.
- The DES predictions were compared to steady-state RANS simulations by using the Menter k-omega model.
- The DES predictions were compared to experimental data obtained in the NASA-Ames 7-ft × 10-ft wind tunnel.
- Comparisons include both time-averaged surface pressure and time-averaged wake velocities.
- A reduced-order model was developed by using self-similar, far-field, turbulent wake concepts to estimate the 2-d drag coefficient for a range of bluff body problems.

Future Direction

- Initial estimates suggest that the Sandia funding levels will be significantly reduced from prior levels.
- Auburn University will examine the DES simulations of the full GTS geometry by using finer meshes.

A. DES Simulations

Introduction

Preliminary results are presented for Detached Eddy Simulations (DES) of a generic tractor/trailer geometry at a Reynolds number of 2 million, on the basis of trailer width. The DES simulations are compared to both experimental data and steady-state Reynolds-Averaged Navier-Stokes (RANS) computations by using the Menter k-w turbulence model. These comparisons include both time-averaged base pressures and wake velocities. The DES results with the truncated geometry do not provide improved agreement with the experimental data relative to the steady-state RANS results with the full geometry. The lack of improved agreement may be due to either insufficient mesh refinement or the use of the truncated geometry. Further details of this work are presented in reference 1.

Approach

The computational fluid dynamics code used herein is SACCARA, the Sandia Advanced Code for Compressible Aerothermodynamics Research and Analysis. The SACCARA code was developed from a parallel distributed memory version of the INCA code, originally written by Amtec Engineering. The SACCARA code is used to solve the Navier-Stokes equations for conservation of mass, momentum, energy, and turbulence transport in either 2D or 3D form. Prior code verification studies with SACCARA include code-to-code comparisons with other Navier-Stokes codes and with the Direct Simulation Monte Carlo method. These studies provide some confidence that the code is free from coding errors affecting the discretization.

For the simulations results presented herein, the turbulence transport equations are integrated all the way to the vehicle walls, thus no wall functions are employed. In all cases, the distance from the wall to the first cell center off the wall is less than unity in normalized turbulence distance (i.e., $y+ < 1$). The steady-state RANS model examined is Menter's hybrid model, which switches from a k-epsilon formulation in the outer flow to a k-omega formulation near solid walls. The hybrid RANS/LES method developed by Spalart and co-workers has been developed the furthest and is called Detached Eddy Simulation, or DES. The DES approach uses the unsteady form of the Spalart-Allmaras one-equation eddy viscosity model to provide the eddy viscosity for use in the sub-grid scale stress model. The Spalart and Allmaras one-equation eddy viscosity model provides the usual RANS-based eddy viscosity in the boundary layer, but it must be modified to the appropriate eddy viscosity for LES outside of the boundary layer.

The flow over the Ground Transportation System (GTS) model has been investigated experimentally at a Reynolds number Re_W of 2 million by Storms et al. [2], where W refers to the width of the trailer base (0.32385 m). The experimental data set is unique in that it presents both ensemble-averaged surface pressure data, as well as multiple planes of instantaneous and ensemble-averaged velocity data in the wake for this high Reynolds number flow.

To perform the computationally intensive DES simulations, the front of the GTS was truncated along with the wind tunnel wall at $x/W = 2$. Note that the wind tunnel wall and the rear posts are included in the simulation. This mesh consists of approximately 4 million grid points and was domain decomposed and run on 32 processors of a Linux cluster.

Accomplishments

Preliminary results were presented for DES of generic tractor/trailer geometry at a Reynolds number of 2 million based on the trailer width for the truncated geometry. The DES simulations were compared to both experimental data and to steady-state RANS computations by using the Menter k-omega turbulence model. These comparisons included both time-averaged base pressures and wake velocities. Although we fully expected the DES simulations to improve the agreement with the experimental data, the results were clearly not better than the steady-state RANS computations (see Figure 1).

The fact that the DES simulations did not provide improved agreement with the experimental data, as compared to the RANS results, could be due to a number of reasons. The residuals for each time step did not obtain the desired iterative convergence level because of the extremely fine mesh spacing near the

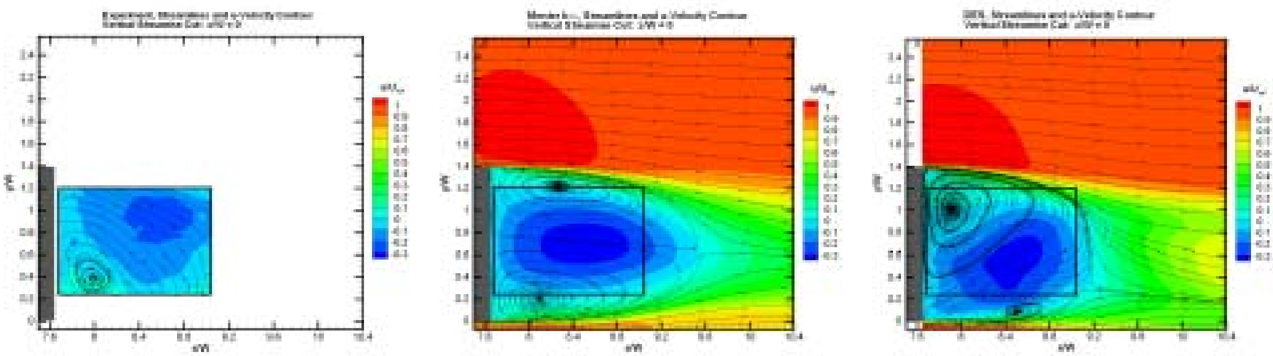

a) experiment b) RANS c) DES

Figure 1. Vertical streamwise cuts of u-velocity and streamlines from (a) experiment, (b) RANS, and (c) DES.

walls; thus, some iterative errors may be polluting the solution. The effects of truncating the forward part of the GTS geometry and the wind tunnel were not assessed. The flow over the forward portion of the GTS does generate some streamwise vorticity, which is not included in the current simulations.

The back pressure was adjusted and then run for 0.1 s before statistics were collected. Examination of the reference pressure indicated that the pressure transients had not yet died out by the time statistics were collected. In addition, the time window for collecting statistics should be increased to ensure that the time-averaged results are statistically converged. Finally, another possible reason for the lack of agreement between the DES simulations and the experiment is insufficient mesh refinement. Comparison of the unsteady pressure signal from the experiment with the same signal from the DES simulations showed that the DES signal had less structure and a larger amplitude. This behavior is likely related to the excessive dissipative errors associated with insufficient mesh refinement.

References

1. C.J. Roy, J.C. Brown, L.J. DeChant, and M.A. Barone, "Unsteady Turbulent Flow Simulations of the Base of a Generic Tractor/Trailer," AIAA Paper 2004-2255, 34th AIAA Fluid Dynamics Meeting, Portland, OR, June 2004.
2. B. Storms, J.C. Ross, J.T. Heineck, S.M. Walker, D.M. Driver, and G.G. Zilliac, "An Experimental Study of the Ground Transportation System (GTS) Model in the NASA Ames 7- by 10-ft Wind Tunnel," NASA TM-2001-209621, 2001.

B. Reduced-Order Model

Introduction

In this study, we extend self-similar, far-field, turbulent wake concepts to estimate the 2-d drag coefficient for a range of bluff body problems. The self-similar wake velocity defect that is normally independent of the near field wake (and hence body geometry) is modified by using a combined approximate Green's function/Gram-Charlier series approach to retain the body geometry information. Formally, a near-field velocity defect profile is created by using small disturbance theory and the inviscid flow field associated with the body of interest. The defect solution is then used as an initial condition in the approximate Green's function solution. Finally, the Green's function solution is matched to the Gram-Charlier series, yielding profiles that are integrated to yield the net form drag on the bluff body. Preliminary results indicate that drag estimates computed by using this method are within approximately 15%, as compared with published values for flows with large separation. This methodology may be of use as a supplement to CFD and experimental solutions in reducing the heavy computational and experimental burden of estimating drag coefficients for blunt body flows for preliminary design-type studies.

Drag estimates for strongly separated flow over blunt bodies is an essential piece of information for many engineering systems. An application that demands our particular attention is aerodynamic drag forces on large ground transportation vehicles (i.e., tractor/trailer trucks). As noted by Roy et al. (2003), in common tractor/trailer, energy losses due to rolling resistance and accessories increase linearly with vehicle speed, while energy losses due to aerodynamic drag increase with the cube of the speed. At a typical highway speed of 70 mph, aerodynamic drag accounts for approximately 65% of the energy output of the engine (McCallen et al. 1999). Because of the large number of tractor/trailers on U.S. highways, even modest reductions in aerodynamic drag can significantly reduce domestic fuel consumption. Lower fuel consumption will result in a reduction in pollution emissions and, significantly, a reduced dependence on foreign oil.

Although most modern computationally based aerodynamic drag reduction studies have focused on Computational Fluid Dynamics (CFD) methods utilizing evermore sophisticated (and concurrently computationally expensive) methodologies, there remains a valuable role for reduced-complexity, analytically based models. Here we describe a model that provides an alternative to computationally expensive models.

2-d Bluff Body Drag

The basic methodology recalls that there must be a self-preservation solution (Tennekes and Lumley, 1972) — for example, self-similar construction for the velocity field is necessary:

$$\frac{U_0 - U}{U_s} = f\left(\frac{y}{l}\right) \tag{1}$$

where U_s is the maximum cross-stream variation in U. Note that for wakes, U_s will be U(y=0) where the relevant coordinate system and associated definitions are shown in Figure 1.

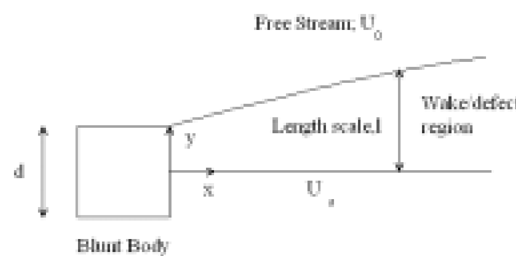

Figure 1. Schematic diagram of wake flow with coordinate, velocity, and length scale definitions.

Unfortunately, the solution obtained by Tennekes and Lumley cannot be strictly valid in the near field since the form of the similarity solution chosen by Tennekes and Lumley (1972) requires that $U_s = Ax^{-1/2} \quad l = Bx^{1/2}$, and A and B are constants to be determined. Obviously, the U_s solution is not (and cannot be) valid for x<<1. This limitation poses no problem in the far-field, of course, and is acceptable in an intermediate overlap region as well, but it cannot be applied in the wake near-field.

The connection to the velocity defect velocity field and the drag coefficient is given by (2-d drag coefficient):

$$C_D = 2\frac{\theta}{d} = \int_{-\infty}^{\infty} f d\eta \qquad (2)$$

The 2-d momentum thickness θ is introduced through equation (2) as well.

Analysis

The classic, self-similar far field wake solution is not valid in the near field of the bluff body. However, by carefully examining the process used to derive the similarity solution, it is possible to achieve other formulations that are valid in the near field.

Approximate Green's Function Solution

An alternative approach to the physically based similarity arguments presented in the text involves the mathematical analysis of a generalized problem. Here, we discuss a range of fundamental solutions to the heat equation (the canonical form of the linearized wake relationship). If, however, we are willing to use the functional form of equation (2), we can form a solution to the governing equations that is self-similar:

$$f_{GF}(\eta) = \frac{1}{\sqrt{\pi}} \int_{0}^{\infty} f_{near}(\overline{\eta}) \begin{bmatrix} \exp\left(-(\eta+\overline{\eta})^2\right) + \\ \exp\left(-(\eta-\overline{\eta})^2\right) \end{bmatrix} d\overline{\eta} \quad (3)$$

where η_0 denotes the dimensionless length scale associated with the bluff body. Note that equation (3) will approximately satisfy the full range of conditions required for solution of the wake problem.

"Initial Condition Velocity Field"; Connection to the Inviscid Flow Field

To utilize equation (2) to obtain the defect velocity field, it is necessary to be able to compute a near-field velocity defect profile (i.e., f_{near}). This function must provide the sum total of the bluff bodies geometric information. In terms of a practical result, it also must be readily obtainable and unique. Perhaps the most obvious closure for the near-field defect solution that satisfies these requirements is to utilize the local inviscid potential flow solution.

For sharp-edged bluff bodies, such as the square cylinder shown in Figure 1, where the separation location is well established, the defect velocity field is readily estimated by the discontinuous step function:

$f_{near} = \begin{cases} 1 & 0 \le \eta \le 1 \\ 0 & otherwise \end{cases}$; where η=2y/d.

Substitution of this near-field relationship into equation yields: $f_{GF} = \frac{\left[erf(\eta+1) - erf(\eta-1)\right]}{2}$.

Note that when integrated, the near-field and Green's function solution give:

$C_D = \int_{-\infty}^{\infty} f_{near} d\eta = \int_{-\infty}^{\infty} f d\eta = 2.$

Although this estimate for 2-d drag is quite good, since C_D,exper=2.1 (White 1986), we note that the Green's function does not modify the net initial defect velocity — hence, in terms of the drag coefficient, the Green's function relationship provides no new information. Our reason to utilize the Green's function form will become apparent later, but we already note that the Green's function relationship will satisfy several essential properties, including:

1. Continuous, differentiable flow field valid over full domain (i.e., $-\infty \rightarrow +\infty$);
2. Satisfies symmetry and far-field boundary conditions; and
3. Approximately satisfies governing linearized, momentum (diffusion) equation.

Gram-Charlier Series

In the previous section, it was clear that it is the local velocity defect solution that provides an estimate of drag since the Green's function relationship, equation (2), preserves the area under the local velocity defect approximation. However, the classical far-field wake profiles derived by Tennekes and Lumley (1972) should be taken into account in any formulation.

We can achieve a far-field wake influence by noting that the far-field wake might represent a single first term in a Gram-Charlier series:

$$f(\xi) = a_0 \exp\left(-\frac{1}{2}\eta^2\right) - a_1\xi\left[\exp\left(-\frac{1}{2}\eta^2\right)\right] - a_2(1-\eta^2)\left[\exp\left(-\frac{1}{2}\eta^2\right)\right] + ... \quad (4)$$

Computing derivatives and then evaluating and collecting terms, we write:

$$\begin{aligned} f_{GF}(0) &= a_0 - a_2 \\ f'_{GF}(0) &= -a_1 \\ f''_{GF}(0) &= 3a_2 - a_1 - a_0 \end{aligned} \quad (5)$$

Note that for symmetric problems (the possibility of asymmetry is included in the complete series), we can write $a_0 = \frac{1}{2}\left[3 f_{GF}(0) - f''_{GF}(0)\right]$.

Results

Preliminary drag-coefficient results for a range of 2-d bluff body shapes are presented in Table 1. Comparison is made with published values given in White (1986) and Hughes and Brighton (1991).

Table 1. Preliminary comparison between published 2-d drag coefficient results and the theoretically based model developed here. Notice that the theoretical model compares adequately with published values for rapidly separated flows (sharp-edged and laminar) but performs poorly for smooth bodies with delayed separation.

Shape	Theor. C_D	Pub. C_D	Reynolds #	Rel. Error (%)
Square Cylinder (step function)	2.1	2.1	Independent	0
2:1 Rectangular Cylinder (num. inviscid)	1.85	1.7	Independent ($Re>10^3$)	10
Equilateral triangle (apex facing flow)	1.35	1.6	Independent	15
Circular Cylinder (laminar B.L.)	1.3	1.2	$10^3<Re<10^5$	8
Circular Cylinder (transition B.L.)	0.63	0.6	$Re\approx 5x10^5$	5
Circular Cylinder (turbulent B.L.)	0.51	0.3	$Re>10^6$	70
Parabolic Cylinder, f=x(1-x) (Small disturbance) (Turbulent B.L.)	0.15	0.2	Re>>>1	25

Although our interest is primarily focused on deriving an estimate for the integrated value C_D, we can also utilize the preceding analysis to obtain estimates of the flow field behavior. Following Tennekes and Lumley (1972), and utilizing their variables $U_s = Ax^{-1/2}$ $\quad l = Bx^{1/2}$ and given that A and B are constants to be determined, we obtain an approximation for the centerline velocity behavior as a function of x: $U_s = 3.16 U_0 d x^{-1}$. Of course, this expression is not valid for x<<1, but we expect that the functional form (i.e., power of x, -1) to be correct. By way of comparison, we consider the centerline velocity data for flow over a square cylinder square cylinder given by Lyn et al. (1995) in Figure 2.

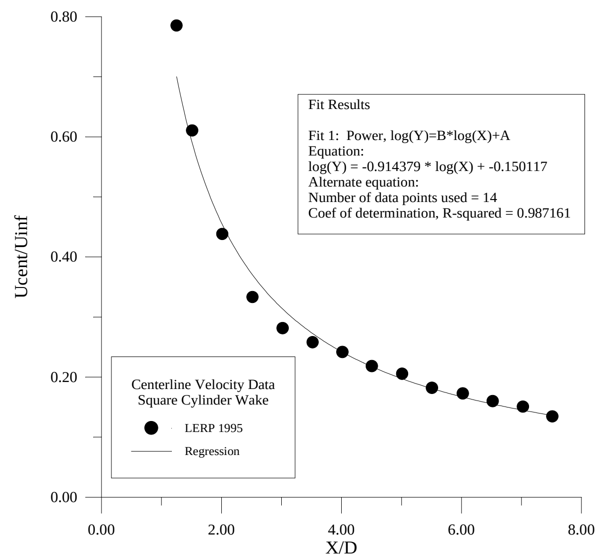

Figure 2. Centerline velocity data for flow over a square cylinder square cylinder given by Lyn et al. (1995) with regression analysis. Note that the curve-fit expression decays to the –0.91 power, which is a value that compares well with the theoretical value, -1.

Conclusions

In this manuscript, we have modified classical self-similar, far-field, turbulent wake concepts to estimate the 2-d drag coefficient for a range of bluff body problems. Preliminary results indicate that drag estimates computed by using this method are within approximately 10–20% of the published values for flows with large separation. The potential value of this method is that it is a way to utilize poorly resolved simulation results to provide an inexpensive estimate of body drag or that it functions as the basis of a physically consistent correlation scheme. This methodology may be of use as a supplement to CFD and experimental solutions in reducing the heavy computational and experimental burden of estimating drag coefficients for blunt body flows for preliminary design-type studies.

References

1. Lyn, D.A.; Einav, S.; Rodi, W.; and Park, J.H., 1995, A Laser-Doppler Velocimetry Study of Ensemble Averaged Characteristics of the Turbulent Near Wake of a Cylinder, *J. of Fluid Mechanics*, 304, pp. 285–319.
2. Tennekes, H., and Lumley, J.L., 1972, *A First Course in Turbulence*, MIT Press, Cambridge, MA.
3. Townsend, A.A., 1976, *The Structure of Turbulent Shear Flow*, Cambridge U. Press, Cambridge, UK.
4. Van Dyke, M., 1975, *Perturbation Methods in Fluid Mechanics*, Parabolic, Stanford, CA.
5. White, F.M., 1986, *Fluid Mechanics*, McGraw-Hill, NY.
6. Hughes, W.F., and Brighton, J.A.,1991, *Fluid Dynamics*, 2nd ed., McGraw-Hill, Inc., NY.
7. McCallen, R.; Couch, R.; Hsu, J.; Browand, F.; Hammache, M.; Leonard, A.; Brady, M.; Salari, K.; Rutledge, W.; Ross, J.; Storms, B.; Heineck, J.T.; Driver, D.; Bell, J.; and Zilliac, G., 1999, "Progress in Reducing Aerodynamic Drag for Higher Efficiency of Heavy Duty Trucks (class 7-8)," SAE Paper 1999-01-223.
8. Roy, C.; McWherter-Payne, M.; and Solari, K., 2002, RANS Simulations of a Simplified Tractor/Trailer Geometry, UEF.
9. Schlichting, H., 1979, *Boundary Layer Theory*, McGraw-Hill, NY.
10. Haberman, R., 1983, *Elementary Applied Partial Differential Equations with Fourier Series and Boundary Value Problems*, Prentice Hall, Englewood Cliffs, NJ.
11. Logan, J.D., 1978, *Applied Mathematics*, Wiley, NY.

H. Commercial CFD Code Benchmarking for External Aerodynamics Simulations of Realistic Heavy-Vehicle Configurations

Principal Investigator: W. David Pointer
Argonne National Laboratory
9700 S Cass Avenue, NE-208, Argonne, IL 60439
(630)252-1052, fax: (630) 252-4500, e-mail: dpointer@anl.gov

Technology Development Area Specialist: Sidney Diamond
(202) 586-8032, fax: (202) 586-1600, e-mail: sid.diamond@ee.doe.gov
Technical Program Manager: Jules Routbort
(630) 252-5065, fax: (630) 252-4289, e-mail: routbort@anl.gov

Contractor: Argonne National Laboratory
Contract No.: W-31-109-ENG-38

Objectives

- Evaluate capabilities in standard commercial computational fluid dynamics (CFD) software for the prediction of aerodynamic characteristics of a conventional U.S. Class 8 tractor-trailer truck.
- Develop “best practice” guidelines for the application of commercial CFD software in the design process of Class 8 vehicles.

Approach

- Develop computational models for the Generic Conventional Model (GCM) geometry.
- Benchmark the GCM simulations for computed aerodynamic drag force and pressure field distributions with NASA Ames 7-ft × 10-ft wind tunnel data.

Accomplishments

- Experimental measurements and computational predictions of the vehicle drag coefficient agreed within experimental uncertainty for the 0° yaw simulations. Experimental measurements and computational predictions of the pressure distribution along the surface of the vehicle agree well everywhere, except in the vicinity of the trailer base and underbody and the gap.
- Comparisons of computational predictions of the vehicle at a yaw angle of 10° using coarse mesh models indicate that the accuracy of the steady RANS simulation capability is reduced at high yaw angles.

Future Direction

- Extend evaluation of capabilities for prediction of aerodynamic drag in cases in which there is a cross-wind component (e.g., wind tunnel experiments where the vehicle is placed at some yaw angle) to fine mesh simulations and lower yaw angles.
- Consider alternative GCM configurations using various add-on devices to examine capabilities for the prediction of changes in drag coefficient.
- Suggest potential drag reduction design options on the basis of knowledge gained from computational effort.

Introduction

In collaboration with the U.S. Department of Energy's Heavy Vehicle Aerodynamic Drag Consortium, Argonne National Laboratory is developing guidelines for the near-term use of existing commercial Computational Fluid Dynamics (CFD) tools by the heavy vehicle manufacturing industry. These guidelines are being developed on the basis of (1) measured drag coefficients and (2) detailed surface pressure distributions from wind tunnel experiments completed at NASA Ames Laboratory by using a generalized 1/8th-scale conventional U.S. tractor-trailer geometry, the Generic Conventional Model (GCM) [1]. Studies consider the effects of selection of global and near-surface mesh-size parameters and selection of turbulence modeling strategies.

Selection of Commercial CFD Software

The guidelines developed by this program are intended to be generic advice for the application of a commercial CFD software package for the prediction of heavy vehicle aerodynamic drag coefficients. Since this market is currently dominated by finite volume formulations, the guidelines will focus upon software using this methodology. Preliminary guideline development will be completed by using the commercial CFD code Star-CD [2]. The Star-CD software was selected for this purpose largely as a result of the flexibility in computational mesh development the code offers, along with the ability to utilize polyhedral "cut" cells and recognize both integral and arbitrary interfaces between regions of the computational domain. It is anticipated that the applicability of the general guidelines to other commercial CFD codes will be examined and that the extension of the guidelines to alternate commercial CFD software methodologies, such as Lattice-Boltzmann, will be pursued following the initial development stage.

The Generic Conventional Model

The GCM is a generalized representation of a conventional U.S. tractor-trailer truck developed by NASA Ames Research Center. The model is 1/8th scale, with approximate dimensions of 97 in. long by 13 in. wide by 21 in. high. The model is mounted at the center of the ground plane of a 10-ft-wide by 7-ft-high wind tunnel test section. Instrumentation includes a force balance, 476 steady pressure transducers, 14 dynamic pressure transducers, and three-dimensional Particle Image Velocimetry (PIV). The nominal configuration (see Figure 1) is a representative model of a current-generation tractor-trailer truck.

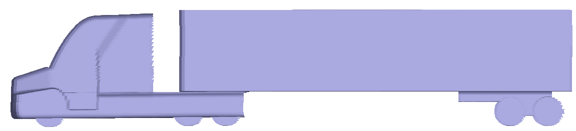

Figure 1. Generic Conventional Model (GCM) standard configuration.

Computational Model

The computational model employed in these studies was developed by using the ES-Aero tool for aerodynamic drag simulation that is available as part of the Star-CD software package. The surface of the standard configuration GCM is defined by using approximately 500,000 triangular surface elements based upon CAD data representations taken from optical scans of the actual model. The computational domain is developed on the basis of this surface definition by using a semi-automated process that begins by creating a hexahedral mesh that is successively refined in smaller zones around vehicle, with 4 cell to 1 cell coupling employed at the interfaces between zones. The dimensions of hexahedral elements that make up the innermost zone are specified by the user as the near-vehicle cell size. The mesh elements near the vehicle surface are then further refined on the basis of local surface features identified by the user or selected automatically on the basis of curvature or gap width. The user specifies a minimum allowable cell size that limits the refinement of the mesh in this step.

By using this locally refined hexahedral mesh, the original surface is "wrapped" by projecting the hexahedral mesh onto the original surface. In this manner, the multiple components defining the GCM are merged into a single surface. The "wrapped" surface definition is then volumetrically expanded to create a subsurface, which is used to cut away the portions of the locally refined hexahedral mesh that fall inside the vehicle. A brick-and-prism cell-extrusion layer is then created to fill the gap between the subsurface and the "wrapped" surface. In this way, the non-hexahedral cut cells are removed some distance from the surface. A final step further refines the wake region and the underbody region in order to better capture important flow features in those regions. An example of the mesh construction of the computational domain used in the GCM simulations is shown in Figure 2.

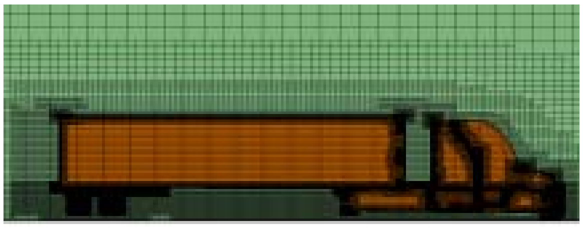

Figure 2. Example of computational mesh structure used in the simulation of the aerodynamic characteristics of Generic Conventional Model (GCM) configurations.

When using locally refined, partially unstructured computational domains with substantial numbers of non-hexahedral cells, the standard practice of evaluating grid convergence by uniformly refining the entire mesh in all directions becomes intractable. In the computational meshes used in these studies (which are based on the sizes of surface features on the vehicle), two separate parameters determine the size of the mesh. The near-vehicle cell size determines the bulk flow resolution surrounding the vehicle, and the minimum cell size determines the level of resolution allowed as a result of feature-based refinement around significant features of the vehicle's surface. Mesh-sensitivity analyses included in these studies examine the effects of changes in these parameters upon the prediction of the drag coefficient; however, this is not equivalent to the traditional grid convergence study for two reasons. First, the grid is not uniformly refined in all directions throughout the domain. Second, the vehicle surface definition cannot be exactly maintained for all models since the final surface definition depends on the local refinement of the computational mesh.

Bulk Flow Resolution

Five unique computational domains were generated on the basis of the standard GCM configuration in order to evaluate the effects of the near-vehicle cell size parameter on the prediction of the drag coefficient. Near-vehicle cell sizes of 16.0, 12.0, 10.0, 8.0, and 6.0 mm were considered. In each case, the minimum cell size resulting from local feature-based refinements is 12.5% of the near-vehicle cell size, and an additional restriction is set so that a minimum of 16 elements are required for the definition of a circle. To ensure that the quality of the vehicle surface is maintained, the cell layer immediately adjacent to the surface is refined to 25% of the original size before trimming. The computational domain characteristics are shown in Table 1.

Table 1. Summary of computational domain characteristics for evaluation of bulk cell size effects.

Near Vehicle Cell Size (mm)	Minimum Cell Size (mm)	Total Number of Volume Elements	Number of Volume Elements on Surface
16.0	2.0	1012338	73574
12.0	1.5	1737085	126119
10.0	1.25	2345640	175105
8.0	1.0	3282426	266666
6.0	0.75	5695622	400382

Each computational domain was considered in a parametric study for evaluation of the sensitivity of the prediction of the vehicle drag coefficient to changes in the bulk flow resolution. A uniform velocity of 51.45 m/s, corresponding to a Reynolds number of 1.1×10^6, was specified at the inlet, and a zero gradient condition is specified at the outlet. In these simulations, the standard high Reynolds number k-ε turbulence model and a logarithmic wall function are employed for prediction of turbulent kinetic energy and dissipation.

For each case, 3,000 iterations were calculated by using Star-CD's standard conjugate gradient solver and the PISO predictor-corrector algorithm. Convergence criteria were set to ensure that all cases would reach 3,000 iterations before stopping. At the 3,000th iteration, all residuals are less than 10^{-4}. In addition to standard flow variable residual monitoring for the mass, momentum, and energy equations, the drag coefficient of the vehicle is monitored as the solution develops to ensure that the drag coefficient reaches a converged value. Total computational time and clock time when using 16 processors for each simulation are shown in Table 2.

Table 2. Summary of computational cost for each case considered in the evaluation of bulk cell size effects.

Near-Vehicle Cell Size (mm)	Total CPU Time (s)	Total Clock Time (s)
16	206072	16454
12	390113	29392
10	417686	32182
8	610958	44967
6	2720956	188577

Predicted drag coefficients from each of the five cases are compared with experimental data from wind tunnel tests in Table 3. While there is a trend of improvement with reduction in near-vehicle cell size, the effects that lead to non-linearity in the trend are not immediately clear. More detailed comparisons of pressure distributions on the surface of the vehicle provide better insight into the sensitivity of the predictive capability to the bulk flow resolution. The pressure coefficient distribution on the surface of the vehicle from the case using the mesh based upon an 8-mm near-vehicle cell size is shown in Figure 3 as an example of a typical predicted pressure distribution on the vehicle surface. Pressure coefficient data were extracted along the centerline of the vehicle for each case and compared with experimental data, as shown in Figure 4. These comparisons show that the difference in the predicted drag coefficient between models using different near-vehicle cell sizes is a result of small differences in the pressure distribution over the entire surface rather than large localized differences.

Table 3. Effects of near-vehicle cell size parameter on accuracy of drag coefficient prediction.

Near-Vehicle Cell Size (mm)	Predicted Drag Coefficient	Error in Drag Coefficient
experiment	0.398	
16	0.449	12.0
12	0.441	10.3
10	0.418	4.9
8	0.415	4.2
6	0.405	1.7

Near-Wall Resolution

Following the assessment of the effects of the near-vehicle cell size parameter on the accuracy of the drag coefficient prediction, the effect of the near-wall cell size parameter was also considered. The near-vehicle cell size was set to 8 mm, and the minimum cell size for local refinement was reduced

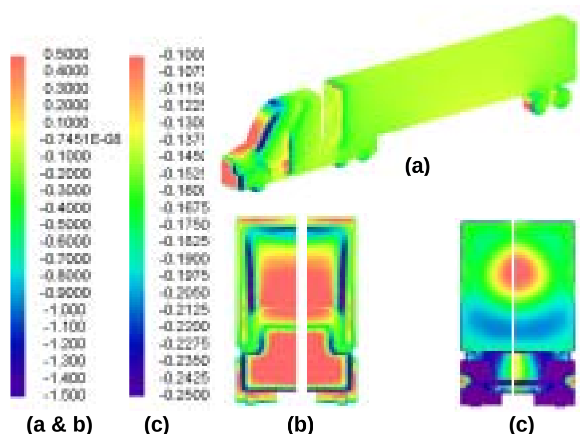

Figure 3. Predicted pressure coefficient distribution on the vehicle surface. Shown are (a) the side view of the full vehicle, (b) the front of the tractor, and (c) the base of the trailer.

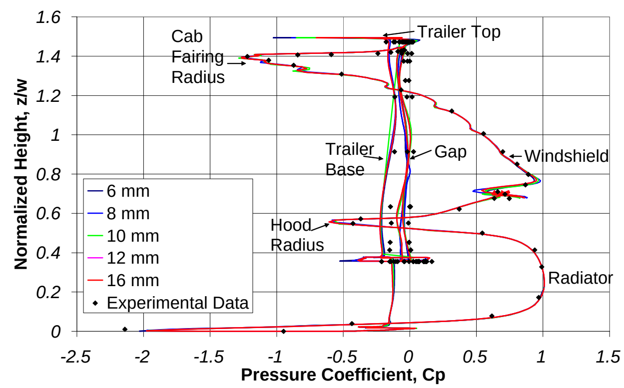

Figure 4. Comparison of predicted pressure coefficient distributions on the vehicle surface for various values of the near-vehicle cell size parameter with experimental data for the GCM geometry.

from 1 mm to 0.5 mm. The change in the near-wall resolution increases the number of computational elements from 3,282,426 to 4,264,232. When selecting near-wall cell size limits, it is important to consider the appropriate limits of the parameter y+, which describes the thickness of the region near the wall where the logarithmic law of the wall function is applied. For the turbulence model and wall function employed in these studies, the value of y+ should fall between 20 and 200. A near-wall computational cell that is too small will result in a value of y+ that is too small, and a near-wall computational cell that is too large will result in a y+ that is too large. As shown in Figure 5, the value of y+ falls within the appropriate range for the turbulence model employed.

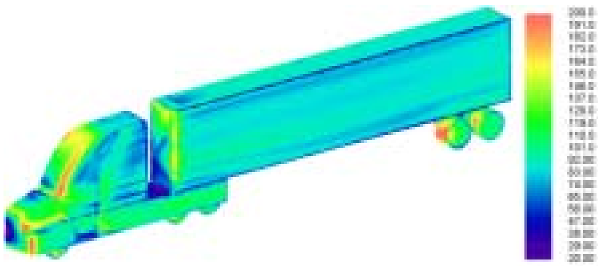

Figure 5. Values of the y^+ parameter along the surface of the computational model of the GCM geometry when the computational mesh uses a near-vehicle cell size of 8 mm and a near-wall cell size limit of 1 mm.

A simulation of the flow of air over the vehicle was completed by using the refined computational mesh for comparison with the previous simulations. As in the previous cases, a uniform inlet velocity condition and a zero-gradient outlet condition were specified, and the standard high Reynolds number k-ε model was utilized. Convergence criteria were set so that 3,000 iterations were completed, and all residuals fall below 10^{-4} by the 3,000th iteration. The change in the computational mesh resolution results in an increase in the total CPU time from 610,958 s to 703,027 s.

The change in the near-wall refinement parameter results in a reduction in the error of the drag coefficient prediction from 4.2% to 1.0%, which is within experimental uncertainty. The predicted surface pressure distributions along the vehicle centerline for both cases are shown in Figure 6, along with the experimentally measured pressure distribution. As in the assessment of the effects of

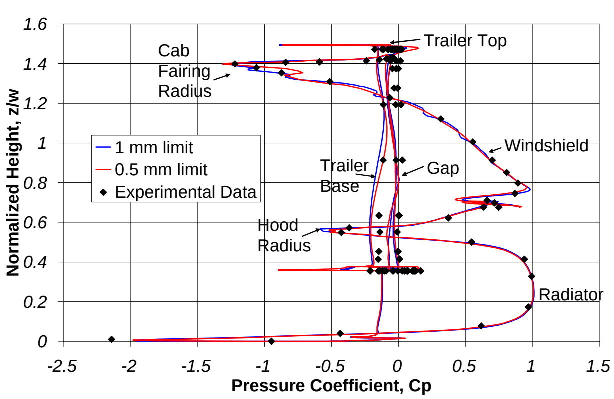

Figure 6. Comparison of predicted pressure coefficient distributions on the vehicle surface for various near wall cell size limits with experimental data for the GCM geometry.

the near-vehicle cell size parameter, comparisons of surface pressure data indicate that the predicted drag coefficient between models using different near-wall cell sizes is a result of small differences in the pressure distribution over the entire surface rather than large localized differences.

Turbulence Model Selection

In all simulations completed as part of the computational mesh sensitivity studies, the high Reynolds number k-ε turbulence model was used in conjunction with a standard logarithmic wall function for the prediction of turbulent kinetic energy and eddy diffusivity. While the high Reynolds number k- ε turbulence model is a robust general purpose turbulence model, the strong adverse pressure gradients and large flow recirculation regions associated with the GCM geometry may limit the applicability of steady state Reynolds Averaged Navier-Stokes (RANS) modeling strategies. Therefore, the sensitivity of the drag coefficient prediction to the choice of two equation steady RANS turbulence model was also assessed.

By using the computational mesh with a near-vehicle cell size of 8 mm and a near-wall cell size limit of 0.5 mm, simulations of the aerodynamic characteristics of the GCM model were repeated by using five steady RANS turbulence models and their associated wall functions:

1. The standard high-Reynolds number k-ε model with logarithmic wall function,
2. The Menter k-ε SST model,
3. The renormalization group (RNG) formulation of the k-ε model,
4. The Chen formulation of the k-ε model, and
5. The quadratic formulation of the k-ε model.

The standard k-ε model and the k-ε SST model are identical in the far field, but the k-ε SST model incorporates additional detail in the near-wall region and in separated flow regions. The RNG model is similar to the standard k-ε model, but it includes an additional term to account for the mean flow distortion of the dissipation. Chen's model is also similar to the standard k-ε model, but it includes an additional term to more effectively account for the effects of changes in the mean strain rate on the energy transfer mechanism of turbulence. The quadratic model is a higher-order model of the k-ε type that includes non-linear terms to allow for the anisotropy of turbulence in some flow fields.

As in the previous cases, a uniform inlet velocity condition and a zero gradient outlet condition were specified, and the standard high-Reynolds-number k-ε model was utilized. Convergence criteria were set so that 3,000 iterations were completed, and all residuals fall below 10^{-4} by the 3,000th iteration. The drag coefficients predicted by using each of the selected steady-RANS turbulence models are shown in Table 4. More detailed comparisons of the predicted pressure coefficient distributions when using each of the selected turbulence models are shown in Figure 7. In contrast to previous studies, the differences in the predicted drag coefficient are largely a result of localized discrepancies in the surface pressure coefficient predictions in the regions of separated flow, as shown in Figure 8.

Table 4. Results of the evaluation of two-equation turbulence models for prediction of drag coefficients for the GCM geometry.

Turbulence Model	Predicted Drag Coefficient	Percent Error in Prediction
Experiment	0.398	--
High-Reynolds-Number k-epsilon Model	0.402	1.0
Menter k-ε SST model	0.401	0.8
RNG model	0.389	2.3
Chen's model	0.3919	1.61
Quadratic model	0.3815	4.32

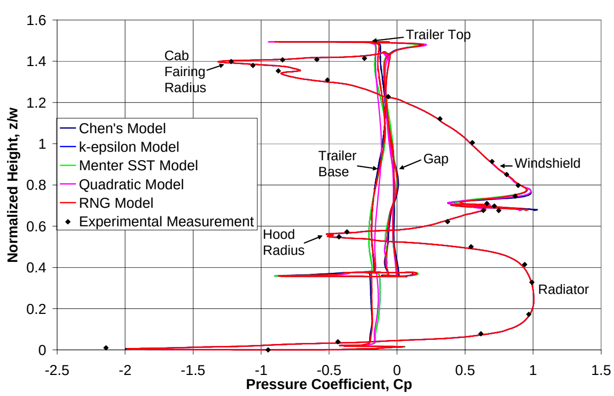

Figure 7. Comparison of predicted pressure coefficient distributions on the vehicle surface with experimental data for selected turbulence models.

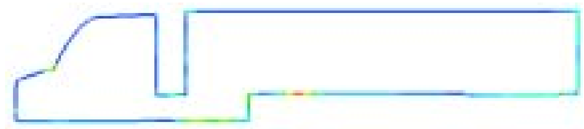

Figure 8. Standard deviation of the surface pressure distribution predictions by using the selected turbulence models.

The differences in the predictions of the surface pressure distribution are a direct result of differences in the predicted flow fields. The predicted velocity magnitude at the centerline is shown for each selected turbulence model in Figure 9. The primary differences in velocity field prediction occur in the recirculation zone under the trailer and in the interaction between the underbody flow and the separated flow region at the trailer base. The location of these differences corresponds to the largest discrepancies between the surface pressure distribution predictions.

Full Vehicle versus Half Vehicle

To evaluate the effects of considering only half of the vehicle rather than the full vehicle, two models were created by using the full vehicle geometry. These models use the same mesh parameter settings as the two coarsest models considered in the mesh sensitivity study. The full vehicle models are based upon near-vehicle cell sizes of 12 mm and 16 mm, with minimum near-wall cell sizes of 1.5 mm and 2.0 mm, respectively. As in all previous studies, 3,000 iterations were completed for each steady-state simulation, and the convergence of the drag coefficient was monitored.

As shown in Table 5, drag coefficient predictions show a slight improvement in agreement with experimental measurements when the full-vehicle model is used. The comparison of more detailed pressure coefficient distributions along the vehicle surface, as shown in Figure 10, reveals that the most substantial discrepancies between the full and half vehicle model predictions occur along the underbody and in the gap between the tractor and trailer. The GCM geometry is, in reality, slightly asymmetric, and the consideration of this geometric asymmetry is likely the primary difference in the models that contributes to these discrepancies.

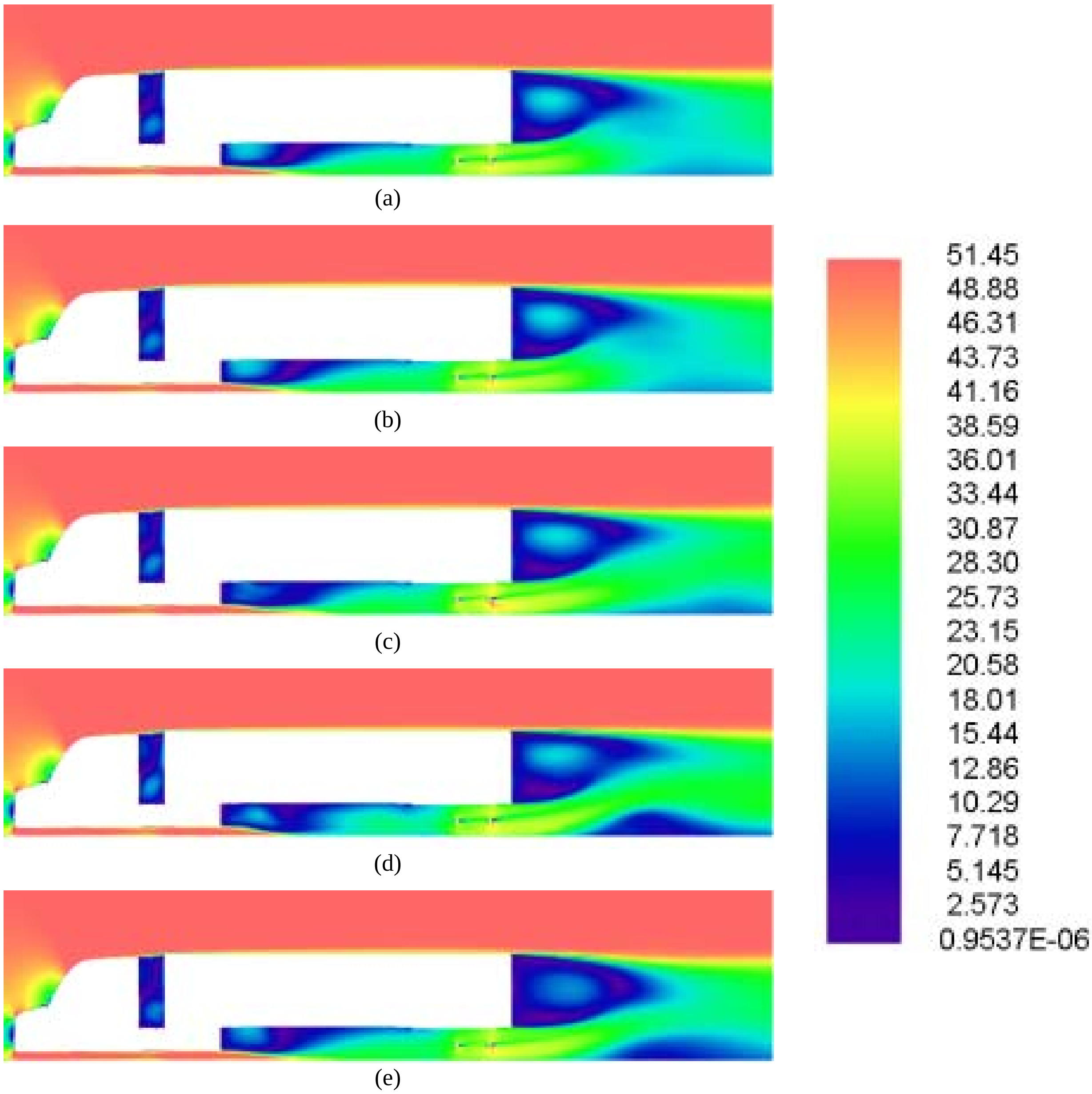

Figure 9. Comparison of predicted steady-state velocity fields for five selections of turbulence model: (a) the high-Reynolds number k-ε model with logarithmic wall function, (b) the Menter k-ε SST model, (c) the renormalization group (RNG) formulation of the k-ε model, (d) the Chen formulation of the k-ε model, and (e) the quadratic formulation of the k-ε model.

Table 5. Comparison of drag coefficient predictions from half-vehicle and full-vehicle models.

	Half-Vehicle	
Near-Vehicle Cell Size (mm)	**Predicted Drag Coefficient**	**Percent Error in Prediction**
16	0.449	12.0
12	0.441	10.3
	Full-Vehicle	
	Predicted Drag Coefficient	**Percent Error in Prediction**
16	0.441	10.3
12	0.426	6.7

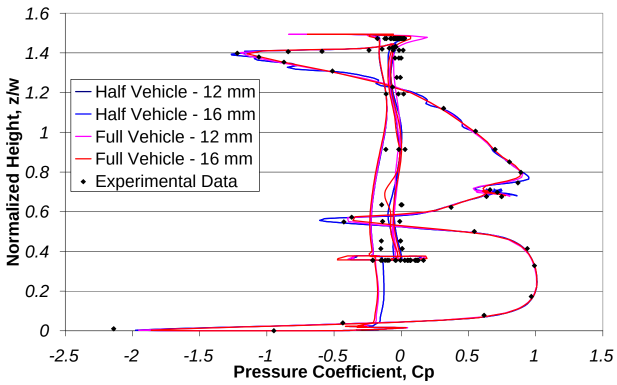

Figure 10. Comparison of predicted pressure coefficient distributions on the vehicle surface when the full vehicle model is used with predicted pressure coefficient distributions when the half vehicle model is used and with experimental data.

Vehicles at Yaw

An assessment of the capabilities available in current-generation commercial CFD software for the prediction of aerodynamic drag characteristics of heavy vehicles at yaw angles greater than zero is under way. A preliminary study using coarse-mesh simulations of the GCM geometry at a yaw angle of ten degrees has been completed. The 10° yaw angle was selected because as the yaw angle of the vehicle increases through 10°, a change from a high drag state to a low drag state occurs (see Figure 11). The prediction of aerodynamic drag coefficients in this region is expected to be more difficult than at lower or higher yaw angles.

As with the no-yaw case, the study begins with an initial assessment of the sensitivity of the drag coefficient prediction to the base cell size in the near-vehicle region. Since the full vehicle must be modeled when the vehicle is placed at a yaw angle other than zero, only coarse mesh models with near-vehicle cell size parameters of 12 mm or 16 mm have been considered to date. As with the previous simulations, 3,000 iterations were completed for each simulation. Results of these simulations are shown (along with the zero yaw angle results) in Figure 12. In going from a no-yaw condition of zero degrees to a yawed condition of 10°, the error in the drag coefficient prediction increases from 10.3% to 33.8% for the 16-mm case and from 6.7% to 23.5% in the 12-mm case.

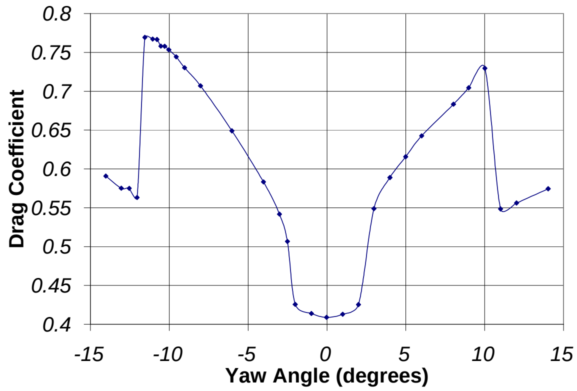

Figure 11. Experimental measurements of drag coefficients for the GCM vehicle geometry at yaw angles ranging from -14 to +14.

By using the coarsest mesh, which is based upon a 16-mm near-vehicle cell size, a preliminary assessment of the sensitivity of the prediction of drag coefficient to the selection of turbulence model has been completed. As in the assessment of steady RANS models for the no-yaw case, five two-equation type models were considered:

1. The high-Reynolds number k-ε model,
2. The Menter k-ε SST model,
3. The RNG formulation of the k-ε model,
4. The Chen formulation of the k-ε model, and
5. The quadratic formulation of the k-ε model.

All five models use appropriate logarithmic wall functions to resolve the boundary layer region. Again, 3,000 iterations were completed for each simulation. Results of these simulations are shown in Table 6. The Mentor k-ε SST model, which uses a k-ε model in separated flow regions and a k-ε model elsewhere, shows the greatest improvement over the

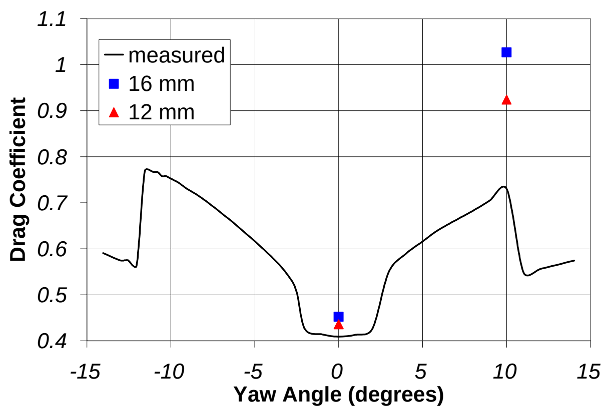

Figure 12. Comparison of computational predictions with experimental measurements of drag coefficients for models based upon near-vehicle cell sizes of 16 mm and 12 mm.

Table 6. Results of the evaluation of two-equation turbulence models for prediction of drag coefficients for the GCM geometry at a yaw angle of 10°.

Turbulence Model	Predicted Drag Coefficient	Percent Error in Prediction
Experiment	0.72955	--
High-Reynolds Number k-ε Model	1.027	33.8
Menter k-ε SST model	0.844	14.5
RNG model	1.014	32.6
Chen's model	1.052	36.3
Quadratic model	1.001	31.3

standard high-Reynolds number k-ε model. The Mentor k-ε SST model also converges much more quickly than the other models, reaching the same level of convergence in fewer than half the iterations required when using other models. The velocity field for this simulation is shown in Figure 13.

Fine Mesh Models for Full Vehicles

The number of cells used by the semi-automatic meshing tool in the process of creating the final computational mesh increases rapidly as the near-vehicle cell size is reduced. Consequently, a 64-bit computational platform with significant memory available to the processors running the meshing tools is needed to construct the fine mesh models of the full truck geometry, both at no yaw and a yaw angle of 10°. The Star-CD software has been installed on a 64-bit Itanium 2 workstation with 24 GB of RAM to allow the construction of more refined computational models. A significant effort has been dedicated to identifying and addressing issues associated with this new port of the software. It is anticipated that assessments using fine meshes will be completed in early FY 2005.

Future Work

Ongoing efforts will continue to focus on the assessment of the capabilities within current generation software by using simple steady RANS modeling strategies for the prediction of changes in drag with changes in geometry or flow conditions. These efforts will consider the standard configuration of the GCM geometry at additional yaw angles, as well as the alternative configurations of the GCM geometry shown in Figure 1. Upon completion of computational studies for each configuration of the geometry, predictions of drag coefficient and surface pressure distributions will be compared with experimentally measured values for that configuration.

Conclusions

These studies are the initial component of an assessment of the capabilities for the prediction of heavy vehicle aerodynamic characteristics by using current generation commercial computational fluid dynamics software. On the basis of the outcomes of these studies, guidelines are being developed for the immediate application of these current generation tools by the heavy vehicle manufacturing community. Initial assessments have shown that full body drag coefficients can be predicted within less than 1% of the measured value, which is within experimental accuracy. The surface pressure distributions can be predicted with reasonable accuracy by using fine mesh models. The coarsest mesh model of the full vehicle provides a prediction of the drag coefficient within 11% of the measured value. When the vehicle is yawed to 10°, the coarsest model provides a prediction within 19% of the measured value if the Menter k-ε SST model is used.

References

1. Satran, D., "An Experimental Study of the Generic Conventional Model (GCM) in the NASA Ames 7-by-10-Foot Wind Tunnel," United Engineering Foundation Conference on The Aerodynamics of Heavy Vehicles: Trucks, Buses, and Trains, United Engineering Foundation, New York, 2002.
2. Star-CD, version 3.150A, CD-Adapco Group, Melville, NY.

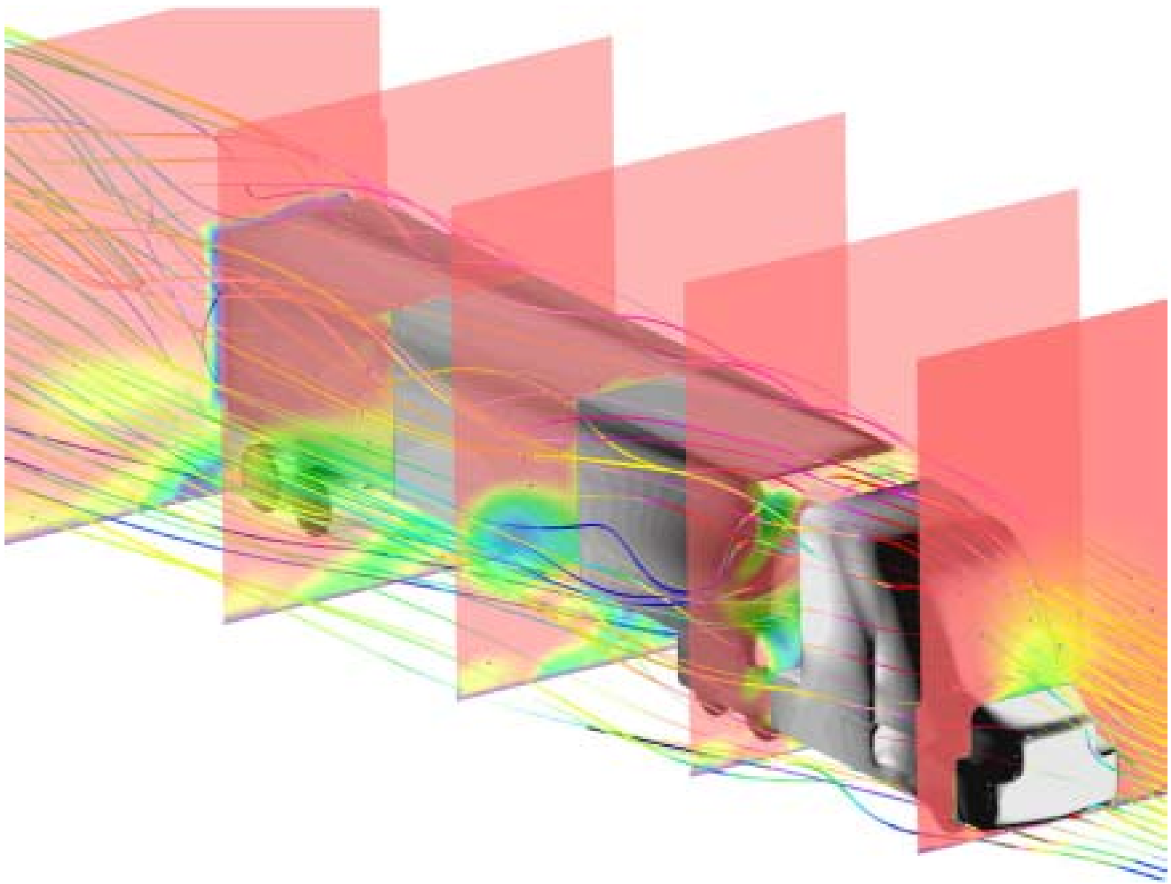

Figure 13. Predicted streamlines across the surface of the GCM geometry when the vehicle is placed at a yaw angle of 10°.

I. Bluff Body Flow Simulation Using a Vortex Element Method

Principal Investigator: Anthony Leonard
California Institute of Technology
1200 E. California Blvd.
Pasadena, CA 91125
(626) 395-4465, fax: (626) 577-9646, e-mail: tony@galcit.caltech.edu

Technology Development Area Specialist: Sidney Diamond
(202) 586-8032, fax: (202) 586-1600, e-mail: sid.diamond@ee.doe.gov
Technical Program Manager: Jules Routbort
(630) 252-5065, fax: (630)252-4289, e-mail: routbort@anl.gov

Participants:
Michael Rubel, Caltech, mrubel@galcit.caltech.edu
Philippe Chatelain, Caltech, philch@galcit.caltech.edu

Contractor: California Institute of Technology
Contract No.: DE-AC03-98EE50506

Objectives

- Study application of vortex particle methods to complex truck geometries at high Reynolds numbers.
- Investigate Large Eddy Simulation (LES) in the context of such solutions.

Approach

- Develop physically and mathematically correct treatments for the generation of vorticity at complex boundaries.
- Extend boundary treatment to cases of spinning bodies, such as tires.
- Reduce the computational work required to arrive at solutions by novel time-integration techniques.
- Reconcile LES theory with this framework.

Accomplishments

- Implemented near-wall vorticity elements with wall stress evaluation and additional Biot-Savart term for spinning objects.
- Performed preliminary simulations of spinning sphere flows at Re=300 for a dimensionless spin rate of 0.5 and 2 spin angles.
- Implemented a multiscale time integration algorithm with clear order of accuracy and convergence properties.
- Developed a new ensemble-averaging theory for LES.

Future Direction

- Compute flows around tumbling objects and spinning tires.
- Perform detailed performance measurements on the multiscale time integrator; extend to parallel computation.
- Test ensemble averaging theory on turbulent flows; ascertain whether the theory will, in fact, be able to predict LES parameters.

Introduction

Heavy ground vehicles, especially those involved in long-haul freight transportation, consume a significant part of our nation's energy supply. It is therefore of utmost importance to improve their efficiency, both to reduce emissions and to decrease reliance on imported oil.

At highway speeds, more than half of the power consumed by a typical semi truck goes into overcoming aerodynamic drag, a fraction that increases with speed and crosswind. Thanks to better tools and increased awareness, recent years have seen substantial aerodynamic improvements by the truck industry, such as tractor/trailer height matching, radiator area reduction, and swept fairings. However, there remains substantial room for improvement as understanding of turbulent fluid dynamics grows.

Our group’s research effort focuses on vortex particle methods, a novel approach for computational fluid dynamics (CFD). Where common CFD methods solve or model the Navier-Stokes equations on a grid that stretches from the truck surface outward, vortex particle methods solve the vorticity equation on a Lagrangian basis of smooth particles and do not require a grid.

We are working to advance the state of the art in vortex particle methods by improving their ability to handle the complicated, high-Reynolds-number flow around heavy vehicles. Specific challenges that we have addressed in the past year include finding strategies to accurately capture vorticity generation and resultant forces at the truck wall, handle the aerodynamics of spinning bodies (such as tires), reduce computation time through improved integration methods, and conduct theoretical treatment work on large eddy simulation (LES) turbulence modeling.

Near-Wall Vorticity

We developed a representation of near-wall vorticity by means of an attached regularized sheet. This sheet has several roles. It interacts viscously with the rest of the flow, receives contributions of elements close to the wall during a redistribution, and helps in capturing the high-vorticity gradients near the wall.

This last role is critical if one needs to accurately measure stresses at the wall. In addition, we introduce a correction that takes into account the gradient of vorticity, which can be estimated from the solution of the panel solver.

Spinning Boundaries

The flow around spinning objects is of particular interest because it is encountered around the wheels of heavy vehicles and will interact with the rest of the flow. It is also interesting because of its impact on the problem of splash-and-spray. Because we use a vorticity-based formulation along with a computation of velocities by Biot-Savart, we need to account for the vorticity inside any rotating object. This term, a volume integral, is not the best suited for our method, which uses a surface mesh to represent boundaries. We thus switch to a surface integral by application of Gauss’s theorem. In 2004, preliminary results were gathered for two configurations involving a spinning sphere: the rotation axis of the sphere was aligned with the stream or set perpendicular to it. Both cases were computed for Re=300 and a dimensionless spin velocity WR/U_∞ of 0.5, where W is the angular velocity. The case of a perpendicular axis is of particular interest because of its resemblance to the geometry of a spinning tire. The problem is not symmetric and does not need to be perturbed to trigger shedding; Figure 1 shows vortex structures identified by contours of $Q = -\frac{1}{2} Tr(\nabla u \cdot \nabla u)$.

Even though the problem is still marked by the initial transient, the sphere sustains an important amount of lift (Figure 4, Figure 3) and develops a wake that comprises a system of counter-rotating vortices.

The stream-wise rotation is also of interest because of the various wake structures that are observed across the ranges of Reynolds numbers and spin rates. Our results show the transition from the axi-symmetric wake typical of a low Reynolds number to an asymmetric periodic wake (Figure 2).

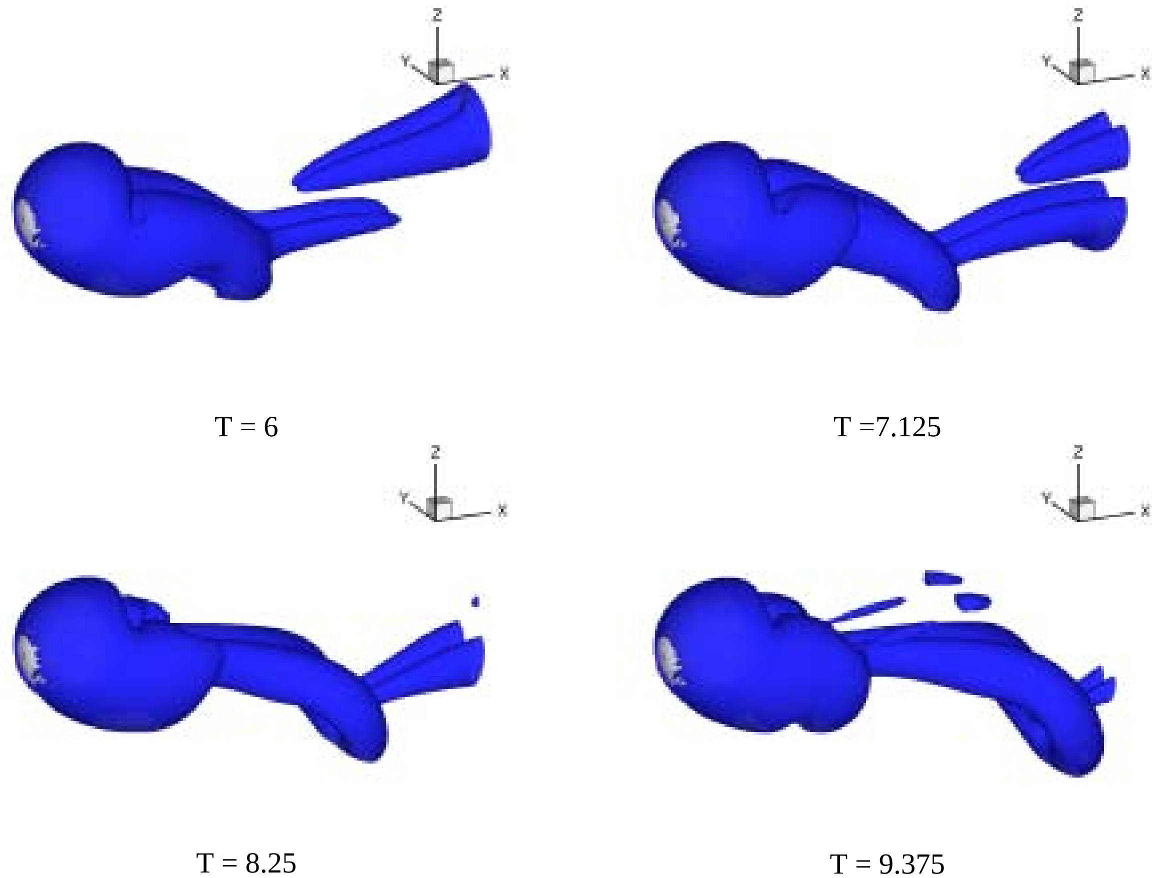

Figure 1. Spinning sphere at Re=300, span-wise rotation (axis of rotation is perpendicular to free stream direction): vorticity structures (q=0 surfaces).

Timestepping

Because contemporary CFD is limited by the power of available computers, it is of interest to reduce the work necessary to compute a given flow. One major area of inefficiency that remains largely untapped is the time integration process.

In Figure 5, one sees a frequency distribution of the strengths of vortex particles from one snapshot of a very low Reynolds number (1000) truck model simulation. By dimensional analysis, the local timescale is inversely proportional to the local strain rate tensor norm, which, for the purpose of this illustration, is taken to be particle strength (a choice that is approximate in that it neglects the symmetric part of the tensor). In a conventional timestepper, even an adaptive one, the CFL condition limits integration rate according to the strongest gradient in the flow. However, even at this unrealistically small Reynolds number, the mean strength is hundreds or thousands of times smaller than that of the strongest particles, so most of the flow is being over-resolved by the same factor. Performing timesteps that are adaptive per-particle, rather than per-step, could potentially reduce the computational workload by orders of magnitude.

Some multiscale integration techniques are available, but they are not suitable for vortex-based fluid flow problems, which operate over a continuous range of scales and involve fairly complicated tree-based right-hand-side evaluation. The goal of this phase of research has been development of a new multiscale time-integration scheme that is tailored to vortex particle methods.

Such a method has been developed and refined over the course of several years, and it is now beginning to yield results. In Figure 6, one sees in the left column several snapshots of a simple vortex particle flow developing in two dimensions, with corresponding particle-specific timesteps on the

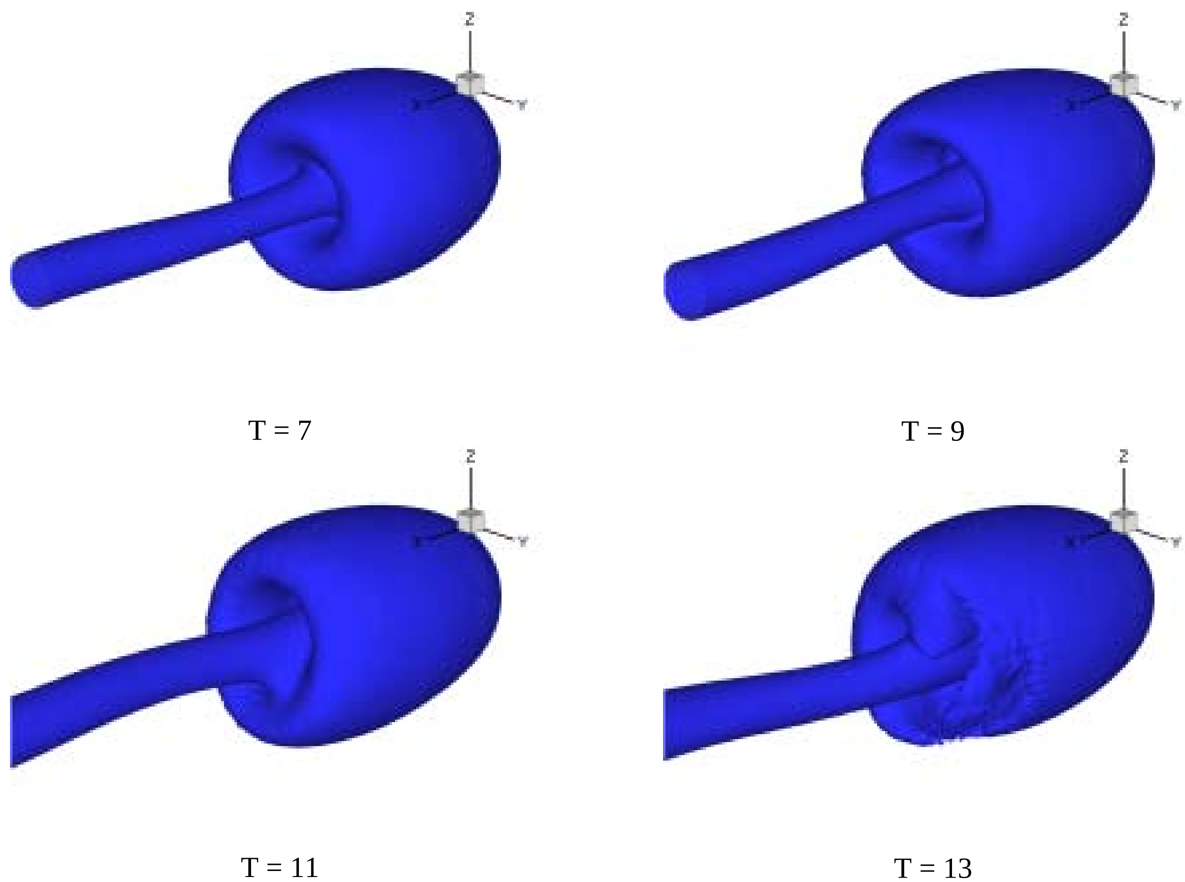

Figure 2. Spinning sphere at Re=300, stream-wise rotation (axis of rotation is aligned with free stream direction): vorticity structures (q=0 surfaces).

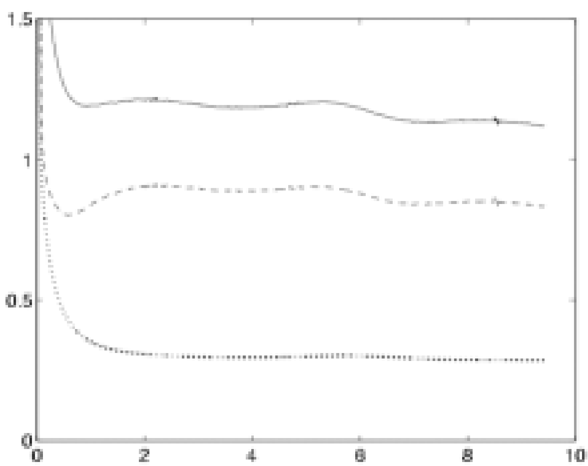

Figure 3. Spinning sphere at Re=300, span-wise rotation: drag coefficient, shear component (dotted), pressure component (dashed), total (solid) versus time.

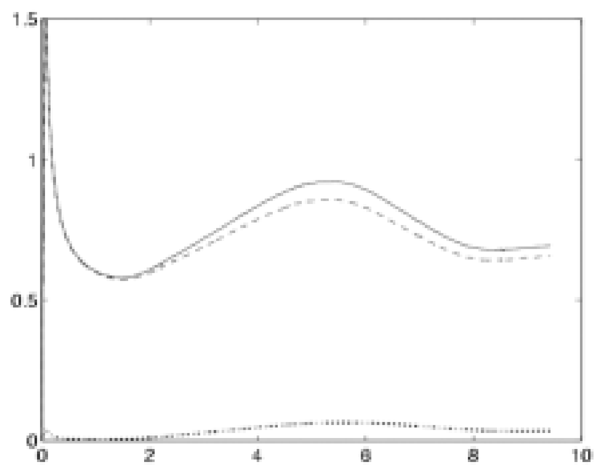

Figure 4. Spinning sphere at Re=300, span-wise rotation: lift coefficient, shear component (dotted), pressure component (dashed), total (solid) versus time.

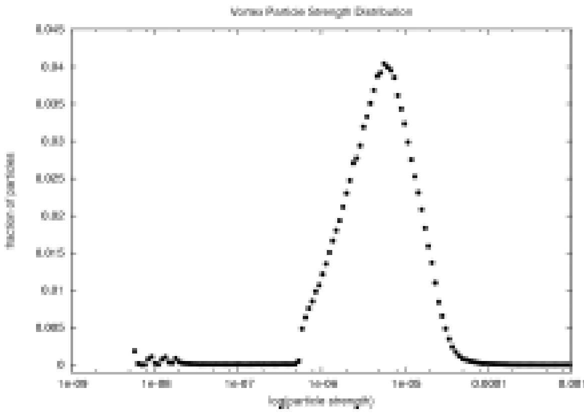

Figure 5. Vortex particle strength distribution around GTS truck model.

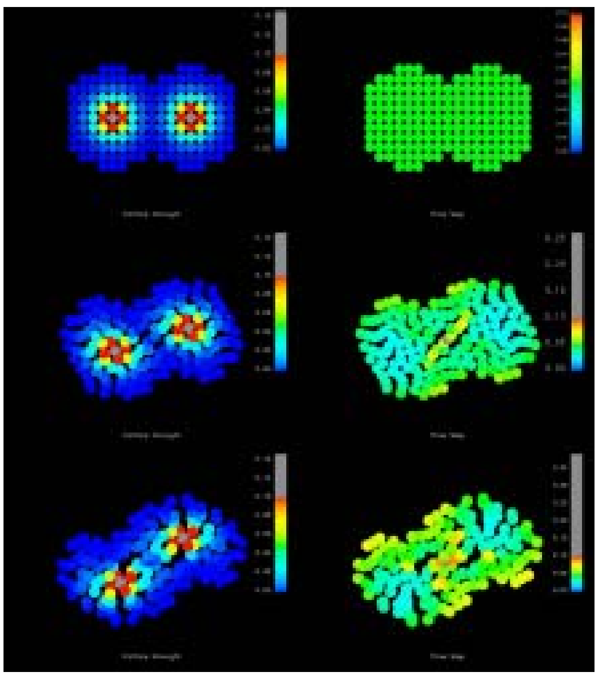

Figure 6. Stages in asynchronous time integration of two vortex patches: strengths (left) and timesteps (right).

right. The most significant challenge in developing the method was achieving decent scaling for large numbers of particles; the latest incarnation scales linearly with the total number of timesteps across all particles, as required.

Rigorous order-of-accuracy estimates have been derived (the method can be made accurate to any order) and a number of successful tests have been performed, although more will be required. A paper detailing the method is in progress.

Theoretical LES Work

There is ongoing debate on the relationship of LES and Reynolds-averaged Navier-Stokes (RANS) solutions to the filtered or time-averaged direct numerical simulations (DNS) they are designed to model. Because of the chaotic nature of turbulence, the modeled solution is not generally the same result one would obtain by applying its simplifying assumption to an exact solution. The problem is not merely an academic one; understanding how a model relates to the flow being modeled is essential for choosing parameters correctly, which, in turn, is essential for finding and interpreting computed turbulent flows in the context of heavy vehicle aerodynamics.

We are investigating the implications of a new theoretical concept that treats LES as an explicit ensemble-averaging procedure. This is still a new idea, but there is hope that it will be applicable to choosing parameters for LES models. It has been tested to an extent on the Lorenz equations. The first nontrivial test on 1-D Burgers' equation is expected to be complete soon; if the test works, the method should be straightforward to extend to 3-D Euler and Navier-Stokes equations.

Conclusions

Vortex method development continues mostly according to plan; developments in FY 2004 mean it should now be possible to simulate complicated flows around truck bodies, including those around rotating tires. Time integration techniques have improved, although these improvements are not yet backported into the main code. Work began on development of Large Eddy Simulation ensemble theory, and preliminary tests to prove or disprove its usefulness will be conducted in the near future.

II. Thermal Management

A. Cooling Fan and System Performance and Efficiency Improvements

Principal Investigator: R.L. Dupree
Caterpillar, Incorporated
Technical Center, Building E
P.O. Box 1875, Peoria, Illinois 61654
(309) 578-0145, fax: (309) 578-4277, e-mail: dupree_ron_l@cat.com

Investigator: D.C. Messmore
Caterpillar, Incorporated
Technical Center, Building E
P.O. Box 1875, Peoria, Illinois 61654
(309) 578-8715, fax: (309) 578-4277, e-mail: messmore_dale_c@cat.com

Technology Development Area Specialist: Sidney Diamond
(202) 586-8032, fax: (202) 586-1600, e-mail: sid.diamond@ee.doe.gov
Field Technical Manager: Philip S. Sklad
(865) 574-5069, fax: (865) 576-4963, e-mail: skladps@ornl.gov

Contractor: Caterpillar, Inc
Contract No.: DE-FC04-2002AL68081

Objective

- Develop cooling system fans and fan systems that will allow off-highway machines to meet Tier 3 emissions regulations and reduce spectator sound levels with improved fuel efficiency and within the functional constraints of machine size.

Approach

- Task 1 is to develop a large, high-performance axial fan.
- Task 2 is to develop an active fan shroud for use with large axial fans.
- Task 3 is to develop fan modeling techniques to improve the ability to predict fan performance and component airflows in cooling systems with side-by-side heat exchangers.
- Task 4 is to demonstrate the performance of a lab-developed swept blade, mixed flow fan in an off-road machine.
- Task 5 is to develop a high-efficiency continuously variable speed fan drive for use in high-horsepower fan systems.
- Task 6 is to develop cooling system air filtration concepts that can allow more dense (higher performance) heat exchangers to be used in off-road machines.

Accomplishments

- Task 1 — Second generation fan has been built and tested from designs developed by using generic algorithms. Performance of second-generation design still does not meet performance goals for flow and efficiency.
- Task 2 — Michigan State University has completed performance measurement of a radiused inlet/radiused outlet fan shroud, with and without secondary airflows. The addition of a secondary airflow to the shroud does

not provide any more performance in the axial flow region of the fan performance curve, but it does significantly change the stall point of the fan.

- Task 3 — Caterpillar has completed initial correlation with fan flow data measured at Michigan State University. Results are the basis of this report.
- Task 4 — Task was completed in 2003. Fan was not able to meet performance goals because of significant performance loss when it was installed close to the front of the engine.
- Task 5 — Task was terminated in 2003 during a performance review. Dual ratio clutch is not able to meet efficiency goals, and alternative CVT concepts will not fit within the space allowed.
- Task 6 — Completing initial lab evaluation of the use of grounding, application of both ac and dc voltages, ionization of the incoming air, ultrasonics, and the use of mechanical vibrations to reduce dust accumulation on heat exchanger surfaces.

Future Direction

- Task 1 — Genetic algorithms cannot provide an acceptable fan design. Will proceed forward with classical fan design methods.
- Task 2 — Michigan State University is evaluating the performance of the active fan shroud concept with two variations of conventional sheet metal fans to determine the sensitivity of shroud performance to fan design.
- Task 3 — Caterpillar is completing a design of experiments to provide final quantification on the sensitivity of CFD performance predictions to various modeling parameters.
- Tasks 4 and 5 — Tasks completed. Final documentation due.
- Task 6 — Results of initial lab evaluations are being reviewed to select the technology most appropriate for further lab evaluation.

Introduction

Accurate CFD analysis of axial fan performance in machine cooling systems is critical to the ability to meet upcoming Tier 3 emissions regulations in off-highway machines. The analyst must be able to provide accurate estimates for both overall fan airflow and individual component airflows in systems with side-by-side heat exchangers, or the finished cooling system will not be able to provide the required inlet manifold temperatures needed for Tier 3 emissions compliance. Many aspects of the CFD modeling process can affect the final solution, but to date there has not been a determination of which aspects are most critical, nor has there been a defined set of modeling guidelines available to the analyst. Toward this end, an extensive set of measured data was obtained on an axial fan in an “installed condition” at Michigan State University in 2003. The data were used as a baseline from which a set of CFD modeling guidelines could be developed. The purpose of this project is to determine the critical modeling factors, and the degree to which they must be controlled, in order to obtain consistent and accurate airflow predictions of axial fans and individual heat exchanger airflows in off-highway machine cooling systems.

Project Deliverables

At the end of this project, the modeling elements critical to consistent, accurate CFD models of axial fans in installed conditions will have been developed and documented.

Baseline Model

Cooling system CFD analysis typically involves simulation of cooling system geometry that includes an axial fan within a shroud with various heat exchangers and other flow obstructions. Models are created in commercially available Fluent® CFD software by using the multiple reference frame (MRF) formulation for steady-state analysis of rotating machinery. There is no “standard” method for generating these CFD models, and analysts each have their own techniques that they use in any particular modeling situation. Overall system flow rate and fan performance degradation (i.e., what percentage of the fan airflow is reduced when a fan is in an installed condition vs. when it is evaluated in an industry standard free inlet/free outlet [FIFO] performance test such, as AMCA® [Air Movement and Control Association] Standard 210) are the typical areas of primary concern, with a lesser emphasis on prediction of airflow through individual heat exchangers mounted in parallel (side-by-side). The individual component airflow data are important because air-to-air aftercooler (ATAAC) cores are often much more restrictive to fan airflow than typical radiator cores. The net result is that the analyst could accurately predict the overall flow, but inaccurately predict the flows through the individual cores, resulting in an incorrect estimation of the performance of both the radiator and the ATAAC. Unfortunately, test data are seldom available against which to validate these CFD models. On the occasion that such test data do become available, it is usually some months after the simulations have been completed, and the models are generally not re-exercised in order to improve on their predictive capability.

To standardize the modeling process, an extensive testing program was undertaken with Michigan State University (MSU). (The MSU test facility and test methods are described in "Performance Measurements and Detailed Flow Field Observations for a Light Truck Cooling Fan" by J.F. Foss [SAE paper 971794].) A 482.6-mm-diameter axial fan was inserted into a 6.35-mm-thick knife-edge shroud at 50% projection (50% of the projected width was upstream of the upstream face of the shroud), which was then placed in one face of an air chamber. Downstream of the fan, in the air chamber, a helper fan regulated the amount of downstream restriction against which the test fan worked. Pressure rise (from atmospheric pressure upstream of the fan to static pressure in the downstream air chamber) and total airflow through the system were measured under a variety of conditions. Figure 1 shows the fan mounted within the test facility.

The testing would represent an AMCA® FIOF fan performance test. The fan would then be modeled in FLUENT® as an MRF model. The second step would be to test (and model) a fan system consisting of heat exchangers mounted in front of the fan, to develop an acceptable performance model. The

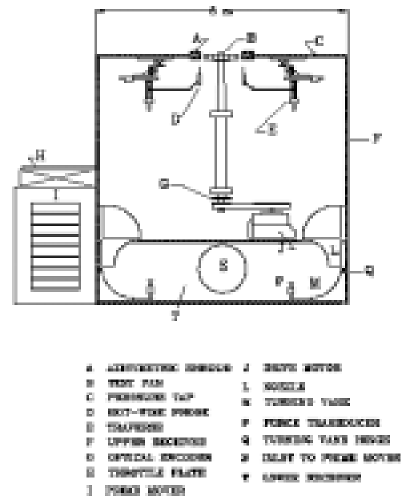

Figure 1. Diagram of fan in test facility.

third step would be to develop a design of experiments to determine the impact of the various modeling variables on the accuracy of the CFD predictions.

Initially, the fan was modeled in the free inlet/free outlet condition (FIFO, no flowstream obstructions other than the fan shroud). Figure 2 shows the fan from below, installed in the top of the exit chamber with the attached driveshaft.

The first critical element to be evaluated was the size of the MRF volume. Initially, it was thought that a smaller MRF volume would produce acceptable results, but subsequent simulations proved this not to

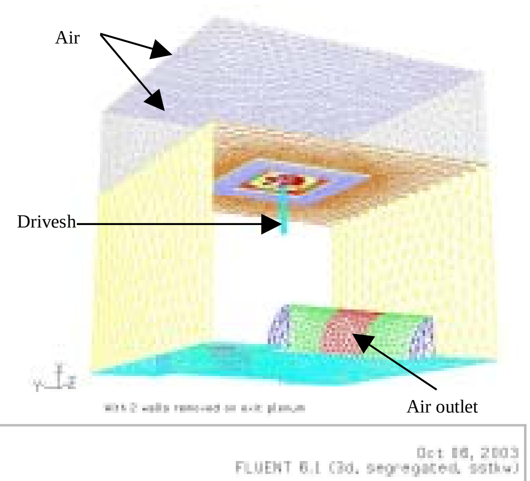

Figure 2. Image of fan as installed in the top of exit chamber.

be the case. Three iterations were made to MRF-volume size: (1) both the axial and radial dimensions were increased, (2) the axial dimension was further increased while maintaining the new radial dimension, and (3) both the axial and radial dimensions were further increased. Figure 3 shows the progression in MRF size.

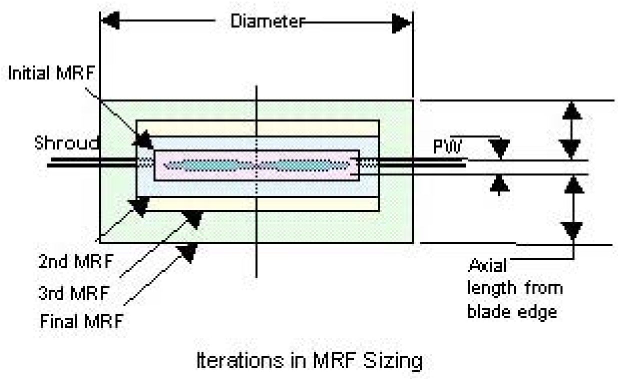

Figure 3. Progression in MRF size.

Initial simulations were run at relatively low pressure rise (204 Pa), resulting in primarily axial flow from the fan. The third MRF size brought the overall flow rate to within about 5% of the measured value. At this point, the model was run with 700 Pa pressure rise, which produces significant radial flow from the fan. Poor correlation led to the MRF's final dimensions. The effect on solution accuracy is shown in Figure 4a and b.

The significant error at high pressure rise (radial flow) is likely because the MRF was expanded to the point at which it included non-axisymmetric stationary features. This introduces some false velocities resulting from the mathematically imposed fluid rotation, in addition to reflecting some flow back into the MRF, which will be discussed later. The final MRF was used throughout the remaining modeling effort as the best compromise between MRF size and fan flow prediction accuracy over the full range of fan performance. Table 1 summarizes the recommended MRF volume.

A FIFO fan performance curve showing Michigan State test data and CFD predictions is shown in Figure 5. AMCA®-recommended tolerance bands for flow measurement variability from facility to

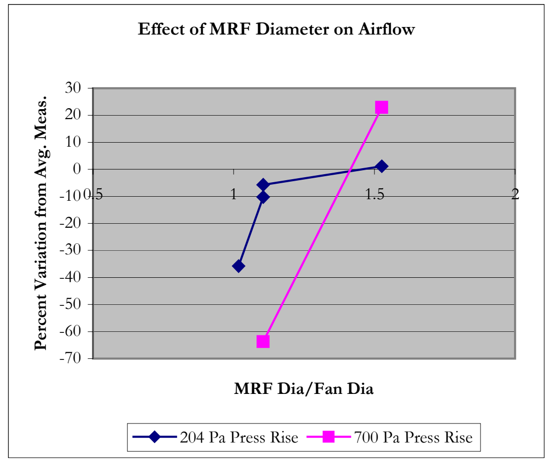

a.

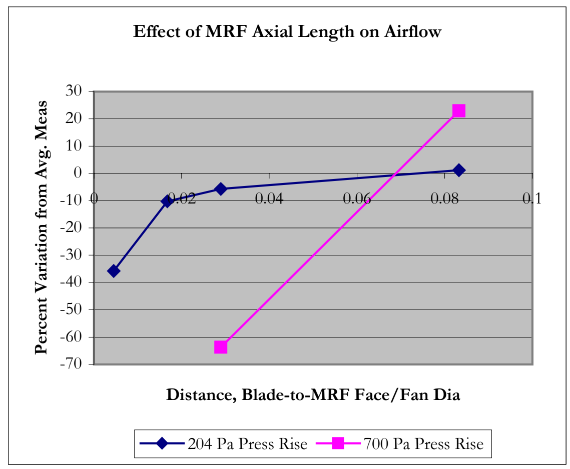

b.

Figure 4. Effect of solution accuracy on fan parameters.

Table 1. Recommended MRF volume.

MRF Diameter as a Percentage of Fan Diameter	Axial Length from Leading/Trailing Edge of Fan to MRF Face as a Percentage of Fan Diameter
150%	10%

facility from its Publication 211-94 are shown for reference (approximately 3–5% error band). Except right at the transition zone, CFD predictions with the baseline model fell within the AMCA® -recommended tolerance.

Simulated Installation

The CFD model was then modified for the installed conditions. Upstream of the fan (outside of the air chamber) was a mock-up simulating a machine

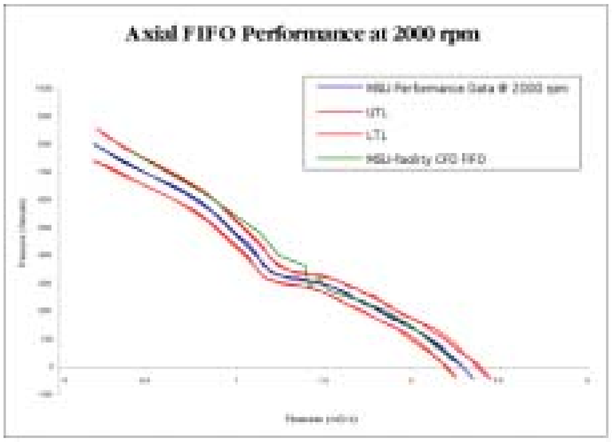

Figure 5. FIFO fan performance.

cooling system with side-by-side heat exchanger cores. The mock-up was divided into two sections along the axis of the fan vertical centerline. The mock-up, shown in Figure 6, contained a five-row, 11-fin/in. heat exchanger, as well as slots for holding perforated sheet metal screens. The use of varying numbers of screens allowed the core restriction to be changed, but the radiator itself did not need to be changed for the duration of the testing.

A sketch of the mock-up mounted above the exit plenum is shown in Figure 7. Inlet air comes from the atmosphere above the mock-up, is drawn through the fan, is then discharged into the exit plenum, and finally exits out through the flow measuring system under the floor.

"Installed conditions" consisted of the heat exchanger alone in the mock-up (low symmetrical restriction), the heat exchanger plus two screens on each side of the mock-up (high symmetrical restriction), and the heat exchanger plus two screens on one side of the mock-up and the heat exchanger

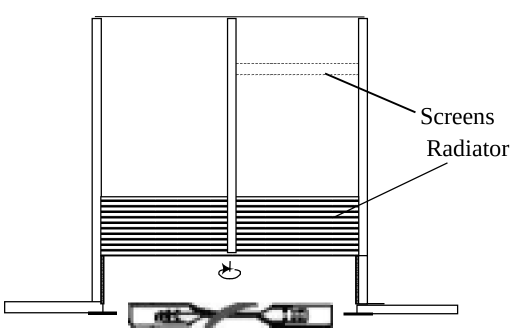

Figure 6. Mock-up of machine cooling system.

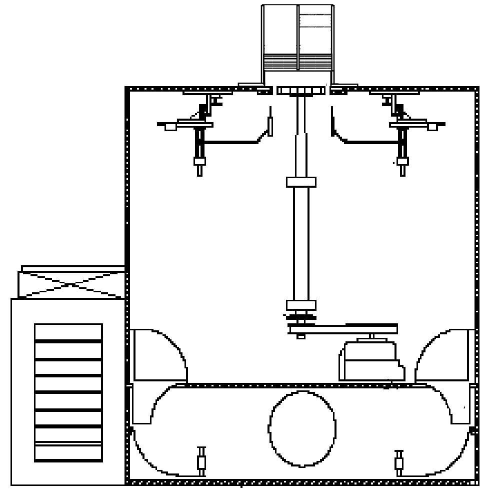

Figure 7. Illustration of mock-up mounted above exit plenum.

alone on the other side (asymmetrical restriction).The symmetrical conditions simulated full-plane cores in front of the fan. The asymmetrical condition simulated partial-plane cores, resulting in uneven loading across the diameter of the fan. CFD predictions were again compared to MSU test data. Correlations between predicted and measured values for both low-symmetric and high-symmetric loading are shown in Figures 8 and 9. Notice also that restriction curves for specific diameter (D_s) values of 1.6 and 1.8 are included. (See the Appendix for a description of specific diameter.) It is particularly important that the model correlate well in this region.

The AMCA® -recommended tolerance bands are again shown around each set of test data. In general, the CFD model under-predicted flow and pressure at any given point, with the prediction falling off more sharply at higher flows and lower pressure. To compensate for this, fan speed was increased by 5% above measured speed (a 5% "boost" to 2100 rpm). This resulted in a 5% increase in overall airflow, with a corresponding increase in pressure rise. It can be seen that just a 5% boost results in considerable improvement in the correlation between predicted and measured. The reason the adjustment is necessary has to do with inaccuracies related to the MRF formulation for steady-state solution of rotating flows.

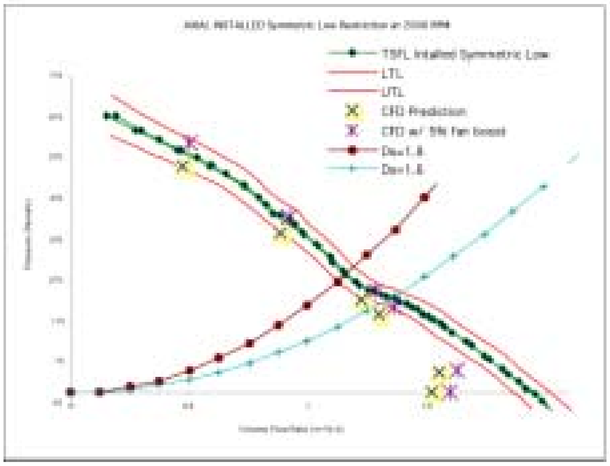

Figure 8. Correlations between predicted and measured values for low-symmetric loading.

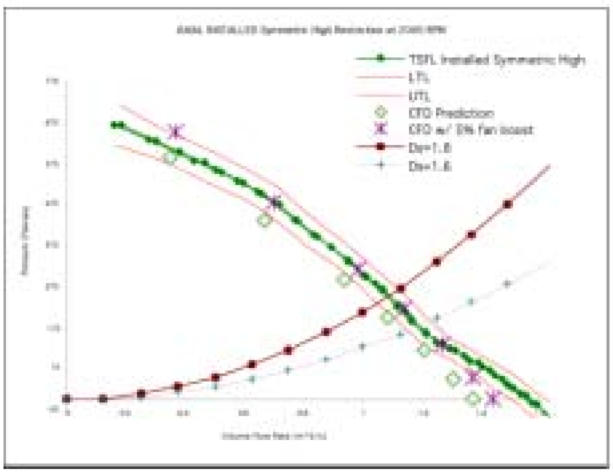

Figure 9. Correlations between predicted and measured values for high-symmetric loading.

In the present case, the shroud and the framing of the plenum all work to reflect air coming radially off the fan back into the MRF volume. This situation would likely exist in actual underhood installations as well. Flow traversing the MRF boundaries in both directions is known to cause problems for the MRF formulation for rotating fluids. Fluent® recommends using sliding mesh methods under these circumstances. One operating condition, low-symmetrical loading with 190-Pa pressure rise, was modeled by using the sliding mesh method. By using MRF, the model predicted an overall flow rate that was 13% below the measured flow rate. With the 5% fan boost, predicted flow rate was 5% flow rate below the measured flow rate. By using the sliding mesh, without fan boost, the predicted flow rate was 0.4% higher than measured flow rate. This was only one simulation point, but the result is encouraging. However, because of the transient nature of the solution, computing time was several times longer than the steady-state solution with MRF, with the fan requiring two complete revolutions before converging to a steadystate flow. Future software and/or computer developments may reduce the computing, but the present state of the art does not allow the cost and CPU time required to use sliding mesh models for cooling system performance analysis. An MRF model with a 5% fan boost provides a more economical solution.

MRF was also used to predict fan performance with different fan projections. However, radial airflow from the fan reflecting off the shroud back into the MRF volume resulted in incorrect prediction of both the performance values and trends. This is a situation where sliding mesh may be able to provide acceptable performance predictions, once solution time becomes more reasonable.

The CFD model was also exercised by using asymmetric fan loading. The objective was not only to match the fan performance curve, but also to match measured flow through each side of the mock-up. Figure 10 shows the fan performance curve correlation.

Again, it can be seen that the prediction drops off quickly as flow rate increases and pressure rise decreases. However, using a 5% fan boost results in acceptable predictions at and near the D_s range of

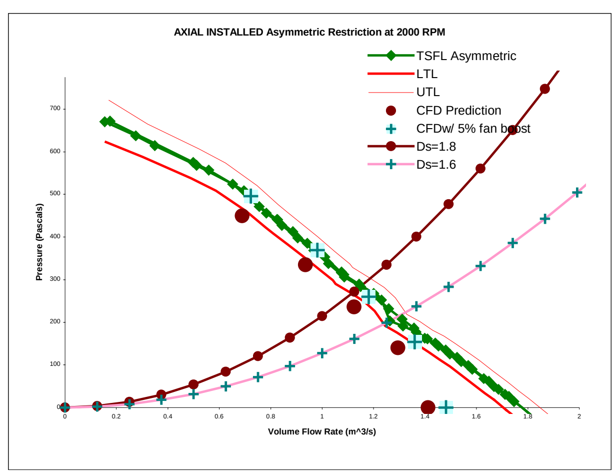

Figure 10. Fan performance curve correlation.

interest. Flows through the individual heat exchangers were also compared with measured data. Measured test data showed a fairly consistent split of 58:42; that is, 58% of the flow went through the low-restriction side (heat exchanger alone), and 42% of the flow went through the high-restriction side (heat exchanger plus screens; see Table 2). Although the CFD predictions displayed a slight flow-rate/pressure rise effect, the error from the measured values was less than 5%.

Table 2. Total flow through each side of mock-up.

Percent of Total Flow through Each Side of Mock-Up (at a given total flow rate)		
m^3/s	Low-restriction side	High-restriction side
1.41	56.0	44.0
1.30	55.8	44.2
1.12	55.2	44.8
0.94	54.8	45.2
0.69	54.3	45.7

Summary

Highlights of the progress made to date include:

- Identified MRF volume size as an extremely important parameter affecting fan performance prediction accuracy for both FIFO and installed fan performance predictions.
- Successfully developed a model of an axial fan with upstream flow restrictions installed in the Michigan State University test facility.
- Exercised the model for upstream symmetrical low- and high-restriction and upstream asymmetrical restriction.
- By using a 5% fan boost, CFD model predictions fell within AMCA® -recommended tolerance bands.
- The existing model provided a basis for determining what factors go into creating a successful model.
- A design of experiments was generated to evaluate factors that contribute to a successful CFD model and to determine the most critical modeling factors.

Conclusions

A CFD model of an axial fan in an installed condition has provided good correlation with an extensive set of detailed flow and pressure measurements taken under a variety of conditions. This model has led to the development of a design of experiments to evaluate the factors that contribute to a successful fan model. The design of experiments is being run, and results will be evaluated to determine the modeling critical success factors and the extent to which they must be controlled.

Appendix

Specific diameter relates the relative fan size to the given restriction. This is evident by noting the definition of the system restriction coefficient (K) and its relationship to specific diameter:

$$K = P_t / Q^2\sigma$$

$$D_s = k_3DK^{0.25}$$

Physical factors may be incorporated; these generally follow from flow and pressure coefficients:

$$\text{Specific diameter} = \text{Pressure Coeff}^{0.25}/\text{Flow Coeff}^{0.5}$$

Some sources use two other interpretations of specific diameter, which should be clarified to avoid confusion.

Specific diameter may be used to indicate the diameter fan required for a unit pressure, unit flow, and unit density, assuming the fan operates at standard density. This results in an additional factor of density to the one-fourth power.

Often specific diameter of a fan refers to single operating point in terms of specific diameter for which fan efficiency is maximum. A given fan design is then given a representative “specific diameter” number. This specific diameter number is related to the aerodynamic fan type.

Some sources also use specific radius as an alternative to specific diameter.

B. Efficient Cooling in Engines with Nucleate Boiling

Principal Investigator: J.R. Hull
Argonne National Laboratory
9700 South Cass Avenue, Building 335, Argonne, IL 60439
(630) 252-8580, fax: (630) 252-5568, e-mail: jhull@anl.gov

Technology Development Manager: Sid Diamond
(202) 586-8032, e-mail: sid.diamond@ee.doe.gov
Technical Program Manager: Jules Routbort
(630) 252-5065, e-mail: routbort@anl.gov

Contractor: Argonne National Laboratory
Contract No.: W-31-109-ENG-38

Objectives

- Investigate the potential of two-phase flow in engine cooling applications.
- Determine the limits on two-phase heat transfer (occurrence of critical heat flux or flow instability).

Approach

- Experimentally determine heat transfer rates and critical heat fluxes in small channels with water and 50% ethylene glycol in water mixture.
- Perform experiments over a concentration range of ethylene glycol in water.
- Perform experiments with alternative fluids.

Accomplishments

- Completed experimental tests and data analysis on single- and two-phase heat transfer over a concentration range of ethylene glycol in water mixtures (concentrations 40/60, 50/50, and 60/40).
- Developed a general correlation for heat transfer coefficients for the prediction of boiling heat transfer rates of flow boiling in small channels including refrigerants, water, and ethylene glycol/water mixtures.
- Modified Chisholm's correlation with a concentration factor to better predict pressure drops for ethylene glycol/water mixtures.

Future Direction

- Build a vertical-flow test section to study the impact of vertical vs. horizontal flows on two-phase heat transfer.
- Perform two-phase heat transfer experiments involving ethylene glycol/water mixtures with vertical flows to provide complete information for nucleate-boiling cooling system design.
- Perform systematic experiments with alternative fluids.

Introduction

Analyses of trends in the motor vehicle development sector indicate that future engine cooling systems will have to cope with greater heat loads because of more powerful engines, more air conditioning, more stringent emissions requirements, and additional auxiliary equipment. Moreover, there is considerable interest in reducing the size of cooling systems to obtain a better aerodynamic profile. To meet these conditions, it is necessary to design cooling systems that occupy less space, are lightweight, have reduced fluid inventory, and exhibit improved performance. Among various new cooling systems proposed by researchers, the nucleate-boiling cooling system has high potential to meet these challenges. Order-of-magnitude higher heat transfer rates can be achieved in nucleate-boiling cooling systems when compared with conventional, single-phase, forced-convective cooling systems. However, successful design and application of nucleate-boiling cooling systems for engine applications requires that the critical heat flux and flow instability not be reached. Therefore, a fundamental understanding of flow boiling mechanisms under engine application conditions is required to develop reliable and effective nucleate-boiling cooling systems.

Cooling engine areas such as the head region often contain small metal masses that lead to small coolant channels. This geometry, in turn, leads to low mass flow rates in order to minimize the pressure drop. Although significant research has been performed on boiling heat transfer and the critical heat flux phenomenon, results on the conditions necessary for engine cooling systems are limited. The purpose of the present study is to experimentally investigate the characteristics of coolant boiling, critical heat flux, and flow instability under conditions of small channel and low mass flux.

The test apparatus used in this investigation was designed and fabricated to study boiling heat transfer, critical heat flux, and flow instability of flowing water, ethylene glycol, and aqueous mixtures of ethylene glycol at high temperatures (up to 250°C) and low pressures (<345 kPa). Figure 1 shows a schematic of the apparatus. It is a closed-loop system that includes two serially arranged pumps with variable speed drives, a set of flowmeters, an accumulator, a preheater, a test section, and a condenser. The flowmeter set, including various types and sizes, was chosen to cover a large range of flow rates and was calibrated with the weighing-with-stop-watch technique. The estimated uncertainty in the measurements of flow

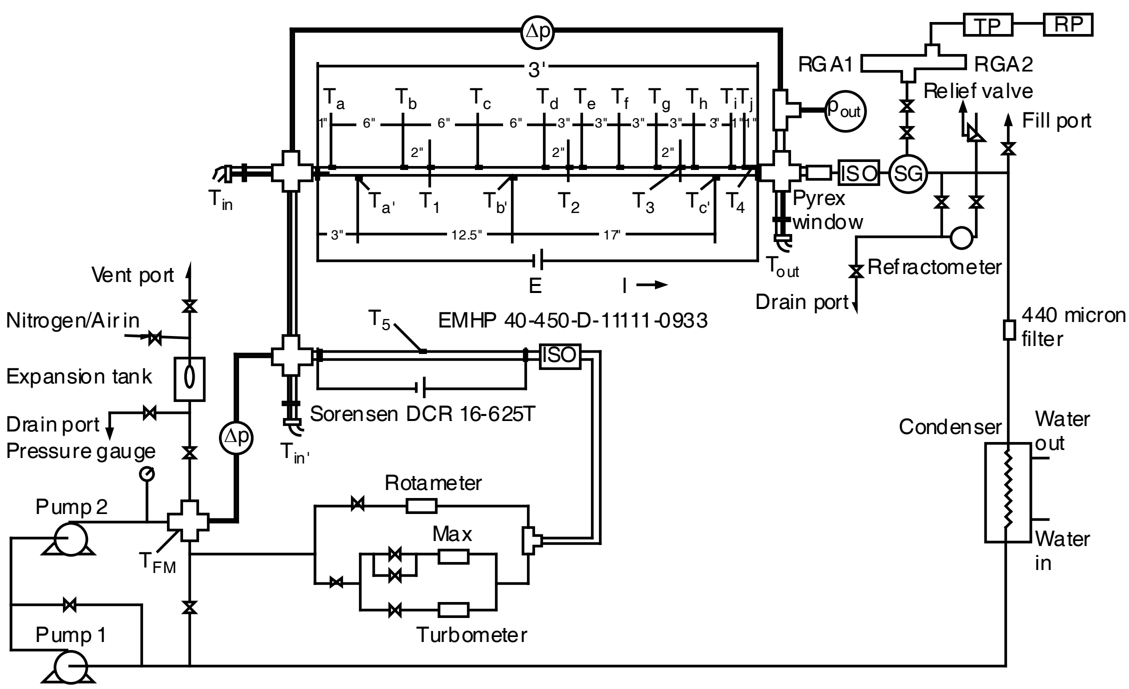

Figure 1. Schematic diagram of nucleate-boiling cooling test apparatus.

rates was ±3%. The bladder-type accumulator allows for stable control of system pressure. The preheater provides a means to set the inlet temperature of the test section at various desired levels. The preheater and the test section were resistance-heated with controllable DC power supplies. Provisions were made to measure temperatures along the test section for calculating heat transfer coefficients. The pressures and temperatures at the inlet and outlet of the test section were also measured. Pressure transducers and thermocouples were calibrated against known standards.

The estimated uncertainties in the measurements of pressures and temperatures were ±3% and ±0.2°C, respectively. As a safety precaution, the preheater and test section were provided with high-temperature limit interlocks, to prevent them from overheating. After leaving the test section, the two-phase flow was condensed into a single-phase flow, which returned to the pumps to close the system.

A data acquisition system, consisting of a computer and a Hewlett-Packard multiplexor, was assembled to record outputs from all sensors. A data acquisition program was written to include all calibration equations and conversions to desired engineering units. The data acquisition system provides not only an on-screen display of analog signals from all sensors and graphs of representative in-stream and wall-temperature measurements, but also a means of recording temperature measurements and pertinent information such as input power, mass flux, outlet pressure, pressure drop across the test section, and outlet quality, for further data reduction.

<u>Results and Discussion</u>

During FY 2004, both experiments and analysis were completed on boiling heat transfer with ethylene glycol/water mixtures over a concentration range (concentrations 40/60, 50/50, 60/40). The main results are reported below.

Boiling Curve

Figure 2 shows the heat flux as a function of wall superheat for boiling water and ethylene glycol/water mixtures in small channels. As it can be seen from Figure 2, the saturation boiling in small channels can be divided into three regions, namely, the convection-dominant-boiling region, the nucleation-dominant-boiling region, and the transition-boiling region. Both convective heat transfer and boiling heat transfer exist in all three regions, but their proportions are different in these three regions. In the convection-dominant-boiling region, the wall superheat is low, usually less than a few degrees centigrade. Although there is boiling heat transfer, the dominant mechanism is convective heat transfer. As a result, the mass quality and heat transfer rate are quite low, in comparison to those in the other two regions. In the nucleation-dominant-boiling region, the wall superheat is higher than that in the convection-dominant-boiling region but lower than certain upper limits that depend on mass flux. Opposite to the convection-dominant-boiling, the boiling heat transfer in the nucleation-dominant-boiling region is so developed that it becomes dominant, and the heat transfer rate is much higher than that in convection-dominant-boiling region. As can be seen from Figure 2, the heat flux in this region is independent of mass flux and can be predicted with a power-law function of wall superheat. This characteristic was used in correlating the heat transfer data. In the transition-boiling region, the wall superheat is relatively high. The heat flux in this region is also high and close to the critical heat flux. The boiling in this region is unstable, and a small change in the heat flux will result in a big change in wall superheat. If the heat flux increases further, it is possible for the system to reach the critical point, producing an undesirably large jump in the wall superheat.

The above discussion shows that nucleation-dominant boiling is desired in engineering applications for both high heat transfer rate and stable flow boiling without reaching the critical point.

Two-Phase Pressure Drop

The concept of two-phase multipliers proposed by Lockhart and Martinelli and the correlation of those multipliers by Chisholm were used to compare with the present experimental data. As can be seen from Figure 3, the experimental data are in reasonable agreement with the Chisholm predictions both in values and trends, although the Chisholm correlation slightly overpredicts the experimental data.

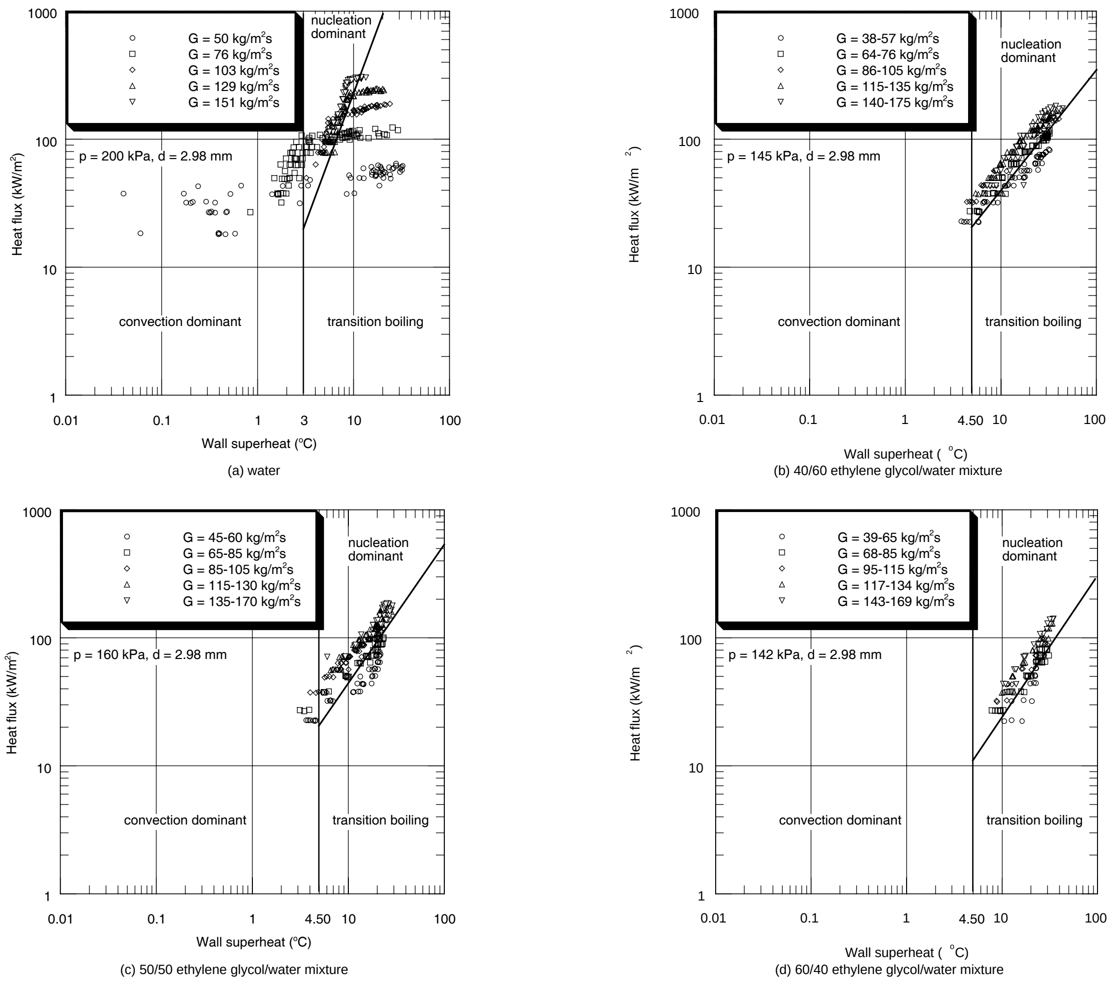

Figure 2. Heat flux as a function of wall superheat.

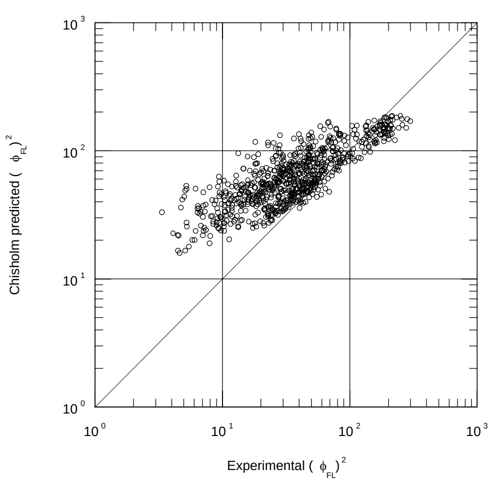

Figure 3. Two-phase frictional pressure gradient.

To better predict the experimental data and to take the concentration factor into account, the constant parameter $C = 12$ in Chisholm's correlation was modified into a function of the volume concentration, v, of ethylene glycol/water mixtures. Thus modified, Chisholm's correlation becomes:

$$h = 1 + \frac{12\left[1 - 2.8v(1-v)\right]}{X} + \frac{1}{X^2} .$$

This correlation reduces to Chisholm's correlation for both pure water ($v = 0$) and pure ethylene glycol ($v = 1$). In Figure 4, the experimental data are compared with the predictions of the modified Chisholm's correlation. This modification improves the predictions both in values and trends.

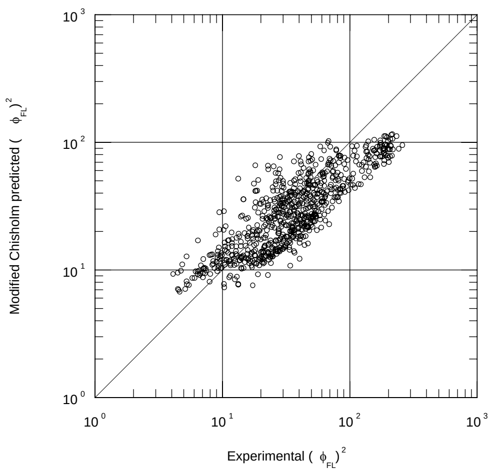

Figure 4. Two-phase frictional pressure gradient.

Heat Transfer Coefficient

In the present study, the nucleation-dominant boiling data have the following characteristics:

(a) Although both convective heat transfer and nucleate-boiling heat transfer exist, the dominant heat transfer mechanism is nucleate boiling. Since nucleate-boiling heat transfer rate is much higher than convective heat transfer, the latter can be neglected.

(b) As shown in Figure 2, the boiling heat transfer is dependent on heat flux but almost independent of mass flux, which means that, for a certain fluid, the boiling heat transfer coefficient can be expressed as a function of heat flux.

(c) The heat transfer coefficients have different dependences on heat flux for different fluids. Therefore, to get a general correlation for boiling heat transfer coefficients, it is necessary to include fluid properties in the correlation.

(d) Argonne researchers employed the dimensionless parameter combination form of Boiling number, Weber number, and liquid-to-vapor density ratio in developing different predicted correlations for boiling heat transfer coefficients to different fluids; and the predicted results are quite good.

On the basis of the above facts, we extended the property term to include the liquid-to-vapor viscosity ratio and were able to correlate boiling heat transfer data for water, 50/50 ethylene glycol/water mixture, refrigerant 12, and refrigerant 134a.

$$h = 135000(BoWe_l^{0.5})^{0.5}\left[(\rho_l/\rho_v)^{-0.5}(\mu_l/\mu_v)^{0.7}\right]^{-1.5}$$

In the above equation, the Boiling number, Bo, and the Weber number, We_l, are defined respectively by $Bo = q''/(Gi_{fg})$ and $We_l = G^2D/(\rho_l\sigma)$, where ρ is the density, μ is the viscosity, G is the mass flux, D is the diameter, and σ is the surface tension. For this equation to be used for the predictions of experimental data of ethylene glycol/water mixtures with concentrations other than 50/50, we further modified the above correlation with a concentration correction factor, which reduces to 1 for concentrations $v = 0$ and $v = 0.5$. The new correlation can be expressed as:

$$h/h^* = [1 + 6v(v - 0.5)](BoWe_l^{0.5})^{0.5}\left[(\rho_l/\rho_v)^{-0.5}(\mu_l/\mu_v)^{0.7}\right]^{-1.5}$$

where h^* is a characteristic heat transfer coefficient of 135 kW/m^{2}K above all of the data.

Figure 5 shows the experimental data and the predicted values obtained with the correlation for all fluids. The predictions of the equation are in good agreement with the experimental data, and most of the predictions are within ±30% of the experimental data. It should be noted that the comparisons are only for the data within the nucleation-dominant-boiling region. The success of the correlation in predicting the heat transfer coefficients of all fluids boiling in small channels is directly related to the trend, as presented in Figure 2, that the heat transfer data are dependent on heat flux but not mass flux. The fact that the equation is also heat flux but not mass flux dependent is in accordant with the experimental data.

Conclusions

Excellent progress has been made on both the experiments and analysis during FY 2004:

(a) Two-phase frictional pressure gradients of ethylene glycol/water mixtures follow similar trends as those of water. The results are in reasonable agreement with the predictions of Chisholm's correlation. A modification has been made to

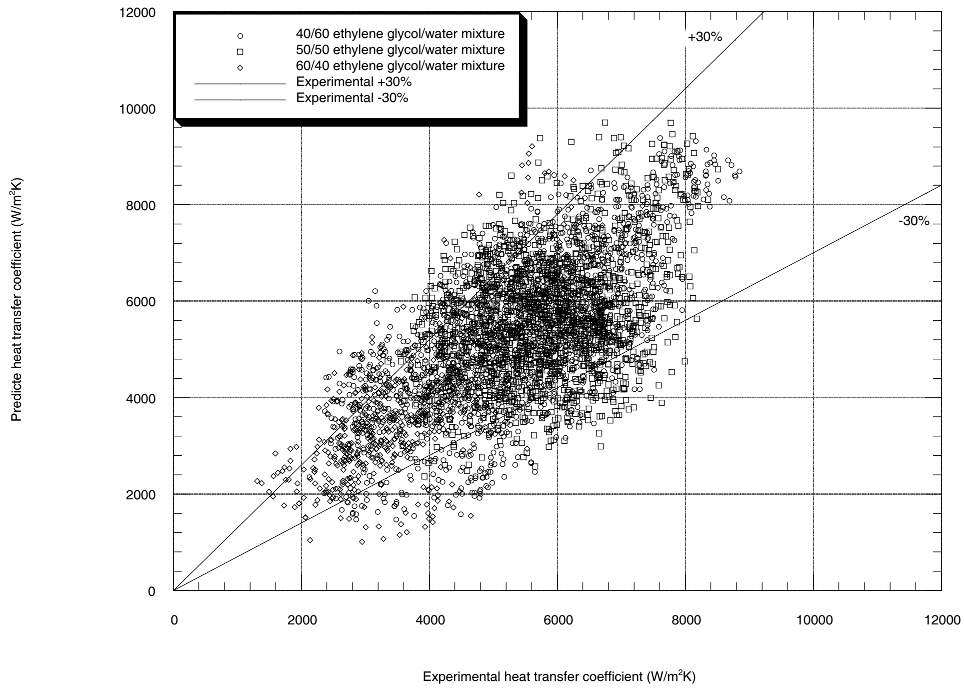

Figure 5. Heat transfer coefficient comparisons (nucleation-dominant-boiling region).

Chisholm's correlation, which reduces to Chisholm's correlation for concentrations $v = 0$ and $v = 1$. This modified Chisholm's correlation improves the predictions of the pressure drop data for ethylene glycol/water mixtures.

(b) The experiments show a very high heat transfer rate with ethylene glycol/water mixtures, which is promising for engine cooling applications. A general correlation has been developed based on data for water, ethylene glycol/water mixtures (concentrations 40/60, 50/50, and 60/40), and refrigerants. This correlation predicts the experimental data quite well, and most of the predicted values are within ±30% of the experimental data.

(c) It was found that the boiling heat transfer of ethylene glycol/water mixtures is mainly limited by flow instability rather than critical heat fluxes, which are usually the limits for water boiling heat transfer. Tests show that stable long-term two-phase boiling flow is possible for ethylene glycol/water mixtures as long as the mass quality is less than a certain critical value (approximately <0.2). The heat transfer rate at this mass quality is significantly higher than that of conventional, single-phase, forced-convective heat transfer.

(d) In the applications of engine cooling, both horizontal and vertical flows exist. Therefore, it is necessary to investigate the impact of vertical flows vs. horizontal flows on two-phase heat transfer. During FY 2005, the test facility will be modified to run vertical flows. Experiments are planned using ethylene glycol/water mixtures for boiling two-phase heat transfer of vertical flows. The tests will provide essential information for the design of nucleate-boiling cooling systems.

C. Evaporative Cooling

Principal Investigator: S.U.S. Choi
Argonne National Laboratory
Argonne, IL 60439
(630) 252-6439, fax: (630) 252-5568, e-mail: choi@anl.gov

Technology Development Manager: Sid Diamond
(202) 586-8032, fax: (202) 586-1600, e-mail: sid.diamond@ee.doe.gov
Technical Program Manager: Jules Routbort
(630) 252-5065, fax: (630) 252-4289, e-mail: routbort@anl.gov

Contractor: Argonne National Laboratory
Contract No.: W-31-109-Eng-38

Objectives

- Improve air-side heat transfer of the radiator.
- Reduce radiator size.
- Reduce radiator weight.

Approach

- Conduct evaporative cooling tests on flat and cylindrical heaters.
- Characterize evaporative cooling with microporous surfaces.
- Develop improved techniques for making microporous and nanoporous coated surfaces.
- Conduct evaporative cooling tests on prototype radiators.

Accomplishments

- Investigated the effects of coating particle sizes and coating thicknesses on evaporative cooling performance.
- Initiated the development of an improved coating technique called thermally conductive microporous coating (TCMC).

Future Direction

- Develop improved techniques for making microporous and nanoporous coated surfaces, including the TCMC technique.
- Conduct evaporative cooling tests on prototype radiators.

Introduction

Evaporative cooling is an effective and economical method to cool heated objects requiring comparatively high heat flux dissipation for numerous industrial applications. Since evaporative cooling involves a liquid-vapor phase change, the increase of heat transfer is significant compared to single-phase forced convection of air. The heat of vaporization augments heat transfer when the tiny water droplets encounter and evaporate from the heated surface. In previous research, we successfully designed, fabricated, and operated an experimental facility to study evaporative cooling with plain and coated surfaces for flat and cylindrical heaters. One of our key findings is that the combination of evaporative cooling and microporous coating on a flat heater enhances the heat transfer coefficient by up to 400% relative to the reference case (dry air cooling with uncoated, plain surface). Furthermore, the microporous coating extended the dryout heat flux significantly (~21 kW/m^2) over the plain surface (15 kW/m^2). These findings clearly show that the performance on the air side of the radiator could be improved if evaporative heat transfer could be used. Therefore, one of the general strategies for improving the thermal management performance in heavy vehicles is to make better use of evaporative cooling.

In FY 2004, we investigated the effects of water flow rates, coating particle sizes, and coating thicknesses on evaporative cooling performance. In addition, we initiated the development of an improved coating technique called thermally conductive microporous coating (TCMC).

Results and Discussion

Effect of Microporous Coating Particle Sizes

Three ranges of particle size, 8-12 μm, 30-60 μm, and 100-300 μm, were employed in forming microporous structures on the flat heater. The coating thicknesses were measured to be ~50 μm for 8-12 μm particles, ~150 μm for 30-60 μm particles, and ~500 μm for 100-300 μm particles. The results shown in Figure 1 reveal that the tested particle sizes produced similar heat transfer curves. The capillary pumping phenomenon should be stronger as the coating particle size decreases. On the other hand, fluid flow resistance for the soaked water within the microporous passageways increases as the particle size decreases. Also, the wall temperature increases due to the additional thermal resistance of conduction as the layer thickness increases for a given heat flux. Therefore, the possible enhancement from less fluid flow resistance due to larger cavity

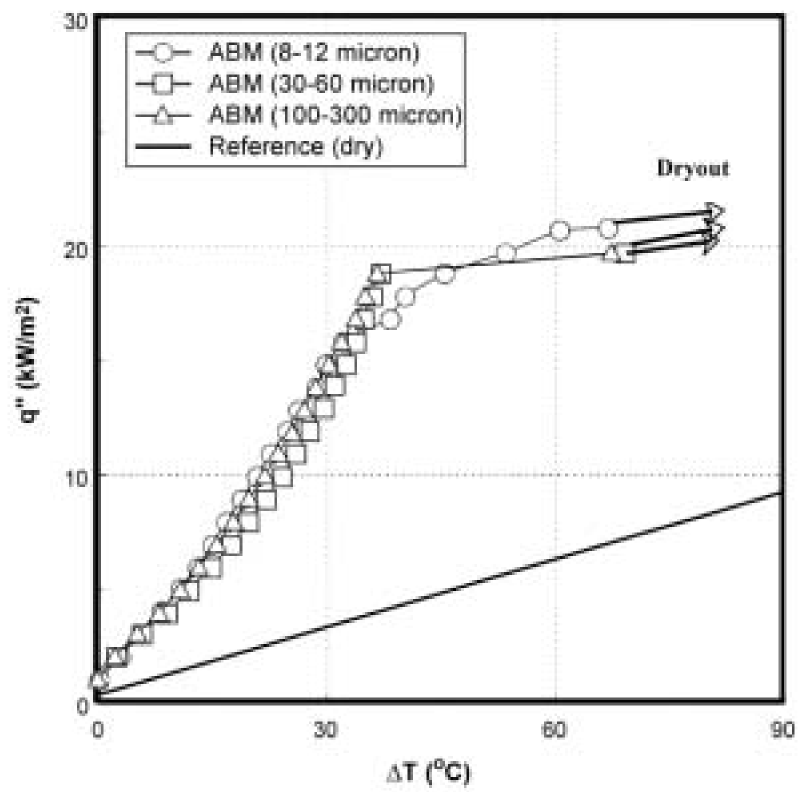

Figure 1. Effect of microporous coating particle sizes on heat transfer performance of flat heater (water flow rate: 1.75 mL/min).

size is believed to be counterbalanced by degradation due to additional thermal resistance from conduction and less capillary pumping power.

Effect of Microporous Coating Thicknesses

The effect of microporous coating thickness was investigated using the smallest particle size (8-12 µm). Figure 2 shows the heat transfer performance with coating thicknesses of 50, 100, 150, and 200 µm on a flat heater during tests with spray cooling and a water flow rate of 1.75 mL/min. Microporous coatings with 150 and 200 µm thicknesses showed smaller enhancement in spray heat transfer than coatings with 50 and 100 µm thicknesses. The 100 µm coating thickness attained the highest heat transfer coefficient among the tested thicknesses. This thickness produced up to ~50% increase in evaporative heat transfer coefficient over the 200 µm thickness. The thicker microporous coating retains more water droplets as the coating thickness increases, due to the larger number of microporous cavities. However, the evaporative heat transfer coefficient degrades extensively due to the additional thermal resistance to conduction as the thickness exceeds 100 µm.

ABM Coating Technique

The University of Texas at Arlington (UTA) has been collaborating with Argonne in the conduct of basic research on the effects of microporous coatings and other techniques on evaporative cooling. The ABM coating technique, named from the initial letters of the three components of the microporous coating: aluminum/brushable ceramic/methyl-ethyl-ketone, is one of the microporous coating methods previously developed to make a porous structure on heat transfer surfaces. After the carrier (M.E.K.) evaporates, the resulting coated layer consists of microporous structures with aluminum particles (8 to 12 µm) and a binder (Devcon® brushable ceramic) having a thickness of ~50 and 100 µm, which was shown to be an optimum thickness for FC-72 and water, respectively.

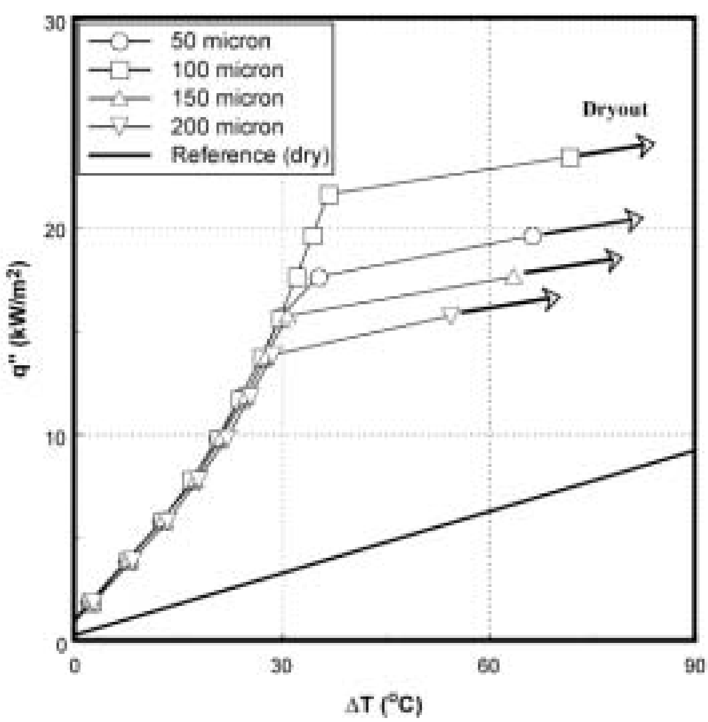

Figure 2. Effect of microporous coating thickness on heat transfer performance of flat heater (water flow rate: 1.75 mL/min).

The previous study on evaporative cooling was achieved by the ABM coating technique. The ABM coating enhances the heat transfer coefficient of evaporative cooling mainly due to capillary pumping action within the microporous structures. However, the epoxy component of the microporous structure has a poor thermal conductivity, and thus potentially increases the conduction thermal resistance through the layer, especially when the coating becomes thick. Also, use of epoxy appears to prohibit the porosity variation within the microporous structures even if the aluminum particle size was changed. To overcome these inferior thermal characteristics in evaporative cooling, a new innovative conductive microporous coating method needs to be developed.

TCMC Coating Technique

We have therefore developed a thermally conductive microporous coating (TCMC) technique that consists of metal particles with various micron-level sizes and thermally conducting binding materials that bond the metal particles to produce numerous microporous cavities on a target surface. The new TCMC technique is similar in concept to the ABM coating (many small metal powders jointed by a thin bonding layer around the particles). However, a thermally conductive layer will be used for TCMC technique, instead of the epoxy layer used for the ABM technique to form the microporous coating. Different particle materials are being tested for this current technique, considering corrosion characteristics and compatibility with various fluids. The microporous coating methods, including the ABM technique, are inexpensive and easy processes compared to sintering/machining methods. However, the coating methods are inferior to sintering/machining methods due to the low thermal conductivity of binders (epoxy). The main advantage of this improved coating technique is the combination of an inexpensive and easy coating process and the low thermal resistance of thermally conductive binding materials. Another advantage is that heat transfer is insensitive to coating thickness due to the high thermal conductivity of the binding structures. In addition, the coating technique is applicable to various working liquids, highly wetting to poorly wetting, simply by changing the size of metal particles, since the surface tension of liquids determines the sizes of porous cavities that optimize heat transfer performance.

Figure 3 shows a SEM image of a TCMC-coated surface with aluminum particles (8 to 12 μm). As shown in the figure, the coating produced numerous microporous cavities. Figure 4 shows the boiling performance comparison between TCMC and ABM with 30-50 μm particles. It is clearly shown that TCMC generates higher boiling heat transfer than ABM. This boiling enhancement could be possibly achieved due to the thermally conducting binder option, which generates very low thermal resistance at high heat flux compared to nonconducting binders.

The TCMC technique using a thermally conductive binder has significant advantages compared to the ABM method:

- ~100 times higher thermal conductivity of the bonding layer than the epoxy binder.
- Thicker coating with higher porosity is possible to strengthen capillary pumping through the coating without degrading thermal performance.

Therefore, the TCMC technique is believed to perform better than the microporous plate in evaporative cooling heat transfer.

Future Direction

In the future, we will develop an improved TCMC technique and conduct evaporative cooling tests on prototype radiators. The work will include the following major tasks and subtasks:

1. Develop improved techniques for making microporous and nanoporous coated surfaces, including the TCMC technique.
   - 1.1 Select a powder material and binder combination.
   - 1.2 Coat the surface of one flat heater with TCMC coating.
   - 1.3 Perform dry and evaporative cooling experiments.
   - 1.4 Compare evaporative cooling data for the plain, ABM-coated, and TCMC-coated surfaces.
   - 1.5 Optimize evaporative cooling with TCMC surfaces by investigating the effect of spray water flow rate, particle size, and coating thickness.

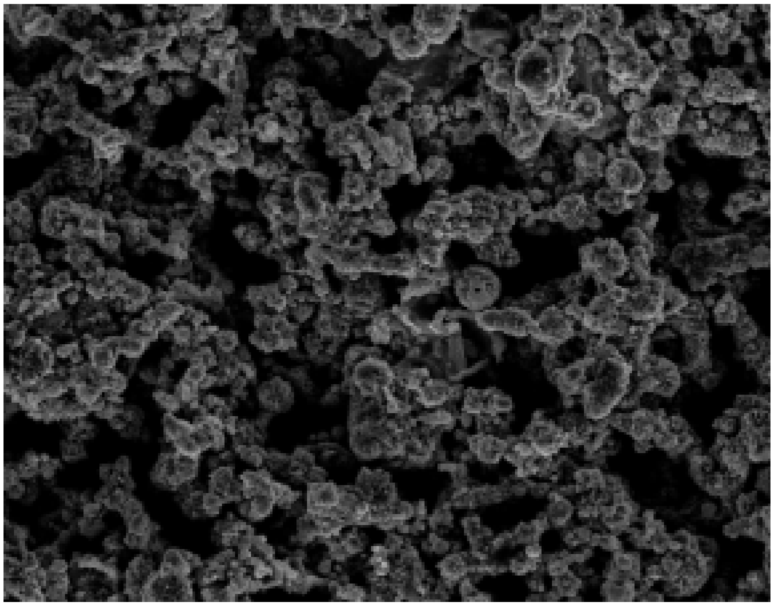

Figure 3. SEM image of thermally conductive microporous coated surface with aluminum particles 8–12 μm in diameter.

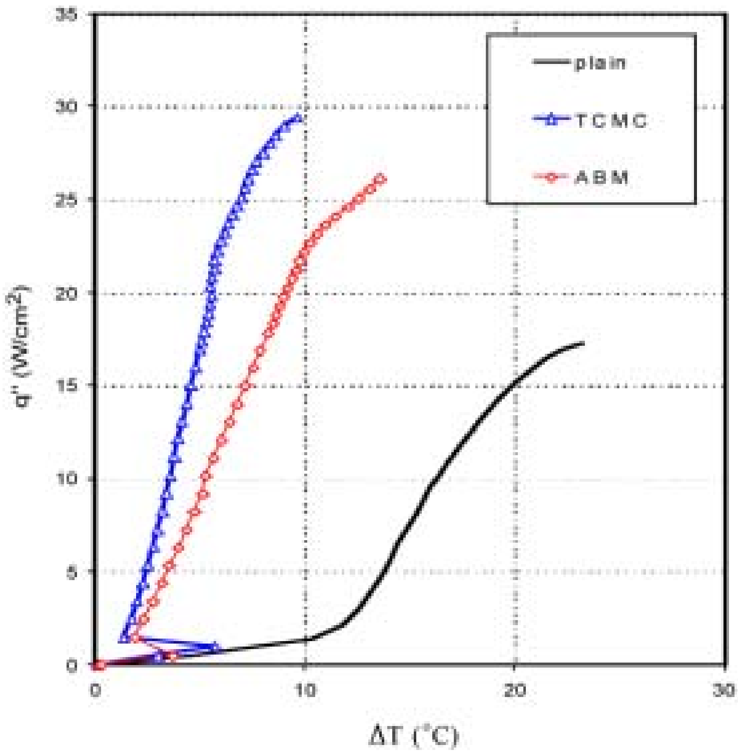

Figure 4. Comparison of heat transfer performance between ABM and TCMC with 30–50-μm aluminum particles.

1.6 Characterize the structure of the selected TCMC surfaces using SEM.

2. Conduct evaporative cooling tests on prototype radiators.
   2.1 Evaluate a number of methods to incorporate evaporative cooling into prototype radiators.
   2.2 Conduct experimental study of evaporative cooling with a TCMC coating on a prototype radiator.

Conclusions

We have characterized evaporative cooling with plain and microporous surfaces with a focus on the effects of particle sizes and thicknesses of coatings on evaporative cooling. The size of coating particles has a negligible effect on heat transfer performance. Therefore, a nanoporous surface is recommended for further study of the particle size effect. The 100-µm coating thickness gave the maximum heat transfer performance.

To overcome the inferior thermal characteristics of the ABM coating in evaporative cooling, a new innovative conductive microporous coating method needs to be developed. We have initiated the development of a thermally conductive microporous coating (TCMC) technique that consists of metal particles and thermally conducting binding materials. The microporous coating methods, including the ABM technique, are inexpensive and easy processes compared to sintering/machining methods. However, the coating methods are inferior to sintering/machining methods due to the low thermal conductivity of binders (epoxy). The main advantage of this improved coating technique involves combining an inexpensive and easy coating process with the low thermal resistance of thermally conductive binding materials. Another advantage is that heat transfer is insensitive to coating thickness, due to the high thermal conductivity of binding structures. Therefore, the TCMC technique is believed to perform better than the microporous plate in evaporative cooling heat transfer.

FY 2004 Publication

J.H. Kim, S.M. You, and S.U.S. Choi, “Evaporative Spray Cooling of Plain and Microporous Coated Surfaces,” International Journal of Heat and Mass Transfer, Vol. 47, pp. 3307–3315, 2004.

D. Nanofluids for Thermal Management Applications

Principal Investigator: S.U.S. Choi
Argonne National Laboratory
Argonne, IL 60439
(630) 252-6439, fax: (630) 252-5568, e-mail: choi@anl.gov

Technology Development Manager: Sid Diamond
(202) 586-8032, fax: (202) 586-1600, e-mail: sid.diamond@ee.doe.gov
Technical Program Manager: Jules Routbort
(630) 252-5065, fax: (630) 252-4289, e-mail: routbort@anl.gov

Contractor: Argonne National Laboratory
Contract No.: W-31-109-Eng-38

Objectives

- Exploit the unique properties of nanoparticles to develop heat transfer fluids with ultra-high thermal conductivity.
- Characterize the thermal properties and heat transfer performance of nanofluids.
- Develop nanofluid technology for vehicle thermal management.

Approach

- Develop simplified models of a nanofluid.
- Measure the thermal conductivity of nanofluids.
- Measure the heat transfer coefficient of nanofluids.

Accomplishments

- Developed a nanofluid model and found that the dynamic interactions between nanoparticles and liquid molecules is a key mechanism of the temperature- and size-dependent thermal conductivity. Our paper was published May 24, 2004, as the cover story of the journal *Applied Physics Letters*.
- Predicted, by using our nanofluid model, that the thermal conductivity of nanofluids increases with decreasing particle size.
- Published, in collaboration with researchers in several universities, the first and second review articles on nanofluids.

Future Direction

- Produce and characterize nanofluids containing nanoparticles less than 10 nm.
- Conduct nanofluid flow and heat transfer experiments in laminar and turbulent flow.
- Modify the one-step nanofluid production system for a larger quantity of nanofluids.
- Characterize metallic and oxide nanofluids in pool boiling for two-phase engine cooling applications.
- Refine models of nanostructure-enhanced and nanoparticle-mobility-enhanced thermal conductivity of nanofluids.

Introduction

The heat rejection requirements are continually increasing as a result of trends toward more power output and stringent emission requirements for engines. Therefore, cooling is one of the top technical challenges facing the transportation industry. The conventional method to increase heat rejection rates is to use extended surfaces (such as fins). However, current designs have already stretched this technology to its limits. Furthermore, conventional heat transfer fluids used in today's thermal management of vehicles, such as lubricants and engine coolants, are inherently poor heat transfer fluids. Therefore, a strong need exists for new and innovative concepts to achieve ultra-high-performance cooling in thermal management systems for vehicles.

Modern fabrication technology provides great opportunities for actively processing materials at the nanoscale. The thermal, mechanical, optical, magnetic, and electrical properties of nanophase materials are superior to those of conventional materials with coarse grain structures. Consequently, the research and development on nanophase materials has drawn considerable attention from material scientists and engineers alike. Taking a different tack from extended surface approaches and exploiting the unique properties of nanoparticles, Argonne National Laboratory (ANL) has pioneered a new kind of ultra-high-thermal-conductivity fluid, called nanofluids, by uniformly and stably suspending a very small quantity (preferably <1% by volume) of nanoparticles in conventional coolants [1].

The potential benefits of using nanofluids include:

- Improve heat transfer of engine coolants and oils,
- Reduce heat exchanger size and weight,
- Reduce heat transfer fluid inventory,
- Reduce vehicle emissions,
- Improve wear resistance,
- Reduce friction coefficient, and
- Reduce pumping energy in existing system.

The objectives of the project are to exploit the unique properties of nanoparticles to develop heat transfer fluids with high thermal conductivity, to characterize the thermal conductivity and heat transfer behavior of nanofluids, and to develop nanofluid technology for increasing the thermal transport of engine coolants and lubricants.

Approach

Our approach to overcoming the poor heat transfer rates of conventional heat transfer fluids is to significantly increase the thermal conductivity of the liquids. An attractive method in that regard is the use of a suspension of solid nanoparticles in a liquid. Solids with thermal conductivities orders of magnitudes higher than those of the liquids are chosen. For example, the thermal conductivity of copper at room temperature is about 3000 times greater than that of engine oil. In fact, numerous theoretical and experimental studies of the effective thermal conductivity of dispersions that contain solid particles have been conducted since Maxwell's theoretical work was published about 100 years ago [2]. However, studies on thermal conductivity of suspensions have been confined to millimeter- or micrometer-sized particles. The major problem with the use of such large particles is the rapid settling of these particles in fluids. Another is the abrasive nature of the suspension. In contrast, use of nanoparticles has the potential to produce the increased thermal conductivity sought in heat transfer fluids without the problems of settling and abrasion. Maxwell's concept of enhancing the thermal conductivity of fluids by dispersing solid particles in them is old, but what is new and innovative with the concept of nanofluids is the idea of using the nanoparticles that have become available to us only recently.

The ANL nanofluid team has developed two techniques to make nanofluids: the single-step direct evaporation method, which simultaneously makes and disperses the nanoparticles directly into the base fluid, and the two-step method, which first makes nanoparticles and then disperses them into the base fluid. Although the two-step technique works well for oxide nanoparticles, it is not as effective for metal nanoparticles, such as copper. For nanofluids containing high-conductivity metals, the single-step direct evaporation technique is preferable to gas-condensation processing. ANL has already produced oxide and carbon nanotube nanofluids by the two-step technique and metal nanofluids by the single-step technique. In particular, it was demonstrated that stable suspensions can be achieved by maintaining the particle size below a threshold level.

The thermal conductivity of nanofluids with low particle concentrations (1–5% by volume) was studied experimentally. The experimental results show that these nanofluids have substantially higher thermal conductivities than the same liquids without nanoparticles. For example, a 20% improvement in the thermal conductivity of ethylene glycol was seen when 4 vol.% copper oxide was dispersed in this fluid. However, recent measurements show that metallic nanoparticles or carbon nanotubes (CNTs) can increase the thermal conductivity by a significant amount over the oxide particles. For example, the dispersion of a tiny amount (<1 vol.%) of copper nanoparticles or carbon nanotubes dispersed in ethylene glycol or oil improves their thermal conductivities by 40 and 150%, respectively [3–4].

Inspired by our discoveries, other groups across the world have begun nanofluid research and provided further breakthroughs. Among them, Das et al. explored the temperature dependence of the thermal conductivity of nanofluids containing Al_2O_3 or CuO nanoparticles [5]. Their discovery of a two- to four-fold increase in thermal conductivity enhancement for nanofluids over a small temperature range (21–51°C) implies that nanofluids could be smart fluids, sensing their thermal environment. This new feature makes nanofluids even more attractive as coolants for devices with high energy density. You et al. [6] measured the critical heat flux (CHF) in a boiling pool of nanofluids containing an extremely small amount of alumina nanoparticles. They discovered a dramatic increase (up to about 200%) in CHF when the nanofluid is used as a cooling liquid instead of pure water.

Since the pioneering work of Choi [1], the four key features of nanofluids have been found to be thermal conductivities far above those of traditional solid/liquid suspensions [3–4], a nonlinear relationship between thermal conductivity and concentration [4], strongly temperature-dependent thermal conductivity [5], and a significant increase in critical heat flux (CHF) [6]. These key features make nanofluids strong candidates for the next generation of coolants for improving the design and performance of thermal management systems.

Results and Discussion

The discoveries of ultra-high thermal conductivity and CHF clearly show the fundamental limits of conventional models for solid-liquid suspensions involving nanoparticles. At present, mechanisms for enhanced CHF are not understood. Several mechanisms that could be responsible for enhanced thermal conductivity in nanofluids have been proposed, including ballistic conduction in nanoparticles, as well as the thermal conductivity being dependent upon the nanoparticle structure and mobility.

We have developed, for the first time, a simplified nanofluid model and found that the dynamic interactions between nanoparticles and liquid molecules is a key mechanism of the temperature- and size-dependent thermal conductivity [7]. Our paper was published as the cover story in the May 24, 2004, issue of the journal *Applied Physics Letters* (see Figure 1). Our nanofluid model predicts that the thermal conductivity of nanofluids increases with decreasing particle size (see Figure 2). This is a major milestone in the development of nanofluid technology. For this technology to become a reality, new techniques are needed for manufacturing nanoparticles smaller than 10 nm. Just several

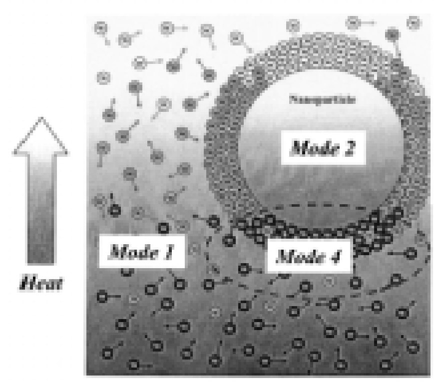

Figure 1. Modes of energy transport in nanofluids. The first mode is collision between base fluid molecules, the second mode is the thermal diffusion in nanoparticles suspended in fluids, the third mode is collision between nanoparticles (not shown), and the fourth mode is thermal interactions of dynamic or dancing nanoparticles with base fluid molecules.

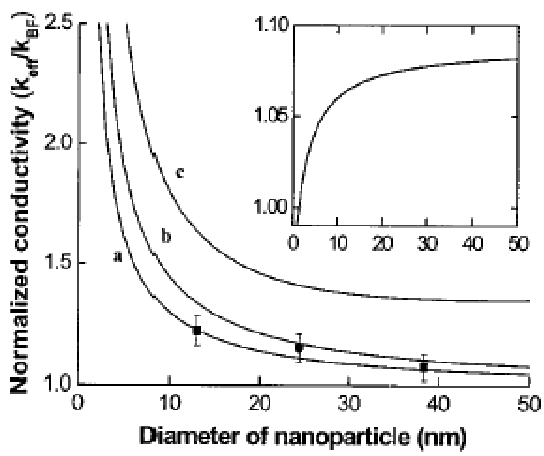

Figure 2. Nanoparticle size-dependent thermal conductivity of nanofluids at a fixed concentration of 3 vol.% and room temperature, normalized to the thermal conductivity of the base fluid. Although experimental data are very limited, model predictions (solid curve a) agree with experimental data (solid squares) for water-based nanofluids containing 13-nm Al_2O_3 nanoparticles and 38.4-nm Al_2O_3 nanoparticles. The same is true of model predictions (solid curve b) and the experimental data point (solid circle) for ethylene glycol-based nanofluids containing 24.4-nm CuO nanoparticles. Surprisingly, the conductivity of the base fluid increases by more than a factor of two with <10-nm Cu particles in ethylene glycol (curve c). In striking contrast, the inset shows that the Maxwell model, together with the nanoparticle thermal conductivity calculated from Chen's equation, predicts decreasing conductivity of nanofluids with decreasing particle size for water-based nanofluids containing Al_2O_3 nanoparticles.

months later another dynamic model of a nanofluid was published in the journal *Physical Review Letters* [8] and confirmed the key role of Brownian motion of nanoparticles in nanofluids. Still, a more comprehensive theory is needed to explain the behavior of nanofluids.

The Nanofluid Heat Transfer Test Facility has been constructed to experimentally determine heat transfer rates to flowing nanofluids under a variety of flow conditions and using a variety of nanofluids. A major constraint on the test facility design is the need to keep the fluid inventory to a bare minimum (~240 mL). Consequently, we applied methods developed over many years in small-scale heat-transfer testing to the nanofluid situation. For over a decade, we have been involved with experimental heat transfer to single-phase, boiling, and condensing of one- and two-component fluids. Test channels have been on the order of 3 mm inside diameter for the most part, with some channels as small as 0.5 mm. To meet the low-fluid-inventory design constraint for the Nanofluid Heat Transfer Test Facility, a test section was chosen with an inside diameter of 2 mm. All components were carefully sized accordingly. Instrumentation and data acquisition techniques developed for previous tests in this small channel size range were adapted to the Nanofluid Heat Transfer Test Facility. A schematic of the facility is shown in Figure 3. It is a closed-loop system that includes a variable-speed drive pump and meter, a preheater, test section, and cooler. The electrically heated test channel is a stainless-steel tube with a length of 508 mm and inside diameter of 2 mm. Inlet pressure (P) and differential pressure across the channel (dP) are measured by means of a piezoresistive-type transducer and strain-gauge-type transducer, respectively. Stream thermocouples measure the fluid temperature at the inlet and outlet of the test channel, and the surface thermocouples placed on the test channel wall measure wall temperature at five locations along the channel length. A data acquisition system (DAS) reads and records all sensor-output voltages.

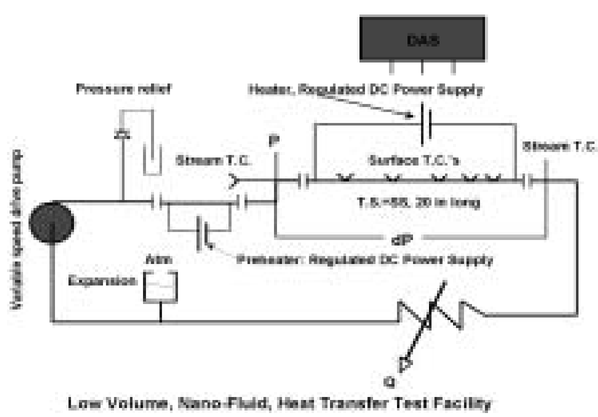

Figure 3. Schematic diagram of nanofluid heat transfer test facility.

ANL has inaugurated a work-for-others project with Nuvonyx. The objective is to develop several water-based nanofluids so that Nuvonyx can assess the feasibility of applying nanofluid technology to microchannel cooling. Since nanofluids in microchannels are expected to dramatically enhance the convection heat transfer and provide a basis for state-of-the-art applications of nanofluid technology to advanced vehicle thermal management systems, this project would directly benefit nanofluid technology development funded by DOE.

FY 2004 Publications

1. Jang, S.P., and Choi, S.U.S., "Role of Brownian Motion in the Enhanced Thermal Conductivity of Nanofluids," *Applied Physics Letters*, Vol. 84, No. 21, pp. 4316–4318 (May 2004). Also in *Virtual Journal of Nanoscale Science and Technology*, May 24, 2004.
2. Choi, S.U.S.; Zhang, Z.G.; and Keblinski, P., "Nanofluids," *Encyclopedia of Nanoscience and Nanotechnology*, Vol. 6, pp. 757–773, H.S. Nalwa, ed., American Scientific Publishers, Stevenson Ranch, CA, 2004.
3. Eastman, J.A.; Phillpot, S.R.; Choi, S.U.S.; and Keblinski, P., "Thermal Transport in Nanofluids," *Annual Review of Materials Research*, Vol. 34, pp. 219–246, 2004.
4. Choi, S.U.S.; Yu, W.; Hull, J.R.; Zhang, Z.G.; and Lockwood, F.E., "Nanofluids for Vehicle Thermal Management," *SAE Transactions J. Passenger Cars: Mech. Systems*, Vol. 111, No. 1021, pp. 38–43, 2003.
5. Xue, L.; Keblinski, P.; Phillpot, S.R.; Choi, S.U.S.; and Eastman, J.A., "Effect of Liquid Layering at the Liquid-Solid Interface on Thermal Transport," submitted to *Int. Journal of Heat and Mass Transfer*, 2004.
6. Yu, W., and Choi, S.U.S., "The Role of Interfacial Layers in the Enhanced Thermal Conductivity of Nanofluids: A Renovated Hamilton-Crosser Model," submitted to *J. Nanoparticle Research*.

Future Direction

Future work will focus on the following five major tasks:

1. Produce and characterize nanofluids containing nanoparticles less than 10 nm. Characterization of the thermal conductivity of nanofluids has led to the discovery that it increases with decreasing nanoparticle size. In contrast, solid-solid composites have the reverse size effect: the thermal conductivity of solid-solid nanocomposites decreases with decreasing particle size. Since our dynamic model shows that particle size is of primary importance in the development of nanofluid technology, we will produce and characterize nanofluids containing nanoparticles less than 10 nm.

2. Conduct nanofluid flow and heat transfer experiments in laminar and turbulent flow. A major focus in nanofluids has been on their thermal conductivity. Nanofluids will be produced and characterized to generate a database on their thermal conductivity. However, a new focus will be on the flow and heat transfer of nanofluids. We believe that it is critical to characterize the flow and heat transfer behavior of nanofluids in tubes in order to explain and exploit nanoparticle size-, shape-, and concentration-dependent pressure drop and heat transfer coefficient of nanofluids in tubes. For example, theories of flow in tubes or porous materials have been developed at the macroscopic level. However, we believe that it is vital to connect the structure and mobility of nanoparticles at the nano- or micro-scale to the properties of nanofluids measured at the macroscopic level. Therefore, we will explore the flow characteristic and measure the heat transfer coefficient of nanofluids in tubes. We will then relate enhanced thermal conductivity and flow characteristic to enhanced heat transfer coefficient of nanofluids. The new Nanofluid Heat Transfer Test Facility will be carefully scrutinized for instrument accuracy, data acquisition process, and test procedure. Control tests will be performed with water as the test fluid. Subsequently, nanofluid flow and heat transfer experiments will be conducted. The flow and heat transfer data for nanofluids will be used to determine whether the flow and heat transfer correlations developed for homogeneous fluids could be applied to nanoparticle dispersions with aspect ratios different from one.

3. Modify the one-step nanofluid production system for a larger quantity of nanofluids. Nanofluids hold significant potential for revolutionizing industries that are dependent on the performance of heat transfer fluids. However, there is one big barrier to commercialization of nanofluids: production scale-up methods to produce nanofluids in volume and at low cost. Finding a way to produce small (1–10 nm) nanoparticles cheaply and disperse them without agglomeration is the key hurdle to commercialization. As a first step toward production scale-up, we will modify ANL's one-step process to produce more nanofluids.

4. Characterize metallic and oxide nanofluids in pool boiling for two-phase engine cooling applications.

Most studies carried out to date are limited to the thermal characterization of nanofluids without evaporation or condensation. However, nanoparticles in nanofluids can play a vital role in two-phase heat transfer systems. Therefore, there is a great need to characterize nanofluids in boiling and condensation heat transfer. The high critical heat flux of nanofluids is important, particularly for two-phase engine cooling. The nanofluid tested by You et al. [6] contains alumina (Al_2O_3) nano-particles dispersed in distilled and deionized water. We will design and fabricate a pool boiling test facility and characterize metallic and oxide nanofluids in pool boiling.

5. Refine models of nanostructure-enhanced and nanoparticle-mobility-enhanced thermal conductivity of nanofluids.

We have developed simple models of nanostructure-enhanced [9] and nanoparticle-mobility-enhanced thermal conductivity of nanofluids [7]. However, much is still unknown about the mechanisms of the anomalous thermal behavior of nanofluids. Therefore, we need to understand the fundamentals of energy transport in nanofluids. As we discover new energy transport mechanisms that are missing in existing theories, we will refine the simple models or develop a new model of energy transport in nanofluids integrating new mechanisms. A better understanding of the mechanisms behind the thermal-conductivity enhancement will likely lead to recommendations for nanofluid design and engineering for transportation applications.

Conclusions

Nanofluids have four key features: (1) thermal conductivities far above those of traditional solid/liquid suspensions, (2) nonlinear relationship between thermal conductivity and concentration, (3) strongly temperature-dependent thermal conductivity, and (4) significant increase in critical heat flux. These key features make nanofluids strong candidates for the next generation of coolants for improving the design and performance of thermal management systems.

To facilitate the development of nanofluid technology, we will focus in FY2005 on thermal conductivity, flow, and heat transfer experiments using present and developmental nanofluids. The improved thermal properties of nanofluids would allow the use of significantly smaller and lighter heat exchangers for vehicles and other performance-driven systems.

References

1. Choi, U.S., “Enhancing Thermal Conductivity of Fluids with Nanoparticles,” *Developments and Applications of Non-Newtonian Flows*, D.A. Siginer and H.P. Wang, eds., The American Society of Mechanical Engineers, New York, FED–Vol. 231/MD-Vol. 66, pp. 99–105 (Nov. 1995).
2. Maxwell, J.C., 1881, *A Treatise on Electricity and Magnetism*, 2nd ed., 1, 435, Clarendon Press.
3. Eastman, J.A.; Choi, S.U.S.; Li, S.; Yu, W.; and Thompson, L.J., “Anomalously Increased Effective Thermal Conductivities of Ethylene Glycol-Based Nanofluids Containing Copper Nanoparticles,” *Appl. Phys. Lett.* **78**(6), pp. 718–720, 2001.
4. Choi, S.U.S.; Zhang, Z.G.; Yu, W.; Lockwood, F.E.; and Grulke, E.A., “Anomalous Thermal Conductivity Enhancement in Nanotube Suspensions,” *Appl. Phys. Lett.* **79**(14), pp. 2252–2254, 2001.
5. Das, S.K.; Putra, N.; Thiesen, P.; and Roetzel, W., “Temperature Dependence of Thermal Conductivity Enhancement for Nanofluids,” *ASME J. Heat Trans*. **125**, pp. 567–574, 2003.
6. You, S.M.; Kim, J.H.; and Kim, K.M., “Effect of Nanoparticles on Critical Heat Flux of Water in Pool Boiling of Heat Transfer,” *Appl. Phys. Lett.* **83**, pp. 3374–3376, 2003.
7. Jang, S.P., and Choi, S.U.S., “Role of Brownian Motion in the Enhanced Thermal Conductivity of Nanofluids,” *Appl. Phys. Lett*. **84**, pp. 4316–4318, 2004.
8. Kumar, D.H.; Patel, H.E.; Rajeev, K.V.R.; Sundararajan, T.; Pradeep, T.; and Das, S.K., “Model for Heat Conduction in Nanofluids,” *Phys. Rev. Lett*. **93**, pp. 144301-1-4, 2004.

9. Yu, W., and Choi, S.U.S., "The Role of Interfacial Layers in the Enhanced Thermal Conductivity of Nanofluids: A Renovated Hamilton-Crosser Model," submitted to *J. Nanoparticle Research.*

E. Erosion of Materials in Nanofluids

Principal Investigator: J.L. Routbort (co-worker: D. Singh)
Argonne National Laboratory
9700 S. Cass Avenue, Argonne, IL 60439-4838
(630) 252-5065, e-mail: routbort@anl.gov

Technology Development Manager: Sid Diamond
(202) 586-8032, e-mail: sid.diamond@ee.doe.gov

Contractor: Argonne National Laboratory
Contract No.: W-31-109-Eng-38

Objectives

- Determine if the use of fluids containing a variety of nanoparticles and nanotubes result in erosive damage to radiator materials.
- Develop models to predict the erosive damage.

Approach

- Develop an experimental apparatus to measure erosive loss.
- Conduct experiments to study erosive damage of fluids on typical radiator materials.
- Develop methods to analyze the results.

Accomplishments

- Built apparatus to study liquid erosion.
- Completed calibration of sample impact area as a function of fluid velocity.
- Gathered baseline data with ethylene glycol and water solutions, and this effort is ongoing.
- Conducted preliminary experiments with nanofluids.

Future Direction

- After accumulation of a baseline data by using ethylene glycol and water, fluids containing a variety of nanoparticles and nanotubes will be tested on typical radiator materials, varying both the angle and velocity of impact, volume percent of nanoparticles, and temperature.

Introduction

Many industrial technologies face the challenge of thermal management. With ever-increasing thermal loads due to trends toward greater power output for engines and exhaust gas recirculation for diesel engines, cooling is a crucial issue in transportation. The conventional approach for increasing cooling rates is the use of extended surfaces (such as fins and microchannels). Reducing radiator size will reduce the frontal area and hence the aerodynamic drag. However, current designs have already stretched this approach to its limits. Therefore, an urgent need exists for new and innovative concepts to achieve ultra-high-performance cooling. Nanofluids seem to show enormous potential as a coolant for radiators. Choi et al. have shown that fluids containing 1 vol.% Cu nanoparticles increase thermal conductivity by 40% [1], while 1 vol.% carbon nanotubes increase thermal conductivity by 250% [2].

To utilize the enhanced thermal conductivity, it must be shown that liquid erosion of typical radiator materials will be tolerable. Hence, the FreedomCar and Vehicle Technologies Program has funded a program on liquid erosion of nanofluids.

Results and Discussion

As reported earlier, an apparatus was designed and constructed to allow the erosion rates of fluids containing various nanoparticles and nanotubes to be determined from ≈ 1 m/s, velocities that are used in heavy-vehicle radiators, to about 15 m/s. Angle of impacts can be varied from 0 to 90°C, and temperatures up to ≈ 95°C can be obtained. A photograph of the apparatus is shown in Figure 1. Figure 2 is a view of the specimen chamber with the cover removed to show the specimen and the nozzle. The experimentally determined variables are (1) pump RPM, (2) temperature, (3) pressure, and (4) weight loss. The velocity is determined by measuring the amount of fluid for a given time at a fixed RPM by using a given nozzle diameter. Such a calibration is shown in Figure 3.

During experimentation over the past year, it was determined that velocity at a fixed RPM during the course of an experiment is dependent on several factors, such as wear of pump gears and clogging of the mesh filter placed in the fluid. To ensure that velocity-RPM behavior remains consistent, modifications were made to the erosion set-up. These modifications included additional pressure gages placed at the pump exit and before the nozzle (Figure 4). Stability of the pressure readings at these locations ensured the constant fluid velocity at a fixed pump RPM per the calibration profiles developed.

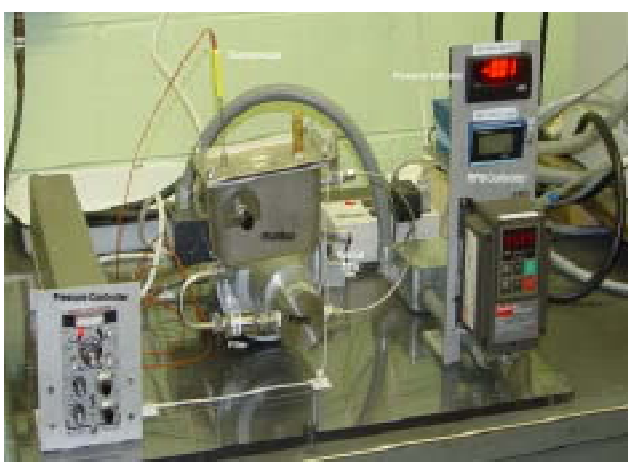

Figure 1. Photograph of the liquid-erosion apparatus with various components labeled.

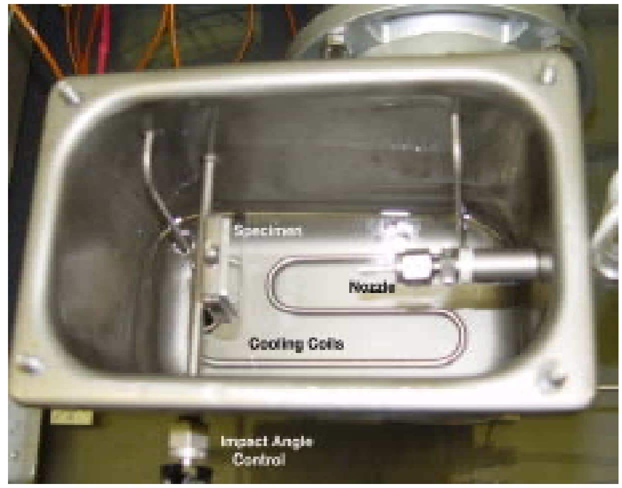

Figure 2. Close-up view of experimental chamber with the cover removed to show the specimen and the nozzle.

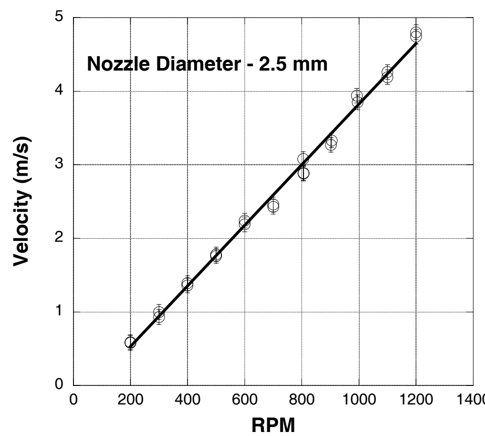

Figure 3. Plot of velocity, determined by measuring the volume of fluid for a fixed time, as a function of pump RPM.

Figure 5 shows the initial result of weight loss of 3003 aluminum sample as a function of time at various velocities. These tests were conducted by using equi-volume solution of ethylene glycol and water. As expected, the weight loss increases with increasing velocity. However, at 3 m/s, no appreciable weight loss was measured. Moreover, at extremely high velocities (> 11 m/s) there is a rapid initial weight loss followed by a decreased rate of weight loss, which indicates saturation in the erosion behavior.

Figure 4. Newly installed pressure gages to ensure appropriate pressures and velocities in the erosion system.

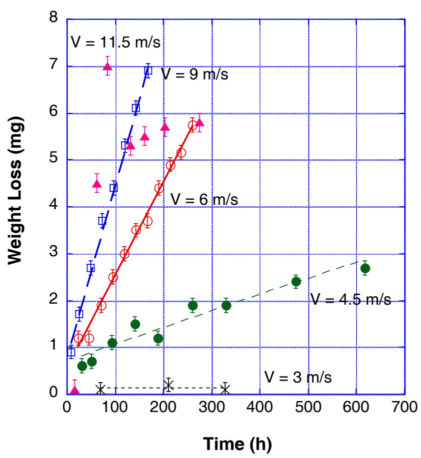

Figure 5. Plot of measured weight loss of 3003 Al vs. time, obtained at ambient temperatures for normal incidence by using ethylene glycol/water solution.

Increasing fluid velocity increases area over which fluid impacts the sample surface. Thus, to compare the erosion behavior at various velocities, it is necessary to normalize slope of the weight-loss time plot with area of erosion at specific velocities. This normalized value can be defined as erosion rate (ER). To identify the area of impact, an aluminum sample was spray painted and exposed to the fluid at the specific velocity.

Figure 6 shows a typical damage pattern that is generated and used for determining the fluid impact area at a fixed velocity. Similar patterns were obtained at other velocities at which erosion behavior has been studied.

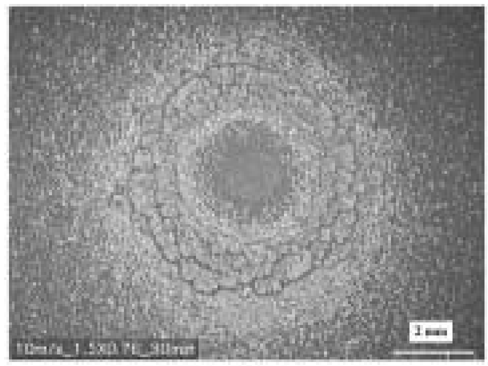

Figure 6. Typical damage zone obtained on a spray-painted aluminum sample at a velocity of 10 m/s. Notice the stagnation zone at the center.

Table 1 provides the erosion rates for Al 3003 under different velocities (3–9 m/s). Also, expected recession rate (rate at which material recedes, ER/aluminum density) is listed.

Preliminary experiments using nanofluids containing copper oxide nanoparticles have been initiated. Nanofluid containing 1 vol.% CuO in ethylene glycol/water solution was provided by S. Choi/ANL. For the preliminary study, the fluid was further diluted to 0.25 vol.% nano-particles by volume. Figure 7 shows the weight loss of Al 3003 with time. These results suggest that the weight loss rate with nanofluids is somewhat similar to that of plain ethylene glycol/water solutions, as shown in Figure 5, at similar velocities. At longer times, the weight loss appears to be saturated (data for V=4 m/s). However, at 2 m/s, weight loss is measurable with nanofluids as opposed to no discernible loss measured with plain fluid at V=3 m/s. It needs to be pointed out that there is adhesion of agglomerated CuO nanoparticles on the sample surface (as shown in Figure 8) that could have affected the weight loss measurements. For future experiments, nanofluids with appropriate dispersants will be used.

Table 1. Erosion and recession rates of Al 3003 as a function of velocity obtained at ambient temperatures at normal incidence.

V (m/s)	Erosion Rate ($g/h\text{-}m^2$)	Recession Rate (μm/h)
3	0	0
4.5	0.005	0.002
6	0.031	0.012
9	1	0.370

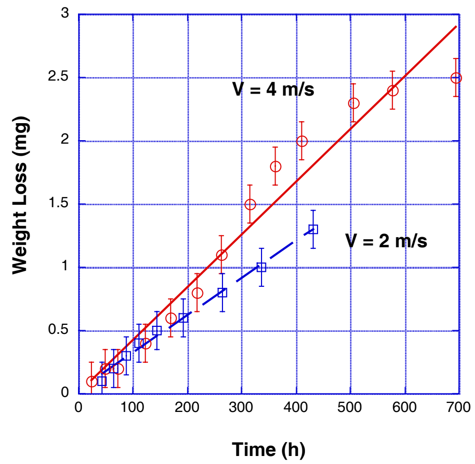

Figure 7. Plot of measured weight loss of 3003 Al vs. time, obtained at ambient temperatures for normal incidence by using 0.25 vol.% CuO nano-fluid.

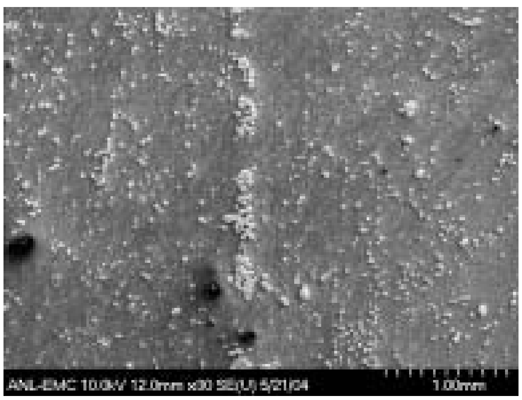

Figure 8. Al 3003 surface showing agglomerated CuO nanoparticles adhering to the surface.

It is well known that Al 3003 is susceptible to corrosion in the presence of ethylene glycol/water solutions [3]. In the presence of small amounts of impurities, Al metal can corrode in ethylene glycol solutions by localized pitting. Evidence of extensive pitting corrosion (Figure 9), on the unimpacted surface, was found in one of the samples that showed weight loss with time. It is believed that there is a galvanic couple formed between the sample holder (steel) and the sample. In the presence of impurities in the fluid, test temperature corrosion of Al sample occurs. However, corrosion is expected to be independent of the hydrodynamic conditions [3]. Thus, the weight loss observed as a function of velocity is probably from a combination of erosive and corrosive actions.

Figure 9. Evidence of corrosion pit with corrosion products in Al 3003 eroded with ethylene-glycol/water solution.

Issues and Future Direction

At present, the cause of the observed sample weight loss is unclear — it may be due to erosion, corrosion, or a combination of erosion/corrosion mechanisms. Understanding the mechanism of weight loss is vital to developing predictive models. It is believed that the difficulty associated with repeatability of experiments is related to the operating mechanism(s). Distinction between erosion and corrosion behaviors will be made by using a corrosion-resistant material or sample holder and/or controlling the temperature during the experiment. Furthermore, the role of aluminum oxide layer in erosion behavior will be investigated. This will require some modifications to the apparatus. Baseline erosion data will be obtained for various impact angles and velocities. Finally, a family of erosion rates as a function of angle and velocity will be measured and correlated with dispersed nanoparticle loadings. Computational fluid dynamics will be used to predict the damage zone as a function of velocity.

Conclusions

An apparatus to measure the erosion of radiator materials using nanofluids has been constructed. An ethylene glycol/water solution has been used to collect baseline data on normal incidence impact. Experimentation using nanofluids has been initiated.

References

1. J.A. Eastman, S.U.S. Choi, S. Li, W. Yu, and L.J. Thompson, "Anomalously Increased Effective Thermal Conductivities of Ethylene Glycol-Based Nano-Fluids Containing Copper Nano-Particles," *Applied Physics Letters*, **78**, 718–720 (2001).
2. S.U.S. Choi, Z.G. Zhang, W. Yu, F.E. Lockwood, and E.A. Grulke, "Anomalous Thermal Conductivity Enhancement in Nano-tube Suspensions," *Applied Physics Letters*, **79**, 2252–2254 (2001).
3. D. Wong, L. Swette, and F.H. Cocks, "Aluminum Corrosion in Uninhibited Ethylene Glycol-water Solutions," J. Electrochem. Soc., **126**, 11–15 (1979).

F. Analysis of Ventilation Airflow and Underhood Temperatures in the Engine Enclosure of an Off-Road Machine

Principal Investigators: Tanju Sofu, Jimmy Chang, John Hull
Argonne National Laboratory
9700 S. Cass Avenue, Argonne, Illinois 60439
(630) 252-9673, fax: (630) 252-4500, e-mail: tsofu@anl.gov

Technology Development Area Specialist: Sidney Diamond
(202) 586-8032, fax: (202) 586-1600, e-mail: sid.diamond@ee.doe.gov
Field Technical Manager: Jules Routbort
(630) 252 5065, fax: (630) 252 4289, e-mail: routbort@anl.gov

Contractor: Argonne National Laboratory
Contract No.: W-31-109-ENG-38

Objective

- Assess a novel simulation technique based on combined use of 3-D CFD and 1-D network flow models for predicting underhood airflow and temperatures in a separated and sealed engine compartment of an off-road machine.

Approach

- A prototypical test-rig that includes an engine and other installation hardware was built by the engineers at Caterpillar, Inc., and the experiments were conducted with controlled ventilation air inlet locations and flow rates.
- The analytical effort focused on combined use of a 1-D network flow model with four loops to simulate the engine and the cooling system, and a 3-D CFD model for the ventilation air circulation in the test rig.
- The goal has been to provide an integrated analysis capability that needs only the flow rates and inlet temperatures as boundary conditions to study the effects of ventilation on heat rejection and component temperatures.

Accomplishments

- Studied five different inlet configurations were studied for various ventilation flow rates and calculated the corresponding flow field and temperature distributions.
- Used the results to determine the pressure drop through the test-rig, the flow splits around the engine, the heat-transfer coefficients on the engine and other heat-generating component surfaces, convected heat with the ventilation air, and the air and surface temperatures on various thermocouple locations.

Future Direction

- By using the data from Caterpillar experiments, the calculated temperatures using the 1-D network flow and the CFD models will be compared with the measured temperatures in the next phase of the project.

Introduction

Mostly because of sound-reduction requirements, modern off-road machines are designed with separate engine and cooling system compartments. Since high underhood temperatures can reduce component durability and life, the assessment of component temperatures in a relatively well sealed engine enclosure is important. The main thermal management challenge for such a configuration is to determine the ventilation airflow needs in the engine enclosure and its effect on the thermal balance. To provide insight, a prototypical test-rig that includes an engine and other installation hardware was built by engineers at Caterpillar, Inc. The experiments were conducted with controlled ventilation air inlet locations and flow rates to help understand the effects of ventilation on heat rejection and component temperatures.

In parallel, an assessment of various simulation methods was initiated by analysts at Argonne National Laboratory (ANL) for predicting underhood ventilation airflow and temperatures in the test-rig. The analytical effort consisted of combined use of a 1-D network flow model to simulate the engine and the cooling system and a 3-D CFD model for the ventilation air circulation in the test rig. The goal has been to provide an integrated analysis capability that needs only the flow rates and inlet temperatures as boundary conditions to assure adequate air cooling and to help identify potential hot-spots.

CFD Model Development

The test rig included an engine installed into a mock-up representing a typical medium-size off-highway machine with a full engine enclosure. Small doors installed at five sides of the enclosure (front, back, intake side, exhaust side, and bottom) served as ventilation air inlet locations. An external blower installed in the outlet pipe at the top was used to control the ventilation airflow rate. This combination of fixed outlet and varying inlet locations helped researchers understand the effect of inlet location on critical component temperatures. The engine coolant temperature and compressed air temperatures at the intake manifold were maintained by laboratory heat exchangers and instrumented to account for the heat rejection closely. The ventilation air and component surface temperatures were measured at various locations.

A CAD model of the test rig was prepared and provided by the Caterpillar team to help assist the model development. This CAD model was used to develop a 3-D CFD model of the test rig by using the commercial CFD code STAR-CD. To capture the ventilation airflow distribution at the enclosure inlet accurately, a large inlet plenum was included for each inlet configuration to represent ambient conditions for pressure and temperature. The CFD model consisted of approximately 1.34 million fluid cells with a 3-mm-thick cell layer surrounding the engine and enclosure surfaces.

To allow the data to be scaled for different engine compartment configurations, the ventilation airflow rate was normalized with respect to the engine combustion airflow rate. This ratio of the ventilation airflow rate to the engine combustion airflow rate was used as the basis for comparing the analytical results with experimental data. The airflow ratio was varied from 0.5 to 3.75 during the experiments. In a traditional underhood compartment with no service wall to separate engine from cooling systems, the airflow ratio is believed to be approximately 10.

Each of the five configurations was studied for five different ventilation airflow rates corresponding to airflow ratios of 0.5, 1.0, 1.5, 2.0, and 2.5. The desired flow rate through the enclosure was assured by imposing a proportional uniform flow field at the plenum inlet as the boundary condition. An option with two-pressure boundary conditions (pressure-driven flow between the inlet plenum and outlet pipe) was also investigated to assess the sensitivity of the flow field to the boundary conditions. The parametric studies did not indicate a strong dependence of thermal mixing inside the enclosure to the turbulence boundary conditions at the inlet. In each case, 10% turbulence intensity and half-window-width mixing length were specified at the plenum inlet. Engine and enclosure boundaries were specified as smooth “non-slip” walls, but the effect of surface roughness on the pressure drop was also evaluated.

A parametric study for inclusion of the buoyancy force in the thermal-fluid calculations revealed that the effect of density variation on the overall flow and temperature fields is negligible. Therefore, the ventilation airflow field was simulated as a steady incompressible flow, decoupled from the energy equation by using constant thermo-physical properties. This allowed a two-step analysis in which first the flow field is established inside the enclosure and then the temperature distributions were obtained for a given set of thermal boundary conditions.

Most of the simulations were performed by using the high-Reynolds number k-epsilon turbulence model in conjunction with logarithmic wall functions; however, a few other turbulence models (such as the renormalization group [RNG] formulation, Chen's variant, and low-Re model), as well as the quadratic and cubic k-epsilon options, were also evaluated. A set of transient calculations was studied to investigate temperature fluctuations observed during the experiments and to assure that the calculated flow field was steady with no small frequency oscillations. The results indicated a negligible difference between the transient and steady-state solutions. The calculations were performed on a Linux cluster, mostly using 4–6 processors.

1-D Network Model Development

As part of the analytical efforts, a 1-D thermal-fluid network model was also developed by using the commercial software FLOWMASTER. In the 1-D model, the air, coolant, and oil loops were represented as different thermal subsystems interacting with each other and the engine structure through discrete heat transfer paths. The 1-D model served as a tool to analyze the interactions of the engine with the air, coolant, and oil loops for predicting the complete thermal system performance and to account for overall energy balance.

Engine Metal Structure: In the network model of engine metal structure, the engine metal structure is cooled by the coolant, oil, and air. FLOWMASTER models the combustion gas as a heat source with a known heat rejection to the cylinder head, liner, and piston. The exhaust is treated as gas flow through the muffler, so the muffler temperature is at the temperature of the exhaust gas. Any components linked to the muffler participate in the modeling of the heat rejection from the exhaust.

Cooling Air Circuit: The entering air gains heat as it passes through individual surface points on the engine mentioned above. FLOWMASTER calculates the amount of heat gain based on the surface area in contact and the heat transfer coefficient. The heat gain by air circuit is calculated through the temperature variation between the component inlet and the component outlet.

Lubrication Oil Loop: In the oil loop of 1-D network model, the oil is supplied in three separate branches: (1) to the turbo and back to the sump; (2) to the cylinder head where the oil gains heat from the valve cover, the cylinder head, and the upper engine block and then returns to the sump; and (3) to the engine block where it gains heat from the piston rings and the lower engine block and then returns to the sump. The oil circuit does not remove any heat from the system; instead, it distributes the heat in the system.

Coolant Water Loop: In the coolant water loop, the water coolant, at a given flow rate, passes through the oil cooler to cool the lubrication oil in oil circuit, circulates inside the upper engine block, and then circulates through the cylinder head. The radiator is simply modeled by a flow source with constant flow rate and by a pressure source with known temperature and pressure.

The 1-D computation has the air inlet at front, bottom, rear, intake, and exhaust side, separately, with assigned airflow rates at all branches. In each computation, the various temperatures in the model are calculated on the basis of the certain physical dimensions and the heat transfer coefficients at the engine-air interface. Some physical data on the engine were supplied by Caterpillar and input in the model. The airflow paths/flow rates and the heat-transfer coefficients were obtained from CFD calculations to compute the system temperature distributions. Steady-state simulation at a given engine rated condition with conduction, convection, and radiation models was carried out. The air enters at the enclosure inlet (front of the enclosure) with given temperature, pressure, and flow rate and then exits at enclosure outlet (top of the enclosure) with temperature, pressure, and flow rate. The heat loads were calculated at the engine surfaces for temperature distribution.

Interface between the 3-D CFD and 1-D Network Flow Models

The ventilation air entering the enclosure was considered to split around the engine block at proportions specified by the CFD model and gain heat as it passes through individual surface points on the engine.

The surface heat flux boundary conditions for the CFD model were deduced from the calculated surface and bulk ventilation air temperatures from the 1-D model by using

$$\frac{q}{A} = h\left(T_s - T_b\right)$$

where q/A is the surface heat flux (the boundary condition for the CFD model), h is the heat transfer coefficient (input to the 1-D network flow model), T_s is the surface temperature, and T_b is the ventilation air temperature near a specific engine or component surface. In return, the results of the 3-D CFD analysis were used to provide the 1-D model with improved ventilation airflow paths and the resulting heat-transfer coefficients between the heat-generating components and ventilation air. Since the 3-D CFD model requires component heat fluxes (q/A) from the 1-D network flow model while the 1-D model requires accurate estimates of heat transfer coefficient (h), an iterative procedure was employed between the two models to obtain consistent solutions. The iterations between the 3-D CFD and 1-D network flow models continued until the difference in the estimated heat transfer coefficients between two subsequent steps were negligible. For most of the underhood components, the convergence was established after a few iterations between the 1-D and CFD solutions.

Results

The ventilation airflow paths around the engine and the surface and ventilation air temperatures in the test-rig are calculated for all five inlet configurations and five different airflow ratios. In agreement with the experimental observations, the CFD results indicate a well-mixed flow inside the enclosure, with no significant difference in component temperatures for different inlet locations. The flow field suggests significant turbulence inside the enclosure since the average viscosity is two orders of magnitude greater than the molecular viscosity of air.

To provide the 1-D thermal-fluid network model with an accurate measure of ventilation airflow paths around the engine for different inlet configurations, the computational domain is considered in six interconnected zones around the engine, and the flow splits are determined from the flow rates through the surfaces separating these zones. When normalized with respect to the inlet flow rate, the calculated splits for each inlet configuration are found to be independent of the inlet flow rate. Since the CFD results do not indicate preferred (unidirectional) flow paths around the engine, the calculated flow splits based on net flux across each side of the engine tend to underestimate the near-surface flow rates. An assessment of the importance of underestimating the flow rates near the component surfaces will be made after comparing the analytical predictions with the experimental data.

To predict the temperature distributions in the test rig by using only the inlet boundary conditions, the thermal calculations are performed by using the surface heat fluxes as the boundary conditions based on the results of the 1-D simulations. Consistent with the nodalization of the 1-D model, the constant heat flux values are specified for the entire surface of heat-generating components. The portions of the enclosure wall near the muffler are also considered as heat transfer surfaces because of exposure to radiation from elevated muffler temperatures. The final heat-transfer coefficients, as estimated by the CFD model and used in 1-D simulations, follow an expected trend and increase almost proportionally with increased airflow ratio within the studied range. At the airflow ratio of 0.5, the heat-transfer coefficient estimates vary between 2 and 22 W/m^2•°C, with an average value of 10 W/m^2•°C. At the airflow ratio of 2.5, the heat-transfer coefficients vary between 10 and 62 W/m^2•°C, with an average value of 21 W/m^2•°C.

As examples of the results, the ventilation air temperatures for the front inlet case and airflow ratio of 1.5 are shown on several vertical planes in Figure 1. For all inlet configurations, the temperatures are significantly higher on the exhaust side of the engine, particularly near the most heat generating components, the muffler and turbo charger. At low-ventilation airflow rates, a substantially large temperature difference (on the order of 50°C) exists with little thermal mixing of the hot and cold jets near the entrance to the outlet pipe. The difference is smaller but still noticeable (about 25°C) at the highest airflow rate studied.

The convected heat from the engine enclosure with the ventilation air is calculated by evaluating the following summation for all the cells at the outlet pipe exit

$$q = \sum \rho v A c_p \left(T_{out} - T_{in}\right)$$

where q is the rejected heat via ventilation air, ρ is the air density, v is cell velocity, A is cell surface area, c_p is specific heat of air, T_{out} is cell temperature, and T_{in} is ventilation air inlet temperature. The results, summarized in Figure 2, show a similar trend for all inlet configurations and suggest a proportional increase in the convected heat with the increase in ventilation airflow rate. On the other hand, the area averaged outlet temperatures at the outlet pipe exit seem to exhibit a nonlinear behavior and saturate at an airflow ratio of 2.0, as shown in Figure 3. With various inlet airflow ratios and different air inlet locations, the 1-D simulation results of both surface- and air-temperatures at some components are shown in Figure 4.

Conclusions

An assessment of combined 1-D and 3-D simulation methods was initiated for predicting ventilation airflow and underhood temperatures in an enclosed engine compartment of an off-road machine. A CFD model was built to determine the 3-D flow field and the rate of heat transfer between engine and ventilation air inside the enclosure. Consistent with the experimental observations, the CFD results indicate a well-mixed flow inside the enclosure with no significant difference in component temperatures for different ventilation inlet locations.

The calculations performed to date indicate that the CFD model generally under-predicts the pressure drop based on the current geometric definition of the test rig. This is perhaps, in part, due to omitted details in the model (various hoses and instrument wires). Although the agreement between the calculations and experiments on system restriction is good for front inlet configuration, it is possible that the CFD model over-predicts the pressure drop in that case because of the ignored effect of high-rpm rotation of the crank-shaft pulley right in front of inlet window.

A 1-D model was used mainly to determine the temperature distributions in engine structure components, air loop, oil loop, and even coolant loop. The predictions show the consistency in temperature distribution with variation of the airflow ratio for all air inlet locations.

By using the data from Caterpillar experiments, the calculated temperatures resulting from the 1-D network flow and the CFD models will be compared with the measured temperatures in the next phase of the project. On the basis of the preliminary assessments (by comparing the calculated results with the only known experimental data for the front-inlet case and airflow ratio of 1.5), the combined model also under-predicts the ventilation air temperatures. After the detailed assessment of the results and comparisons with experiments, the model discretization issues and other uncertainties will be addressed to improve the accuracy of predictions.

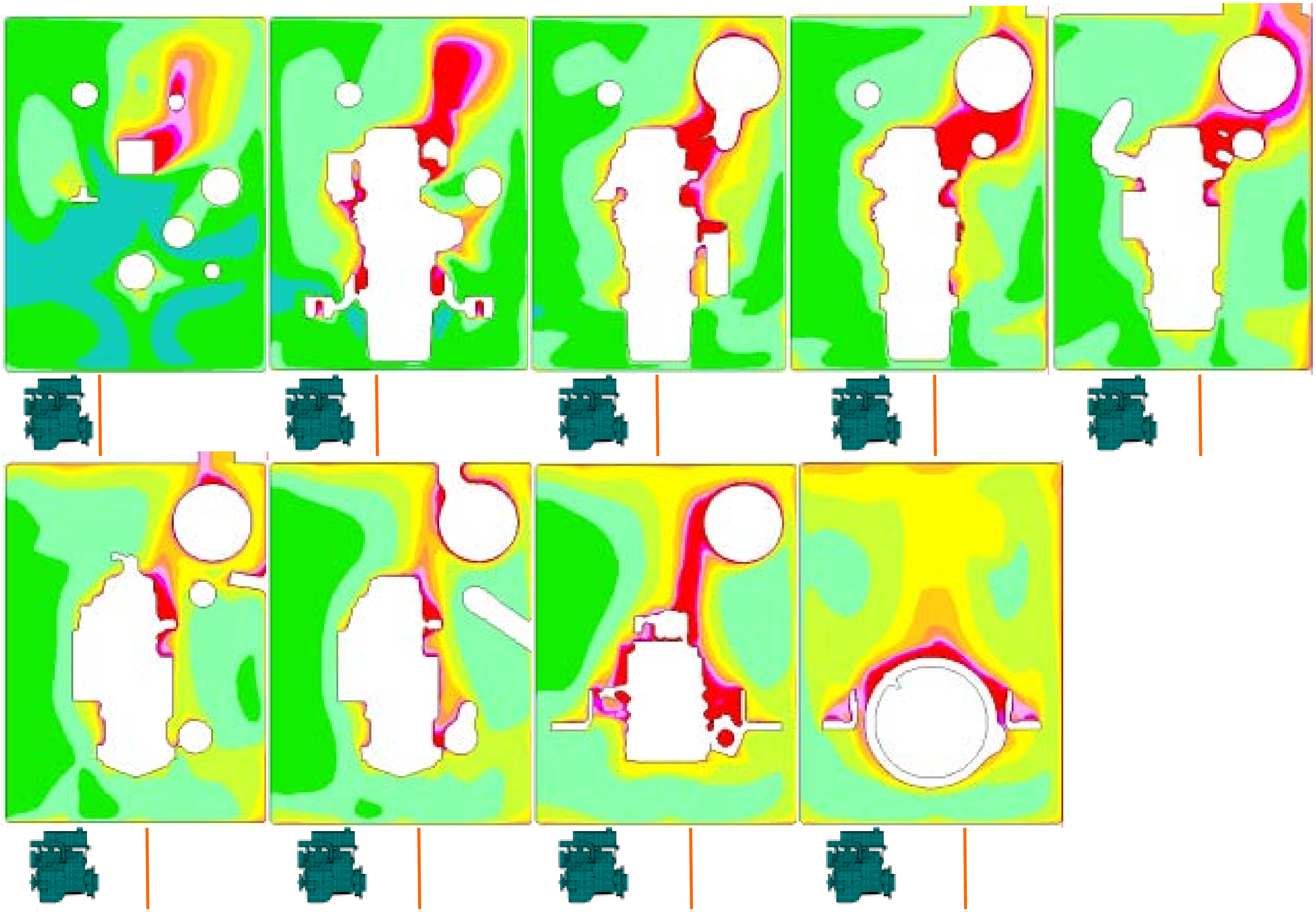

Figure 1. Temperature contours in vertical planes with equal increments from front to back. The results for front inlet configuration with airflow ratio of 1.5.

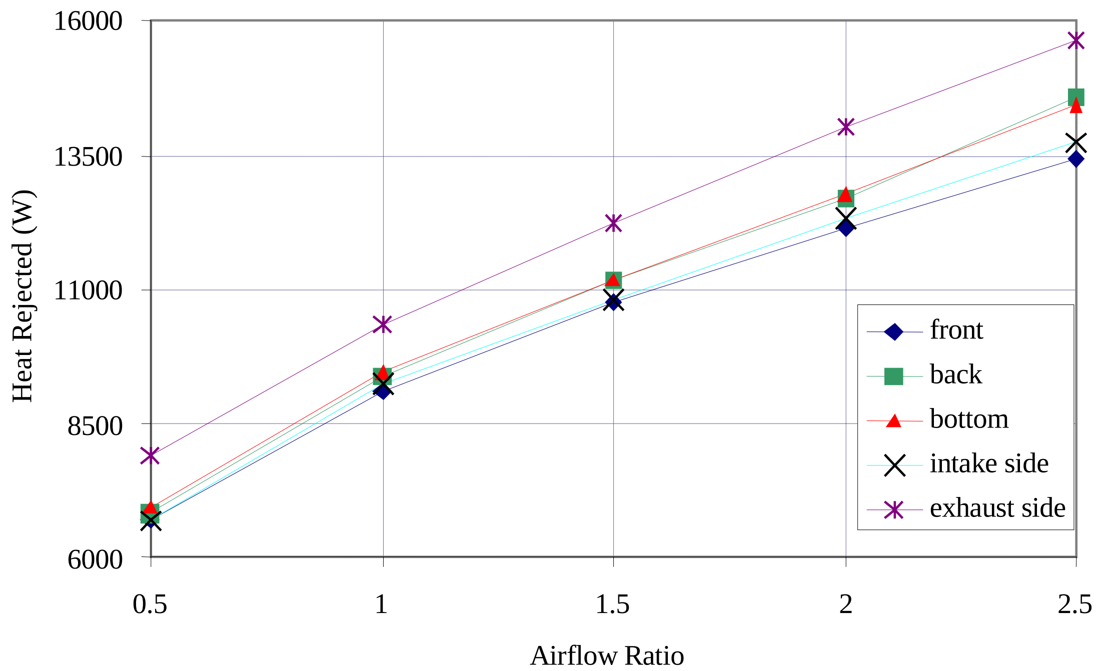

Figure 2. Heat rejected via the ventilation air through the engine enclosure as a function of airflow ratio.

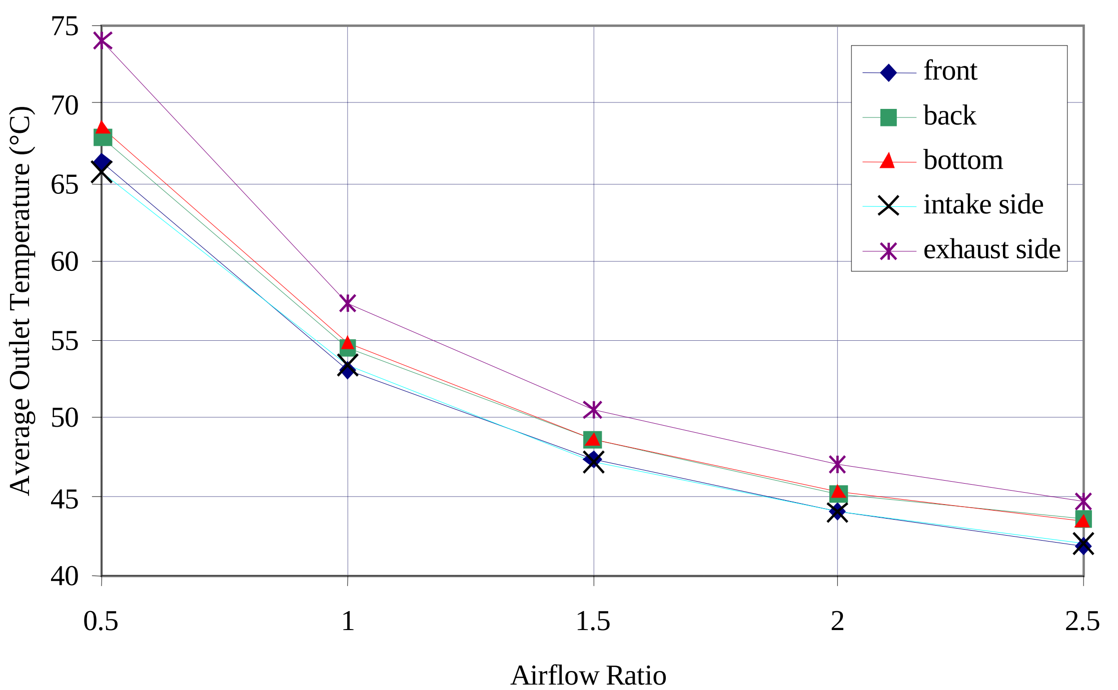

Figure 3. Area averaged outlet temperatures at the outlet pipe exit as a function of airflow rate.

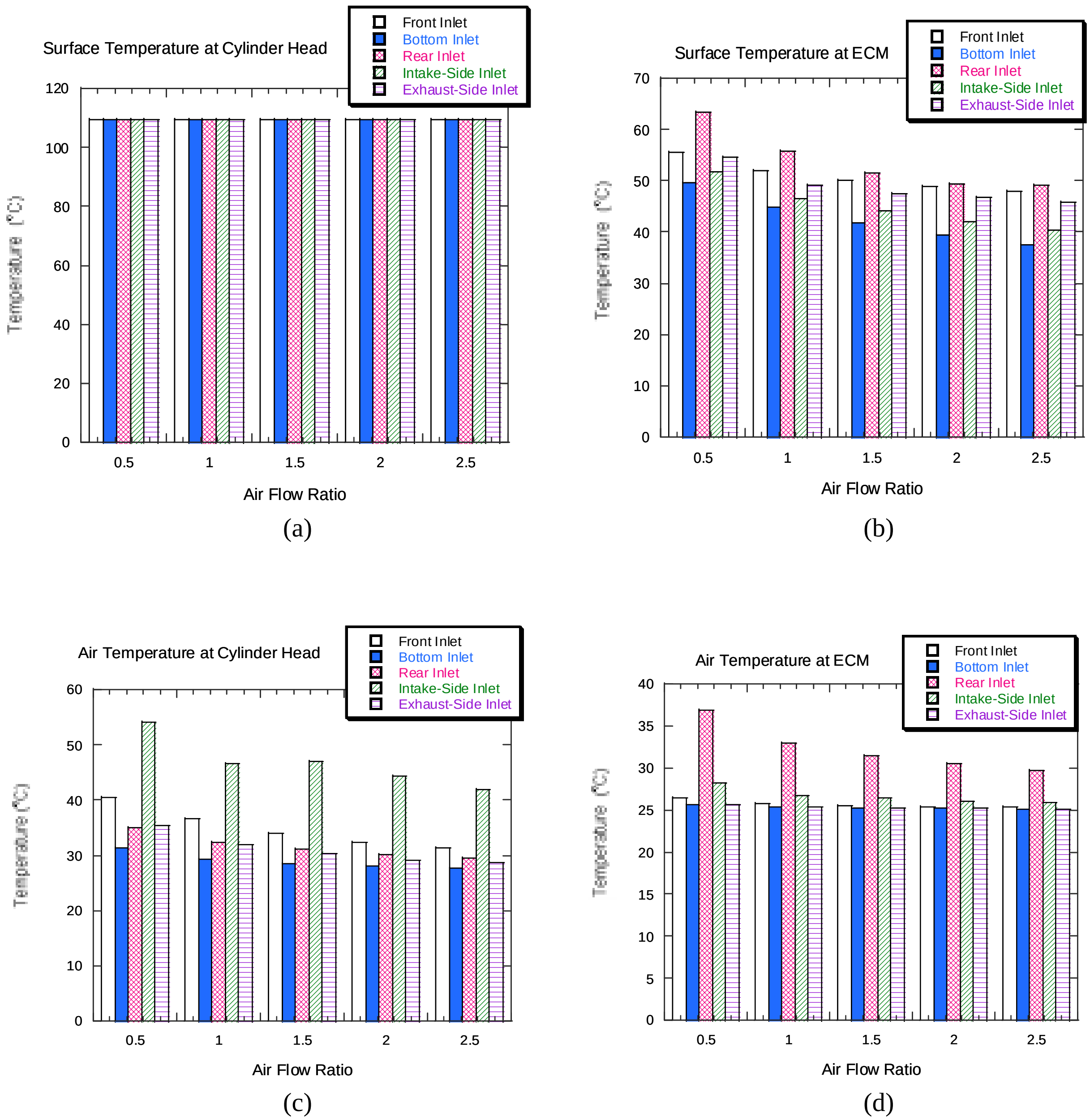

Figure 4. 1-D network predictions: surface temperatures at (a) cylinder head and (b) ECM and air temperatures at (c) cylinder head and (d) ECM for various airflow ratios under different air inlet locations.

III. Friction and Wear

A. Boundary Lubrication Mechanisms

Principal Investigators: O.O. Ajayi, J.G. Hershberger, and G.R. Fenske
Argonne National Laboratory
9700 South Cass Avenue, Argonne, IL 60439
(630) 252-9021, fax: (630) 252-4798, e-mail: ajayi@anl.gov

Technology Development Manager: Sid Diamond
(202) 586-8032, e-mail: sid.diamond@ee.doe.gov
Technical Program Manager: Jules Routbort
(630) 252-5065, e-mail: routbort@anl.gov

Contractor: Argonne National Laboratory, Argonne, Illinois
Prime Contract No.: W-31-109-Eng-38.

Objectives

Develop a better understanding of the mechanisms and reactions that occur on component surfaces under boundary lubrication regimes. Specific objectives are to:

- Determine the basic mechanisms of catastrophic failure in lubricated surfaces in terms of materials behavior.
- Determine the basic mechanisms of chemical boundary lubrication.
- Establish and validate performance and failure prediction methodologies for lubricated components.
- Integrate coating and lubrication technologies for maximum enhancement of lubricated-surface performance.

Approach

- Characterize the dynamic changes in the near-surface material during scuffing. Formulate a material-behavior-based scuffing mechanism.
- Determine the chemical kinetics of boundary film formation and loss rate by in situ X-ray characterization of tribological interfaces at the Advanced Photon Source (APS) at Argonne National Laboratory (ANL).
- Characterize the physical, mechanical, and tribological properties of tribo-chemical films, including the failure mechanisms.
- Integrate the performance and failure mechanisms of all the structural elements of a lubricated interface to formulate performance and/or failure prediction methodology; this will include incorporation of surface coatings.

Accomplishments

- Conducted extensive characterization of microstructural changes during scuffing of 4340 steel, by using scanning electron microscopy (SEM) and X-ray analysis.
- Developed a model of scuffing initiation on the basis of an adiabatic shear instability mechanism.
- Formulated a preliminary model of scuffing propagation on the basis of a balance between heat generation and heat dissipation rates.
- Characterized the mechanical properties and scuffing resistance of a graded nanocrystalline surface layer produced by the scuffing process.

- Using X-ray fluorescence, reflectivity, and diffraction at the APS, demonstrated the ability to characterize tribo-chemical films generated from model oil additives.

Future Direction

- Integrate scuffing initiation and propagation models for a comprehensive scuffing prediction method.
- Experimentally validate the comprehensive scuffing theory for various engineering materials, including ceramics.
- Design and construct a tribo-tester for in situ characterization of tribochemical surface film at the APS.
- By using various techniques, continue to characterize tribochemical films formed by model lubricant additives.
- Characterize the physical, mechanical, and failure mechanisms of tribochemical films with nano-contact probe devices.
- Evaluate the impact of various surface technologies, such as coating and laser texturing, on boundary lubrication mechanisms.

Introduction

Many critical components in diesel engines and transportation vehicle subsystems are oil lubricated. Satisfactory performance of these components and systems is achieved through a combination of materials, surface finish, and lubricant oil formulation technologies. To that end, an Edisonian trial-and-error approach is often followed. Indeed, experience is likely the sole basis for new design and solutions to failure problems in lubricated components. With more severe operating conditions expected for component surfaces in advanced engines and vehicles, the trial-and-error approach to effective lubrication is inadequate and certainly inefficient. Departure from this approach will require a better understanding of the fundamentals of both boundary lubrication and surface failure mechanisms.

A major area of focus for the U.S. Department of Energy in the development of diesel engine technology is emission reduction. Some essential oil lubricants and diesel-fuel additives, such as sulfur, phosphorus, and chlorine, are known to poison the catalysts in emission-reducing after-treatment devices. Although reduction or elimination of these additives will make emission after-treatment devices more effective and durable, it will also render the surfaces of many lubricated components vulnerable to catastrophic failure. Many of the effective methods to reduce diesel engine emissions may also render critical-component surfaces vulnerable to catastrophic failure, thereby compromising their reliability.

Increases in vehicle efficiency will require an increase in power density, resulting in increased severity of contact between many components in the engine and powertrain systems. This, again, will compromise the reliability of various critical components, unless they are effectively lubricated. The efficacy of oil additives in protecting component surfaces depends on the nature and extent of the chemical interactions between the surface and the oil additives.

In addition to reliability issues, the durability of lubricated components also depends on the effectiveness of oil lubrication mechanisms. Components will eventually fail or wear out over time. Failure mechanisms that limit the durability of lubricated surfaces are wear, in its various forms, and contact fatigue. Wear is the gradual removal of material from contacting surfaces, and it can occur by various mechanisms, such as abrasion, adhesion, and corrosion. Also, the repeated contact stress cycles to which component contact surfaces are subjected can initiate and propagate fatigue cracks and, ultimately lead to the loss of a chunk of material from the surface. This damage mode is often referred to as “pitting.” Wear and contact fatigue are both closely related to boundary lubrication mechanisms. Antiwear additives in lubricants are designed to form a wear-resistant protective layer on the surface. The role of lubricant additives on the contact fatigue failure mode is not fully understood, although it is clear that the lubricant chemistry significantly affects contact fatigue. Again, lack of an adequate, comprehensive understanding of basic mechanisms of boundary lubrication is a major obstacle to a reasonable prediction of component surface durability.

The desire to extend the drain interval for diesel engine oil, with an ultimate goal of a fill-for-life system, is increasing. Successful implementation of the fill-for-life concept will require optimization of surface lubrication through the integration of materials, lubricant, and, perhaps, coating technologies. Such an effort will require an adequate fundamental understanding of surface material behavior, chemical interactions between the material surface and the lubricant, and the behavior of material and lubricant over time.

Some common threads run through all of the challenges and problems in the area of surface lubrication of engine components and systems briefly described above. The two key ones are (1) lack of adequate basic and quantitative understanding of the failure mechanisms of component surfaces and (2) lack of understanding of basic mechanisms of boundary lubrication (i.e., how lubricant chemistry and additives interact with rubbing surfaces and how this affects performance). To progress beyond the empirical trial-and-error approach for predicting lubricated component performance, a better understanding is required of the basic mechanisms regarding the events that occur on lubricated surfaces. Consequently, the primary objective of the present project is to determine the fundamental mechanisms of boundary lubrication and failure processes of lubricated surfaces.

The technical approach taken in this study differs from the usual one of posttest characterization of lubricated surfaces, and, rather, will involve developing and applying in situ characterization techniques for lubricated interfaces that will use the X-ray beam at the APS located at ANL. Using a combination of X-ray fluorescence, reflectivity, and diffraction techniques, we will study, in real time, the interactions between oil lubricants and their additives and the surfaces they lubricate. Such study will provide the basic mechanisms of boundary lubrication. In addition to surface chemical changes, materials aspects of various tribological failure mechanisms will be studied.

<u>Results and Discussion</u>

Efforts during the past year (FY 04) were devoted to the development of a scuffing propagation model, study of near-surface microstructural changes and their implication for enhancing scuffing resistance, and refinement of the X-ray characterization of tribochemical boundary films.

Scuffing Propagation

Scuffing, which is a sudden catastrophic failure of sliding surfaces, is perhaps the least understood of the various failure mechanisms in lubricated surfaces. Numerous phenomenological observations about scuffing have been made over the years by various investigators. It is known that sometimes scuffing will initiate but not propagate. In some cases, scuffing occurs so fast that it is difficult to identify distinctive stages in the process. Nonetheless, on the basis of various observations on scuffing, a useful approach to study the basic mechanism is to separate the process into the initiation and propagation stages. This approach can adequately account for the many cases of initiation without propagation.

In the previous year, we developed a model for initiation of scuffing based on adiabatic plastic shear instability, which occurs when the rate of thermal softening exceeds the rate of work hardening. The large amount of heat generated by the severe plastic deformation of shear instability is the driving force for scuffing propagation. Thermal softening of the materials in the vicinity of the initiation sites could be large enough to propagate the scuffing front. Like the scuffing initiation process, which involves a competition between work hardening and thermal softening, scuffing propagation involves a competition between heat dissipation and heat generation. We propose that scuffing will propagate when the rate of dissipation of heat produced by adiabatic shear instability is less than the rate of heat generation by the same process. If the rate of heat dissipation exceeds the rate of heat generation, the scuffing process can be “quenched,” in which case only microscuffing events are observed. Scuffing propagation can thus be controlled either by increasing the rate of heat dissipation or by reducing the rate of heat generation.

On the basis of balancing the heat dissipation and heat generation from shear instability, the velocity (V) of propagation of the scuffing front can be described by the following simplified equation in 1-D:

$$V = \frac{d\delta}{dt} = \frac{\frac{\beta\tau\dot{\gamma}}{\rho C} - \frac{\lambda}{\rho C}\left(\frac{\partial^2 T}{\partial X^2}_{\delta} - \frac{\partial^2 T}{\partial X^2}\right)}{\frac{\partial T}{\partial X}_{\delta}} \quad (1)$$

where:

- β = fraction of plastic work converted to heat (0.9),
- τ = shear stress,
- λ = thermal conductivity,
- γ = strain rate,
- ρ = density, and
- C = heat capacity.

In Equation 1, the first term in the numerator describes the rate of heat generation, while the second term describes the rate of heat conduction across the boundary of the scuffing propagation front. When the propagation front velocity V is positive, scuffing propagates. When the velocity is zero or negative, scuffing does not propagate.

In conjunction with the initiation model, it should be possible to predict the occurrence of scuffing failure from pertinent material properties and operating conditions. Some of our future efforts will be devoted to the integration of the initiation and propagation models for scuffing.

Graded Nanophase Surface Layer

Microstructural characterization of the near-surface layer of a scuffed steel surface showed the formation of a 20-μm-thick graded nanophase layer. The grain size in the top layer is about 20–30 nm. This layer is produced by a severe plastic deformation process associated with the scuffing failure. It is well known that one method of grain refinement to the nanometer size range in metallic material is by severe plastic deformation.

The mechanical properties of the nanocrystalline surface layer produced on a hardened 4340 steel surface were characterized by the nano-indentation technique. As shown in Figure 1, the hardness of the topmost layer with the finest grain size is substantially higher than that of the original material (13 GPa compared to 3.5 GPa). Similarly, the elastic modulus of the top layer is increased from the original 235 GPa to 294 GPa. Indeed, the hardness and elastic modulus of the nanocrystalline top layer produced during scuffing are comparable to the values for structural ceramic materials. This observation represents a new approach to surface engineering.

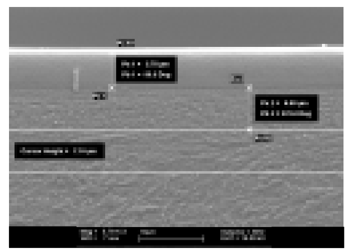

	H (Gpa	Hv	RWC)	E (GPa)
First Layer	13.1	1336	85?	294.7
Second layer	9.0	918	67	232.2
Third layer	3.4	347	35	216.3
Bulk	3.5	367	36	235.8

Figure 1. SEM micrograph of graded nanocrystalline surface layer on a steel surface after scuffing. Mechanical properties (hardness and modulus) are shown in table next to the micrograph.

In view of the changes to the microstructure and surface mechanical properties resulting from scuffing, we evaluated the effect of the new or modified surface layer on subsequent scuffing failure. Figure 2a shows the statistical distribution of scuffing occurrence in polished, hardened 440C steel, and Figure 2b shows the result for the same material that was previously scuffed. The modified layer showed scuffing resistance equal to or better than that of the unmodified surface. More significantly, the tendency toward premature failure was significantly reduced in the modified layer. The better predictability of scuffing in the modified layer will certainly reduce the challenge of designing tribological sliding systems against premature scuffing failure.

X-Ray Characterization of Tribo-Chemical Films

Characterization of tribochemical films formed by lubricant additives with the various X-ray techniques available at the APS is ongoing. Films formed by

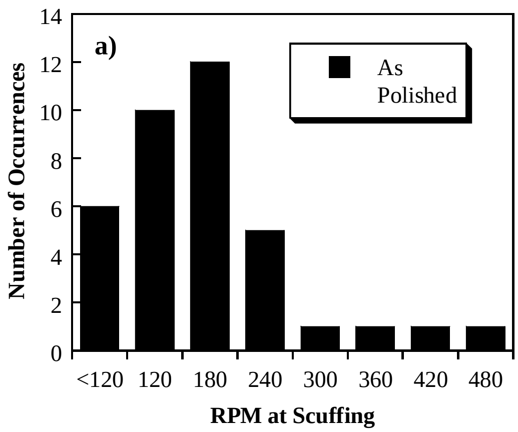

Figure 2a. Histogram of scuffing occurrence at various speeds for a polished steel surface.

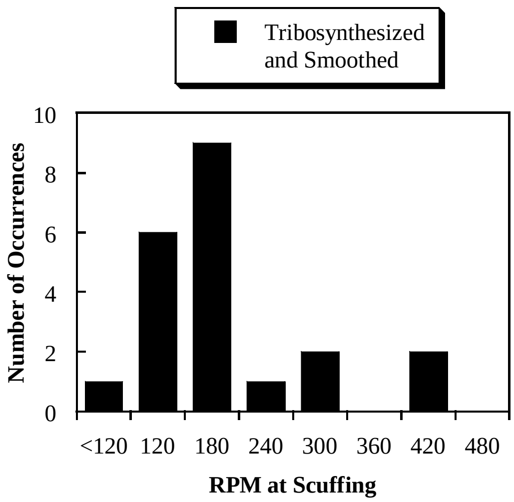

Figure 2b. Histogram of scuffing occurrence at various speeds for a steel surface with graded nanocrystalline layer from prior scuffing.

two methods with zinc diathiophosphate (ZDDP) oil additive were analyzed with glancing-incident-angle X-ray fluorescence, diffraction, and reflectivity. The goal is to assess the ability of these techniques to detect small differences in tribochemical films formed by the same additives.

Figure 3 shows the variation of Zn content in films formed by either tribo contact (mechanical) or thermally for different concentrations of ZDDP additive in polyalphaolefin (PAO) lubricant. The results clearly show that the compositions of the mechanical films and the thermal films are different. This observation is very significant, as experience has shown that small differences between

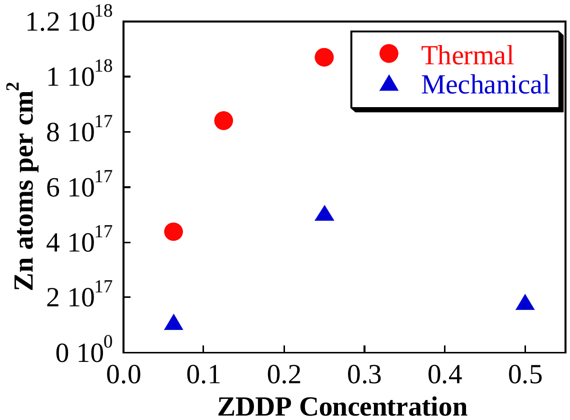

Figure 3. Areal density of Zn atoms in tribochemical films formed thermally and mechanically as a function of ZDDP additive concentration.

tribochemical-films composition and structure can translate into significant differences in performance. The ability to detect small differences in tribo-chemical films is critical to a better understanding of their performance and optimization.

Conclusions

During the past year, a preliminary model for scuffing propagation was developed. This is the next step in the separation of the scuffing process into initiation and propagation stages. While the scuffing initiation is by adiabatic shear instability, scuffing propagation is governed by the balance between heat dissipation and heat generation as a result of severe plastic deformation of shear instability. When the rate of heat dissipation exceeds the rate of heat generation, scuffing does not propagate.

Mechanical properties of the graded nanocrystalline surface layer from scuffing were characterized. Both the hardness and the elastic modulus of the new surface layer were significantly increased to values comparable to those of structural ceramics. This new layer was also shown to reduce the tendency toward premature scuffing failure. It was also demonstrated that the suite of X-ray characterization techniques available at APS can detect differences in the tribochemical surface films formed from the same oil additive by two methods.

Publications

1. J. Hershberger, O.O. Ajayi, and G.R. Fenske, "Improvement in Scuffing Resistance due to Tribosynthesis of a Modified Surface Layer," Thin Solid Films (in press).
2. O.O. Ajayi, J. Hershberger, J. Zhang, H. Yoon, and G.R. Fenske, "Microstructural Evolution during Scuffing of 4340 Steel – Implication for Scuffing Mechanism," Tribology International (in press).
3. J. Hershberger, O.O. Ajayi, and G.R. Fenske, "Composition of ZDDP Films Formed Thermally and Mechanically," Tribology International (in press).

B. Parasitic Engine Loss Models

Principal Investigator: George Fenske, co-workers: Ali Erdemir, Layo Ajayi, and Andriy Kovalchenko
Argonne National Laboratory, Energy Technology Division
Argonne, IL 60439
(630) 252-5190, fax: (630) 252-4798, e-mail: gfenske@anl.gov

Bill Brogdon, Troy Torbeck, Isaac Fox, and Jim Kezerle
Ricardo, Inc.
7850 Grant Street
Burr Ridge, IL 60527-5852
(630) 789-0003, fax: (630) 789-0127

Technology Development Manager: Sid Diamond
(202) 586-8032, e-mail: sid.diamond@ee.doe.gov
Technical Program Manager: Jules Routbort
(630) 252-5065, e-mail: routbort@anl.gov

Contractor: Argonne National Laboratory, Argonne, Illinois
Contract No.: W-31-109-ENG-38

Objectives

- Develop and integrate a set of software packages to predict the impact of advanced low-fiction coating technologies on parasitic energy losses from diesel engine components.
- Develop a suite of computer codes to predict the wear and durability of engine components when exposed to low-viscosity lubricants.

Approach

- Predict fuel economy improvements over a wide range of oil viscosity.
- Predict change in wear loads due to reduced oil viscosity.
- Develop superhard and low-friction coatings that can reduce friction and wear in low-viscosity oils.

Accomplishments

- Modeled the impact of low-friction coatings and low-viscosity lubricants on fuel savings (up to 4%), and predicted the impact of low-viscosity lubricants on the wear/durability of critical engine components.
- Developed experimental protocols to evaluate the friction and wear performance of advanced engine materials, coatings, and surface treatments under prototypical piston/ring environments.

Future Direction

- Apply superhard and low-friction coatings on actual engine components and demonstrate their usefulness in low-viscosity oils.
- Optimize coating composition, surface finish, thickness, and adhesion to achieve maximum fuel savings.

Introduction

Friction, wear, and lubrication impact energy efficiency, durability, and environmental soundness of all kinds of transportation systems, including diesel engines. Total frictional losses in a typical diesel engine may alone account for more than 10% of the total fuel energy (depending on the engine size, driving condition, etc.). The amount of emissions produced by these engines is related to the fuel economy of that engine. In general, the higher the fuel economy, the lower the emissions. Higher fuel economy and lower emission in future diesel engines may be achieved by the development and widespread use of novel materials, lubricants, and coatings. For example, with increased use of lower-viscosity oils (that also contain the lowest amounts of sulfur and phosphorus-bearing additives), the fuel economy and environmental soundness of future engine systems can be dramatically improved. Furthermore, with the development and increased use of smart surface-engineering and coating technologies, even higher fuel economy and better environmental soundness will be feasible.

The main goal of this project is to develop a suite of software packages that can predict the impact of smart surface engineering and coating technologies (e.g., laser dimpling, near-frictionless carbon, and superhard nitride coatings) on parasitic energy losses from diesel engine components. The project also aims to validate the predictions by using experimental friction and wear studies at Argonne National Laboratory. Such information will help identify critical engine components that can benefit the most from the use of novel surface technologies, especially when low-viscosity engine oils are used to maximize the fuel economy of these engines by reducing churning and/or hydrodynamic losses. A longer-term objective is to develop a suite of computer codes capable of predicting the lifetime/durability of critical components exposed to low-viscosity lubricants.

In FY 2004, Argonne and Ricardo, Inc., worked together to identify engine components that can benefit from low-friction coatings and/or surface treatments. The specific components considered included rings, piston skirt, piston pin bearings, crankshaft main and connecting rod bearings, and cam bearings. Using computer codes, Ricardo quantified the impact of low-viscosity engine oils on fuel economy. Ricardo also identified conditions that can result in direct metal-to-metal contacts, which, in turn, can accelerate engine wear and asperity friction. Efforts were also initiated to identify approaches to validate the predictions under fired conditions.

Argonne also worked on the development and testing of a series of low-friction coatings under a wide range of sliding conditions by using low- and high-viscosity engine oils. These coatings (such as near-frictionless carbon), as well as laser-textured surfaces, were subjected to extensive tests using bench-top friction test rigs. The test conditions (i.e., speeds, loads, and temperatures) were selected to create conditions in which direct metal-to-metal contacts will prevail, as well as situations in which mixed or hydrodynamic regimes will dominate. Using the ranges of frictional data generated by Argonne, Ricardo estimated the extent of potential energy savings in diesel engines and identified those components that can benefit the most from such low-friction coatings and/or surface treatments. Argonne developed a test rig to simulate engine conditions for piston rings sliding against cylinder liners — one of the major sources of parasitic energy losses identified in Ricardo's studies. Wear data generated by Argonne can be used to develop models and computer codes that predict the lifetime/durability of diesel engine components.

Results

In a series of computer simulations, Ricardo analyzed the effects of lubricant viscosity on engine wear loads, engine friction, and fuel consumption. With drastic reductions in oil viscosity, it was found that in addition to other engine components, crank-shaft bearings would become vulnerable to high friction and wear losses. The situation with crank shaft bearings was analyzed by using ORBIT software, which takes into account non-circular bearing/journal geometry, distortions, cavitation, and boundary-lubricated sliding conditions, where asperity contact and elastohydrodynamic lubrication may dominate. In addition to the ORBIT software, PISDYN, RINGPACK, and VALDYN simulations were carried out under both baseline and reduced viscosity conditions. The objective was to determine the impact of oil viscosity on overall engine friction and wear.

Engine Friction Studies

The Ricardo suite of engine component simulation codes was run at varying levels of lubricant viscosities (and four levels of boundary friction – baseline, and 30, 60, and 90% reductions) at eight load and speed conditions. Hydrodynamic and asperity friction predictions were tabulated for each case. The predicted optimum lubricant grade for the baseline piston was SAE 20. With a 30% reduction in asperity friction, the allowed reduction in lubricant viscosity did not result in a large reduction in frictional mean effective pressure (FMEP). A 60% reduction in asperity friction allowed a larger reduction in lubricant viscosity. With a 90% reduction in asperity friction, the predicted optimum viscosity was lower than SAE 5, and the reduction in hydrodynamic friction was significant. These findings are summarized in Figure 1.

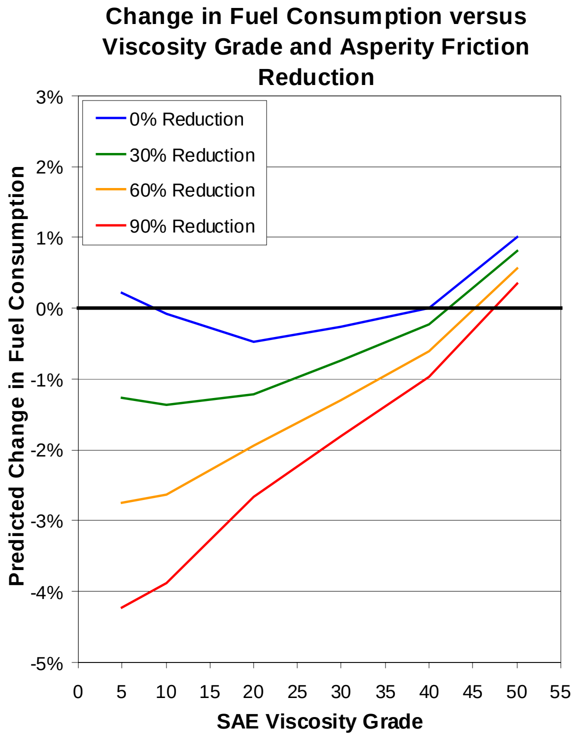

Figure 1. PISDYN predictions of FMEP vs. SAE lubricant viscosity grades and asperity friction reduction.

According to these predictions, for the piston skirt alone, with a 90% reduction in asperity friction, reducing lubricant viscosity reduced parasitic piston losses by nearly 50%.

Piston Wear Studies

As lubricant viscosity was reduced, wear loads on the piston skirt and cylinder liner were increased in both magnitude and extent, thus increasing the vulnerability of these components to rapid wear. As shown in Figure 2, the total average wear load per cycle is above four times higher for SAE 5 than SAE 40 oil. These findings suggest that, to allow the use of SAE 5 oil, a surface treatment is needed to provide approximately four times the wear resistance of the baseline engine material.

Coating Studies

At Argonne, systematic studies are being performed to develop low-friction and high-wear resistant coatings for use in critical engine parts and components. One of the coatings studied extensively was near-frictionless carbon (NFC), which can provide friction coefficients of 0.001–0.01 under dry sliding conditions, especially

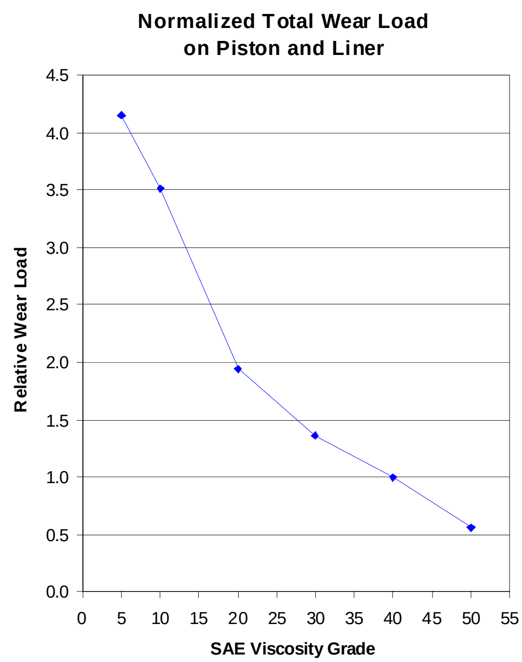

Figure 2. The effect of SAE lubricant viscosity grade on relative wear load index of piston and liner in an engine.

in inert gas environments. Another coating (superhard nanocomposite – SHNC) under development is extremely hard (67 GPa hardness) and has a surface chemistry that enhances its performance in the presence of commercial oil additives. A third approach at Argonne (in conjunction with Technion University) involves the use of laser-textured surfaces to modify the Stribeck response of the surface — essentially lowering frictional losses under boundary lubrication regimes. Under boundary lubrication conditions, NFC and SHNC coatings have been shown to reduce friction by up to 90%. Laser-surface textured-treated surfaces to reduce friction by similar amounts.

Recent studies at Argonne have been initiated to investigate the impact of coatings on wear. In these studies, a laboratory test rig is used to impose unidirectional or reciprocating motion on test coupons to investigate the wear (and friction) properties. Figure 3 shows a schematic (and photograph) of the high-frequency reciprocating rig. In the tests presented below, the ball was 52100 steel (either uncoated or uncoated), and the plate was hardened H-13 steel (uncoated or coated). The 20-N load produced an initial Hertzian contact pressure of 1.05 GPa. The oil was an unformulated basestock poly-alpha olefin (PAO), a formulated PAO, or an unformulated paraffin oil.

Tests were performed under a wide range of conditions (speed, load, lubricant, and coating). For the NFC coatings, three grades of coatings were used: NFC2, NFC6, and NFC7, which show distinct differences in terms of friction, hardness,

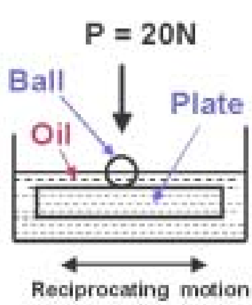

Figure 3. Schematic and photograph of a reciprocating test rig used to study friction and wear.

and hence wear. The wear rates for uncoated 52100 steel balls sliding against coated (and uncoated) H-13 steel plates are shown in Figure 4. The wear of the NFC-coated plates during the 1-h test was below the limit of detection (approximately 50 µm), except for the NFC6 coating exposed to the basestock PAO lubricant. Nevertheless, the results demonstrate that the use of a low-friction, wear-resistant coating can reduce wear rates by several orders of magnitude — sufficient for the factor of 4 increase in wear load severity for the low-viscosity lubricant.

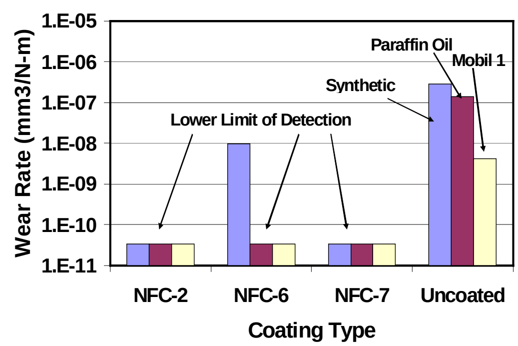

Figure 4. Wear rate of NFC-coated (and uncoated) H-13 steel plates reciprocating against 52100 steel balls.

Even larger improvements in wear resistance have been observed (up to five orders of magnitude). The extent of improvement depends on the coating and tribological environment. Preliminary results on the SHNC coatings are very promising — the high hardness, coupled with the surface chemistry between the SHNC and the oil additives, suggests an extremely high level of wear resistance.

Discussion

Preliminary results from computer simulations showed that hydrodynamic friction decreased with reductions in lubricant viscosity, while wear loads and asperity friction increased. This trend is mainly due to the reduction of churning losses associated with the shear rheology of high-viscosity oils. However, the decline in hydrodynamic friction is eventually offset by the increase in asperity friction. For each level of asperity friction reduction, there is a lubricant viscosity that provides the minimum overall fuel consumption (Figure 1). For SAE 5 grade oil, simulations predict an overall fuel savings of greater than 4%, if a surface treatment is used to reduce boundary friction by 90%. Contact severity and wear loads are substantially increased in such low-viscosity environments, and they would need to be mitigated to avoid increased wear by using superhard coatings.

Work at Argonne has resulted in the development of NFC films as well as SHNC coatings, both of which provide not only very low friction but also much needed wear resistance in low-viscosity oils. With further development and optimization, these coatings may, indeed, prevent wear during sliding under conditions where low-viscosity oils are used. They can also provide low friction to help further increase fuel efficiency. Laser dimpling of selected engine components offers additional benefits in terms of reducing friction and thus increasing the fuel economy of engines. Some of these surface treatments and/or coatings will soon be applied on portions or segments of real piston rings and cylinder liners to further substantiate their effectiveness under conditions that closely simulate the actual engines. In FY 2004, work at Argonne has focused on developing a reciprocating test rig that uses segments of heavy-duty piston rings and cylinder liners to measure friction and wear.

Conclusions

Computer simulation studies to date have confirmed that using low-viscosity engine oils will increase the fuel efficiency of future diesel engines. However, wear load and asperity friction will increase substantially. The use of a low-friction, superhard coating on critical engine components should mitigate asperity friction and reduce wear, thereby enabling the use of low-viscosity oils to increase the fuel efficiency.

Efforts are in progress to experimentally validate the computer simulations. These efforts include (1) lab-scale tests to provide experimental friction and wear data on NFC, SHNC, and textured surfaces and (2) single-cylinder fired engine tests designed to directly measure friction forces between the liner and piston skirt and rings.

The lab tests will use segments of production rings, piston skirts, and liners, the surfaces of which have been modified with NFC and SHNC coatings and/or laser texturing. The test configuration will replicate the reciprocating motion of the rings and pistons. Information will be recorded continuously on the friction coefficient, and the wear data will be determined from post-test characterization of the components. Figure 5 shows photos of a ring and liner mounted in test fixtures.

The Argonne rig will provide continuous friction measurements during the reciprocating tests. Post-test optical and interferometry will provide wear data. The rig shown in Figure 5 will be used to provide wear and friction data under boundary and mixed lubrication regimes for use by Ricardo in its simulation studies. Tests will be performed with uncoated, coated, and textured surfaces, as well as with formulated and unformulated oils.

Ricardo examined a number of potential fired-engine techniques to validate the simulation studies. These included (1) direct fuel consumption measurements in mass-production engines, (2) friction-force measurements in an instrumented mass-production engine, and (3) friction measurements in an instrumented single-cylinder engine. The third approach was selected, and efforts are in progress to install a fixed-sleeve adaptor on a Ricardo single-cylinder Hydra engine. Load cells mounted on the fixed sleeve will enable continuous, direct measurement of the friction forces between the ring/piston assembly and the cylinder liner during fired operation. Tests will be performed under a range of operating conditions (load and speed) to compare the piston assembly friction losses of modified pistons and rings against a baseline assembly.

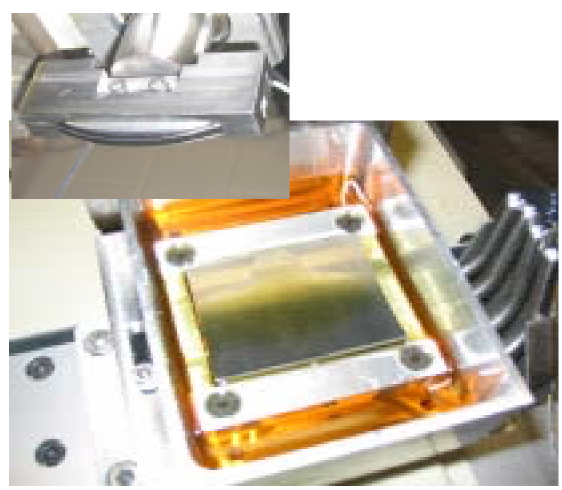

Figure 5. Photographs of ring and liner segments mounted in a high-frequency reciprocating rig.

Publications

1. Fox, I., "Numerical Evaluation of the Potential for Fuel Economy Improvement due to Boundary Friction Reduction within Heavy-Duty Diesel Engines," ECI International Conf. on Boundary Layer Lubrication, Copper Mountain, CO, Aug. 2003.
2. Fenske, G., Erdemir, A., and Ajayi, O., "Low Friction Coatings and Lubricant SYSTEMS," presentation at the 95th Annual AOCS Meeting & Expo, Cincinnati, OH, May 2004.

C. Superhard Nanocrystalline Coatings for Wear and Friction Reduction

Principal Investigators: A. Erdemir, L. Ajayi, O. Eryilmaz, K. Kazmanli, and I. Etsion
Argonne National Laboratory, Energy Technology Division
Argonne, IL 60439
(630) 252-6571, fax: (630) 252-4798, e-mail: erdemir@anl.gov

Technology Development Area Specialist: Sidney Diamond
(202) 586-8032, fax: (202) 586-1600, e-mail: sid.diamond@ee.doe.gov
Field Technical Manager: Jules Routbort
(630) 252 5065, fax: (630) 252 4289, e-mail: routbort@anl.gov

Contractor: Argonne National Laboratory
Contract No.: W-31-109-ENG-38

Objectives:

- Design, develop, and optimize low-friction, super-hard, nano-composite coatings for use in diesel engines and drivetrain components of heavy vehicles.
- Demonstrate scalability and large-scale production of such coatings by using a large physical vapor deposition system.
- Characterize structural, mechanical, and tribological properties of these nano-composite coatings.
- Explore integration of these coatings with laser-textured surfaces.
- Demonstrate application and superior performance of these coatings in diesel engine and drivetrain components.

Approach:

- Prepare test samples for the deposition of superhard and low-friction coatings.
- Identify and optimize deposition parameters that are critically important for the synthesis of nano-composite and super-hard coatings on these samples.
- Assess structural, mechanical, and tribological properties of coatings.
- Analyze test results and examine sliding surfaces.
- Integrate optimized superhard coating technology with laser surface texturing.
- Report results on friction and wear properties.

Accomplishments:

- Successfully demonstrated large-scale production of superhard coatings in a commercial system.
- Optimized deposition conditions (i.e., bias voltage, substrate temperature, deposition pressure, etc.) and developed a deposition protocol that can provide consistent reproducibility and reliability on coated samples.
- Achieved friction coefficients of less than 0.03 under boundary lubricated sliding conditions on highly optimized superhard coatings.
- Virtually eliminated wear of coated surfaces.
- Successfully produced superhard coatings on a series of laser-dimpled surfaces and achieved very uniform coverage and strong bonding to steel substrate.

- Demonstrated superior wear performance for sliding surfaces that were laser textured and then superhard coated.
- Produced superhard coatings on cut segments of rings and liners in order to assess their friction and wear behavior under boundary lubricated sliding conditions and at elevated temperatures.

Future Direction:

- Further optimize coating microstructure, chemistry, property, and performance.
- Control size of grains and chemistry of grain boundaries to achieve even better mechanical properties.
- Perform more detailed characterization studies by using both the surface and structure-sensitive techniques (i.e., HRTEM, AES, XPS, nano-mechanical characterization).
- Produce laser-textured dimples on superhard coated-steel surfaces and assess their tribological behavior under boundary lubricated sliding regimes.
- Perform long-duration friction and wear tests by using a reciprocating ring-on-liner test machine and demonstrate usefulness of new coatings with and without laser texturing under conditions that are typical of actual engine components (load, speed, temperature).
- Evaluate effect of viscosity on friction and wear performance of laser-textured plus superhard coated surfaces (several more samples were sent to Technion University in Israel for laser texturing).
- Elucidate lubrication mechanism by using surface sensitive techniques; determine the chemistry of boundary films.
- Explore other promising coatings systems (other than the current one).
- Transfer this technology to diesel engine industry.

Introduction

Increasing demands for higher fuel economy, lower emissions, and longer durability in diesel and other engine systems are pushing current materials and lubricants to their limits. Reduction of oil viscosity as well as sulfur- and phosphorous-bearing additives in future engine oils are making current engine materials increasingly more vulnerable to severe wear and high frictional losses. Therefore, it is very important to develop new materials and/or coatings that can resist wear and, at the same time, provide low friction when used in future diesel engines and drivetrain components. Accordingly, the major goal of this project was to design, develop, and optimize novel superhard and low-friction coatings for use in critical diesel engine parts and components, in particular piston rings and cylinder liners. Another important goal of this research was to integrate superhard coatings with a laser surface texturing process in order to achieve much higher performance and durability under boundary lubricated sliding conditions where direct metal-to-metal contacts occur.

Synthesis and Large-Scale Production of Superhard Coatings

One of the major goals of this project was to demonstrate the production of superhard coatings on selected test samples and engine components by using a commercially viable deposition system. With the procurement of a production-scale sputter ion plating system (Model # CC800/9XL, see Figure 1) from CemeCon-USA, Inc., we have made great strides in meeting this goal. Specifically, we have successfully synthesized high-quality superhard and low-friction coatings at very large scales. These coatings were jointly conceived by scientists at Argonne and Istanbul Technical University and were produced originally by using an arc physical vapor deposition (arc-PVD) system. In recent months, we were able to produce similar quality films by using the commercial-scale sputter-ion plating system shown in Figure 1. This system is equipped with two sputtering targets and/or cathodes so that the ceramic-based films can be doped with varying amounts of alloying elements and/or chemical compounds to result in a nanostructured and nano-composite microstructure. These alloying

Figure 1. General view of CemeCon CC800/9XL Coating system.

elements are strategically selected to enhance the chemical reactivity or responsiveness of coating surface to additives in oils and thus produce low-friction, scuff-resistant boundary films during lubricated rolling, sliding, or rotating contacts. Ceramic phases within the films are expected to increase hardness and thus resist adhesive and abrasive wear.

Structural Characterization

Figure 2 shows the cross-section SEM photomicrographs of a nano-composite film produced on a H13 steel substrate. High-resolution SEM studies of ion-etched film cross-sections revealed clear evidence of a nano-composite morphology. Combined X-ray diffraction and TEM studies have further confirmed that the individual grains within the films were around 50 nm and made of the hard ceramic phase. The softer metallic phase was found at the grain boundaries and was extremely thin. To produce such a dense and nano-composite film morphology, we identified and effectively controlled several important deposition parameters (such as bias on sputtering target and substrate holder, chamber pressure, deposition temperature, sputtering rate, plasma gas composition, and the rotational speed of sample holder) that seemed to have a very strong influence on both film morphology and chemistry.

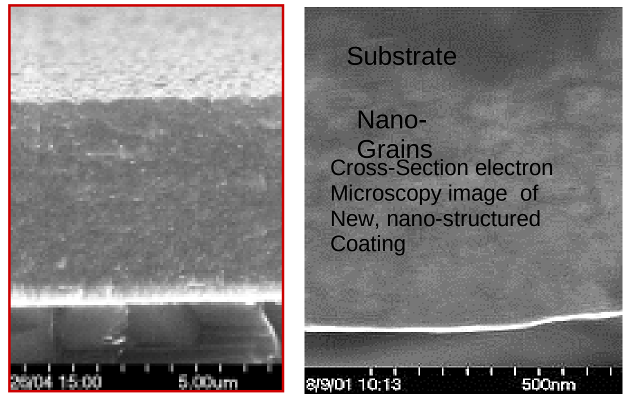

Figure 2. (a) General and (b) high-resolution SEM photomicrograph of cross-section of a superhard coating.

Mechanical and Tribological Characterization

Initial mechanical characterization of nanostructured coatings was carried out by using a Fischersope-H100 nanohardness test machine. Hardness measurements have revealed that these coatings were truly superhard, with typical hardness values ranging from 40 to 60 GPa. We have also noticed that there were certain regions or phases within the surveyed coating surface that exhibited hardness values as high as 70 GPa.

To assess film-to-substrate adhesion, we used a Rockwell C indentation method. Specifically, a diamond indenter was pressed against the superhard coated surface until a spherical indent was created. Mainly because of the very large elastic and plastic strain in and around the indented region, if the film adhesion was poor, then one would expect wide spread film delamination or detachment from these regions. However, as shown in Figure 3, there were some cracks near the indented spot but no signs of film detachment, thus verifying that the film-to-substrate adhesion was very strong.

Tribological testing of superhard coatings was carried out by using pin-on-disk and reciprocating test machines. These tests were performed under oil-lubricated sliding conditions at very low velocities and under very heavy loads in order to create a boundary-

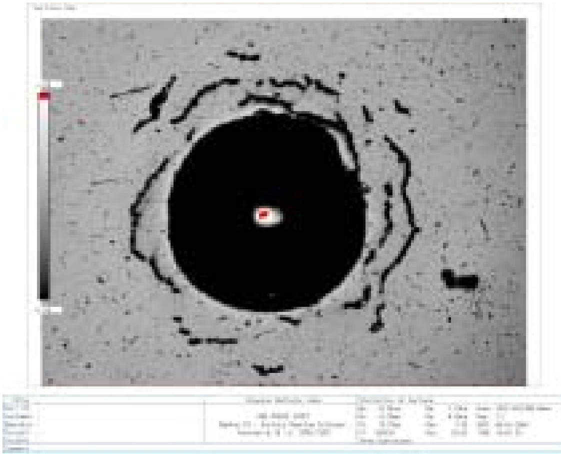

Figure 3. Optical photomicrograph of an indent verifying that there is no film detachment from substrate steel.

lubricated sliding regime in which direct metal-to-metal contact occurs. As a baseline, we have also run a few tests under dry sliding conditions. The friction coefficients of nano-composite films under dry sliding conditions were between 0.2 and 0.4 against steel or ceramic counterfaces. However, when tested under boundary-lubricated sliding conditions, their friction coefficients were significantly lower (i.e., 0.03–0.07) compared to steel/steel test pairs, which provided friction coefficients of 0.1–0.15 under boundary-lubricated sliding conditions. Figure 4 shows the actual frictional behavior of a nano-composite coating under the boundary-lubricated sliding regime. Note that the steady-state friction coefficient of this coating is less than 0.03. It is obvious that the presence of such a coating on one of the sliding

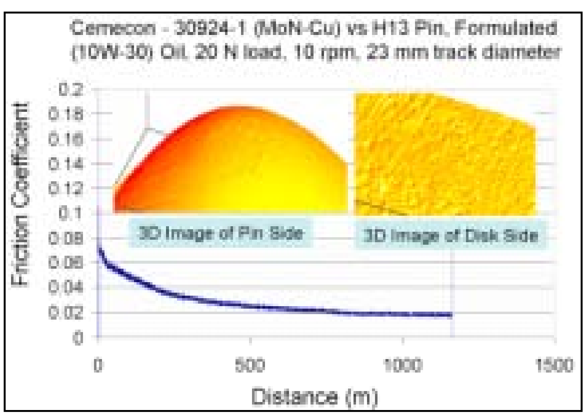

Figure 4. Typical friction behavior of superhard coating during sliding against a steel pin under boundary lubricated sliding condition.

surfaces can reduce friction by 75%. Such an improvement in lubricity of sliding surfaces can have a broad positive impact on actual engine parts and components. Because of their excellent compatibility with or favorable response to lubricated test environments, these coatings can be regarded as smart or highly adaptive tribological coatings. These coatings may further be optimized to provide low friction and wear, even in the near absence of sulfur and phosphorous-bearing additives in future engine oils.

Combining Superhard Coatings with Laser Texturing

During this work period, we have also explored the synergistic effects of combined uses of superhard coatings and laser-textured surfaces on friction and wear. Laser texturing produces shallow dimples on metallic or ceramic surfaces and when used under lubricated sliding conditions, these dimples can significantly improve mixed and hydrodynamic lubrication behavior of such surfaces. Shallow dimples can also trap abrasive wear debris that are created and thus reduce wear damage on sliding contact surfaces. Earlier work in our laboratory has verified that dimpled surfaces work extremely well under mixed or hydrodynamic sliding regimes of lubricated contacts; however, under boundary lubricated sliding conditions, they provide marginal improvements in friction but may cause increased wear losses. We felt that by applying a superhard coating over dimpled surfaces, we can also achieve very high wear resistance. Accordingly, during this work period, we have prepared a batch of laser-textured H-13 steel flats and later coated them with a superhard coating. It is expected that when applied on a textured surface, superhard coatings may further improve friction and wear performance of such surfaces, especially under high-load, low-speed sliding conditions that can lead to scuffing and hence major wear losses. Figure 5 shows a dimpled region with superhard coating on the surface.

Some of the dimpled and superhard coated-steel samples were subjected to friction and wear by using a reciprocating test machine under lubricated sliding conditions. Figure 6 compares the friction performance of as-received base steel, laser-dimpled

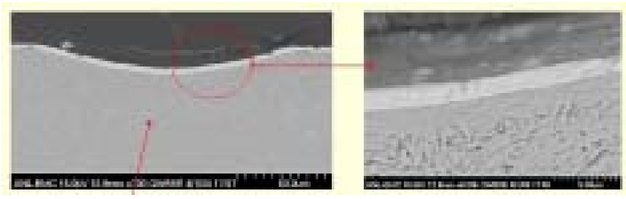

Figure 5. Hard coating applied over a dimple and magnified details of a segment showing coating and steel substrate.

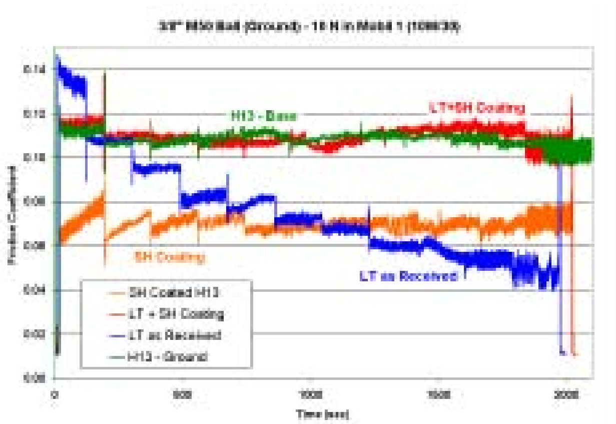

Figure 6. Friction behavior of as-received, laser-dimpled, and laser dimpled plus superhard coated surfaces under boundary lubricated sliding conditions.

steel, and superhard coated plus laser-dimpled steel surfaces under boundary lubricated sliding conditions.

On the basis of the results shown in Figure 6, it is clear that laser-dimpled and superhard coated-steel surfaces give fairly low friction coefficients, while base steel and combined laser-dimpled plus superhard coated surface provide same levels of friction. Surface studies after the tests indicated that despite their relatively higher friction coefficients, laser-dimpled plus superhard coated surfaces suffered the least amount of wear regardless of the contact loads; thus, verifying that the combined uses of superhard coatings and laser-textured surfaces can alleviate the wear problems of these surfaces observed during sliding under boundary lubricated sliding conditions.

In addition to sliding friction and wear studies mentioned above, we have explored the possibility of applying superhard coatings on cut segments of actual piston rings and cylinder liners for friction and wear studies by using a dedicated ring-on-liner type test machine.

Figure 7 shows cut segments of a ring and a liner that were coated with superhard coatings. This work is still in progress, and we expect to obtain preliminary friction and wear data very soon.

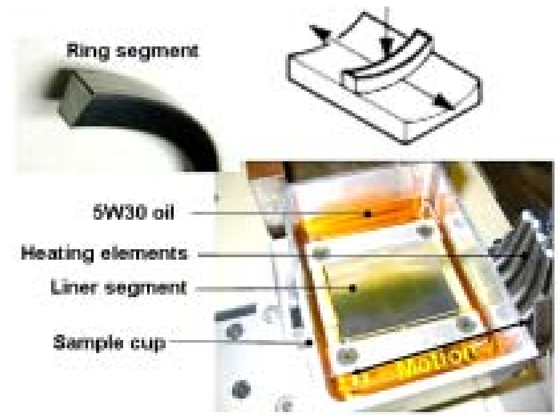

Figure 7. General layout of cut segments of dimpled piston ring and cylinder liner placed in its holder in a reciprocating test machine.

Conclusions

We have successfully demonstrated large-scale production of superhard coatings in a commercial-size deposition system. We have also optimized the deposition conditions (i.e., bias voltage, substrate temperature, deposition pressure, etc.) and hence achieved excellent reproducibility and reliability on coated samples. We have fully characterized these coatings by using a variety of mechanical and tribological test machines. Highly optimized superhard coatings were able to provide friction coefficients of less than 0.03 under boundary lubricated sliding conditions. The amount of wear of sliding surfaces was difficult to measure. We have also produced superhard coatings over laser-textured surfaces and demonstrated their superior wear properties under boundary lubricated sliding conditions. Optimized superhard coatings were also produced on cut segments of piston rings and cylinder liners, and they are currently being tested in a ring-liner type test machine.

Patents and Publications

So far, we have filed two invention disclosures on the work that we have done under this project. One of them (titled: low-friction, long wear coatings for conveyor assemblies) deals with the application of superhard coatings on chain links of automotive assembly plants. The second disclosure (titled: method to produce modulated composite surfaces) deals with the application of low-friction, superhard, and soft coatings over laser-textured surfaces.

During this period, we published and/or presented several papers on the subject. Below is a list of most significant ones.

1. Erdemir, A., "Review of Engineered Tribological Interfaces for Improved Boundary Lubrication," Tribology International, In Press, 2004.
2. Erdemir, A., "Smart Surface Engineering for Improved Boundary Lubrication," Invited Keynote Paper, Published in the Proc. of the 14th International Colloquium on Tribology and Lubrication Engineering, Stuttgart, Germany, January 13–15, 2004, Pages 13–20.
3. Donnet, C., and Erdemir, A., "Historical Developments and New Trends in Tribological and Solid Lubricant Coatings," Surface and Coatings Technology, 180–81:76–84, 2004.
4. Kazmanli, K.; Eryilmaz, O.L.; Ajayi, O.O.; Erdemir, A.; and Etsion, I., "Effects of Soft and Hard Coatings on Tribological Behavior of Laser Textured Surfaces," paper submitted for presentation at 2005 Annual Meeting of the Society of Tribologists and Lubrication Engineers, May 15–19, 2005, Las Vegas, NV.
5. Erdemir, A., "Engineered Tribological Interfaces for Improved Friction, Wear and Lubrication in Engines," Invited Panel Presentation at the Engine and Drivetrain Session of the 59th Annual Meeting of the Society of Tribologists and Lubrication Engineers, Toronto, Canada, May 17–20, 2004.
6. Eryilmaz, O.L.; Urgen, M.; and Erdemir, A., "Production and Characterization of Nano-composite Coatings Produced by Arc and Magnetron Sputtering Physical Vapor Deposition Techniques," Presented at the International Conference on Metallurgical Coatings and Thin Films, San Diego, CA, April 19–23, 2004.

IV. Fuel Reformer Systems

A. Diesel Fuel Reformer Technology

Principal Investigator: M. Krumpelt
Argonne National Laboratory
9700 S Cass Ave., Argonne, IL 60439
(630) 252-8520, fax: (630) 252-4176, e-mail: krumpelt@anl.gov

Technology Development Area Specialist: Sidney Diamond
(202) 586-8032, fax: (202) 586-1600, e-mail: sid.diamond@ee.doe.gov
Field Technical Manager: Jules Routbort
(630) 252-5065, e-mail: routbort@anl.gov

Participants
Hual-Te Chien, Argonne National Laboratory
Shuh-Haw Sheen, Argonne National Laboratory

Contractor: Argonne National Laboratory
Contract No.: 49099

Objectives

- Develop an autothermal reforming process to convert diesel fuel into hydrogen-rich gas on-board a heavy-duty vehicle in a small fuel processor.
- Develop a fuel-air mixing device to achieve perfect mixing and reduce coke formation.
- Determine operating parameters for establishing “cool flame” conditions and evaluate the effects on reforming process.

Approach

- Evaluate engineering issues that need to be better understood with regard to diesel fuel reforming. The main issues are how to avoid pre-ignition and coke formation and how to achieve catalyst stability.
- Construct a test facility with single-nozzle diesel fuel reforming.
- Develop a fuel/steam/air injection and mixing system that can achieve homogeneous mixing and stable cool flame conditions.
- Conduct diesel fuel-reforming tests to evaluate the catalytic autothermal reforming process.
- Develop a compact diesel-fuel reforming system that complies with industrial needs.
- Conduct field tests and document the results.

Accomplishments

- Completed construction of the fuel/steam/air mixing test facility.
- Completed the Argonne safety review of the facility.
- Evaluated the fuel-injection control system provided by International Truck and Engine Corporation (ITEC).
- Designed and constructed a steam/air injection device.

Future Direction

- Complete development of the fuel/steam/air mixing apparatus.
- Conduct fuel injection/mixing tests to determine the operating parameters for cool flame.
- Modify the facility for autothermal reforming tests.
- Conduct autothermal reforming tests.

Introduction

Converting diesel fuel into a hydrogen-rich gas has potential applications in auxiliary power units (APUs) for heavy-duty vehicles and emissions control of diesel engines. An APU of 3–10-kW electric capacity can provide enough electric power to operate the air conditioners and heaters for the cabin and the cargo space while the vehicle is parked. It is common practice in the trucking industry today to keep the diesel engines running to generate electricity while drivers rest or are held at customer sites. The efficiency of diesel engines is only 9% in this idling mode. Significant fuel savings and emission reductions would be achieved if kW-capacity APUs for trucks were available and the engines could be turned off. Argonne National Laboratory (ANL) has developed a catalytic autothermal reforming process that may be used as a compact and potentially cost-effective technology for diesel-fuel reforming. However, because diesel fuel is more difficult to process because of high sulfur content and large aromatic molecules, the autothermal reforming process may encounter pre-ignition and coke formation problems. Operating at higher temperatures mitigates these problems but leads to rapid catalyst deactivation. This program will explore the feasibility of achieving the diesel-fuel reforming by optimizing fuel/exhaust-gas mixing dynamics. Several engineering issues, such as how to avoid pre-ignition and coke formation and how to maintain catalyst stability, will be examined.

Diesel Fuel Injection/Mixing Facility

In FY 2004, we completed the construction and safety review of the fuel-injection/mixing test facility. Figure 1 shows the schematic diagram of the facility, which consists of a fuel-injection assembly, simulated exhaust gas generating system, and fuel-exhaust-gas mixing apparatus. The facility's injector system is a commercially available G-2 fuel injector provided by the International Engine and Truck Company (ITEC). The injector is controlled by the ITEC's PCM (Powertrain Control Module) simulator and can be operated under two injection modes: single shot and pulsed injection. The pulsing rate varies from 10 to 70 Hz, and the injection duration is typically between 1 ms and 20 ms, giving a maximum fuel injection volume of about 8 cm^3/s.

Results

The injector-controlling software provided by ITEC was installed in a desktop PC and run on the Labview platform. Injection tests were conducted, and a CCD camera (Canon PowerShot A80) that has a resolution of 72 pixels/in. when operated under the dynamic mode was used to capture the spray appearance of diesel fuel. Figure 2 shows a picture of the spray structure generated with 7-MPa injection pressure into ambient conditions. The estimated fuel flow rate under the single-shot mode of injection is 30 mm^3/s. The figure shows primarily a two-dimensional (2-D) image of the general structure of the dense spray region. The stable fuel jet extends to about 200 times the nozzle diameter (~ 0.18 mm). On the basis of the reported data [1], this finding indicates that the liquid volume fraction at the boundary of the dense spray region is less than 10%. Detailed characteristics of the diffuse phase cannot be resolved with the present CCD camera.

Future Plan

In FY 2005, we will focus on development of a steam/air injection device that can deliver controlled volumes of steam and hot air into the mixing chamber. The state of fuel/steam/air mixing will be monitored with a 2-D array of temperature sensors. Tests will be conducted at different air temperature, fuel injection rate, and steam concentration. Results from the tests will be used to determine the optimal conditions for producing a cool flame from the diesel fuel.

Reference

1. G.A. Ruff and G.M. Faeth, "Nonintrusive measurement of the structure of dense sprays," Progress in Astronautics and Aeronautics, Vol. 166, "Recent Advances in Spray Combustion: Spray Atomization and Drop Burning Phenomena, Vol. 1," Chapter 11, 1996.

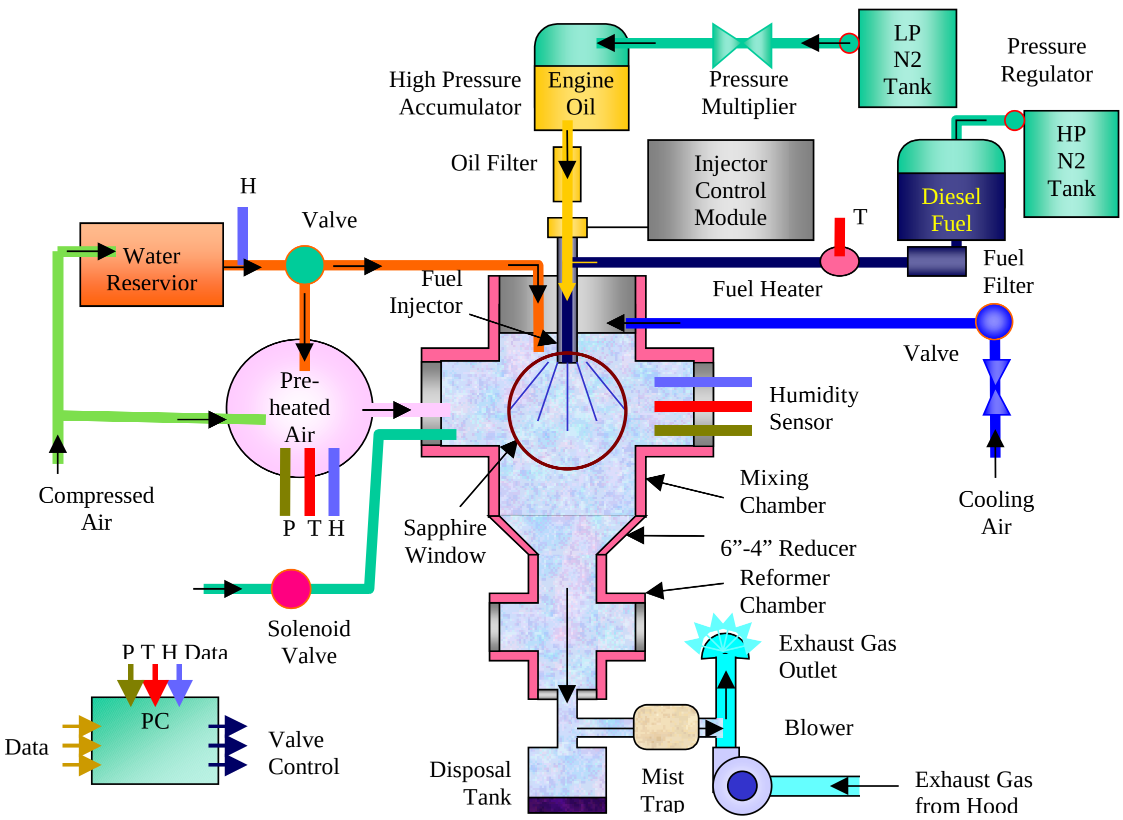

Figure 1. Diesel fuel injection and mixing facility.

Figure 2. A typical spray structure of G-2 injector.

B. On-Board Plasmatron Hydrogen Production for Improved Vehicle Efficiency

Principal Investigators: Daniel R. Cohn, Leslie Bromberg
Plasma Science and Fusion Center, Massachusetts Institute of Technology
MIT PSFC NW16-104, 77 Massachusetts Avenue, Cambridge MA 02139
(617) 253-5524, fax: (617) 253-0700, e-mail: cohn@psfc.mit.edu

Technology Development Area Specialist: Sidney Diamond
(202) 586-803, fax: (202) 586-1600, e-mail: sid.diamond@ee.doe.gov
Field Technical Manager: Philip S. Sklad
(865) 574-5069, fax: (865) 576-4963, e-mail: skladps@ornl.gov

Contractor: Massachusetts Institute of Technology
Contract No.: DE-AC03-99EE50565

Objectives

- Develop attractive applications of plasmatron fuel reformer technology to internal combustion engine vehicles using diesel, gasoline, and biofuels.
- Develop means of reducing NO_x and particulate matter emissions from diesel engines by using plasmatron reformer generated hydrogen-rich gas.
- Investigate conversion of ethanol and bio-oils into hydrogen-rich gas.
- Develop concepts for the use of plasmatron fuel reformers for enablement of HCCI engines.

Approach

- Optimization of plasmatron fuel reformer configurations, including gas and fuel management, plasma geometry, and reactor chamber variations.
- Optimization of catalytic and other materials-enhanced plasmatron reforming.
- Determination of reforming characteristics of pure and hydrated ethanol, refined and unrefined bio-oils, and with commercial-grade diesel fuel.
- Development of instrumentation for investigating fast transients when using the plasmatron in a pulsed configuration, as would be the case of NO_x trap regeneration.
- Modeling of plasmatron fuel reformer operation by using computational studies of the chemistry of simple gaseous hydrocarbons (mainly methane) because of the complicated effects from liquid fuels and CFD calculations of the flows upstream from the plasma discharge.
- Test of plasmatron fuel-reformer-enhanced NO_x regeneration both in laboratory and on vehicles.

Accomplishments

- Demonstrated efficient conversion of biofuels to hydrogen, CO, and light hydrocarbons by using non-catalytic reforming, opening new potential applications of these fuels in the transportation sector.
- Demonstrated rapid response and high hydrogen yields for ethanol reforming.
- Demonstrated increased hydrogen production by using Ni catalysts and Rh catalysts on an alumina substrate.
- Demonstrated increased hydrogen production by using metallic plates in the reactor.
- Developed an improved method for the use of mass spectrometer for the quantitative measurement of flow rates of gases of interest.

- Demonstrated hydrogen-rich gas as an effective reductant for converting NO_x in NO_x traps to N_2, in vehicular tests carried out by our industrial partner, ArvinMeritor.
- Showed that hydrogen-rich gas significantly improves NO_x trap catalyst operating temperature range:
  - Demonstrated decreased fuel penalty for diesel NO_x emissions exhaust treatment and
  - Demonstrated advantages of hydrogen-rich gas from plasmatron fuel reformers for desulfation of NO_x traps.
- Developed a power supply and an electrical configuration for the elimination of electromagnetic interference (EMI), which had affected measurements during tests in laboratory.
- Continued collaboration with ArvinMeritor with the goal of commercialization of plasmatron fuel reformer technology.
- Developed additional MIT intellectual property and filed patent applications; also, some previously filed patent applications have been granted in 2004.

Future Directions

- Demonstrate through experiments and modeling increased capability of plasmatron fuel reformers for higher flow rates (4 g/s of fuel) and applications in on-line regeneration of NO_x traps and lean-NO_x catalysts.
- Investigate new approaches to increase hydrogen yield for enhanced reforming from metallic materials.
- Investigate new approaches of thermal control of catalyst in plasmatron fuel reformers.
- Investigate operation of plasmatron reformers over a range of oxygen-to-carbon ratios (O/C), from O/C ~1 (stoichiometric partial oxidation) to full combustion to optimize regeneration of diesel particulate filters.
- Investigate use of pulsed operation of plasmatron reformer to obtain variable flow rate.
- Initial tests of plasmatron fuel converter regeneration of diesel particulate filter.
- Investigate concept of hydrogen regeneration of SCR catalyst.

Introduction

To meet stringent U.S. emissions regulations that will be implemented in the 2007–2010 diesel vehicle model years, new after-treatment technology is being developed. Both particulate and NO_x emissions after-treatment technology will be necessary, as it appears that engine in-cylinder techniques alone will be unable to meet the regulations.

MIT, in collaboration with ArvinMeritor, has been developing a plasmatron fuel reformer for vehicular on-board applications, including engine fuel conditioning as well as diesel engine after-treatment. The MIT technology has been licensed by ArvinMeritor. The DOE program is aimed at realizing the broad potential of plasmatron fuel reformer technology for hydrogen-based diesel engine exhaust after-treatment and for expanding opportunities for use of renewable energy biomass derived fuels.

Plasmatron fuel reformer technology has the potential to be an important enabling technology for a range of practical vehicular applications. It can provide unique capability for reforming diesel and bio-oils into hydrogen-rich gas for vehicular applications. Plasmatron hydrogen generation technology has the potential to play a major role in the development of practical NO_x and diesel particulate after-treatment technology needed to meet the 2010 EPA mandate for emissions reductions. Recent concerns about the possible contribution of diesel soot to global warming provide additional impetus for development of these technologies.

The potential value of the hydrogen-based vehicle enhancement has been validated by successful vehicular tests of diesel exhaust after-treatment by using plasmatron hydrogen-enhanced lean-NO_x trap technology in a bus and pickup truck by ArvinMeritor, our industrial collaborator. ArvinMeritor, a $7-billion/yr U.S. automobile and truck components manufacturer, has licensed the plasmatron fuel reformer technology from MIT.

Plasmatron Fuel Reformer

Plasmatron fuel reformer technology consists in the use of a special plasma discharge for the initiation of reformation process. Proper placement of the plasma discharge is used in a flowing air/fuel mixture that is very rich. Proper preparation of the fuel and fuel/air mixture is required for optimal operation.

The plasmatron fuel reformer technology is attractive because of capability for fast response, elimination or relaxation of catalyst requirements, and fuel flexibility. Fast response is needed for on-board applications in SI engines, where on-demand, wide-dynamic-range hydrogen-rich gas requirements are stringent, as well as in aftertreatment applications, where short bursts of hydrogen-rich gas are needed. Moderate hydrogen yields (defined as the ratio between the hydrogen gas in the reformate to the hydrogen in the hydrocarbon fuel) have been achieved without the use of catalysts (about 40%), The yield increases to ~70% when hydrogen in light hydrocarbons is also included. The use of a catalyst downstream from the plasma region can increase the hydrogen yield to ~70%, as discussed below. Experiments have been conducted with gasoline, diesel, ethanol and hard-to-reform bio-oils.

To increase hydrogen yield, a catalyst can be placed downstream from the homogeneous reforming region. The homogeneous stage of the plasmatron fuel reformer converts the liquid hydrocarbons into hydrogen, CO, and light hydrocarbons, plus a small amount of carbon dioxide and water. The catalyst is useful in converting light hydrocarbons into additional hydrogen.

Diesel Reforming

In 2004, the input fuel flow rate of a diesel plasmatron fuel reformer at MIT was operated with an increased diesel fuel flow rate of 2 g/s, corresponding to 80 kW of fuel reformate. This reformer produced about 1.5 L/s of hydrogen without the use of a reforming catalyst for additional hydrogen generation. This type of higher-flow-rate operation can facilitate quick regeneration of single-leg NO_x trap systems.

The characteristics of the plasmatron diesel fuel converter and the reformate it produces are shown in Table 1. The goal of reformation of diesel by the plasmatron fuel converter is the conversion of the heavy diesel compounds into hydrogen, carbon monoxide, and light hydrocarbons for use in after-treatment applications. The diesel reformate produced by the plasmatron fuel converter has little residual oxygen and little or no soot. The diesel plasmatron can be cycled on and off quickly (~3–5 s). For diesel after-treatment applications, the dynamic performance of the plasmatron fuel reformer is important because of the low duty cycle of operation. For NO_x catalyst regeneration applications, the plasmatron may be turned on for several seconds with a duty cycle of ~10%. For diesel particulate filter (DPF) applications, the plasmatron could well be operated for a few minutes every few hours, resulting in much smaller duty cycles.

Hydrogen is a powerful reductant, and its use for the regeneration of NO_x traps has been researched in catalyst development laboratories. The goal of the plasmatron reformer program is to determine the advantages of hydrogen-assisted NO_x trap regeneration, by using the plasmatron fuel reformer as the source of on-board hydrogen. Tests at ArvinMeritor have demonstrated the advantages of using hydrogen-rich gas for NO_x regeneration and desulfation of NO_x traps. Substantially higher regeneration of NO_x traps with hydrogen can be obtained with hydrogen-rich gas. In contrast to the use of diesel fuel for regeneration, adequate regeneration can be obtained at low exhaust temperatures (in the 150–200°C range), which can significantly increase the range of vehicle conditions in which the technology can be used. In addition, a lower fuel penalty is observed when comparing hydrogen-rich gas regeneration to diesel fuel regeneration. The temperatures required for desulfation are also substantially decreased.

Table 1. Experimental results of homogeneous diesel reforming.

Parameter	Value
Electric power (W)	200
O/C	1.2
Diesel flow rate (g/s)	0.8
Corresponding chemical power (kW)	36
Reformate composition (vol %)	
H_2	7.6
O_2	1.3
N_2	64.0
CH_4	2.4
CO	13.0
CO_2	4.4
C_2H_4	2.2
C_2H_2	0.0
H_2O	7.1
Energy efficiency to hydrogen, CO and light HC (%)	65
H_2 flow rate (L/min [STP])	20
Soot (%; opacity meter)	0.0

Enhanced Reforming with Metallic Materials

Use of conventional catalysts can be hampered by limits on reliability and lifetime. We have studied the use of metallic materials for enhanced reforming as an alternative to conventional catalysts. Reforming experiments of diesel and ethanol have been carried out by using a bed of metallic spheres of different materials and sizes in the reactor. These experiments resulted in a hydrogen concentration of up to 18% in the reformate gas (in contrast to 8% without the metallic material) and a high energy efficiency. However, none of the spheres used lasted very long, as the material deteriorated and turned into a metallic dust. On the basis of these results, ceramic (alumina) bids have been tested to counter the destruction effect of heat. The results yielded a low hydrogen concentration in the reformate, indicating that the reforming phenomenon on surfaces could not be linked only to surface area and heat.

On the basis of the same idea of using non-conventional materials for homogeneous reforming, metallic plates of different forms, shapes, and materials have been used. Experiments using steel plates yielded a hydrogen concentration of 18%, but the plates deteriorated just as in the case of the spheres. Inconel plates have also been tested and were also shown to deteriorate. Finally, nickel plates showed the most promising results: the hydrogen concentration obtained with these plates was 17%, and the material did deteriorate much less than other materials.

Instrumentation Development

A new approach was developed that allowed quantitative fast measurements of flow rates. Since the flow rates of air are known (from the inputs), and air contains substantial amounts of Ar (about 1%), the flow rate of Ar in the reformate is known. By taking ratios between the signals of the gases of interest and Ar, the flow rates of the gases of interest can be determined. This avoids problems of absolute calibration of the mass spectrometer, which is subject to variations and drifts due to temperature effects, partial blockages of the capillary, and other environmental effects. The setup can be used for determining flow rates with appropriate choice of Ar concentration in the calibration mixture. Alternatively, the N+ ion can be used instead of Ar, but our preliminary results indicate that lower noise is obtained with Ar as the benchmark. The device was optimized for making measurements of 10 ions every 200 ms. A technical paper is being prepared that describes this approach.

Reformation of Biofuels

Reformation experiments of renewable energy biomass derived fuels have been carried out. Ethanol and vegetable oils, (including soy and canola oils) have been efficiently reformed, with no soot production at input rates up to 1 g/s, corresponding to about 34 kW of heating power. Both non-catalytic and catalytic (with a catalyst downstream from a homogeneous reforming zone) have been studied. On-board conversion of biofuels into hydrogen-rich gas opens up a range of opportunities for reducing petroleum consumption.

Bio-Oils

Dependence of the homogeneous reforming process on the ratio of oxygen to carbon (O/C ratio) in the reagents indicates almost constant yield over a broad range of O/C ratios. As the O/C is increased, the temperature of the reformate increases as a result of increased exothermicity of the reaction, compensating for the fact that a fraction of the fuel is converted into hydrogen.

The hydrogen yield for the reformation of corn and soybean oils in the presence of a catalyst is higher, as is the conversion, than that for homogeneous reforming, with little difference between the fuels. In this case, there is a broad maximum at O/C ratios close to 1.5. The catalyst is useful in converting light hydrocarbons into additional hydrogen. The corn and soybean catalytic experiments were done with a volume of 85 cm^3 of catalyst, whereas only 25 cm^3 of catalyst was used during the canola oil experiments (to explore the effect of space velocity). A nickel catalyst was used.

Studies of effect of catalyst on the hydrogen yield indicate that for homogeneous reformation of soybean oil, the hydrogen yields are about 30%, while the yield increases to about 70% in the presence of a catalyst. The difference between the yield of 70% and the ideal yield of 100% is due primarily to the loss of hydrogen resulting from full oxidation into water. For homogeneous reformation, the ratio of the heating value of the hydrogen, CO, and light hydrocarbons by-products to the heating value of the fuel was typically between 60 and 70%.

The non-catalytic investigations indicate that the plasmatron converts the biofuels into hydrogen, carbon monoxide, and light hydrocarbons, with minimal soot production, and virtually eliminates all free oxygen. The catalyst then takes the oxygen-free plasmatron gas and roughly doubles the hydrogen yield, performing CO_2 and possibly steam reforming (the CO_2 concentration decreases downstream the catalyst; water is not monitored).

It should be stressed that the performance of the system was not optimized, and higher hydrogen yields could be possible by converting the substantial amounts of C2s present in the gas downstream from the catalyst.

For all of the experiments performed with veggie oils, the opacity was below the sensitivity limit of the instrumentation.

Ethanol

Two sets of experiments have been conducted with ethanol. The first set of homogeneous and catalytic experiments used the same experimental protocol as described for the bio-oils. The maximum hydrogen yield obtained for catalytic reforming of a fuel flow rate of 0.35 g/s was 75%, as shown in Figure 1. From this figure, it appears that the hydrogen yield depends upon the O/C ratio and the maximum value is obtained for an optimum O/C of 1.6.

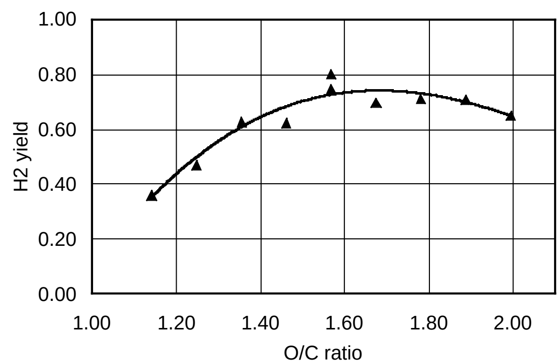

Figure 1. Hydrogen yield for the plasma-catalytic reformation of ethanol vs. O/C ratio.

Other experiments have also shown that the hydrogen yield depends upon the fuel flow rate through the reactor. Figure 2 gives the hydrogen yield for catalytic reforming of ethanol versus the fuel flow rate. It shows that the hydrogen yield increases with decreased flow rate. This indicates clearly that higher hydrogen yields for the catalytic reforming of ethanol are possible for lower space velocities. The space velocity is defined as the ratio of the airflow rate at STP that passes through the catalyst to the volume of this catalyst.

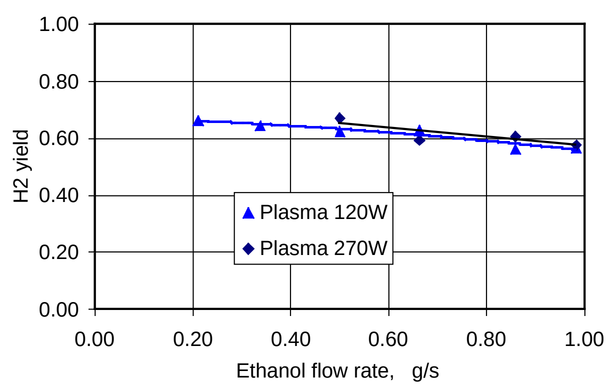

Figure 2. Hydrogen yield vs. ethanol flow rate for plasma-catalytic reforming.

The second set of catalytic experiments was conducted by using rhodium catalyst deposited on alumina cylindrical substrate beads. The beads were 2 mm long by 1 mm in diameter, and the rhodium content was 0.5% by weight. The catalytic experiments were performed by using 50 g of catalyst.

Plasmatron cold start, with the reactor initially at room temperature, was investigated for ethanol reforming by using the mass spectrometer described above.

Figure 3 shows the concentration (vol. %) of hydrogen, carbon monoxide, ethane, and methane for the case of homogeneous reforming of ethanol. The hydrogen concentration is about 6% right at start, and it increases slowly to about 12% (in 150 s). These results have been obtained by using a discharge power of 200 W with an ethanol flow rate of 0.9 g/s, corresponding to 26 kW of heating power. The O/C was ramped from an initial value of 2.3 at start-up to 1.73 after 12 s of reforming. It should be noted that at O/C ~1.73, a good amount of ethanol is combusted, and some of the hydrogen is turned into water. The hydrogen yield could be increased and response time could be decreased by optimizing the O/C start-up ramp.

Combined homogeneous and catalytic reforming was explored as means of increasing the hydrogen yield. The electrical power in the discharge is the same as that for homogeneous reforming, as is the ethanol flow rate. The ramp of the O/C ratio, however, is slightly different, as the final O/C ratio

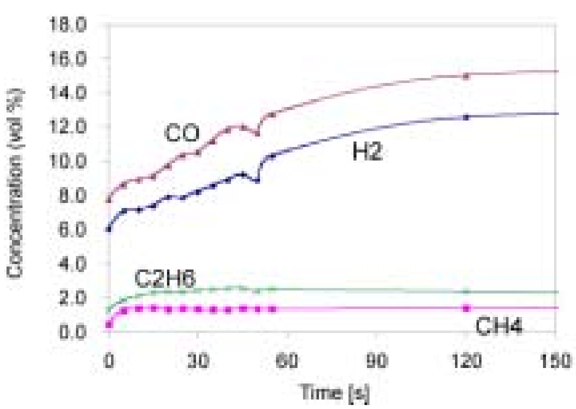

Figure 3. Concentration of H_2, CO, and C_2H_6 in the reformate as a function of time for homogeneous reforming, with variable O/C ratio during the first 12 s.

in the case of catalytic reforming is lower than that for homogeneous reforming.

In the case of plasma catalytic reforming, the O/C ratio is ramped from O/C ~ 2.3 at start-up to O/C ~ 1.56 at 12 s. The hydrogen concentration and yields are higher than in the case of homogeneous reforming, even at start-up, with an initial hydrogen concentration of 10%. In addition, the steady-state value of the hydrogen concentration and yields are substantially higher than in the case of homogeneous reforming. In addition to higher yields, the time to achieve high conversion is significantly shorter than in the homogeneous case, reaching near steady state at the end of the 12-s ramp-up. The energy efficiency (ratio of the heating value of the reformate to the heating value of the ethanol) is greater than 70% at steady state.

DPF Regeneration

Options of using reformate from a plasmatron fuel reformer for the controlled regeneration of DPFs are being explored.

Hydrogen-rich gas could provide important advantages for controlled regeneration of DPF. The reformate can provide clean-burning fuel to initiate and control the burnup of soot in a trap during regeneration. Alternatively, the use of hydrogen-rich gas may result in DPF regeneration at lower soot levels. This regeneration scheme could allow more frequent regenerations, the advantage of which would be a decreased chance of large uncontrolled regeneration thermal excursion that could negatively impact the performance of the trap, thus resulting in increased reliability and longevity.

Active techniques for the regeneration of DPF use a burner to achieve the temperatures at the catalyst required for filter regeneration. This technology burns fuel to generate heat, carbon dioxide, and water. Alternatively, plasmatron technology could be used not only as an igniter to combust part of the fuel using the oxygen present in the diesel exhaust and generate heat, but also as a means to produce hydrogen-rich gas. The fuel combustion can take place even under conditions where the free-oxygen-to-fuel ratio is larger than unity (i.e., lean-burn conditions in the plasmatron).

The advantage of combusting the fuel in the exhaust is that it is possible to provide the heat for regeneration while minimizing the amount of extra air introduced into the system. The hydrogen-rich gas with exhaust gas as oxidizer results in a net decrease of the amount of free oxygen in the exhaust, decreasing the combustion rate of the soot on the DPF and decreasing the possibility of uncontrolled regeneration. This technology is also attractive because the plasmatron hardware may eventually already exist on-board the vehicle for regeneration of NO_x absorber traps.

The plasmatron fuel reformer can thus be used as a powerful combustor, operating with exhaust as the oxidizer. There is thermal output from the combustor, but no hydrogen or light hydrocarbons. Alternatively, the reformer operates under conditions close to partial oxidation (free-oxygen-to-carbon ratio of 1), producing hydrogen, CO, light hydrocarbons, and limited thermal output (~ 1/5 of the thermal output is the fuel is combusted). These two are extremes, with the plasmatron operating anywhere in between, generating both easily combustible gases and thermal output.

Reformate requirements for achieving DPF regeneration have been calculated on the basis of simple models. It has been determined that the flow rates requirements for a 6-L turbocharged engine are within the range of today's plasmatron capabilities. Larger engines can be regenerated by using (1) multiple plasmatrons or (2) thermal management/non-uniform regeneration techniques.

It has been determined that the hydrogen-rich gas will not spontaneously combust before reaching the soot trap under normal operating conditions of the engine. Thus, slow, uniform regeneration of the DPF could be achieved by using both the thermal effect from the reformate and the reducing capabilities and localized thermal effect of the hydrogen rich gas.

Industrial Collaboration

MIT is collaborating with ArvinMeritor in developing the plasmatron fuel reformer regeneration of NO_x absorber catalysts as a means of controlling emissions from trucks, buses, and on vehicles. MIT has licensed plasmatron fuel reformer technology to ArvinMeritor for their applications.

The intellectual property includes both the technology relevant for plasmatron fuel reformers operating on diesel fuel, as well as system patents where plasma-based reformers are used in the regeneration process.

ArvinMeritor has studied the implications of hydrogen-rich gas regeneration of NO_x absorber catalysts in the laboratory, by using hydrogen-rich gas from bottled gas. These tests demonstrated the usefulness of using hydrogen-rich gas instead of diesel fuel for regenerating the catalysts. The advantages were both in decreased fuel penalty at moderate temperatures and in enabling regeneration at lower temperatures (where diesel fuel is ineffective). After these experiments in which synthetic reformate was used, the systems were placed on vehicles to investigate issues of integration and packaging. Successful tests have been performed on a bus. ArvinMeritor is also developing plasmatron fuel reformer technology for increasing the efficiency of gasoline engines.

The substantial ArvinMeritor investment in plasmatron fuel reformer technology represents a strong leveraging of a much smaller DOE investment. The integrated DOE investment over the time that is has supported the MIT plasmatron program has already led to an ArvinMeritor investment that is more than five times greater. Further strong interaction between MIT and ArvinMeritor is anticipated.

Summary

Highlights during FY 2004 are:

- On-board testing of plasma-fuel-reformer-based hydrogen-rich gas regeneration of NO_x traps has been carried out in a bus at ArvinMeritor's test track.
- Significant benefits (relative to diesel fuel regeneration) have been demonstrated, including decreased fuel penalty and lower regeneration temperature.
- Desulfation of traps by using hydrogen-rich gas from a plasmatron diesel reformer, with lower temperature regeneration, has been demonstrated by ArvinMeritor.
- Fast turn-on reformation from diesel and ethanol, with instantaneous (< 1 s) yield of 32% to hydrogen and light hydrocarbons and 20% to

hydrogen, has been demonstrated by using homogeneous reforming, facilitated by fuel vaporization, enlarged volume reaction initiation, and enthalpy addition.
- High yields into hydrogen and light hydrocarbons were obtained in homogeneous reforming of ethanol and bio-oils.

Conclusions

- On-board generation of H_2-rich gas can provide important benefits for diesel engine NO_x exhaust aftertreatment.
- Plasmatron fuel reformer is a promising technology for practical on-board generation of hydrogen-rich gas for other applications where diesel and gasoline are used.
- Plasma fuel reformers can facilitate increased use of biofuels

Patents and Publications

Four patents were issued since May 2003:
- US Patent 6793899: *Plasmatron-Catalyst System*, L. Bromberg, D.R. Cohn, A. Rabinovich, and N. Alexeev, issued September 21, 2004.
- US Patent 6718753: L. Bromberg, D.R. Cohn, and A. Rabinovich, *Emission Abatement System Utilizing Particulate Trap*, issued April 13, 2004.
- US Patent 6655324: *High Compression Ratio, Hydrogen Enhanced Gasoline Engine System*, D.R. Cohn, L. Bromberg, A. Rabinovich, and J.B. Heywood, issued December 2, 2003.
- US patent 6560958 *Emission Abatement System*, L. Bromberg, D.R. Cohn, and A. Rabinovich, issued May 13, 2003.

Publications include:
- L. Bromberg, D.R. Cohn, K. Hadidi, J.B. Heywood, and A. Rabinovich, *Plasmatron Fuel Reformer Development and Internal Combustion Engine Vehicle Applications*, presented at the Diesel Engine Emission Reduction (DEER) Workshop, 2004, Coronado CA, August 29–September 2, 2004.
- K. Hadidi, L. Bromberg, D.R. Cohn, A. Rabinovich, *Plasma Catalytic Reforming of Biofuels*, report PSFC-03-28; http://www.psfc.mit.edu/library/03ja/03JA028/03JA028_abs.html; presented at World Energy Conference, Denver, CO, August 2004.

V. EM Regenerative Shocks

EM Shock Absorber

Principal Investigator: John R. Hull
Argonne National Laboratory
Argonne, Illinois 60439
(630) 252-8580, fax: (630) 252-5568, e-mail: jhull@anl.gov

Technology Development Manager: Sid Diamond
(201) 586-8032, e-mail: sid.diamond@ee.doe.gov
Technical Program Manager: Jules Routbort
(630) 252-5065, e-mail: routbort@anl.gov

Contractor: Argonne National Laboratory
Contract No.: W-31-109-ENG-38

Objectives

- Develop model to predict performance of regenerative shock absorber.
- Conduct experiment on a small-scale vehicle to verify the energy recovery from road-induced vehicle motion.
- Compare the experimental results with theoretical prediction.
- Develop road data to use as input to the model.

Approach

- Mount regenerative shock on small vehicle and accrue test data.
- Instrument truck and run it over local roads to obtain data.

Accomplishments

- Tested experimental electromagnetic shocks on all-terrain vehicle and used the data from it to verify model of regenerative shock performance.
- Instrumented truck and accumulated data on acceleration over local roads.

Future Direction

- More road data need to be accumulated for a complete database.
- The road data need to be used in the regenerative shock model to predict expected performance.
- Explore potential of developing technologies for dynamic control of vehicle.

Introduction

The up-and-down motion of a vehicle traversing a road is unwanted from a passenger comfort perspective. In present vehicles, where the motion is damped by shock absorbers, the energy provided by the prime power plant is diverted from its intended purpose and gets dissipated in heat. Prevention of this motion in the first place could be accomplished by construction and maintenance of smooth roads. However, in the absence of such a societal program, the energy diverted into the vertical motion can potentially be recovered by a regenerative shock absorber that converts the up and down motion into electrical energy. The goal of this project is to ascertain whether this can be accomplished in a cost-effective manner.

To estimate the power generated by the EM shocks, experimental regenerative shocks were mounted in an ATV, as shown in Figure 1. This vehicle was tested on local roads and on a specially constructed obstacle course to determine the performance of the experimental shock absorber.

Figure 1. ATV used for EM shock testing.

In a separate series of experiments, the performance of experimental regenerative shocks has been obtained by subjecting them to forced oscillations of a shaker, as shown in Figure 2.

Figure 2. Shaker testing of Mark 1 EM shock.

<u>Results</u>

By using data from both experimental programs, a mathematical model of regenerative shock performance was established and verified. Sample data used in the model are shown in Figure 3. In this instance, the ATV was driven over a 4-by-4 beam.

To use the model to predict actual performance under real conditions, it is necessary to have the expected forcing function of a vehicle traveling on

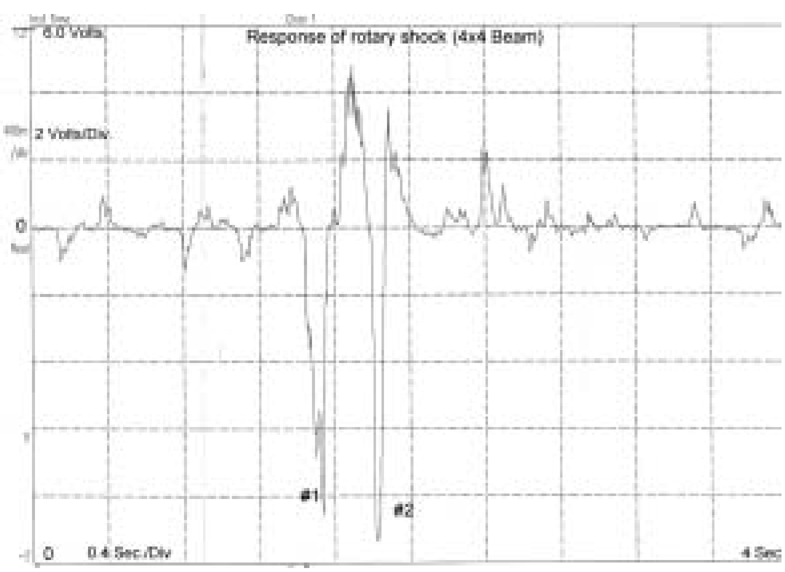

Figure 3. Response of Mark 2 (rotary) shock absorber transversing 4-by-4 beam.

real roads. Examination of existing databases suggested that the required data were not sufficient. Therefore, we instrumented a road vehicle to acquire the data.

Discussion

An LVDT was mounted in a dump truck between the axle and the chassis, as shown in Figure 4. The purpose of this experiment was to record the suspension (conventional) relative displacement to get an estimate of the available energy.

Figure 4. LVDT mounted in the trunk.

The voltage output from the LVDT was sent to a tape deck on board the truck cabin (as shown in Figure 5) as the truck was driven around a road inside Argonne National Laboratory.

Figure 5. Tape recorder inside the trunk.

The tape gain was set to 2 so that the actual voltage is twice the voltage shown in the graph (i.e., 2-V peak in the graph implies 4-V peak signal from LVDT). A segment of the time domain signal recorded is shown in Figure 6. The LVDT scale factor was 3.3 V/in. and the frequency spectrum of the above signal is shown in Figure 7.

From Figure 7, a 0.374 mv at 4 Hz implies 0.226 in peak displacement at 4 Hz, which is approximately 5.6 in./s or 0.142 m/s. Since the actual value of the suspension damping constant of the dump truck is unavailable, a suspension damping constant of 89 kN•s/m, which may be typical of a single-axle flat bed truck, is assumed. This leads to power of 900 W at 4 Hz. However, if we consider the time domain signal of Figure 6 (which accounts for contribution from all frequencies), it seems maximum velocity (after considering a 2:1 factor of tape and an LVDT scale factor of 3.3 V/in.) is approximately 13.3 in./s (0.338 m/s). Again assuming the same damping constant, peak power is approximately 5 kW. However, it may be cautioned that this 5-kW calculation is for peak power (when the truck hits a pot hole) and not average power, and so designing an electromagnetic shock with such a damping constant may not be easy.

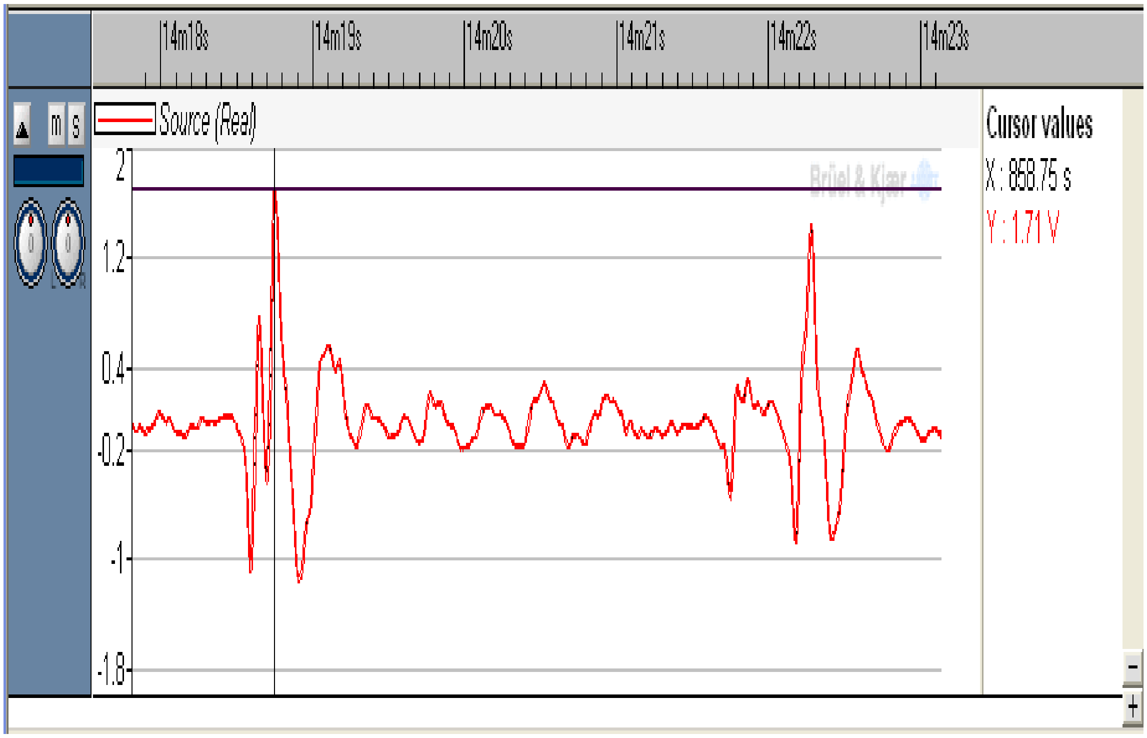

Figure 6. Time domain signal (with 2:1 reduction).

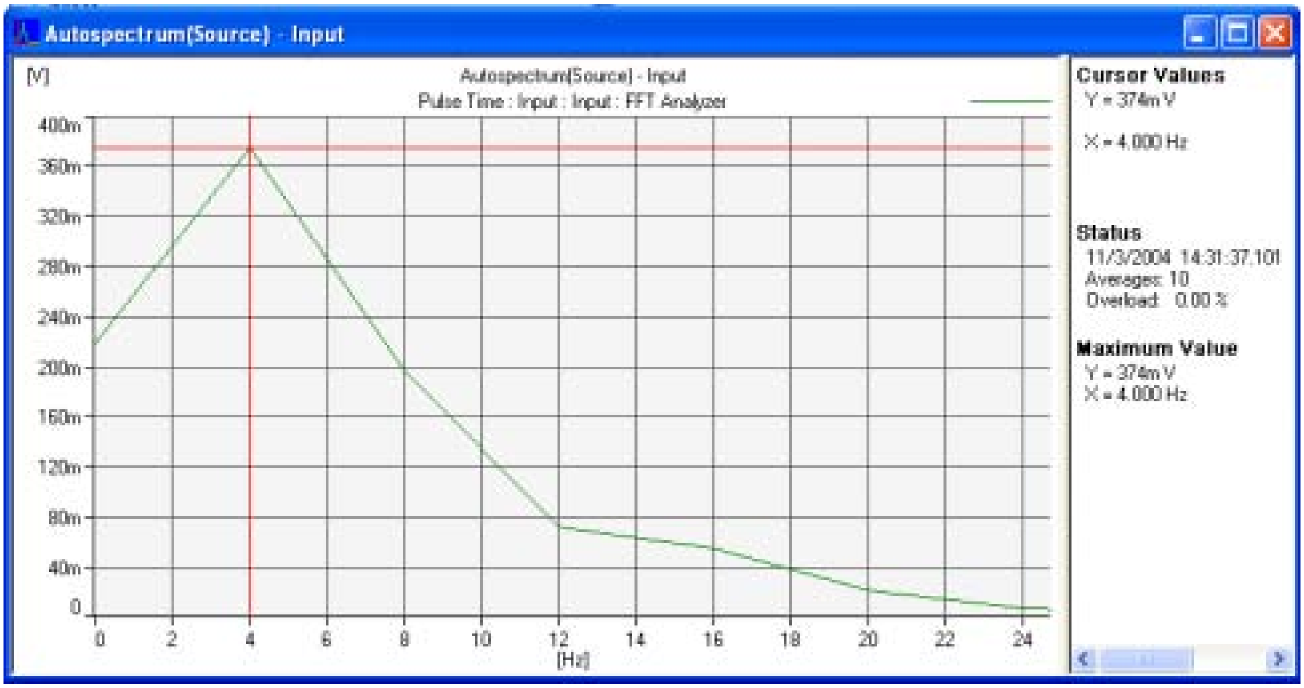

Figure 7. Frequency spectrum of the signal.

VI. Joining Carbon Composites

Innovative Structural and Joining Concepts for Lightweight Design of Heavy Vehicle Systems

Principal Investigators: J. Prucz and S. Shoukry
Department of Mechanical and Aerospace Engineering
West Virginia University
Morgantown, WV 26506-6106
(304) 293-3111 ext. 2314, fax: (304) 293-8823, e-mail: Jacky.Prucz@mail.wvu.edu

Investigators: G. William, T. Damiani, T. Evans, P. Shankaranarayana
West Virginia University
Morgantown, WV 26506-6106
(304) 293-3111, fax: (304) 293-6689

Technology Development Manager: Sid Diamond
(202) 586-8032, e-mail: sid.diamond@ee.doe.gov
Technical Program Manager: Jules Routbort
(630) 252-5065, e-mail: routbort@anl.gov

Contractor: West Virginia University
Contract No.: EE50692

Objectives

- Devise and evaluate lightweight structural configurations for heavy vehicles.
- Study the feasibility of using Metal Matrix Composites (MMC) for critical structural components and joints in heavy vehicles.
- Develop analysis tools, methods, and validated test data for comparative assessments of innovative design and joining concepts.
- Develop analytical models and software for durability predictions of typical heavy vehicle components made of particulate MMC or fiber-reinforced composites.

Approach

- Devise integrated design concepts for critical structural components of van trailers.
- Develop innovative, fastener-less joints for composite and dissimilar materials.
- Prototype and evaluate experimentally new composite design and joining concepts.
- Model damage effects at the mesoscale level to predict the durability of composite materials in heavy vehicle structures.

Accomplishments

- Alternative structural arrangements for the floor of a heavy van trailer have been devised and analyzed, leading to the conclusion that sandwich panels allow minimum weight designs for a variety of core configurations.

- Alternative material selections have been considered for the structural floor of a heavy van trailer, leading to the conclusion that carbon-carbon composites enable the greatest weight savings, depending on the specific floor design configuration.
- Alternative fastener-less joining methods between sandwich panels in various sections of a typical van trailer structure have been devised and evaluated, both through theoretical modeling and actual prototyping.
- Double-lap-bolted joints made of different MMC materials have been evaluated both through standard ASTM tests and failure simulations based on finite-element analysis, leading to the conclusion that such joints are likely to fail early in the bearing mode, because of the brittle behavior of MMC materials.

Future Directions

- Develop and validate integrated, minimum-weight design concepts of full-scale structural assemblies for van trailers, based on sandwich panels with optimized face sheet and core configurations.
- Build a full-scale baseline prototype of a lightweight van trailer for extensive instrumentation and testing in realistic operation scenarios, as well as for showcasing the new concepts to producers and operators of heavy vehicles.
- Establish a knowledgebase for reliable durability predictions in terms of either fatigue life or damage tolerance of composite materials, for decision support in both the design and repair of structural components in heavy vehicle systems.

Introduction

This report summarizes the second year of a project initiated at West Virginia University (WVU) to investigate practical ways of reducing the structural weight and increasing the durability of heavy vehicles, through judicious and innovative use of lightweight composite materials. While the project was initially focused on specific components in a trailer structure and on a specific Aluminum/ Silicone Carbide (Al/SiC) MMC, namely the "LANXIDE" material [1], the second-year effort was expanded from the component to the system level and from MMC to other composite material systems. Broadening the scope of this research is warranted not only by the structural and economical deficiencies of the "LANXIDE" MMC material, as outlined in the previous report [1], but also by the strong coupling that exists between the material and the geometric characteristics of the structure. Such coupling requires a truly integrated design approach, focused on the heaviest sections of a van trailer. It is obvious that the lightweight design methods developed through this work will not be implemented by the commercial industry unless the weight savings are, indeed, impressive and are proven to be economically beneficial in the context of Life Cycle Costs (LCC).

Integrated Design Concepts for Critical Structural Components

The chassis assembly contributes about 73% of the overall weight of a typical van trailer (15,100 lb for a 48-ft-long trailer), of which 47% is contributed by the oak floor panels and the cross beams that support the floor [1].

The baseline loading scenario assumed for integrated structural design of the chassis components consists of structural dead loads and the live load applied by a moving loaded forklift [1]. The corresponding baseline minimum weight design of a structural floor built on steel I-cross beams was evaluated in terms of its factor of safety by calculating the stress and deformation fields associated with such loading.

Alternative design concepts for the structural floor of a van trailer were devised to reduce its weight below that of the current baseline configuration. All of these lightweight designs rely on sandwich panels with various material and geometric characteristics of the core. The main design objective stated for their comparative evaluation is an optimal trade-off between the overall weight and stiffness of the floor. The alternative floor design configurations have to satisfy the following design criteria:

- The factor of safety in flexure must not be lower than 2.0.
- The free-edge deflection of any cross beam must not exceed that calculated for a similar steel beam currently used in the baseline floor configuration.

Alternative 1: The core of the floor consists in this case of I-cross beams made of various candidate materials, spaced at a distance of 1 ft apart, and connected by two fiberglass "bearing" bars "running" along the trailer through holes drilled in the web sections of the cross-bars (Figure 1).

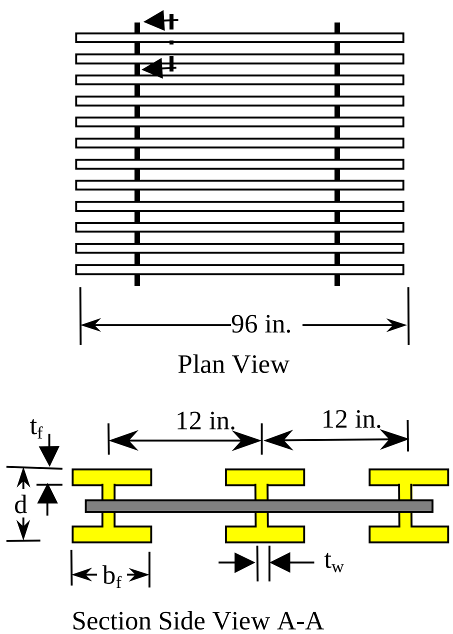

Figure 1. I-cross beam flooring.

For each alternative material selection for the I-cross beams, Table 1 specifies the minimum standard dimensions required for the I-beam cross-section in order to meet the design criteria outlined above. In addition, Table 1 displays the factors of safety corresponding to these dimensions, the edge deflection, and the weight of the unit floor area corresponding to every material option for the I-cross beams.

The results presented in Table 1 reveal that the current weight of a baseline van floor can be reduced by as much as 69% or 66% when the steel I-cross beams are replaced, through an integrated design approach, by I cross-beams made of carbon-carbon composite or magnesium alloy, respectively. These results demonstrate the drastic reductions in structural weight that can be achieved through rational applications of lightweight materials in heavy vehicles that integrate the layout and geometric design with the material selection process. This conclusion is further supported by similar studies on three other alternative design concepts for the trailer floor, as follows:

- **Alternative 2:** Sandwich panel consisting of top and bottom fiberglass faceplates and a core formed of transverse C-channel cross beams, as shown in Figure 2-a.
- **Alternative 3:** Sandwich panel built of ribbed fiberglass faceplates with a core consisting of hollow cross tubes of either rectangular or circular cross-section, as shown in Figure 2-b.
- **Alternative 4:** Floor constructed from sandwich panel with a homogeneous, lightweight core.

Table 1. Alternative material solution for I-beam floor.

Material	SIZE				Ultimate Strength (ksi)	Factor of Safety	Max. Edge Deflection (in.)	Unit Weight (Lb/ft^3)	Weight (lb/ft^2)
	d in.	b_f in.	t_w in.	t_f in.					
STEEL	4	2.5	0.16	0.25	80	4.38	4	2.5	0.16
Aluminum	8	2.25	0.13	0.19	35	3.38	8	2.25	0.13
EXTREN 525	8	4	0.38	0.38	30	8.70	8	4	0.38
Carbon-Carbon	6	3	0.25	0.25	155	17.78	6	3	0.25
Nitronic 19D Stainless Steel	4	2.5	0.16	0.25	103.6	5.69	4	2.5	0.16
Nitronic 60 Stainless Steel	4	2.5	0.16	0.25	160	8.84	4	2.5	0.16
Nitronic 30 Stainless Steel	4	2.5	0.16	0.25	117	6.46	4	2.5	0.16
Magnesium	6	2.5	0.16	0.25	26.8	3.0	6	2.5	0.16

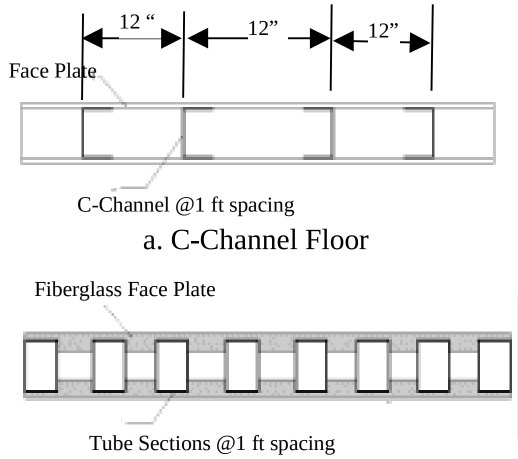

b. Tube Core Floor

Figure 2. Alternative floor designs.

The results of minimum weight, integrated design studies for all of the above four alternative sandwich panel configurations of the trailer floor are summarized in Table 2 for eight different material selections for the core of the panel. Both the maximum deflection and the minimum weight per unit area shown in Table 2 for every design option considered here meet the design criteria defined earlier in terms of the factors of safety and deflection limits.

The results displayed in Table 2 indicate that, for any core material selection, the best design configuration for maximum weight savings is that of sandwich panels with a light homogeneous core. On the other hand, the sandwich floor panel with a core formed of cross C-channel beams may even increase the required weight of the floor for certain material choices for the core C-channels. However, for most of the material candidates listed in Table 2, this structural arrangement appears to provide higher stiffness than the other options compared here. Carbon-carbon composites allow the largest weight reductions and the minimum deflections for any design configuration. Obviously, the benefits of using carbon-carbon cores are strongly dependent on the structural configuration of the floor. Emerging technologies for producing low-cost carbon-carbon composites are expected to make them affordable for high-volume applications in heavy-vehicle structures [2–5].

(Note: Every structural arrangement evaluated above could be further optimized by altering, for example, the spacing between cross beams, the number of longitudinal bars in Figure 1, or the characteristics of the face sheets. However, the main objective of this study is to assess the predicted trade-offs between weight savings and stiffness for alternate core material selections and not the optimization of any one particular structural arrangement or another.)

Table 2. Weight and deflection comparison of structural-material integrated design concepts.

	I-Cross Beams Connected by Bars through Web Centers **(Alternative I)**		Fiberglass Faceplates C-Channels Core **(Alternative II)**		Ribbed Fiberglass Faceplates with Core of Hollow Cross Tubes **(III)**		Sandwich Panels with Light Core **(Alternative IV)**	
Material	Deflection (in.)	Weight (lb/ft^2)	Deflection (in.)	Weight (lb/ft^2)	Deflection (in.)	Weight (lb/ft^2)	Deflection (in.)	Weight (lb/ft^2)
STEEL	0.11	6.47	0.08	6.70	0.08	12.70	0.09	5.14
Aluminum	0.09	6.50	0.08	4.03	0.08	5.83	0.13	1.77
EXTREN 525	0.11	4.61	0.07	5.50	0.25	6.99	0.07	4.10
Carbon-Carbon	0.05	1.98	0.06	2.21	0.06	6.00	0.09	1.04
Nitronic 19D Stainless Steel	0.13	6.38	0.08	6.59	0.08	12.49	0.10	5.06
Nitronic 60 Stainless Steel	0.12	6.50	0.09	6.72	0.09	12.72	0.11	5.15
Nitronic 30 Stainless Steel	0.13	6.30	0.08	6.51	0.08	12.32	0.10	5.00
Magnesium	0.17	2.18	0.13	2.59	0.13	3.76	0.10	1.28

Innovative Joining Concepts for Composites

The development of advanced joining concepts for heavy trailer structures requires both theoretical models and experimental results. This effort was directed mainly toward adhesive bonding of sandwich panels and bolted joints of MMC plate strips. It is difficult to join sandwich panels since the load transfer has to be distributed over large areas in order to prevent highly localized, concentrated stresses [7–9].

Various forms of joints between sandwich panels have been devised and prototyped in the process of constructing a scaled, all-composite van-trailer, as described in the next section of this report. All of these joints are free from mechanical fasteners and utilize different combinations of adhesive bonding and special connector parts to join (1) the side walls of the trailer to its floor and roof, (2) segments of the side walls, or (3) segments of the roof to each other. An example of a three-dimensional finite-element model (3D FEM) developed for theoretical analysis of a corner joint between sandwich panels (Alternative 4 in Table 2) is depicted in Figure 3. Since the panels connected through such a joint represent a corner section of a box trailer, their free ends in Figure 3 are constrained by symmetry boundary conditions. Both the vertical and horizontal panels penetrate the tailored connector part to an insertion depth of "L," along which a perfectly bonded interface is assumed to exist on all sides. Such a model provides an effective tool for trade-off studies of various material and geometric characteristics of the joint before an optimal configuration is prototyped and tested. Typical results for theoretical analysis of such a joint are illustrated, at two different loading levels, in Figure 4 for sandwich panels consisting of 0.02-in.-thick aluminum faceplates and 0.75-in.-thick, continuous wood core. They indicate that the bending stress in the sandwich panel reaches its maximum value just outside the corner connector, but its magnitude can be slightly reduced by increasing the "interlocking" length, "L." However, this design parameter has no significant effect on the maximum deformations depicted in Figure 4 for certain loading levels.

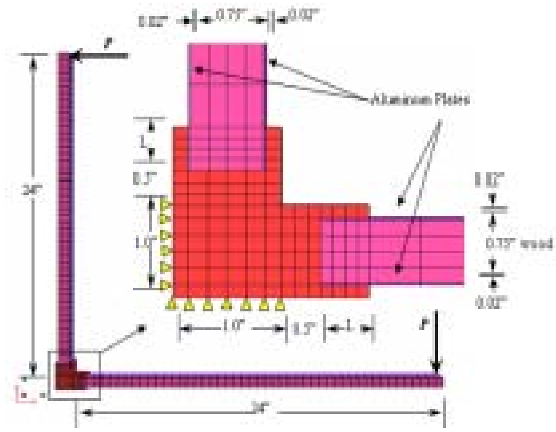

Figure 3. FE model of corner joint.

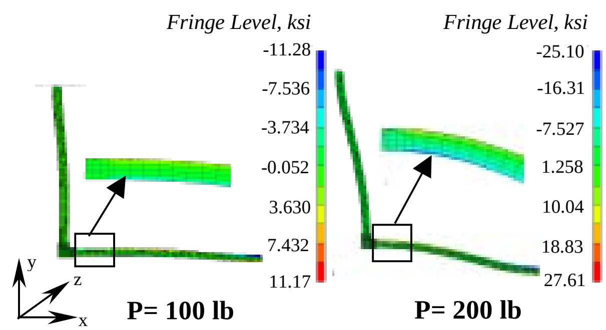

Figure 4. Fringes of bending stress.

Three-dimensional finite-element modeling (3DFEM) was also used for failure simulation of double-lap-bolted joints made of "Duralcan" and "LANXIDE" Metal-Matrix Composite (MMC). Both materials consist of an aluminum matrix reinforced by silicon carbide particles in various concentrations. The 3DFE models were built to match bolted joint specimens of different geometric configurations that were tested to failure under unixial tensile loading, as illustrated in Figure 5.

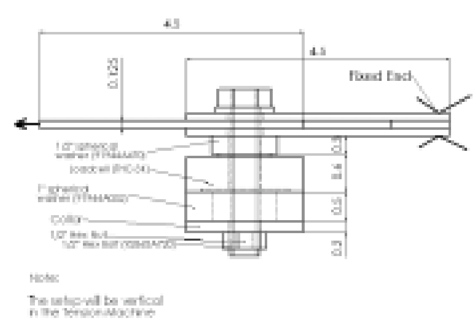

Figure 5. Testing setup of bolted joint.

The material properties used in the 3DFE model for the Duralcan and LANXIDE composites were verified experimentally through tests conducted in accordance with the ASTM standards E8M and D-70. The results obtained from these material characterization tests are summarized in Table 3.

Table 3. LANXIDE vs. Duralcan properties.

	Lanxide 30% Sic		Duralcan 20 % Sic	
	Measured	Published	Measured	Published
Young's Modulus (Msi)	15.45	15.97	17.73	14.6
Ultimate Strength (Ksi)	15.6	32.6	25.39	42.0

Table 4 displays a comparison between predicted and measured failure characteristics of Duralcan and Lanxide double-lap-bolted joint specimens of various "e/w" configurations (where "w" is the width of the face-plate, and "e" is the distance of the hole from the closest end edge). Excellent agreement can be observed between the theoretical and experimental results for Duralcan specimens. However, the test results for the LANXIDE specimens deviate significantly from the corresponding 3DFEM predictions, possibly because of inconsistent material properties and the existence of manufacturing defects in these specimens. The 3DFE model developed for design and failure analysis of MMC bolted joints was validated experimentally not only by the correlation between the calculated and measured failure loads, but also by comparing the predicted and the actual modes of failure, as illustrated in Figure 6.

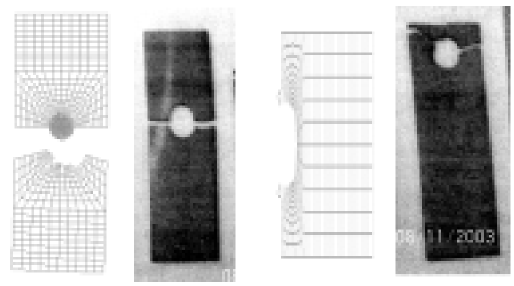

Net Section Shear Pullout

Figure 6. Failure modes of MMC joints.

Prototyping of Scaled Trailer Model

A 1:4-scale model of a van trailer was designed and fabricated, as shown in Figure 7, to investigate new joining concepts and assess their feasibility and benefits as alternatives to conventional riveted, bolted or welded joints in heavy vehicle structures. The entire prototype was constructed manually from commercial, standard parts, such as glass fiber-reinforced polymer-matrix composite (PMC) panels, beams, rods, angles, and anodized aluminum "H," "J," "U," and corner channels, as a preliminary test-bed for evaluating innovative design, assembly, and fabrication methods.

The fabrication of the scaled trailer model required judicious combination of aluminum parts with tailored fiberglass composite panels, I-beams, rods, and angles to fit design specifications aimed at building a lightweight, modular prototype, with strong structural integrity. This was a step-by-step process whereby the feasibility of new concepts was explored one-by-one, incrementally. The rear section of the model was completed in the first phase, thus

Table 4. Comparison of test and 3DFE model results for Duralcan and LANXIDE bolted joints.

Specimen	e (in.)	w (in.)	Duralcan Failure Load (Lb)			LANXIDE Failure Load (lb)			Failure Mode
			Measured	3D FE	Difference	Measured	3D FE	Difference	
Specimen 1	2.5	2.0	3561	3776	6%	2277	1350	-41%	Net Section
Specimen 2	1.5	2.0	2516	3500	39%	1740	1350	-22%	Net Section
Specimen 3	0.6	2.0	1294	1348	4%	516	700	36%	Shear pullout
Specimen 4	2.5	1.5	2139	2360	10%	2121	1300	-39%	Net Section
Specimen 5	0.6	1.5	1353	1264	-7%	490	674	38%	Shear pullout

Figure 7. Views of the van trailer model and joining details.

providing ideas and lessons that were subsequently applied to the rest of the trailer.

The fiberglass panels are used for the roof and side-walls of the trailer and for floor covering. I-beams are the main load-bearing elements of the floor. These cross-beams are reinforced by fiberglass "bearing bars," which run perpendicular to and through the web of each I-beam. They also provide connection points to the bogey, landing gear, and kingpin on the underside of the trailer. It is obvious that the design configuration selected for the floor of the prototype trailer is similar to the design Alternative I (Figure 1) discussed in this report. Aluminum H-channels and edge corners were cut and manufactured to provide connections between adjacent side panels, as well as connections between the side panels and the top panel. The H-channels are anodized aluminum with 0.25-in. openings to accept the thickness of the side panels. The H-channels had to be cut to the proper height and trimmed to allow proper spacing with the corner edge trim. The U-channels and J-channels are used as trim for the rear door of the trailer.

The side-walls of the trailer were segmented to provide a reasonable level of flexibility for absorbing dynamic forces. Bonding was utilized extensively along the contact surfaces between the various aluminum channels and the fiberglass panels in order to secure the joints and enhance the overall stability, or integrity, of the model. The bonding process requires thorough cleaning of the aluminum channels and roughing the fiberglass panels with sandpaper. *Araldite 2021* toughened methacrylate adhesive has been used to bond the fiberglass to the metal. *Araldite 2021* provides a strong bond that fills voids between the mating parts and exhibits elastic behavior in its cured state.

The prototype model was designed and constructed in a modular configuration that includes three removable or replaceable middle segments. The overall length of the model can therefore be changed in steps of one foot within the 9–12-ft range corresponding to the dimensions of the 1:4-scale model. In a real trailer, this feature would allow the adjustment of the trailer length to the volume of cargo that has to be transported in a particular run. Furthermore, it allows modular repair or replacement of damaged sections, without affecting the entire trailer.

In conclusion, the prototype model provides a scaled-down physical representation of an actual trailer that is used to assess the feasibility, benefits, and deficiencies of alternative joining concepts, floor designs, side and top panel configurations, and bonding techniques. It has stimulated additional creative ideas for developing effective design, assembly, and construction methods for heavy van trailers.

Durability Predictions of Particulate MMC Materials

A new task has been initiated in the second year of this project to develop a predictive model for the effects of intrinsic and/or externally induced multi-scale damage on the residual service life of fiber- and particulate-reinforced composite materials in critical components of heavy vehicle structures. The model relies on the periodic microstructure of such materials and leverages earlier research performed at West Virginia University in the area of Continuum Damage Mechanics (CDM) of fiber-reinforced Polymer Matrix Composites (PMC). The major contribution of those efforts so far is the development of a CDM model formulated in terms of parameters that can be measured easily from standard ASTM tests of single lamina coupon specimens and utilized for predicting the non-linear response of macro-scale laminates in the presence of damage [10, 11].

The main objective of the current task is to develop an analytical model for analyzing the behavior of damaged particulate-reinforced metal matrix composites (PMMC) subjected to monotonic loading, by expanding and modifying the prior work on fiber-reinforced composites. This approach allows cost-effective quantification and analysis of material property loss associated with damage initiation and accumulation in structural components made of PMMC or other composite materials. To achieve this goal, the model will be developed as a user-defined input to a commercial finite-element software package, such as ANSYS. A survey of pertinent literature dealing with the onset of localized micro-scale crack initiation and growth in extruded PMMC materials [12, 13] reveals that damage initiates at the micro-scale from clustering of the reinforcement particulate in certain regions throughout the PMMC material [14]. Consequently, this task is currently focused on the implementation of periodic microstructure techniques, along with CDM modeling, in order to describe the constitutive behavior of PMMC materials subject to monotonic loading through the analysis of clustering regions. Periodic microstructure techniques are used to determine the effective properties of the PMMC material with homogenized clustering regions, as depicted in Figure 8.

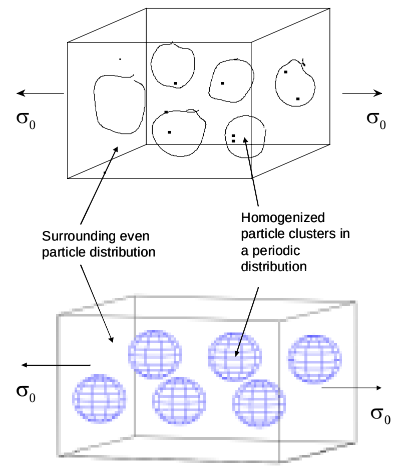

Figure 8. Homogenization of particle clusters in MMC model.

References

1. J. Prucz and S. Shoukry (2003). "Structural Characterization and Joining of MMC Components for Heavy Vehicles." 2003 Annual Progress Report on Heavy Vehicle System Optimization, U.S. Department of Energy, Washington, D.C., pp. 115–120.
2. C.F. Leiteen, W.L. Griffith, and A.L. Compere (2002). "Low-Cost Carbon Fibers from Renewable Resources." 2002 Annual Progress Report on Automotive Lightweighting Materials, U.S. Department of Energy, Washington, D.C., pp. 115–119.
3. H. Dasarathy, C.L. Leon, S. Smith, and B. Hansen (2002). "Low-Cost Carbon Fiber Development Program." 2002 Annual Progress Report on Automotive Lightweighting Materials, U.S. Department of Energy, Washington, D.C., pp. 121–132.
4. D.G. Baird, A.A. Ogale, J.E. McGrath, D.D. Edie (2002). "Low-Cost Carbon Fiber for Automotive Composite Materials." 2002 Annual Progress Report on Automotive Lightweighting Materials, U.S. Department of Energy, Washington, D.C., pp. 133–136.

5. F.L. Paulauskas (2002). "Microwave Assisted Manufacturing of Carbon Fibers." 2002 Annual Progress Report on Automotive Lightweighting Materials, U.S. Department of Energy, Washington, D.C., pp. 137–142.
6. J.R. Vinson (1999). "The Behavior of Sandwich Structures of Isotropic and Composite Materials." Technomic Publishing Company, Inc. Lancaster, Pennsylvania.
7. I. Kuch and F. Henning (2000). "Thermoplastic Sandwich Structures with High Content of Recycled Material — An Innovative One-Step Technology." 21st SAMPE Europe International Conference, Paris, France, April 18–20, 2000.
8. S.E. Mouring and R.P. Reichard (2001). "Fabrication of a Composite Superstructure Using a new Assembly Method." Proceedings of the 11th International offshore and Polar Engineering Conference.
9. Hexel Composites. Adhesive Bonding of Honeycomb Structures. http:// www.heselcomposites.com
10. E.J. Barbero and L. DeVivo (2001). "A Constitutive Model for Elastic Damage in Fiber-Reinforced PMC Laminae." J. of Damage Mechanics, 10(1) 73–93.
11. E.J. Barbero and P. Lonetti (2001). "Damage Model for Composites Defined in Terms of Available Data." Mechanics Of Composite Materials And Structures, 8(4), 299–315.
12. D.L. Davidson (1991). "Fracture Characteristics of Al-4% Mg Mechanically Alloyed with SiC." Metal. Trans. A. 18A, pp. 2115–2138.
13. L. Mishnaevsky, M. Dong, S. Honle, and S. Schauder (1999). "Computational Mesomechanics of Particle-Reinforced Composites." Computational Materials Science, v. 16, pp. 133–143.
14. J. Brockenbrough, W. Hunt, and O. Richmond (1992). "A Reinforced Material Model Using Actual Microstructure Geometry." Scripta Metal. Mater., 27, pp. 385–390.

VII. Analysis

Systems Analysis for Heavy Vehicles

Principal Investigator: Linda Gaines
Argonne National Laboratory
Argonne, IL 60439
(630) 252-4919, fax: (630)252-3443, e-mail: lgaines@anl.gov

Technology Development Area Specialist: Sidney Diamond
(202) 586-8032, fax: (202) 586-1600, e-mail: sid.diamond@ee.doe.gov

Contractor: Argonne National Laboratory
Contract No.: W-31-109-Eng-38

Objectives

- Analyze transportation technologies and fuel-efficiency measures objectively.
- Provide critical and unbiased evaluation of transportation or materials-related projects.
- Serve as a key idling-reduction resource for DOE.

Approach

- Analyze technical and economic characteristics of competing technologies.
- Represent DOE at idling-reduction meetings.
- Coordinate efforts by DOE and other agencies.
- Supply technical input to policy-makers.
- Maintain awareness with latest technical and political developments related to idling.

Accomplishments

- Revised and expanded technology sections of idling-reduction report.
- Planned and acted as technical chair for National Idling Reduction Planning Conference.
- Provided tutorials on idling reduction at numerous Clean Cities and other meetings.
- Completed short study of dynamic brake energy recovery for locomotives and presented at Railroad Environmental Conference.
- Managed awarding of contract to Antares for analysis of wear due to idling.

Future Direction

- Complete revised and expanded technical report.
- Lead Technology Working Group (with Lee Slezak).
- Complete and promulgate National Idling Reduction Plan (with other working group chairs).
- Evaluate technology options for domestic liquid fuel production.

Truck Idle-Reduction Technology Comparison

Before comparing energy savings or economics, it is useful to clarify the basic differences among the available devices for reducing long-duration idling. They do not all supply the same services, and so their relative merits will depend on several factors, including services required and number of hours of idling that would be avoided. Table 1 summarizes the basic differences among the technologies and points out any particular advantages or disadvantages of each.

Table 1. Benefits and drawbacks of truck idle-reduction technologies.

Technology	Benefits	Drawbacks
Automatic start/stop	Intermittent services anywhere	Noise disrupts rest; uses main engine
Direct-fired heater	Heat anywhere; small and inexpensive	Cannot supply cooling; uses battery
Auxiliary power unit (APU)	HVAC and power anywhere	High cost and weight
Truck stop electrification (TSE)	All services; no local emissions	Only at fixed locations; limited potential
Integrated electrical accessories with APU	HVAC and power anywhere	In development (2005 intro); only on new trucks

Energy Use and Emissions

Energy Use

Diesel fuel saved by reducing idling is fairly simple to estimate; it is simply the difference between the fuel that would have been used idling and that consumed by the alternative system. For the automatic start/stop systems, the fuel saved is simply that percent of idling fuel use that corresponds to the period when the engine is off. Emissions are similarly reduced. If the idle-reduction technology burns diesel fuel, savings are reduced by the device's own fuel consumption, typically 5–25% of the savings. Emissions may be reduced by more or less than the same percentage, depending on how clean the idle-reduction technology is. Such devices all meet appropriate small engine standards, but these are generally less stringent than those for truck engines. Emissions from several devices have been measured by the EPA. For devices that plug in, all of the idling diesel fuel use and emissions are avoided, but the fuel use and emissions from electricity generation at the power plant must be accounted for. Several earlier publications have neglected to do this.

Finally, there is the more complicated case of devices that run off of power from batteries that have been charged during the vehicle's operation. No information was found about the additional fuel consumed due to battery charging. Because systems that run off a battery do not burn fuel while they are providing services, vendors generally do not recognize and report fuel use for their systems. We estimate it here. If the unit draws a maximum of 8 Amps at 12 V, and we assume that it operates at 75% capacity for 8 h, for an average power draw of 72 W, it consumes 2074 KJ of energy directly. From the Bosch Automotive Handbook, automotive alternators are approximately 50% efficient — meaning that 50% of the rotational energy from the accessory-drive belt is converted into electrical power. The charging efficiency of typical automotive-style charging systems is between 50 and 65%, meaning that 50–65% of the electrical power delivered to the battery actually goes into increasing its state of charge, and the rest is lost as heat. The faster the battery charges, the more inefficient the process becomes. We assume that the battery is charged relatively slowly while the truck is operating, and charges efficiently (65%).

That means that the engine-work-to-battery-charge efficiency is 32.5%. Therefore, the amount of energy the engine must provide to make up for what the air conditioner consumed is 6382 kJ. That amounts to 221 W of engine power. This is the most optimistic case, assuming a separate battery pack for this purpose. If the starting battery is used, the minimum level of charge needs to be maintained to ensure starting, so the charging rate must be higher, which means lower efficiency.

The 6383 kJ of energy is required at the drive belt. This energy is supplied by the truck's diesel engine, which is about 40% efficient in turning fuel energy into shaft power. Therefore, it needed to burn 15,958 kJ (15,196 Btu) of fuel, or about 0.112 gal of fuel (0.014 gal/h). This is a best-case estimate; actual fuel use could easily be doubled, depending on conditions and weather (battery-charging efficiency is very low in cold weather). This is still very low energy use, because the 72 W power demand is less than that of most light bulbs. Even if the unit drew 350 W, total fuel use would only be 0.14 gal/h in cold weather.

Emissions

Until recently, one had to rely on measurements by equipment manufacturers to estimate emission reductions achieved by use of alternative devices. However, recent experiments funded by the U.S. EPA, New Jersey DOT, and DOE at the Army's Aberdeen Test Center carefully measured emissions of CO_2, CO, NO_x, HC, particulates, and aldehydes from idling trucks, and from installed auxiliary power units and heaters, under several sets of conditions. Measurements were taken at several idling speeds, in hot, cold, and mild atmospheric conditions, and with several different trucks. The results of this work clearly demonstrate the environmental benefits of reducing truck idling. The detailed results are presented in two papers [1,2]; we summarize them and draw some conclusions here. The exact numbers vary with truck model; we chose to provide as an example the impact reductions achieved with the newest truck tested (2001 Freightliner), because of the rapid turnover of truck fleets. We determined that it was most meaningful to compare impacts from a heater or APU at 0°F to those from the truck idling at the speed at which it would normally idle to supply heat (700–800 RPM). Therefore, we interpolated the detailed data provided and estimated truck heating emissions at 750 RPM and similarly estimated idling emissions during cooling at 90°F at 900 RPM. Note that the conditions chosen are somewhat extreme; impacts at more moderate temperatures are expected to be lower. An accurate estimate of annual impacts and benefits would require integration over typical annual conditions and loads. It would also require measurement of APU impacts at 65°F, when it would be run for electrical loads only.

The emissions for the truck and alternatives at these two extreme conditions are shown in Table 2. As expected, all of the impacts are very low from the heater, but it is only supplying heat and no electricity.

All of the impacts from the APU are lower than those from idling, for both heating and cooling. It is interesting to note that the emission reductions are greater on a percentage basis (in most cases) than the fuel use reductions (as represented by the CO_2 emissions). This could be because idling represents a non-optimal engine condition, compared to that of the auxiliary device. The one glaring exception is the PM emissions from the APU when supplying air conditioning. These are reduced by only 50%, even though fuel use is reduced 75%. Since only one APU was tested, this may or may not be typical. However, note that the NO_x emissions have been reduced disproportionately, and it is likely that the APU's engine could be adjusted to trade NO_x for PM.

Impacts from those devices that run off the battery would be equal to the marginal emissions from increasing fuel consumption on the road. The impacts from shore power are simply the emissions from generation of the electricity that they draw. Although this actually varies by region with fuel mix, we will use the national average for technology comparisons in this report.

Economics

The economic benefits of idling-reduction technologies depend on the costs avoided by not idling and on the costs incurred to purchase or lease and use the idling-reduction technology. Benefits are expected to increase as the number of idling hours displaced increases. The largest avoided cost, that

Table 2. Emissions from idling and alternatives.

Device	Condition	CO_2 g/h (% red.)	NO_x g/h (% red.)	HC g/h (% red.)	PM g/h (% red.)	CO g/h (% red.)
Truck	Heat	7500	158	26.2	3.43	115
APU	Heat	2146 (71)	8.7 (94)	7.8 (70)	0.478 (86)	25.0 (78)
Heater	Heat	445 (94)	0.2 (99+)	0.04 (99+)	0.055 (98)	0.1 (99+)
Truck	AC	9500	137	35.7	2.0	60
APU	AC	2351 (75)	11.4 (92)	4.2 (88)	0.995 (50)	10.8 (82)

for fuel, can be calculated simply for on-board technologies that burn diesel fuel (e.g., APUs and heaters). For these, the fuel savings are simply the difference in hourly fuel use (in gallons per hour) between idling and APU use, multiplied by the number of hours of idling displaced during the period in question, times the fuel cost per gallon. For devices that plug in, the avoided fuel cost is simply the cost of the diesel that would have been burned idling minus the cost of the electricity purchased. The situation is more complicated for systems that run off of batteries that are charged while the engine is running. In that case, it is appropriate to estimate, and bear the cost for, the extra fuel burned during truck operation in order to charge the batteries, as was estimated above.

In addition to savings from reduced fuel consumption, not idling a truck reduces maintenance costs. Oil changes can be performed less frequently if the engine is operated for fewer hours; thus, the cost for oil changes can be reduced. The Technology and Maintenance Council (formerly the Truck Maintenance Council) of the American Trucking Associations has published two Recommended Practice (RP) Bulletins to help truckers estimate maintenance costs due to idling. The first, published in 1985, was superceded by another (RP1108) in 1995 [3], in which the cost estimates were drastically reduced due to the reduction in fuel sulfur and changes in idling practice. Care must be taken to use the updated version; several recent publications have cited the older one. The main difference is the number of “equivalent miles” represented by one hour of idling. The revised RP estimates this from the fuel consumption (i.e., each gallon of fuel used idling is accounted for as if it were used at the truck’s average miles per gallon). So one hour of idling is typically equivalent to about 6 or 7 miles of driving. Then, if an oil change costs $150 and is done every 35,000 miles, the cost per hour of idling is about $0.03. This calculation should be done more carefully, based on the actual fuel economy and oil change cost and frequency for the truck or fleet to be costed; this can be done by using the worksheet included here as Figure 1.

A similar calculation can be done for the cost due to overhaul. If a truck requires an overhaul after 500,000 miles, and the overhaul costs $10,000, the cost per hour of idling is $0.14. Again, this is simply an example. Some trucks just need part replacements, costing about $2500, while others might need a full engine-out overhaul, costing as much as $20,000. There is also considerable variation in mileage to overhaul; a typical mileage used to be 300,000, but now may be up to 1,000,000 miles, and no overhaul may ever be performed.[1] The worksheet allows the user to select appropriate entries for these parameters. It would be very useful to obtain actual data on the effects of idling on oil quality and engine wear.

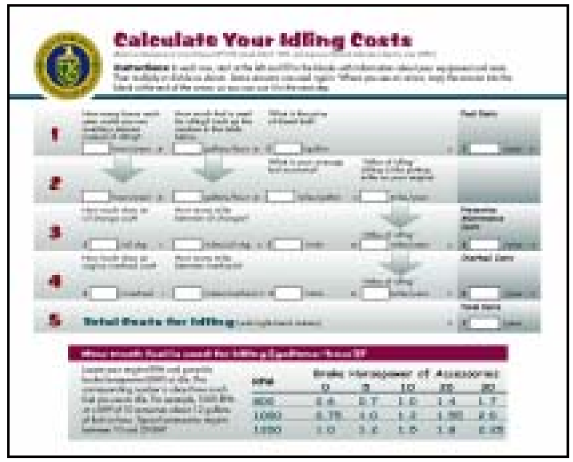

Figure 1. Idling cost worksheet.

Note that many truck owners, especially fleet owners, sell their trucks before it would be time for an overhaul, and therefore may not choose to include this component in their cost estimates. However, if the buyer can see the truck’s idling history in its computer records, the purchase price will theoretically be reduced for a truck that has idled excessively. However, mileage does not seem to be a key parameter cited in ads for used trucks.

Once the fuel and maintenance costs for idling have been estimated, the savings and payback times for the various idle-reduction technologies can also be estimated. Figure 2 shows the payback time for several alternatives, as a function of idling hours displaced. The times in the table are durations of device operation; for example, if the device is a heater, those hours are during the winter only, so the months until payback are also winter only, and it may take two years to accumulate 12 months of payback time. Payback times for a truck with low

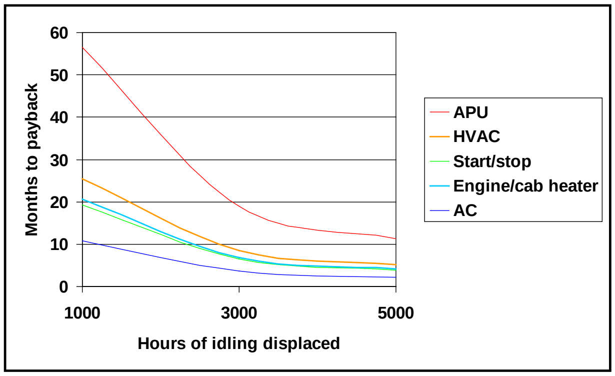

Figure 2. Reduction of payback time with increased idling hours.

yearly idling time are very long. Thus, a firm that has reduced its idling by changing the operating practices of its drivers might not find it economical to install equipment to further reduce idling.

Truck stop electrification (TSE) costs are slightly complicated because some are borne by the truck owner and some by the owner of the electrified system. Both must see an appropriate payback if the systems are to be installed and used. For standard TSE, the trucker sees the cost of the equipment required to electrify the truck, and the marginal cost of using an electrified space at a truck stop (the extra cost over standard space rental). This is presumably greater than the actual electricity price. The truck stop owner must pay (1) to install and maintain the electric plug system and (2) for the actual utility bill. There is little incentive at this time to electrify truck stops; the few that have been demonstrated have rather low utilization because so few trucks are able to use the spaces so far. [2]

Advanced TSE is a win for the truck owner; the avoided idling costs are as above, and the cost to use the system is simply the small initial cost of the window template (about $10) plus the hourly charge of $1.50 ($1.25 for subscribers). The economics of the system itself are less clear. The system is installed by its manufacturer, with the truck stop owner receiving a portion of the proceeds. The installation cost is as much as $17,000 per space and is generally shared by a government agency in order to demonstrate the technology. Operating revenues are the fees collected for the service, minus any cut to the truck stop owner, minus any maintenance costs. These may not be small, given the reported 12–20 staff members required per 100 parking spaces. Detailed costs have not been published, but it is likely that high utilization would be required to make the project economical.

Conclusions

In summary, although numerous technologies are available to reduce idling of heavy-duty trucks, there is no one perfect device that will satisfy the needs of every trucker. The appropriate device to choose depends on the region that is traveled (for instance, a southern route might need just air conditioning), the schedule (shorter hauls might not justify APU costs), and the equipment available (highly traveled routes will install electrification faster). Better operating data and continued technological development will allow truck owners to make purchase decisions with more confidence in the future.

References

1. Particulate Matter and Aldehyde Emissions from Idling Heavy-Duty Trucks, J. Storey, et al., SAE Paper 2003-01-0289 (2003).
2. Study of Exhaust Emissions from Idling Heavy-Duty Diesel Trucks and Commercially Available Idle-Reducing Devices, H. Lim, U.S. EPA Office of Transportation and Air Quality, EPA420-R-02-025 (October 2002).
3. TMC Recommended Practice 1108, Analysis of Costs from Idling and Parasitic Devices for Heavy Duty Trucks, American Trucking Associations, March 1995.

[1] Personal communication, A. Laible, Cox Transfer, January 2004.

[2] T. Perrot et al., Transportation Research Board, January 2004.

VIII. Off-Highway

A. 21st Century Locomotive Technology

Principal Investigator: Lembit Salasoo
General Electric Global Research
1 Research Circle, Niskayuna, NY 12309
(518) 387 5024, fax: (518) 387 6675, e-mail: salasoo@crd.ge.com

Technology Development Area Specialist: Sidney Diamond
(202) 586-8032, fax: (202) 586-1600, e-mail: sid.diamond@ee.doe.gov
Field Technical Manager: Jules L. Routbort
(630) 252-5065, fax: (630) 252-4289, e-mail: routbort@anl.gov

Participant: Paul K. Houpt, General Electric Global Research

Contractor: General Electric Global Research
Contract No.: DE-FC04-2002AL68284

Objectives

- Develop and demonstrate locomotive system technologies targeting gross fuel efficiency gains.
- Demonstrate a modular energy storage system for hybrid locomotive system on a hybrid locomotive platform.
- Develop optimization software for minimizing fuel consumption in both hybrid and non-hybrid locomotives and demonstrate the consist optimizer on the test track.
- Demonstrate the combination of a modular energy storage system and a fuel optimizer on a hybrid locomotive with a full-scale energy storage system.

Approach

- Specify and develop advanced modular energy storage units and lab test prototype modules.
- Design and bench test advanced hybrid locomotive energy management system (EMS) controls and demonstrate controls on a hybrid locomotive on a test track.
- Develop suitable models for dynamic optimization of fuel use.
- Develop practical, robust fuel-use-optimization algorithms capable of locomotive implementation.
- Demonstrate fuel use optimization algorithms in off-line interactive simulation environment.
- Complete field demonstrations of selected fuel saving algorithms.
- Fabricate and bench test full-scale energy storage modules and associated controls.
- Integrate full-scale energy storage modules to hybrid locomotive.
- Design, fabricate, and bench test hybrid fuel optimizer controls.
- Integrate fuel optimizer controls on hybrid locomotive; demonstrate on test track.
- Measure and verify fuel savings benefit.

Accomplishments

- Downselected advanced battery technology for hybrid locomotive and initiated development of advanced modular energy storage units.
- Initiated advanced battery technology long-term life testing.
- Designed and bench tested advanced hybrid locomotive energy management system controls. Integration to hybrid locomotive under way.
- Conducted successful 3400-mi field test of Consist Manager system, demonstrating fuel savings of 1–3% (1.5% average).
- Designed and evaluated robust optimal and greatly simplified near-optimal approaches to compute fuel-saving driving plans.
- Developed real-time simulation platform for interactive demonstration of Consist Manager and Trip Optimizer.

Future Direction

- Fabricate and evaluate locomotive-worthy hybrid energy storage modules.
- Design the integration of a hybrid energy storage system to the hybrid locomotive platform.
- Fabricate full locomotive set of hybrid energy storage modules, integrate system to the hybrid locomotive, and track test.
- Develop "bullet-proof" and simple operator interface for fuel optimization.
- Conduct on-locomotive test of hybrid fuel optimization controls.
- Measure and verify fuel performance of combined system.

Introduction

A systems view of the locomotive and its consist reveals significant opportunities for double-digit reduction in locomotive fuel use through the following:

- Add new means to store and recover braking energy that would otherwise be dissipated as heat and
- Exploit new ways to coordinate train driving and energy storage through advanced controls, which leverages energy management throughout the trip.

When applied to the North American Class 1 railroad fleet, advanced hybrid-electric propulsion technology for storing and recovering the braking energy would save 450 million gallons of diesel fuel annually, consist fuel optimizer techniques would save 55 million gallons annually, and trip fuel optimization together with hybrid technology would save an additional 230 million gallons annually.

Two major fuel optimization strategies are being developed: (1) Consist Manager — control logic that takes the commanded power by the driver (throttle notch) and distributes it among operating locomotives in the most fuel efficient manner and (2) Trip Optimizer — control logic that works in collaboration with the driver and dispatcher to plan and drive a trip, taking into account the power consist, terrain, freight load, and operating constraints along the way. FY 2004 efforts culminated in the highly successful demonstration of consist optimizer fuel savings on a group of Class 1 railroad revenue missions. As a direct result of this DOE project, a commercial Consist Manager system product has been launched. In addition, the best battery technology solution was downselected from the available advanced hybrid battery technologies. Development started of a locomotive-worthy system for freight locomotive demonstration in 2006.

Advanced Modular Hybrid Energy Storage Development

Typical hybrid operation scenarios were determined from existing locomotive field data in order to determine the requirements of the hybrid energy storage system's performance. Studies to address battery system technology developments that would meet the hybrid locomotive requirements were carried out by advanced battery vendors. A comparative assessment of the results was carried out, in terms of footprint (weight and volume) driven by life, power, and energy requirements; thermal and electrical management requirements; and readiness for locomotive deployment. It was seen that the capabilities of the vendors and energy storage technologies were clearly differentiated. One technology and one vendor were selected for development and delivery of enhanced-capability modules. Agreement was secured with the advanced energy storage vendor to work to meet the project schedule and deliver prototype modular energy storage units for evaluation in the next project year and to subsequently deliver the full set of advanced modular energy storage units for on-locomotive testing in FY 2006. Battery composition modifications were evaluated for customization to meet locomotive requirements.

The life of hybrid locomotive battery systems is critical to acceptance by the railroad industry. Battery cycling life depends on many operating parameters, such as duty cycle, depth of discharge, and operating temperature, and there is a significant gap in published data applicable to candidate advanced battery technology performance in hybrid locomotive application. A battery subassembly testing program was set up to develop detailed data to extend understanding of the life in the locomotive application. A systematic life-testing protocol was developed to establish the baseline cycling life entitlement of the advanced energy storage technology. It was expected to continue long-term testing for at least 12 months.

Initial results of life-cycle testing indicated that some of the electrochemical cells under test had drifted away from their operating point due to inaccurate measurement of charge. Figure 1 shows module voltage over selected charge-discharge cycles. It can be seen that the end-of-discharge voltages at approximately 750 s and end-of-charge voltages at approximately 1500 s are trending lower from cycle 100 to cycle 300. This indicates that the cycle mean state of charge is trending down and is not being maintained constant as is required by the life-testing protocol. Assessment of the condition of the modules indicated that some had been exercised beyond manufacturer's recommended limits, and so they may have suffered premature aging and thus should not be used further for life testing. The test protocol was revised and a new set of battery modules was obtained for restarting life tests with appropriate control of operating point.

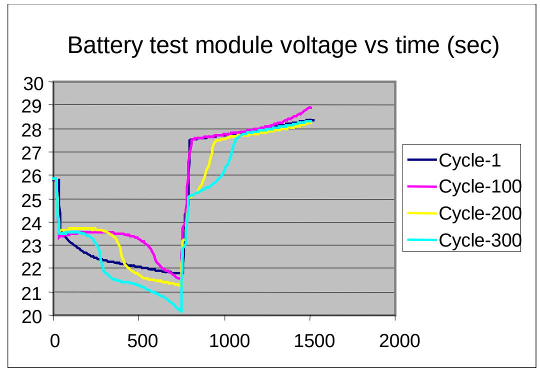

Figure 1. SOC drift of battery test module.

Advanced Hybrid Locomotive Energy Management System Controls

Detailed analysis was carried out of hybrid locomotive field test data to confirm performance gaps in battery management. It was decided that battery management enhancements would address thermal compensation and accurate internal state determination.

Extensive laboratory testing of battery modules of the types to be used in the upcoming advanced hybrid EMS locomotive track test was carried out to develop a database for use in battery state prediction. The performance of the battery state computation in a hybrid locomotive duty cycle was assessed by exercising the battery modules with data collected from the previous field test. The first battery state prediction algorithm was not successful, and so a follow-up round of laboratory testing was performed in more detail. A temperature compensation algorithm was successfully developed, which will enable better utilization of energy storage battery capabilities.

The hybrid locomotive advanced energy management system track test will be carried out on a more advanced platform than presented in the proposal. In the April 2002 21st Century Locomotive proposal, the platform for demonstrating an advanced energy management system was shown to consist of a towed energy storage container mounted on a flatcar, electrically connected to a GE AC-4400 locomotive. This hybrid testbed configuration has been upgraded by GE through introduction of nickel-metal-hydride technology of the type developed by the U.S. Advanced Battery Consortium, and the hybrid energy storage system was mounted onto the locomotive platform itself (Figure 2).

This "on-board hybrid" locomotive is suitable for field testing in freight hauling service. Future testing under task 3 of this program will have enhanced value, as it will be using more advanced battery technology and a realistic locomotive platform. GE Rail is completing required software and hardware modifications to the hybrid locomotive (at no cost to the program) to measure key hybrid battery parameters and interface these to the advanced EMS controls.

The DOE team was able to inspect the GE Rail on-board hybrid locomotive and ride the locomotive on the GE test track during the May 13, 2004, project review in Erie, PA.

A test plan for track testing of the hybrid locomotive with advanced EMS control was prepared. An extensive evaluation of the installed hybrid batteries was performed. After consultation with the battery manufacturers (including an on-site visit), the batteries were cleaned, overhauled and tested to

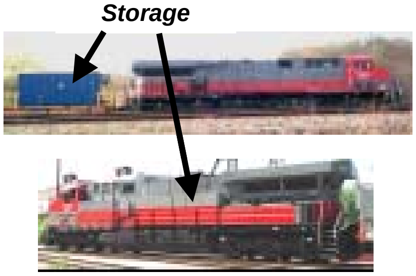

Figure 2. Tow-behind and on-board hybrid locomotive configurations.

establish their existing capability. When the battery parameter measurement modifications to the hybrid locomotive are completed, the track test of the advanced EMS algorithms will be carried out.

Models for Fuel Use Dynamic Optimization

Hybrid energy storage capability was added to our conventional locomotive and train analysis tools. This enabled setting up the hybrid trip optimization problem, which can be formulated in several ways. In one approach, the energy storage control is treated as an additional optimization variable. This approach will enable us to explore generalized strategies of hybrid energy management that may be non-intuitive. The integrated model allows study of the impact of energy management strategies on the trip optimization problem.

Trip Optimizer Algorithm

Computing a driving strategy for a freight consist to minimize fuel subject to operating constraints is difficult because of the many constraints and conflicting objectives. For example, over a 100-mi journey, speed limits may change 50 times and have thousands of decision variables (e.g., 50 m.p.h. average speed with 1-s control updates). To form a numerically reliable baseline in solving these optimal control problems, the goal is to develop numerically robust solution techniques, accomplished with proprietary software. In this problem formulation, the objective function can include fuel consumed, total emissions generated, target arrival time, rate of change of throttle position (e.g., as a penalty against induced slack-action), and other performance-related variables. Constraints incorporated can include speed restrictions along the route and power limits. Information about the track grade and curvature is part of locomotive train dynamic model. We have achieved major progress in development of reliable methods for computing optimal driving plans in Trip Optimizer and have developed a simplified way to re-optimize a partially completed plan in an efficient way.

We have completed simulation studies of optimized trajectories on a variety of terrains, grades, and speed restriction profiles. Our analysis shows the typical trade-off of fuel savings versus journey time that results. While the exact shape of the trade-off curve varies with terrain, the load, and the specific speed constraints, they all exhibit the large reduction in fuel consumption per marginal hour of additional travel time. This means even small increases in journey time taken when slack time is available or slow orders are ahead have large potential fuel savings.

Sample results are shown in Figures 3 and 4 for a 100-mi trip segment on BNSF's southwest territory. This is for a 3500-ton consist pulled by 2 GE Dash 9 locomotives operating on a relatively flat stretch between Kansas City, MO, and Wellington, KS. As the travel time objective varies, Figure 4 shows the resulting fuel consumption. While it is not a typical goal for a railroad to slow down, the curve does show the strong sensitivity of optimal fuel use to small changes in travel time, without hybrid energy storage, and is illustrative of potential for savings in the real world where speed restrictions are common due to traffic, work crews, or other problems.

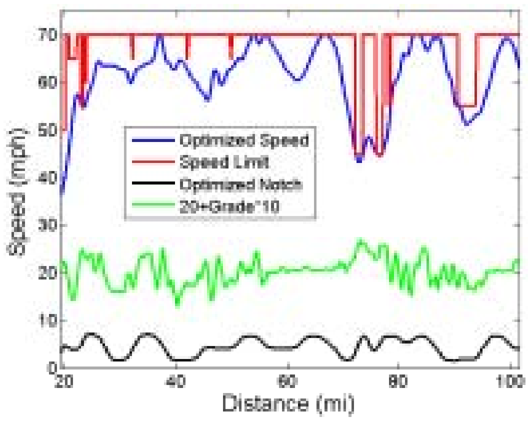

Figure 3. Example optimal driving trajectory (1.9 h travel time).

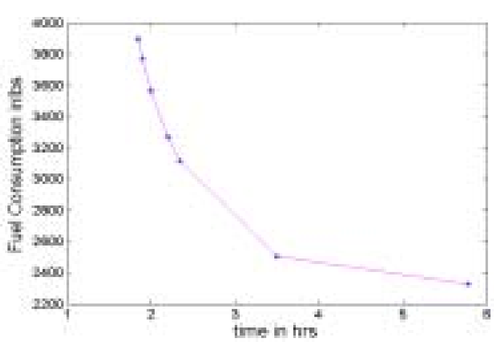

Figure 4. Example of fuel use vs. travel time.

Simplified Trip Optimization Algorithms

This year, we have developed a new search algorithm that we think can radically reduce the complexity of applying Trip Optimizer to longer trips and, more importantly, to allow on-the-fly recalculation of plans following an interrupt. Our approach partitions the journey segment and then matches up and links the subsegments back together on each journey segment to meet the overall time objectives with the least average fuel. Since no large optimizations are carried out, it can be done in real time or nearly so. Moreover, if conditions change at some point during a journey, the plan can be re-optimized over the remaining segments, taking into account the changed conditions.

Figure 5 shows just one example of the effectiveness of this approximation method for a 200-mi trip on a portion of the BNSF Kansas City to LA route again. For this trip, our benchmark optimization software found the optimal fuel use to be 6830 lb. The approximation technique was able to complete the trip with 6880 lb, which is only 0.7% worse, but the problem could be solved three orders of magnitude faster. Note that all of the speed limits are preserved in the approximate solution.

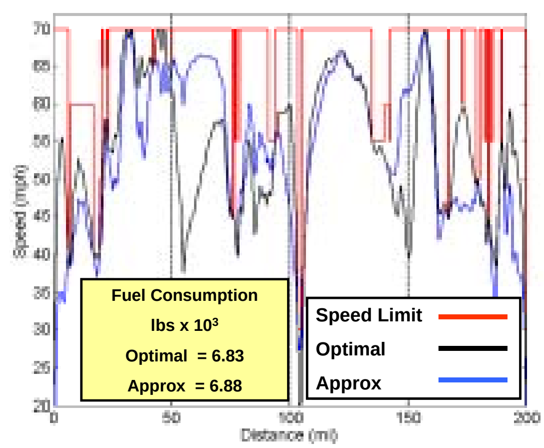

Figure 5. Comparison of optimal solution with approximate technique.

Real-Time Interactive Demonstration of Optimizer Algorithms

A real-time simulation system has been constructed to serve two purposes: (1) demonstrate Consist Manager in a simulation close to its commercial embodiment and (2) provide a platform for later interactive simulation demonstration of Trip Optimizer. Figure 6 shows a block diagram of the computing platform used.

With this system, we can use our engineering simulation to model drivetrains with and without optimized solutions concurrently. In addition, we can show a fully animated, real-time 3D view outside the locomotive to convey some realism to anyone operating the consist through a control interface panel. While this display is not essential to calculating the quantitative performance in either Consist or Trip Optimizers, it will be an important element in the demonstration of the Trip Optimizer before implementation in a locomotive during this project. The demonstration system was first prototyped for the 2004 RSI Rail Show in Chicago (Figure 7), which was the first public offering of the Consist Manager system developed in part under this DOE contract. By allowing customers direct real-time access to the Consist Manager controller, it was easy to show the simplicity and efficacy of the new product.

Consist Manager Field Demonstration

The goal was to build a prototype of the Consist Manager system and field test it on a Class 1 railroad. BNSF railroad agreed to host GE on a cross-country trip in a revenue service train operating in high-priority service. The Consist Manager control strategy was implemented on a revenue service "Z-train" on BNSF's southwest "Transcon" route (Figure 8). The 1–3% fuel savings

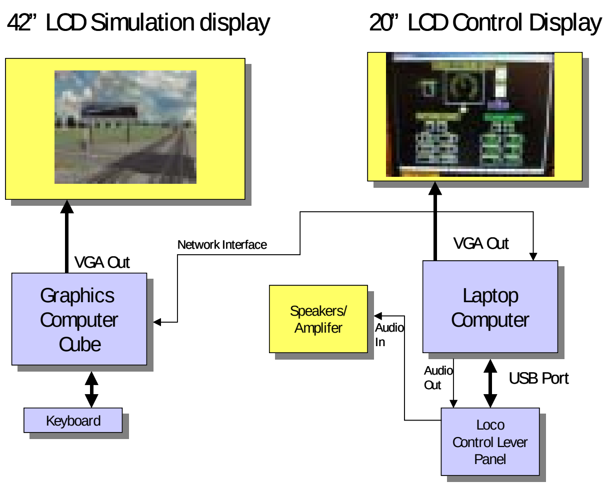

Figure 6. Simulation environment for Consist Manager and Trip Optimizer.

Figure 7. Consist Manager display setup for RSI Rail Show (Chicago, September 2004).

Figure 8. BNSF route for Consist Manager test.

demonstrated, together with flawless operation of the prototype system, have generated strong interest by the participating railroad.

Four GE Dash 9 locomotives and a 3000-ton container and trailer on flatcar cargo comprised the overall 4500-ft train consist. The consist was a regularly scheduled priority cargo train that runs from Kansas City to Los Angeles and back with a short layover, a total distance of 3400 mi at an average speed of 41 mph. The Consist Manager was operational with no problems for the entire journey in both directions.

By using algorithms prototyped and tested against a dynamic train simulation, software was coded for real-time execution by using an "xPC" target platform. "xPC" is a PC-class computer controller interfaced to the locomotive consist by using commercial off-the-shelf digital and analog I/O (Figure 9), which is physically located in the second of the four locomotive units.

Figure 9. xPC control computer and I/O on locomotive.

While the ultimate implementation of Consist Manager is likely to be within the locomotive microprocessor control system software, this version allowed rapid prototyping of the controller without the inconvenience of having to modify locomotive wiring. The wiring changes consisted of interfaces to the master control throttle in the lead unit and the MU-train line and CAB controllers in the both the first and second units. The trailing third and fourth units required no changes. All changes were quickly reversible. The control computer was monitored from a computer host located in a test car attached to the rear of the power consist.

In a conventional multi-unit locomotive consist, the throttle commanded in the lead unit is relayed to all the trailing units. With Consist Manager, the commanded power to each locomotive is computed to deliver the total required power to within a specified tolerance with the best overall fuel economy: it exploits the fact that specific fuel consumption varies with locomotive power output. Part of the control strategy is the dynamic logic that manages transitions from one optimized notch to another for best performance. Thus, one goal of the revenue test was to evaluate our strategy for managing the transient transitions.

The prototype Consist Manager system was operated throughout the run from Kansas City to Los Angeles and back. All hardware and software operated reliably for close to 100% of the trip, allowing Consist Manager to be in the loop for more than 3000 revenue service operation miles; more than 1 GB of data on performance was collected.

Fuel savings were estimated to be between 1% and 3%, with an average of 1.5%. These estimates were obtained by using a model for the fuel use vs. notch for a typical Dash 9 locomotive, multiplied by the duty cycle in each notch as observed on the trip with optimizer enabled compared to what the fuel would have been with all locomotives in the same notch. To avoid overstating the fuel savings, the estimate assuming un-optimized operation was normalized so that both calculations of savings had the same horsepower-hours:

$$\Delta\text{savings} = \frac{\left[\mathrm{f_u} / E_u\right] - \left[\mathrm{f_o} / E_o\right]}{\mathrm{f_u} / E_u}$$

where f_u is fuel used in pounds and E_u the total energy (hp-h) for unoptimized operation; "o" subscripts denote the corresponding optimized quantities.

Ten different crews and their managers, including the BNSF Vice President for Operations, had an opportunity to drive the train with the system active. They reported only minor issues and had no problem adjusting their driving style to the minor changes in transient response with Consist Manager active. Detailed questionnaires from all crew were collected and are being analyzed. We observed qualitatively that some crews had an easier time adapting to the changes in power response with the Consist Manager enabled than others — in particular, those who anticipate power changes better could hold speed and get better performance, suggesting that with experience, these fuel savings projections may be surpassed.

BNSF provided a 24-hour window of draw-bar buff and draft forces, which showed that no unusual transient slack-action forces were produced with the Consist Manager active.

Conclusions

A comprehensive locomotive hybrid technology development program is well under way. The unique energy storage requirements for a hybrid locomotive have been specified, and the appropriate battery chemistry solution has been selected. A comprehensive hybrid energy storage system technology development has been initiated with the vendor, who will deliver locomotive-worthy evaluation systems in the upcoming year and a full system for hybrid locomotive installation early in FY 2006. Advanced energy-management techniques have been developed this year and are being installed in a hybrid locomotive.

We have met or exceeded all the goals set out for the project fuel optimization task, particularly with the revenue service locomotive demonstration of Consist Manager. This test has built credibility with our partner railroad BNSF. The 1–1.5% average fuel savings offered by Consist Manager has proven sufficiently attractive that it is on track for commercial release as a product during the first quarter of 2005.

It is a big step to go to the Trip Optimizer, requiring changes among crew and dispatchers to achieve the fuel saving potential of 4% or more. Our confidence in robust and efficient ways to calculate optimal trajectories has greatly increased, and we will begin application to models with hybrid storage next year. Building on the database developed in the January 2004 Consist Manager test, we will continue to conduct case studies with varying terrains, consists, and loads representative of realistic Class 1 railroad freight operations. Our latest results are showing that even with the same travel time, it is possible to achieve significant (4–5%) fuel savings by carefully managing power and braking. These will be used to form fuel use reference baselines, enabling us to compare the range of benefits: from Consist Manager "assistance," to optimal and sub-optimal Trip Optimizer solutions, to the same Trip Optimized consists working with hybrid storage.

Our belief is that the viability of Trip Optimizer hinges on a bullet-proof and simple operator interface. To allow design and evaluation of potential operator interfaces for Trip Optimizer, we will also be expanding the real-time interactive work station described above. This real-time facility will use our Simulink simulation models with actual cab hardware control inputs. Outputs from the simulator will be displayed in a 3D graphics display with an "out the window" world view. This will allow design and testing of trip planning scenarios with a simplified but realistic cab environment that a driver might experience, to gain insight into the best way to interactively carry out a plan and also handle the train safely.

Our major task for next year will be to capture enough of the core functionality in trip planning, with and without hybrid storage in the locomotive, and conduct an on-locomotive field test. We are exploring options with several Class 1 railroads to perform the field test again on a revenue-service train.

B. Advanced Hybrid Propulsion and Energy Management System for High Efficiency, Off Highway, 320 Ton Class, Diesel Electric Haul Trucks

Principal Investigator: Tim Richter
GE Global Research, 1 Research Circle, EP110C, Niskayuna, NY 12309
(518) 387-5670, fax: (518) 387-6675, e-mail: tim.richter@research.ge.com

Technology Development Area Specialist: Sidney Diamond
(202) 586-8032, fax: (202) 586-1600, e-mail: sid.diamond@ee.doe.gov

Field Technical Manager: Jules Routburt
(630) 252-5065, fax: (630) 252-4289, e-mail: routburt@anl.gov

Contractor: GE Global Research
Contract No.: DE-FC04-2002AL68080

Objective

- Reduce the fuel consumption of off-highway vehicles, specifically large tonnage mine haul trucks, as shown to the right. (A hybrid energy storage and management system will be added to a conventional diesel-electric truck that will allow capture of braking energy normally dissipated in grid resistors as heat. The captured energy will be used during acceleration and motoring reducing the diesel engine load, thus conserving fuel.)

Komatsu 830E-AC Mine Haul Truck
Las Vegas Mine Expo

Approach

- The project will work towards an on-board demonstration of the hybrid system by first selecting an energy storage subsystem and energy management subsystem.
- Laboratory testing at a subscale level will evaluate these selections and then a full-scale laboratory test will be performed.
- After the subsystems have been proven at the full-scale lab, equipment will be mounted on a mine haul truck and integrated with the vehicle systems.
- The integrated hybrid components will be exercised to show functionality, capability, and fuel economy impacts in a mine setting.

Accomplishments

- Completed subscale battery testing. Testing confirmed operation of battery cells for mine haul applications and provided validation for the vehicle battery model.
- Improved vehicle model by applying coastdown data collected from several trucks at Komatsu's Proving Ground.
- Preliminary energy system enclosure and mounting designs for several truck models is completed.
- Started design of full-scale prototype and specified components. Several components have been received and assembly of prototype has commenced.

Future Direction

- Following the on-board demonstration, work could continue investigating the commercialization paths and next-generation energy storage systems.

- Beyond improving fuel economy, the use of hybrid technology for reducing emissions would also be developed.
- By considering the energy storage system and related hybrid components during design, the next-generation hybrid mine haul truck will provide increased benefits in many areas.

Introduction

The conventional mine haul truck, also referred to as an Off-Highway Vehicle (OHV), uses a diesel engine to turn an alternator that generates alternating current (AC) electricity. The electricity is rectified to DC voltage that is applied to the main electrical bus called the DC Link. Power electronics convert the DC link voltage to variable frequency, three-phase AC that drives the wheel motors during motoring. When braking is required, the wheel motors function as generators and electrical power is directed to the Braking Grid Resistors, also known as the “Grid Box,” to be dissipated as heat.

In addition to traction motors, the diesel engine must power auxiliary loads, such as radiator cooling fans, operator air conditioning, steering, hydraulics, and control circuits. These auxiliary loads are powered by mechanical means and with a smaller, second alternator connected to the vehicle’s 24-V battery system.

Figure 1 shows a block diagram of the planned hybrid vehicle system. Three primary components will be added to the conventional OHV: Energy Management System, Energy Storage Electronic Interface, and Energy Storage System. Each component plays a specific role in the recovery of braking energy.

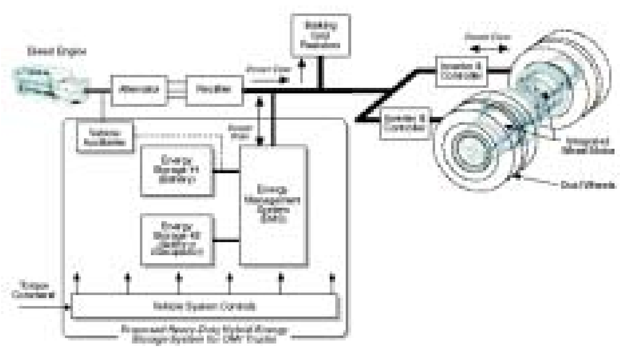

Figure 1. Hybrid electric system block diagram.

The Energy Management System (EMS) performs the high-level supervisory functions of the hybrid vehicle, primarily controlling the balance of engine power, grid dissipation, and battery charging or discharging. Performing these functions requires intimate connections to all of the truck systems.

The Energy Storage Electronic Interface, also referred to as the Hybrid Control Group, acts to convert electrical power on the DC link into levels compatible with the Energy Storage System. The hybrid control group is essentially a high-power DC-DC converter.

The Energy Storage System (ESS) consists of the batteries and manual disconnects, fuses, and related safety and protective components.

Subscale Battery Testing

To investigate the performance of the target battery for the demonstration, individual cells were tested in a subscale apparatus. Subscale testing allows thorough instrumentation of battery cells and tight control of battery current. Figure 2 shows the laboratory setup for testing the “hardware-in-the-loop” experiments.

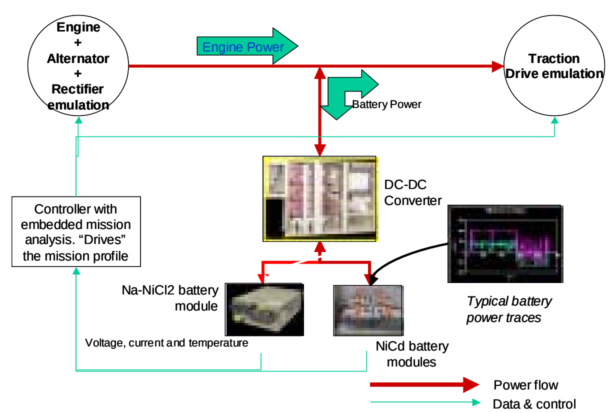

Figure 2. Subscale laboratory configuration.

One DC source emulates a diesel engine/alternator-rectifier that supplies electrical power to the DC link. Another bidirectional DC power source emulates the traction drive, with capability to act in motoring (power sink) and retard (power source). A two-channel bidirectional DC-DC converter independently controls power flow between the battery modules and the DC link.

The controller commands the alternator and traction drive power flows as defined by the hybrid truck mission. The controller also monitors power flow within the system and implements the energy management algorithms. Data are acquired and stored for display on a graphical user interface and further analysis.

Figure 3 shows one instance of hybrid performance compared to the baseline vehicle speed as demonstrated by using the subscale test equipment. The hybrid system is switched on during the uphill portion of a mine haul while the truck is fully loaded. The additional power supplied by the hybrid system results in additional motoring power available at the wheels and allows approximately 3 MPH faster speed-on-grade.

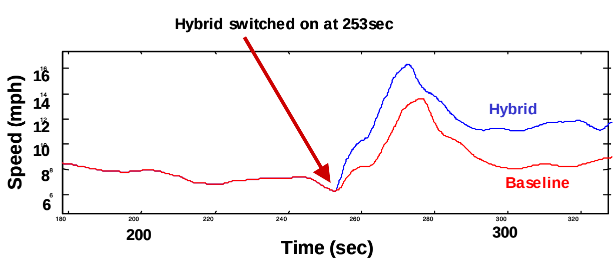

Figure 3. Hybrid performance.

The higher speed-on-grade is important when considering the impact of hybrid system weight on productivity. Any hybrid system weight must be subtracted from the working payload of the truck to maintain the same gross vehicle weight (GVW). Because the truck is moving downhill as fast as possible, productivity, expressed in tons/hour, can only be maintained by decreasing the uphill haul time. The hybrid system allows this while saving fuel.

The initial configuration was planned to utilize two battery banks, each comprised of different chemistries. This configuration was chosen to reduce risk in using an advanced battery.

Figure 4 shows the results of one subscale test of two battery types. One complication of this system is in balancing the state-of-charge (SOC) for each system. Charge balance must be enforced during the overall haul cycle or the system will deplete or overcharge. The right-hand graph of Figure 4 illustrates one system maintaining proper balance while the other (magenta) overcharges.

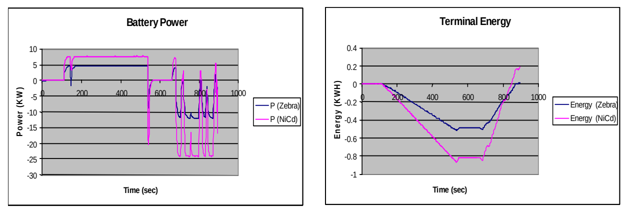

Figure 4. Two-battery ESS.

Controlling this SOC balance adds complexity to the EMS. One solution is to utilize one battery technology for the ESS. A single-battery system is currently being planned for the truck demonstration.

The battery application has an impact on life. The subscale tests have completed over 12,500 cycles over 9 months, demonstrating excellent performance. The life tests were cut short because of a long-term drift of SOC that resulted in overdischarge of the cells.

Full-Scale Battery Testing

Following the subscale evaluation, full-scale testing will be performed at GE Transportation in Erie, PA, where the testing facility has recently been upgraded. Facilities are available to emulate all vehicle systems in a controlled environment, allowing instrumentation of the system for analysis and troubleshooting (Figure 5).

Components for the full-scale testing have been specified, and most have been ordered and received. Electrical schematics were generated to show the integration of the hybrid components with the existing vehicle design.

Batteries were received and tested for functionality and performance before they were installed in the full-scale setup. Part of the testing checked the

Figure 5. Control room and power electronics cabinet.

operation of the communication bus (CAN) used by the batteries and supervisory control. Several issues were discovered in integrating lab equipment, the truck's vehicle controller, and the EMS. The battery vendor has been especially helpful in resolving the communication gaps. A bank of four batteries has been connected successfully in parallel for testing. Hardware to allow the vehicle controller to interface to the EMS and ESS has been received and will be tested shortly.

Full-scale evaluation work will continue into FY 2005, leading up to the integration of the hybrid components on the mine haul truck (Figure 6).

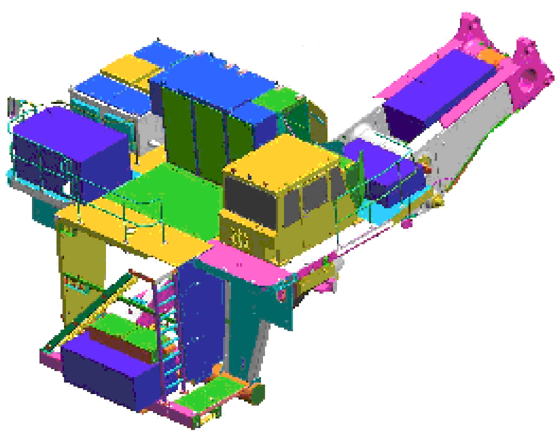

Figure 6. Mine haul truck with hybrid equipment shown in purple.

Vehicle Integration

In preparation for the truck integration, layouts of hybrid components on the truck have been created. Several configurations are being discussed, and Komatsu is analyzing structural requirements needed to support the additional hybrid weight.

Five general areas of the truck are available to add hybrid equipment: RF upper deck, front bumper, behind operator cap, and between the frame rails. The preferred configuration for mounting the hybrid subsystems is to locate one battery bank on the RF deck. A second battery bank will be located on the front bumper. The hybrid control group will sit behind the operator cabinet, close to the main control group.

The hybrid system will require at least one reactor to smooth current from the hybrid control group switching electronics. The reactor will be located the inductors between the frame rails, beneath the dump body.

Another design uses the space between the frame rails for a battery bank, but this moves the inductors to the upper deck in front of the control cabinet. This configuration is not desirable as it clutters the deck and will make access to the main control cabinet and upper battery bank difficult.

Conclusions

The work performed in FY 2004 has shown the feasibility of the hybrid demonstration, and the expected benefits are sufficient to continue work toward the on-board demonstration.

The subscale laboratory testing has provided valuable experience with advanced battery technology and has added confidence to the vehicle modeling and performance estimates.

Initial designs of the vehicle integration show there is sufficient space on the truck for mounting a hybrid energy system and controls. The designs suggest a clean installation with room for changes as the design matures.

Full-scale laboratory testing is well under way, with primary components purchased and received and schematics complete. Construction of test equipment specific to the full-scale testing has begun and acceptance testing of the batteries is nearly complete.

The demonstration at Komatsu Proving Grounds, shown in Figure 7, will show operation of the hybrid OHV and validate model estimates for energy savings.

Figure 7. Komatsu Proving Grounds.

IX. Particulate Matter Characterization

Morphology, Chemistry, and Dynamics of Diesel Particulates

Principal Investigator: Kyeong O. Lee
Argonne National Laboratory
9700 S. Cass Ave.
Argonne, IL 60564
(630) 252-9403, fax: (630) 252-3443, e-mail: klee@anl.gov

Technology Development Area Specialist: Sidney Diamond
(202) 586-803, fax: (202) 586-1600, e-mail: sid.diamond@ee.doe.gov
Technical Program Manager: Jules Routbort
(630) 252-5065, e-mail: routbort@anl.gov

Contractor: Argonne National Laboratory
Contract No.: W-31-109-Eng-38

Objectives

- To investigate the evolution of diesel particulates along the exhaust pipe.
- To provide technical data for the development of advanced diesel aftertreatment systems.

Approach

- Collect diesel particulates along the exhaust pipe from a light-duty diesel engine.
- Analyze morphological parameters along the exhaust pipe.

Accomplishments

- Developed a thermophoretic soot sampling device that can collect soot particles at four different positions along the exhaust pipe.
- Analyzed the morphology, sizes, fractal geometry, and chemistry of diesel particulates along the exhaust pipe.
- Identified the significant changes in particle morphology, sizes, and fractal geometry of diesel particulates caused by the oxidation catalysts, as well as other exhaust components along the exhaust pipe.
- Found catalytically reacted particulates immediately after the oxidation catalyst, indicating the importance of this research for development of advanced diesel aftertreatment systems.

Future Direction

- Analyze morphological parameters immediately before and after a diesel particulate filter installed on the exhaust system.
- Analyze parameters as different properties of diesel fuel are used, e.g., different levels of sulfur, paraffins and aromatics concentrations, oxygen concentration, and Cetane numbers.
- Compare those parameters with those measured for gasoline engine particulates.

Introduction

Particulate matter (PM) is a chemically and physically sophisticated substance that is formed via a series of rapid thermal and chemical reactions as a by-product of diesel engine combustion. Measurement of the physical dimensions of diesel particulates is an important issue, because their nano-size characteristics are directly related to human health, particularly in the pulmonary system. The size measurements need to be carried out for two different types of particles: primary and aggregate particles. In combustion physics, the growth of individual primary particles is responsible for the total mass of particulate emissions, while the aggregate particles, formed through agglomeration of primary particles and smaller aggregates, are emitted to the atmosphere and may affect human life. Indeed, the particle growth through agglomeration is irrespective of the change in total particulate emissions. Therefore, measurement of both sizes is necessary.

Many investigators reported the size measurements of diesel particulates, typically in a form of aerodynamic or mobility diameter. These size measurements of diesel aggregate particles were conducted mostly by using commercial instruments. In principle, these instruments measure the equivalent diameters (volume-based) of aggregate particles; they assume that the particles are spherical. These measured particle sizes are, in general, classified into two different size categories – nucleation and accumulation modes – at a threshold size of 50 nm, (i.e., the particles smaller than 50 nm are considered to be in the nucleation mode and the ones larger than 50 nm are in the accumulation mode). In our previous experiments performed for a light-duty diesel engine, the average sizes of primary particles were appeared to be in a range of 20–30 nm in diameter at various engine-operating conditions, under which the primary particles should undergo the growth and oxidation processes during combustion. The nucleation of incipient soot particles occurs at a very early stage of soot formation; the sizes of these particles are much smaller than the average sizes of the particles that are typically measured after the termination of major combustion reactions. In combustion experiments for a laminar diffusion flame, the incipient soot particles in nucleation, which are usually detected in the low-temperature region, appear to be extremely small and are known to be chemically unstable. To reveal the detailed properties of complex diesel particulates, therefore, accurate measurements of physical dimensions and morphology of diesel particulates are necessary.

In addition to the measurement of particle sizes, the efficient control of diesel particulate emissions is another important issue that has been discussed extensively. Many researchers have attempted to reduce diesel particulate emissions using various technologies: the development of in-cylinder combustion control systems, improvement of engine hardware, and development of a new concept of diesel engine combustion. Recently, the use of aftertreatment systems, such as particulate filters or oxidation catalysts, has been considered as a more substantial and practical technology to control diesel PM emissions. Detailed characterization of diesel particulates along the exhaust system will be necessary to develop advanced aftertreatment systems.

In this investigation, we observed the morphology of diesel particulates on the PM samples collected at different locations along the exhaust system by using a high-resolution transmission electron microscope (TEM). The samples were collected by using a thermophoretic soot sampling device first developed at Argonne. The sizes of both primary and aggregate particles were measured along the exhaust pipe. The geometry of the particulates was standardized at each sampling location through fractal analysis. Detailed investigation of particle size and morphology along the exhaust system is rare in the literature.

Experimental Descriptions

Engine Specifications and PM Sampling

A 1.7-L light-duty diesel engine was used to sample PM at four different positions along the exhaust system. The specifications of the engine used are listed below:

Displacement (4 cyl.):	1.7 L
Aspiration:	Turbocharged and inter-cooled
Compression ratio:	19:1
Rated power:	66 kW at 4,200 rpm

Rated torque:	180 Nm at 1,600–3,200 rpm
Maximum speed:	4,800 rpm
Fuel injection system/ injection pressure:	Common-rail, direct-injection/200–1,400 bar
Test fuel:	California low-sulfur commercial diesel fuel, HF-328

A thermophoretic sampling system was used to collect particulates from the engine exhaust system. Detailed descriptions for the use of this system appeared in our previous publications. The sampling technique offers several unique advantages, such as rapid sampling (as fast as 20 ms max.), minimal interference of sampling events to the exhaust stream, no need for air dilution, and no extra treatments for subsequent morphological and chemical analyses. The samples collected from engines are directly inserted into the TEM to observe the morphology of collected particles and obtain their images.

Diesel PM was collected from four different positions along the exhaust system: right after the exhaust valves (Port 1 or P1), between the turbocharger and first oxidation catalyst (Port 2 or P2), between two oxidation catalysts (Port 3 or P3), and further downstream, removed from the second catalyst by about 200 cm (Port 4 or P4), as shown in Figure 1. The engine operating condition for sampling was 2,500 rpm and 25% of the maximum torque. To obtain consistent data, the engine was warmed up to stabilize its operation at a medium speed/load condition for about 40 minutes prior to each experiment. During each sampling experiment, other important parameters, such as the temperature and pressure of exhaust gas, cooling water, and fuel, and equivalence ratios, were monitored to ensure consistent sampling conditions. Particles were collected at the four different positions at one time. Because the exhaust gas temperature at each sampling position was different, the residence time of the sampling probe in the exhaust stream had to be optimized to enable us to collect a sufficient number of particles while avoiding possible overlapping or additional agglomeration between particles.

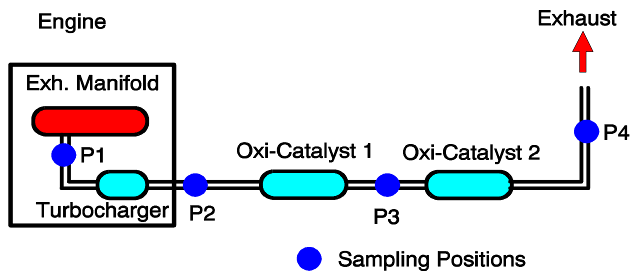

Figure 1. Schematic of PM sampling positions along the exhaust system.

TEM Image Analysis and Energy Dispersion Spectroscopy

A Philips CM30 TEM was used to observe particulate samples and photograph the images. Then the TEM micrographs were digitized with a high-resolution CCD camera and a data acquisition/image processing system, and detailed morphological properties of each particle — such as the primary particle diameter, radius of gyration, and fractal dimension — were statistically measured to provide average values. An energy dispersion spectrometer (EDS) was used to analyze chemical elements dissolved in sample particles with a detection area as small as 95 nm in diameter.

Results and Discussion

Morphological Observation

Numerous soot particles were observed through a TEM and photographed to characterize the evolution of particle morphology and sizes along the exhaust system. Figure 2 shows the TEM images of the diesel particulates collected at the four different sampling positions depicted in Figure.1. All four micrographs have the same magnification (21,000×) to allow a direct comparison of particle properties among the images. Each micrograph displayed was carefully selected to exhibit a representative trend of morphological characteristics of the particulates collected at a specific sampling position. As seen in the figure, a common morphological characteristic was found: small near-spherical primary particles agglomerate to form a larger aggregate particle, and those aggregate particles appear to be stretched, chain-like structures. An interesting observation is that the particles collected at Port 1 (P1, on the exhaust manifold) appeared to be larger in overall aggregate size and higher in particle number density than the ones collected at other sampling ports. In

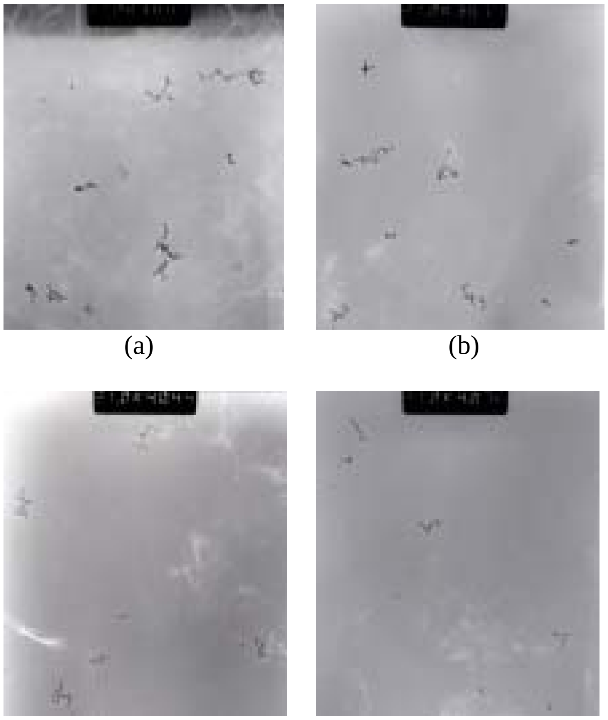

(a) (b) (c) (d)

Figure 2. TEM images of diesel particulates collected at different positions along the exhaust pipe, (a) Port 1, (b) Port 2, (c) Port 3, and (d) Port 4.

particular, the number density and sizes of particles collected at Port 3 and 4 were quite different from the others. This observation indicated that the oxidation catalysts installed on this engine had a significant influence on the size and concentration of particulate emissions, which will finally reduce the tailpipe PM emissions.

Particle Sizes

Measurement of primary particle sizes is important because soot yield is determined basically by the sizes and number of particles. Also, detailed mechanisms of the particle growth and oxidation that occur during combustion processes can possibly be explained with further analysis of the microstructures and chemistry of the particles. To better understand particle sizes, a schematic of an aggregate particle was developed (Figure 3). A chain-like aggregate particle consists of an agglomeration of tens to hundreds of near-spherical primary particles, where the size of a spherule is represented by a diameter of d_p. The size of an aggregate particle is represented by the radius of gyration, R_g, which is more reasonable to represent

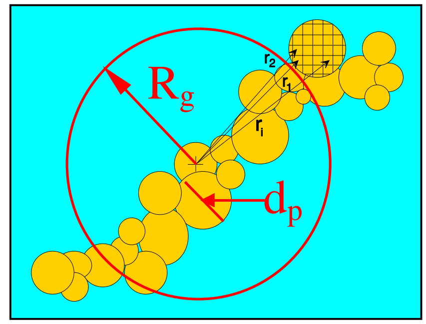

Figure 3. Schematic of an aggregate particle consisting of near-spherical primary particles.

the size of complex-shaped diesel particulates than other equivalent diameters.

The sizes of primary particles were measured from TEM micrographs by using a digital image processing system. From the soot images, more than 200 primary particles were randomly selected from different aggregates to determine an average diameter of primary particles at a specific sampling position. In most cases, the size distribution of primary particles represented a standard Gaussian distribution. Figure 4(a)–(d) shows the histograms of primary particle diameters measured at Ports 1 through 4, respectively. As seen in the figures, primary particles in a size range of 6–42 nm were selected to measure average diameters at four different sampling positions, which appeared to be 28.6 nm, 26.8 nm, 21.8 nm, and 19.1 nm at Ports 1 through 4, respectively. It is apparent in the figure that the sizes of particles representing a majority of counts shifts toward smaller sizes as the sampling position moves downstream along the exhaust stream. The average diameter measured at Port 4, where sampled particulates should have experienced oxidation after traveling through two oxidation catalysts, was decreased by 33% compared to the one measured for engine-out particulates at Port 1. It will be interesting to compare the reduction of primary particle size with measurements of overall concentrations of particulate emissions, in light of assessing the contribution of particle size reduction through oxidation to total particulate emissions.

The spheroidal shape of primary particles was verified by measuring the diameters of primary particles constituting an aggregate particle at two different viewing angles, 0° and 50°. The

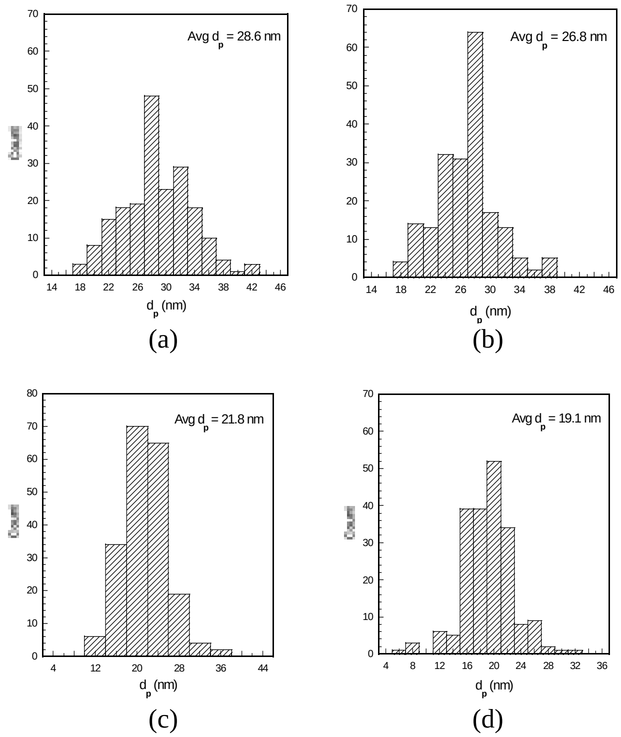

Figure 4. Size distributions of primary particles sampled at (a) Port 1 through (d) Port 4, respectively.

sample was rotated in the TEM to obtain soot images at a 50° viewing angle. Figure 5 shows the size distributions of primary particles at 0° and 50° viewing angles, respectively. The particulate samples were collected at the exhaust manifold at 2,500 rpm and 70% load. The measured average particle diameters of 24.6 nm and 24.4 nm differ by less than 1%, which implies that the measurement of primary particles is not sensitive to orientation and that primary particles are fairly spherical in shape.

The sizes of aggregate particles were measured in terms of radius of gyration that represents a physical dimension. The radius of gyration (R_g) of a single aggregate particle is defined by the following equation:

$$R_g = \sqrt{\frac{1}{n}\sum_{i=1}^{n} r_i^2} \qquad (1)$$

where r_I is the distance between the center of an individual primary particle and the centroid of the associated aggregate (see Figure 3), and n is the number of primary particles within a single aggregate particle. For a specific engine condition,

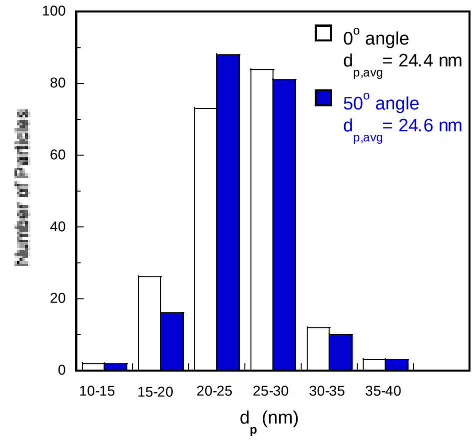

Figure 5. Size distributions of primary particles measured at different viewing angles, 0° and 50° (2,500 rpm/70% load).

more than 200 aggregate particles were randomly chosen to determine the number average of R_gs.

Figure 6 shows the size distributions of aggregate particles sampled from four different sampling ports. A bin of the particle size representing a majority of particles tends to shift to a smaller radius of gyrations along the exhaust pipe; for example, from 80 nm at Port 1 to 40 nm at Port 4. The largest particle size measured at each port appeared to be smaller than R_g = 300 nm (a diameter of 600 nm), although the particles larger than this size were not selected for measurement because of their rarity. These size measurements revealed that the physical sizes of a majority of diesel particulates, particularly near the tail pipe (Port 4), are distributed in quite a narrow size range, close to the lower limit of the U.S. Environmental Protection Agency's (EPA's) size standard of $PM_{1.0}$ and far from the upper limit of 1.0 micron.

Indeed, the sizes of a majority of particles at the tailpipe are close to those of $PM_{0.1}$ particles. On the basis of these physical size data, none of the particles in the size ranges of EPA standards $PM_{2.5}$ or PM_{10} were emitted from this diesel engine.

Fractal Geometry

The morphology of highly complex diesel particulates can be standardized by evaluating fractal dimensions in fractal analysis. Fractal dimensions demonstrate the growth mechanism that dominates the formation of aggregate particles during a

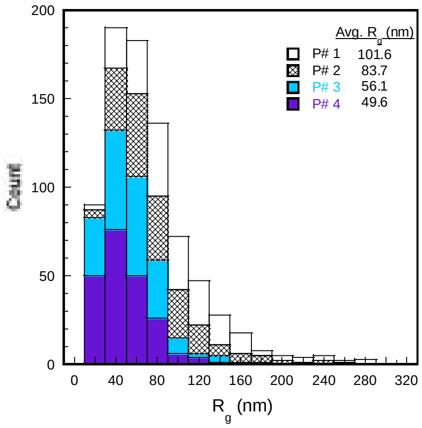

Figure 6. Size distributions of aggregate particles at four different positions along the exhaust system.

combustion process. The fractal dimension (D_f) is defined as

$$n = k_f \left(\frac{R_g}{d_p} \right)^{D_f} \qquad (2)$$

where n is the total number of primary particles within an aggregate particle, k_f is a prefactor, R_g is the radius of gyration of an aggregate, d_p is the average primary particle diameter, and D_f is the magnitude of fractal dimensions. By plotting ln(n) versus $\ln(R_g/d_p)$, the fractal dimension can be obtained by evaluating the gradient of linear regression line.

Figure 7 shows the linear regression lines for the particulate data collected at the four different sampling positions. The hollow circles display the data for particulates sampled at Port 1 (other data were omitted). The gradients of the regression lines were evaluated at 1.62, 1.52, 1.73, and 1.53 along the exhaust pipe, respectively (The regression coefficients for all the fitting lines are above 0.95.). The magnitudes of these fractal dimensions lie in the same range as the ones previously measured for light-duty diesel engine particulates at various engine-operating conditions. This result supports the former conclusion that the light-duty diesel engine produces more chain-like stretched particles than does the heavy-duty diesel engine.

Figure 8 displays data for the average diameters of primary particles, the radius of gyrations of aggregate particles, and the fractal dimensions at all four sampling positions. As shown in the figure, the

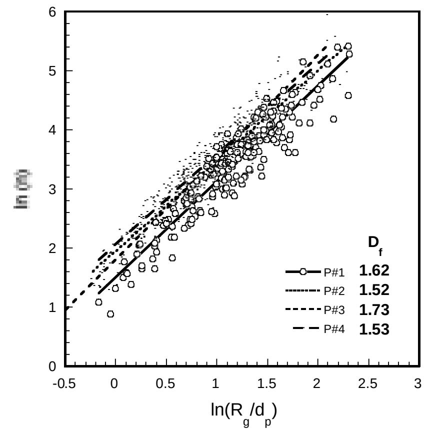

Figure 7. Evaluation of fractal dimensions of the particulates collected at four different positions along the exhaust pipe.

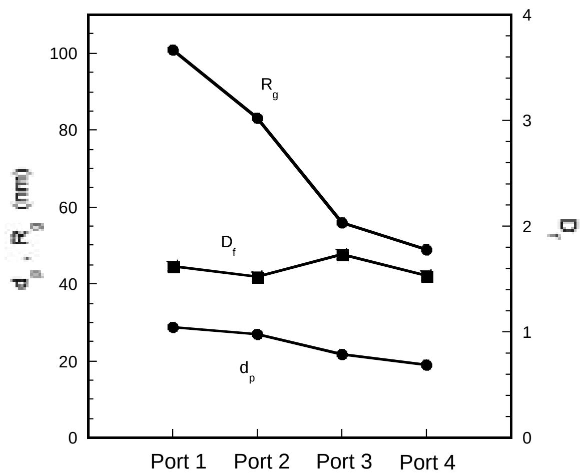

Figure 8. Average sizes of primary and aggregate particles and fractal dimensions at four different sampling positions.

primary particle size (d_p) gradually decreased along the exhaust pipe: the size was reduced by 33%, from 28.6 nm at Port 1 to 19.1 nm at Port 4 (tailpipe). The radius of gyrations of aggregate particles also decreased quite significantly as particles move downstream along the exhaust pipe: about a 50% reduction along the entire exhaust system (101.6 nm to 49.6 nm). These reductions in particle sizes occurred after particles traveled through oxidation catalysts, where they should have undergone catalytic oxidation. Detailed information about the oxidation catalysts is not available at present. Meanwhile, the magnitude of fractal dimensions (D_f) slightly increased at Port 3, while the D_f values at other ports are quite even. The larger D_f indicates that these particles are more spherical in shape than those sampled from other ports.

These analyses trigger an interesting discussion about the possible mechanisms of particle evolution in the exhaust system. The particles formed in combustion chambers were emitted to the exhaust system and underwent further thermal reactions and aerodynamic interactions with a fairly high temperature of gaseous emissions and particulates in the system. As a result, their sizes were significantly reduced: the sizes of aggregate and primary particles were reduced by 50% and 33%, respectively, along the exhaust pipe. Note that the reduction percentage of aggregate particle size is larger than that of primary particle size. The following hypothesis may account for the particle evolution: both a partial breakdown (or disintegration) of single primary particles from an aggregate and the reduction of interstitial distances between primary particles in the aggregate can reduce the aggregate particle size. These two physical processes are explained mainly by aerodynamics in the exhaust stream and particle oxidation in the catalysts, respectively. Our microscopic observations support this hypothesis: the particulates emitted immediately from the catalysts appeared to be smaller in size and more spherical and compact in shape, particularly at Port 3, where the catalytic oxidation should have occurred.

The chemistry of particulates sampled at an idling speed was analyzed by using an EDS. As seen in Figure 9, the major portion of diesel PM consisted of elemental carbons, while a few percent of sulfur was also detected from this particulate sample. Although quantitative measurement of these chemical elements is still required for comparison, the sulfur content measured from these particulates was quite significant, considering the sulfur concentration of 110 ppm in the fuel. An accurate calibration with a standard specimen of carbon and sulfur is required to measure the absolute amount of sulfur dissolved in diesel PM. The copper and silicon were detected from the soot sampling grid, not from particulates.

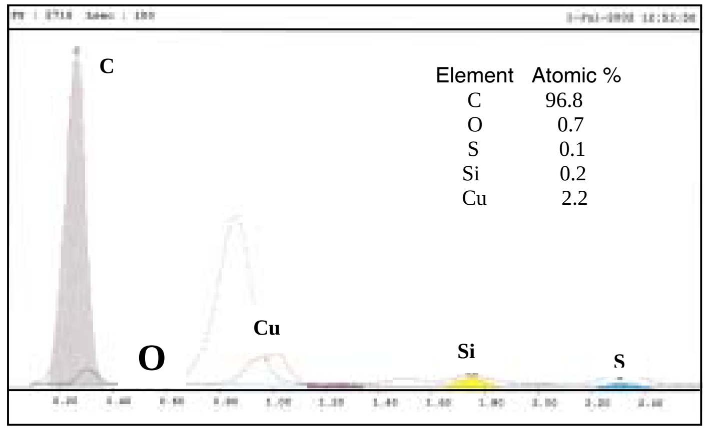

Figure 9. Spectrum of chemical elements in diesel particulates measured by an EDS.

Conclusions

This microscopic study, which basically used a series of PM sampling and measurement systems, including a thermophoretic soot sampling system, a TEM, and an image processing system, was successfully conducted to analyze the morphology, sizes, and fractal geometry of light-duty diesel particulates at various positions along the exhaust system. The sizes of both primary and aggregate particles were significantly reduced, mainly by oxidation catalysts. The degree of size reduction of the aggregate particles exceeded that of the primary particles through the entire exhaust system. It is likely to be attributed to particle breakdown by aerodynamic interactions in the exhaust stream and reduction of interstitial distances between primary particles caused by catalytic oxidation. The EDS analysis revealed that a majority of the diesel particulates consists of elemental carbons, along with a significant amount of sulfur.

Acknowledgments

The authors would like to acknowledge strong support from Dr. Sidney Diamond at the FreedomCAR and Vehicle Technologies Program of the U.S. Department of Energy. We also thank Dr. James Eberhardt at DOE for in-depth discussions relevant to the environmental safety and health impacts of diesel PM.

X. Brake Systems

Advanced Brake Systems for Heavy-Duty Vehicles

Project Manager: Glenn Grant
Pacific Northwest National Laboratory
P.O. Box 999, Richland, WA 99352
(509) 375-6890, e-mail: glenn.grant@pnl.gov

Technology Development Manager: Sidney Diamond
(202) 586-8032, fax: (202) 586-1600, e-mail: sid.diamond@ee.doe.gov

Field Technical Manager: Jules Routbort
(630) 252-5065, fax: (630) 252-4798, e-mail: routbort@anl.gov

Contractor: Pacific Northwest National Laboratory
Contract No.: DE-AC06-76RL01830

Objective

- Assess the potential of alternate disc brake designs and technology concepts, in conjunction with emerging friction materials. The expected outcome of this project is identification of an appropriate disc brake system design and friction pair sets, with improved thermal, wear, and durability properties that can be applied to heavy-duty vehicles for enhanced braking performance and improved safety. The emerging innovative concepts will be examined in collaboration with brake suppliers and/or truck original equipment manufacturers (OEMs).

Approach

- Disc brake design and thermal management, which will be achieved through a combination of theoretical modeling and experimental investigation and validation.
- Enhanced performance and durability of friction pairs, which will be achieved through a combination of theoretical modeling and experimental investigation and validation.
- Alternate or auxiliary retarding/stopping methods, which will be achieved through an evaluation of emerging braking systems and a concept feasibility study of novel methods to scrub kinetic energy from a moving vehicle. Methods that show promise will be presented to brake suppliers and OEMs and investigated further as appropriate.

Accomplishments

- Developed a disc-brake rotor model for thermal performance studies and evolution of rotor design concepts and waste-heat recovery methods.
- Selected candidate friction materials.
- Initiated friction and wear evaluation of candidate materials at Tribo Materials and Rockwell Scientific.
- Demonstrated friction stir reaction processing (FSRP) as a manufacturing method for friction materials that have a selectively graded, wear-resistant structure.

Future Direction

- Investigate multi-disc brake rotor arrangements and other new design concepts and determine benefits and sensitivity of each to braking performance.
- Identify alternate energy absorption/conversion and heat management/rejection methods for potential system concept redesign.
- Evaluate of system response to noise-vibration-harshness (NVH) for friction pair combinations.
- Further down-select of friction materials based on wear rate, thermal stability, friction characteristics, NVH, and cost.
- Coordinate with OEMs and create a project steering committee.

Introduction

Reducing parasitic losses (primarily drivetrain friction and rolling resistance) and aerodynamic drag improves the fuel efficiency of trucks and buses. However, such reductions in drag make it more difficult to stop the vehicles, and place a higher burden on the vehicle brake materials and system. Higher brake loads, combined with the desire and legislation to reduce the stopping distance of trucks and buses, mean that the performance of the braking systems must be improved substantially over what is available today. The desire to reduce vehicle weight and operating costs also calls for new brake materials that are lightweight and last longer.

The trend is toward higher operating temperatures, beyond the safe envelope of the current generation of brakes that use gray cast-iron, and in particular the phenolic binder friction materials (brake pads). The consequence of using such conventional materials in heavy vehicles is poor and unreliable performance, excessive wear, and more wear debris. These lead to increased environmental impact, higher maintenance costs, and, ultimately, lower safety and productivity.

For future vehicles, especially on-highway long-haul vehicles (Class 7 and 8 trucks), it is likely that conventional propulsion platforms will be used; whereas for city and military operations, hybrid and/or electric propulsion systems will be prevalent. Both of these systems will likely require wheel-mounted friction brake systems.

The main operational difference is that, for on-highway long-haul vehicles, most of the braking is expected to be accomplished by the friction brakes; for hybrid systems, most of the braking will be done by regenerative braking using the electric drive motors as generators, and the balance will be done by a wheel friction brake. The latter could reduce the brake temperature for vehicles operated in stop-and-go mode, compared to today's brakes that run hotter and have a much shorter lifespan between replacements than brakes for on-highway long-haul vehicles.

Unfortunately, it appears that U.S. suppliers of heavy vehicle brakes are not aggressively pursuing research on new materials or designs for disc brakes, potentially because of their vested interest in drum brake systems. This project will address disc brake system design and development needs, as well as friction pair and brake rotor material needs that can be applied to disc brake systems.

Approach

This project addresses the broad goal of producing higher-performance braking systems for heavy vehicles with a multifaceted approach. An investigative and development approach aimed at determining the feasibility of new disc brake system designs and application methods will be pursued. The main project tasks include: (1) development of novel disc brake designs and thermal management approaches, (2) enhanced performance and durable friction pair development, and (3) exploration of the concept feasibility of alternate or auxiliary retarding/stopping methods.

Fiscal year 2004 was the first of a multi-year program, and as such, a brief description of the project scope is warranted.

Task 1 – Disc Brake Design and System Modeling

With the need to improve braking performance and durability beyond the 500,000-mile minimum expected life of the vehicle, new friction materials will be required. However, direct material substitution from current drum brake systems to advanced disc brake geometries is not likely to be effective. As such, disc brake design and system packaging are critical to achieving the project objectives. This task will focus on developing and evaluating innovative disc brake designs, with the emphasis on enhanced thermal management.

Modeling methods, such as computational fluid dynamic (CFD) approaches, will be used to assist in the design and evaluation of novel disc geometries and system components. The goal of the modeling will be to develop a functional solid model and use predictive tools to simulate the performance (thermal and fluid profiles, as well as stress analysis) of the proposed disc brake systems.

Some of the brake system design concepts that will be explored include, but are not limited to, floating single or twin rotors, full-phase pad/rotor, and mechanical/electric actuation.

Task 2 – High-Performance Friction Pairs

For this task, we will acquire several candidate rotor and friction materials and evaluate them in various friction pair combinations that simulate typical braking scenarios for on-highway and vocational heavy-duty vehicles. The friction and wear will be measured and the failure mode(s) determined. The tribology assessment will be done by Tribo Materials at Rockwell Scientific Company (RSC). The relevant physical and mechanical properties of the most promising materials will be measured by PNNL, which will also complete an assessment of manufacturing technologies for metallic and ceramic composite materials. These data will delineate the safe operating envelope of the materials that is needed by the brake designers to determine where and how the materials can be employed for current and next-generation braking systems.

The outcome of this task will be to provide brake designers with relevant data on new materials, enabling them to explore new brake concepts that, until now, have not been possible with currently available gray iron and phenolic-binder friction materials.

Task 3 – Concept Feasibility of Alternative Braking Technologies

The third task is generally focused on analyzing specific concepts that may be employable for brake systems to either enhance braking efficiency, improve thermal management of friction surfaces, or recover and store of waste heat for use at a later time to drive an electrical motor/pump or in the propulsion of the vehicle.

Task objectives will be achieved through evaluation of emerging braking system concepts — such as the use of electromagnetic techniques — to scrub kinetic energy from a moving vehicle.

Thermal management is critical in brake system durability and maintaining adequate friction performance. Methods such as employing duel-phase materials will be investigated, in which the frictional energy from braking is used to make a phase change within a rotor, instead of generating heat that must be conducted or convected away from the friction surface. Methods that show promise will be presented to brake suppliers and OEMs and investigated further as appropriate.

Results

Friction pair selection is a critical aspect of designing a disc brake system. As such, friction pair evaluation and selection for a high-performance, high-durability heavy-vehicle disc brake system was the predominate focus for initial project tasks. In addition, a simplified disc brake rotor model was developed to (1) evaluate rotor geometries, component sizing, and location and (2) assist in material selection.

Task 1 – Disc Brake Design and System Modeling

A model was developed for a simplified disc brake rotor geometry that consists of a solid disc and brake pad. This model was created to predict the fluid distribution (airflow) around the brake assembly and to allow thermal profile and stress analysis. The model will be used to establish design limits (bounding loads) in potential disc brake designs. The thermally induced stresses are proportional to spatial and temporal gradients in temperature that develop during braking and cooling.

The analysis and CFD simulation predict disc temperatures and heat flux during a maximum braking stop from highway speed. This analysis includes essential features of the vehicle wheel well airflow that determine convective cooling rates at the disc surface. Full-vehicle CFD simulations from manufacturers and other FreedomCAR projects will be used, as available, as guidance for the convective cooling portion of this model. Radiation heat transfer is also expected to significantly affect disc cooling. Conduction from the rotating disc to the caliper, hub, and wheel components is also accounted for in the simulation. The simulation employs a two-step approach in order to minimize time and computing requirements. StarCD was selected for the CFD part of this application. This software has been used by Volvo for a similar disc brake cooling application. PNNL results of near-disc flow for a preliminary isothermal simulation of a disc brake are shown in Figure 1.

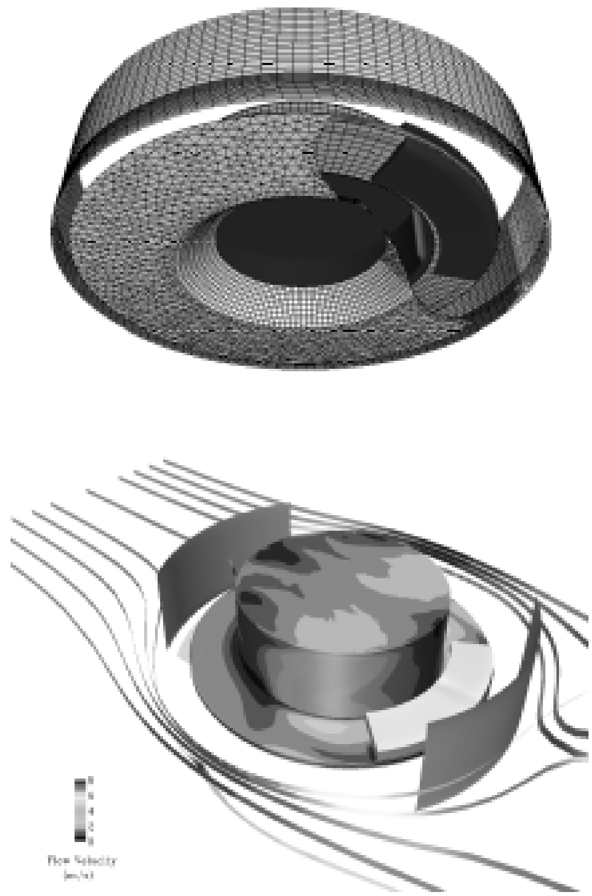

Figure 1. Simplified geometry and flow-fields results for preliminary disc brake simulation using StarCD.

Because the CFD analysis will be a time-consuming transient simulation, selected results from StarCD will be used to form inputs to an additional thermal analysis tool that can be used efficiently for preliminary/scoping sensitivity analyses. The tool selected for this purpose is RadTherm, because it is widely used by industry for brake thermal analysis.

RadTherm is typically used to predict component temperature distributions during repetitive braking test sequences. This package is capable of simulating simple radiation heat transfer from surfaces and also includes the capability of simulating conduction through solids. The efficiency of this tool is realized by not solving for cooling airflow, but by applying convective heat transfer as surface heat transfer coefficients. These heat transfer coefficients are obtained from the preceding StarCD CFD simulation. Sensitivity to parameters such as disc thickness, thermal radiation emissivities, or thermal contact resistances can be investigated with this software to better define the bounding conditions for the stress analysis.

The time history of predicted temperatures in the disc will be transferred to the stress analysis software to determine worst-case thermally induced stress loading. The mesh geometry and associated results sets from the CFD analysis will be used directly to perform the stress analysis using the general-purpose finite-element analysis (FEA) software package ANSYS. Selected conditions stemming from expected bounding cases will be analyzed. Disc material properties sensitivity will be investigated by comparing stress states to material degradation/failure limits. This evaluation cycle will be iteratively applied to arrive at an optimized disc design.

Task 2 – High-Performance Friction Pairs

A survey of was conducted of friction pair materials, which included commercial and emerging materials options, as well as those still in the research and development phase by various vendors. Over 20 friction material options and vendors were surveyed and, based on the technology readiness level and cursory economic considerations, four were down-selected. These four friction pair and rotor material candidates will be pursued further in order to evaluate their full potential as cost-competitive and technically viable options for disc brake systems.

A description of the down-selected candidate materials is given below. The features they have in common are that all have the potential to be low-cost cermets materials fabricated by liquid metal infiltration, by reaction processing, or by friction stir processing.

1. Excera Materials Group – $50SiC/35Al_2O_3$/W1461-XBr, in situ composite.
2. Starfire Systems – Rotors – polymer-based ceramic reinforced with chopped PAN carbon fibers. Pads – conventional material with SiOC polymer substituted for phenolic.
3. MER Corp. – Composite of pitch-based graphite cloth in SiC matrix, in situ attached to high-temperature (1,000°C) MMC core.
4. PNNL – Steel with TiB2 particles incorporated by friction stir processing. Cast iron with TiC particles incorporated by in situ friction stir reaction processing.

<u>Excera Materials Group</u>

The structure of ONNEX material is produced by a low-cost SiO_2-Alliq in situ reaction method that uses a net-shape ceramic preform. The precursor materials are chemically transformed into the ONNEX cermet material by using the company's patented immersion process. This process creates an interwoven ceramic and metallic network. The aluminum matrix is then substituted with bronze for high-temperature applications.

The Excera ONNEX materials feature a unique and tailorable array of physical and mechanical properties. While these properties can be modified to match the demands of specific applications, they can be generally classified by the following:

- Low density (half the density of steel)
- High stiffness (slightly stiffer than steel)
- Good strength (similar to aluminum castings)
- High fracture toughness (similar to cast iron)
- Low thermal expansion (30% less than steel)
- High thermal conductivity (between twice that of cast iron and aluminum alloys)
- Exceptional wear resistance (better than most ceramic materials)

The manufacturer claims that for automotive applications, ONNEX materials exhibit ten times the wear resistance of iron-based materials, and under severe conditions, can operate at temperatures approximately 100°C cooler — which yields shorter stopping distance for brake applications.

<u>Starfire Systems</u>

Starfire materials utilize a polymer infiltration and pyrolysis (PIP) process that is the latest technique resulting from years of research to develop a process that enables the fabrication of advanced ceramics more efficiently than conventional processes. This technique involves soaking a fiber preform or powder compact with a liquid polymer precursor that converts to ceramic material upon pyrolysis. Pre-ceramic polymers are available that form silicon carbide, silicon nitride, silicon oxycarbide, and silicon oxynitride. Advantages of PIP include simpler, less costly equipment, lower process temperatures, shorter cycle times, and the capability to produce more complex parts. Also, polymers afford the potential to control materials chemistry at the molecular level.

Starfire's material systems offer a wide range of potential solutions for transportation markets, such as high-wear engine components, exhaust structures, diesel particulate filtration systems, and (presumably) friction materials that are suitable for heavy-vehicle brakes. These materials can be modified for high-wear applications. Starfire material claims for a silicon carbide material system currently under development are as follows:

- One-third the weight of steel and up to 20% lighter than carbon/carbon (C/C).
- Excellent static friction and stable base friction (0.2) that can be tailored to exceed 0.35; both static and dynamic friction.
- Significantly lower wear rates versus C/C.
- Greater mechanical stability versus C/C.
- Demonstrated 30–50% lower cost compared to C/C.
- Friction performance is unaffected by fluids or temperature.
- Improved oxidation resistance.
- Suitable for automobiles due to low wear and stable friction.
- Can eliminate overheating or fade associated with current heavy truck brakes under extreme highway braking conditions.

MER Corporation

The MER friction materials are still in a development stage, but they show strong promise as friction pairs for vehicle braking systems. These composites are made from pitch-based graphite cloth in a SiC matrix, which is created via an in situ process. The reacted C/SiC product is attached to a high-temperature (1,000°C) MMC core. MER SiC/SiC composites are produced using CVR SiC fibers, as well as commercially available SiC fibers (including Nicalon and others). The SiC matrix is produced using preceramic polymers, chemical vapor infiltration (CVI), and hybrid combinations of these and other processing methodologies. The C/C composites are converted to SiC/SiC or C/SiC composites, as well as to other carbides, including ZrC and HfC. It is possible to produce pure SiC/SiC composites without carbon, BN, or other debonding layers and achieve two to five times the through-the-thickness thermal conductivities as state-of-the-art SiC/SiC composites. These C/SiC and SiC/SiC composites are thermally stable to at least 1,800°C. Cost projections for C/SiC or SiC/SiC composites are typically high, but MER claims its process is economical. These materials will be evaluated for their wear resistance and thermal stability. Furthermore, MER will provide updated cost information for further evaluation.

Pacific Northwest National Laboratory

PNNL, in conjunction with South Dakota School of Mines & Technology (SDSMT), have initiated work to develop friction stir reaction-processing (FSRP) to create an in situ surface composite in steel, cast iron, or other appropriate base-metal system. A schematic of the friction stir processing method is shown in Figure 2.

Material systems currently being investigated include steel with imbedded TiB_2 particles and cast iron with TiC particles. Figure 3 shows that

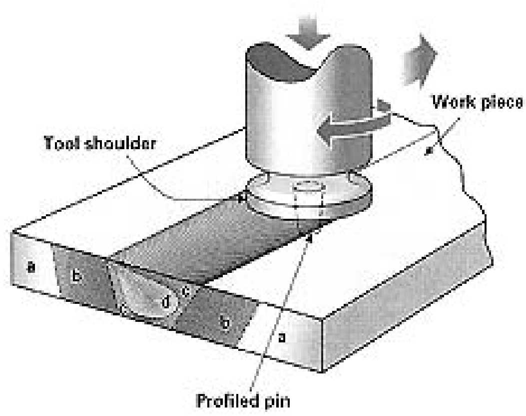

Figure 2. Friction stir processing is accomplished by plunging a spinning tool into a material and translating the tool across the surface. Ceramic powders, or other materials, can be captured under the shoulder of the tool and mixed downward into the processed region.

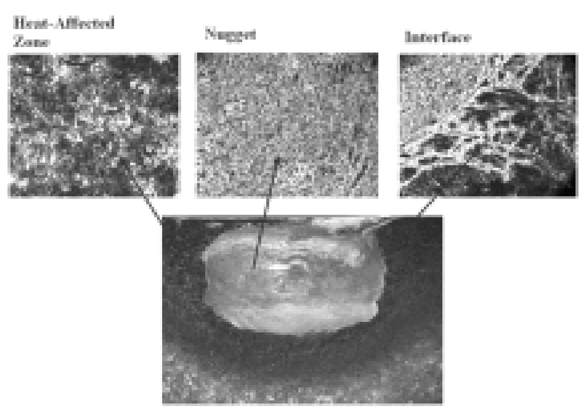

Figure 3. Friction stir processed cast iron (Ramasubramanian et. al. 2004).

cast iron can be plasticized by means of FSRP. Recent work at PNNL on FSRP wear-resistant surfaces has demonstrated the incorporation of SiC particulate into the surface of aluminum at depths of 2 mm. These and other systems, including TiC or WC-reinforced high-strength steels, will also be investigated, as appropriate.

FSRP was invented by PNNL and SDSMT within the last two years, so the economics for the process are currently unknown. Samples of these materials will be produced and evaluated for their merit as brake friction pairs. If the initial technical feasibility study shows promise for this class of material, the economics of the process will be modeled to determine whether the resulting materials are a feasible option for heavy-vehicle brake systems.

Future Direction

The scope of work for FY 2005 will focus predominantly on brake rotor geometry design, thermal management, and model simulation activities in support of system design considerations. Multi-disc brake rotor geometries will be investigated for thermal and braking performance. Other new design concepts will be investigated to determine (1) what benefits they may provide and (2) the impact of each on braking performance. The modeling task will continue to investigate heat generation, fluid flow, and the resulting surface temperature of the brake system components.

The modeling task will require thermomechanical data on proposed rotor/pad material combinations, as well as material physical properties such as conductivity, diffusivity, density, wear resistance, and friction coefficients, and other mechanical properties. These properties will be determined, along with the evaluation of system response to NVH for the various friction pair combinations, and used as input to the model. The model will be updated with more complex geometries as necessary.

In addition, alternative energy absorption/ conversion and heat management/rejection methods will be investigated for their potential as primary or secondary methods to control vehicle speed.

Acknowledgments

The principal investigators would like to acknowledge the valuable contributions of James Fort and Harold Adkins of the Pacific Northwest National Laboratory for their work in developing the brake model and simulations.

References

1. Jerhamre and Bergstrom, “Numerical Study of Brake Disc Cooling Accounting for both Aerodynamic Drag Force and Cooling Efficiency,” SAE Tech Paper 2001-01-0948.
2. Jansen, “Vehicle Disc Brake Cooling Factor Analysis,” RadTherm Users Meeting.

XI. More Electric Truck

Parasitic Energy Loss Reduction and Enabling Technologies for Class 7/8 Trucks

Program Manager: William Lane
Caterpillar, Inc., Technology and Solutions Division
P.O. Box 1875, Peoria, IL 61656
(309) 578-8643, fax: (309) 578-4722, e-mail: bill.lane@cat.com

Technology Development Manager: Sid Diamond
(202) 586-8032, fax: (202) 586-1600, e-mail: sid.diamond@ee.doe.gov

Technical Program Manager: Jules Routbort
(630) 252-5065, fax: (630) 252-4798, e-mail: routbort@anl.gov

Contractor: U.S. Department of Energy, Albuquerque, New Mexico
Contract No.: DE-FC04-2000AL67017

Objectives

- Reduce parasitic losses for fuel savings.
- Provide idle-reduction solutions.
- Reduce radiator heat load.

Approach

- Electrify truck accessory functions and hotel-type loads.
- Decouple accessories from main truck engine.
- Match accessory power demand to real-time need.
- Enable use of alternative power sources.
- Develop and implement comprehensive systems-level perspective.

Accomplishments

- Conducted idling, over-the-road, and dyno fuel economy testing on technology demonstration truck.
- Exhibited technology demonstration truck at Mid-America Truck Show, Louisville, KY.
- Developed virtual simulation model of demonstration truck for exploration of advanced power management control strategies.

Future Direction

- Utilize existing technology demonstration truck as platform for “Advanced Electric Systems & Aerodynamics for Efficiency Improvements in Heavy Duty Trucks” DOE Program Award.
- Evaluate additional fuel savings opportunities enabled by truck electrification.
- Upgrade modular HVAC component.

Introduction

As fuel prices increase, there is more interest in the development of electric and hybrid electric vehicles and in their higher operational efficiency. The majority of developments have focused on propulsion systems. Parasitic losses from truck auxiliary functions, (such as pumps, compressors, etc.) are another source of inefficiencies that have remained unchallenged. This research program covers developments associated with the electrification of Class 8 on-highway trucks to reduce parasitic losses. Incremental gains in fuel economy could be attained by using the present 12-V electrical system, if the alternator efficiency were improved. However, elevating efficiency from less than 50% to over 80% would require the application of different alternator/generator technology. Such an improvement may come with a cost premium that is unacceptable to the trucking industry. This creates a significant cost challenge for improving truck fuel efficiency by boosting the efficiency of individual components.

An alternative to component-by-component replacement is to take an overall system perspective to truck electrification. In some cases, electrifying a component may only provide marginal improvements in fuel savings when used in the same manner as its conventional counterpart. However, an electric component could also be the enabler to a different mode of operation that may realize significant fuel savings. For example, overnight idling of a truck engine is the common means of providing cabin heat or cooling. This practice uses fuel inefficiently, increases engine maintenance, creates additional exhaust emissions, and increases operating expenses. The electrification of the heating, ventilation, and air conditioning (HVAC) system provides the capability of conditioning the air to the cabin without having to run the truck engine. This is important because large quantities of fuel are burned just for that purpose.

With that precedent, this research program focused on converting conventional belt- or gear-driven accessories to electric variable-speed motor-driven ones. This allows them to operate independently of the main engine, at only the actual speed, pressure, or flow required. By continuously adjusting to the desired operating points, there are multiple opportunities for parasitic loss reduction and control features. To demonstrate and test the benefits of truck electrification, a prototype Class 8 heavy-duty truck was built. This More Electric Truck (MET), with associated accessory components, is illustrated in Figure 1.

Figure 1. Demonstration vehicle.

The MET is based on a Kenworth T-2000 truck chassis with a Caterpillar® C-15 engine rated at 500 HP. On it is implemented a comprehensive electrification of truck accessory functions as a means to improve fuel economy, heat rejection, reliability, power management, and packaging flexibility. Several high-power accessories were demonstrated to quantify the benefits of truck electrification, during both normal “over-the-road” and “overnight idling” operating conditions. Among the electrical accessory systems demonstrated in this program were an integrated starter-generator (ISG), a modular heating ventilation and air-conditioner (MHVAC), a shore power converter, an electronic battery charger (down converter), a water pump, an oil pump, a service-brake air compressor, and an auxiliary power unit (APU). These components and their functions have been described in previous reports [1].

A comprehensive series of fuel economy tests was conducted during the third and fourth quarter of calendar year 2003 to quantify the fuel savings made possible by the MET electrification. These tests were designed to obtain real-world truck performance data by using the MET and a control vehicle over a range of terrain and conditions and conformed to SAE

Type-II (J1321) procedure [2]. The MET vehicle, before conversion to electrified accessories, was tested for baseline fuel economy in September and October of 2002. The MET vehicle's engine, transmission, and drivetrain were consistent between baseline (BL) and experimental (EX) tests.

Quantification of fuel savings for an average over-the-road cycle is challenging. The savings largely depend on how the truck is used, weather conditions, and road characteristics, among other factors. It is difficult to conceive of a single test cycle that would be representative of the average truck. Truck fleets use their own load cycles based on their more common routes. Engine manufacturers use proprietary engine load profiles to baseline the fuel economy of their engines. For quantification of MET over-the-road fuel economy benefits, both a track test and interstate highway route test were undertaken. Environmentally controlled truck idling fuel consumption tests were also conducted with the MET.

Test Results: Idling

A major fuel savings opportunity for long-haul trucks is to curtail overnight idling of the main engine. It has been estimated that long-haul trucks idle an average of 1,830 hours per year. Engine idling speeds range from 600 to 1,000 rpm, depending on the driver's preferences and weather conditions. Thus, truck idling fuel consumption can be calculated, for defined climatic conditions, by using measured engine fuel consumption at fractional loads.

As part of the MET truck electrification, a diesel-powered, variable-speed generator was designed, fabricated, and mounted on the truck chassis, to provide DC power to the HVAC systems during overnight idling conditions. Quantification of fuel savings as a result of using the APU and modular HVAC (versus a baseline of using the main engine and conventional HVAC) to cool the cab over during idling periods was sought as an objective of this program. The MET was tested for APU fuel consumption to maintain cab cooling in the controlled environmental chamber of the Paccar Cooling Test Cell in Everett, Washington, October 2003. Ambient temperature was maintained to 95°F, and the humidity was 45%. The results of both the baseline (C15 at 1000 rpm) and the APU testing are shown in Table 1. The figures shown in the table reflect the average temperatures and fuel rate over a 4-h period of stable, steady-state cab temperatures.

Table 1. MET idling fuel testing results.

	Avg. Fuel Rate (gal/h)	Avg. Cab Temp (°F)	Avg. Sleeper Temp (°F)	Avg. APU Power (kW)
C15 at 1000 rpm	1.31	65	69	2.8
APU	0.21	71	76	-

From the table, a reduction from 1.31 to 0.21 gal/h, or an 84% improvement, is evident from the baseline to the APU test. The fuel consumption during the APU test may be slightly low because the cab and sleeper temperatures could not be maintained at the same temperatures as those measured in the baseline test, probably because there was inadequate air mass flow from the MHVAC blower and ducting system.

Also of interest is the amount of fuel used by the C-15 in the baseline test. In separate engine-only testing of the C-15 at Caterpillar test facilities, the engine fuel consumption with a 4-kW output load was measured at 1.1 gal/h. With the assumption of similar loading in the baseline idle test, a 0.21 gal/h increase is seen. The likely cause for this increase is the 50% duty cycle recorded for the time that the cooling fan was on in the baseline test. This provides additional evidence for possible benefits provided by using an APU for cab cooling.

The APU engine coolant system was integrated with the main engine so that the main engine and radiator acted to dissipate the heat energy produced by the APU. It was desired to see if the APU heat could be rejected in this manner to a high ambient air temperature. Testing of the APU in high ambient conditions (85°F) also revealed the need for supplemental cooling-fan-provided airflow across the truck radiator. With only passive, natural convective airflow through the radiator, heat transfer was impeded, insufficient heat was rejected to the atmosphere, and coolant temperature rose above acceptable levels. The addition of two small, 12-in.-diameter, 12-V fans in front of the radiator resulted in enough forced air through the radiator to maintain adequate cooling for the APU.

The levels of cab interior acoustic noise during idle engine and APU operation were measured at Paccar Technical Center. The baseline test, with the main engine idling at 1000 rpm and AC blower fan set to medium, resulted in a sound pressure level near the driver's head of 68.3 dB and 66.1 dB at the sleeper bunk. The test with the APU at 2400 rpm (typical speed for normal cab cooling power needs), and electric HVAC at medium blower speed, resulted in a sound pressure level near the driver's head of 60.2 dB and 57.5 dB at the sleeper bunk. This amounts to a reduction of about 8 dB for both cab and sleeper, which is well over a 50% reduction. This reduction allows for a more comfortable rest environment for a truck operator, further increasing the value of an onboard APU.

Test Results: Test Track

The track testing was undertaken at Paccar Technical Center. The test track was a 1.6-mi banked turn oval, where a test run consisted of 50 mi distance at 60 mph average speed. This type of test provided consistent, constant-speed, and level cruising conditions for the truck.

The baseline track test was performed September 3, 2002, with the MET (pre-electric accessories) as the test truck (TT) combined with a loaded trailer for a GVW of 76,240 lb. The control truck (CT) used for both the baseline and experimental test was a Kenworth T-2000, with a Caterpillar C15 engine rated at 475 HP and a loaded trailer for a GVW of 74,940 lb. A summary of the track testing results is shown in Table 2. The columns in the table correspond to each of five separate test segments – each test segment consisted of three individual test runs. For a test segment to be valid, the test run's TT/CT fuel used ratio must have been within a 1% spread. The fuel consumption for each truck in each run was measured by weighing of removable fuel tanks before and after each run. All fuel use shown in the table has been normalized to the control truck fuel use from the baseline segment [3].

From Table 2, it can be seen that a significant decrease (ranging from 2.7% to 5.8%) in the control truck fuel use was measured between the baseline and experimental segments. Some of this decrease can be attributed to a slight decrease in average wind speed, along with a small increase in average ambient temperature. From Chu [4], a 5-mph headwind or crosswind can account for a 5–10% increase in fuel use in long-haul trucks, and a 10°F increase in temperature may result in a 1–2% decrease in fuel use in long-haul trucks. Separate analysis of the individual test runs with associated temperatures and wind speeds resulted in a factor of 0.65% increase in fuel consumption for each 1-mph increment in wind speed.

Table 2. Baseline and MET test track results, normalized to baseline control truck fuel use.

Date	9/3/02	9/22/03	9/23/03	9/24/03	9/25/03
Test	BL	EX	EX	EX	EX
Temperature	65.2	69.0	65.0	69.8	70.0
Wind Speed	6.0	4.9	7.9	3.7	4.4
CT Fuel Use	1.000	0.944	0.973	0.942	0.944
TT Fuel Use	1.013	0.981	1.010	0.969	0.954
TT/CT Ratio	1.013	1.039	1.038	1.029	1.010
TT Fuel Use Change from BL (%)		2.49	2.38	1.49	-0.32
CT Change from BL (%)	0.0	-5.6	-2.7	-5.8	-5.6
CT Comp. by 4 %	1.000	0.982	1.012	0.980	0.982
Corrected TT/CT Ratio	1.013	0.999	0.998	0.989	0.971
Corrected TT Fuel Use Change from BL (%)		-1.45	-1.56	-2.41	-4.16
Other Cond.	BL GVW	BL GVW +1200 lb	BL GVW +1200 lb	BL GVW	BL GVW, APU Pwd. Acc.

Comparing the 9-23-03 segment with the baseline segment, the temperatures are virtually identical: a 1.9-mph increase in wind speed is seen, and the control truck used 2.7% less fuel. Canceling out the wind speed effect by 1.3% (1.9 mph × 0.65%/mph), and adding this to the 2.7% decrease in fuel use, gives a compensated fuel use decrease for the control truck of 4.0%. This means that the overall fuel consumption of the control truck used for the tests decreased by 4% from the time the baseline segment was performed to the time the experimental segments were performed. This decrease in fuel consumption is likely due to an additional 10,000 mi of break-in time on the control truck's engine and possibly the tires, which, from to Chu, can result in a 2–5% reduction in fuel use.

On the basis of the analysis above, the fuel use of the control truck in the experimental segments was corrected to compensate for the decrease in actual fuel used and to give more accurate results to the testing. This is shown in the "CT Comp. By 4%" row of the table, and results in the corrected TT/CT ratio and the corrected test truck fuel use change relative to the baseline, as shown in the subsequent two rows of the table.

The two experimental segments from 9-22-03 and 9-23-03 were performed with the test truck at its baseline GVW plus 1200 lb; the additional weight was attributable to the increase from additional electric components and APU. The two experimental test segments from 9-24-03 and 9-25-03 were performed with the 1220 lb subtracted from the trailer cargo weight, to give the same GVW for the test truck in both the baseline and experimental tests. Also, the segment performed on 9-25-03 was performed with the electric accessories powered solely by the onboard APU, to give a better indication of the contribution of electric components to fuel consumption.

The corrected results in Table 2 show that the MET version of the test truck had decreased fuel usage of about 1.5% (average for the 9-22-03 and 9-23-03 segments, both with an additional 1200 lb of GVW) and 2.4% for the 9-24-03 segment with GVW equal to the baseline segment. This difference of 0.9% is in line with the findings of Chu, who reported an increase in fuel use of about 1% for each 1000 lb increase in vehicle weight.

Regarding the difference in weight, for the test vehicle MET of 1200 lb, approximately 400 lb can be attributed to the APU for idle reduction. About 150 lb might be saved by using a cast-aluminum instead of a cast-iron flywheel/ISG housing. Also, more-efficient, production-intended packaging and size reduction of power electronics may result in an additional 200 lb weight reduction. The MET also had approximately 50 lb of additional weight in the form of an AC inverter. This is mentioned to assuage concerns about the GVW as tested for the 9-24-03 segment, in which the trailer ballast was removed to counter the 1200-lb weight increase for the MET. Of this 1200 lb, one-third is attributable to the APU, and one-third would be eliminated in more-production-intent versions. Therefore, it was felt that the best comparison for the MET fuel economy would be a GVW matched to the baseline.

It is important to note that the MET experimental test segments were performed with a non-functioning air conditioning unit, whereas in the baseline segment, the test truck was tested with the air conditioning functioning and set to mid range. A component failure occurred in the MET HVAC prior to the tests, and because of tight test-track scheduling, the tests were continued before the module could be repaired.

The last experimental segment was performed with the MET electric accessories powered exclusively by the APU, eliminating all the electric parasitics on the main engine. This was done to quantify the contribution of the combined electric accessory load and resulted in an additional decrease in fuel use of 1.75%, for a total decrease over the baseline of 4.16%. The fuel consumption by the APU was not measured in this test segment. This segment also helped to carry out a component-by-component breakdown of accessory contribution percentage to overall truck fuel use. This was made possible by sampling electric current and voltage sensor data to each of the components and then calculating the required fuel rate, by engine brake-specific fuel consumption, needed to produce mechanical power that was then converted to electrical power by the ISG. A similar breakdown of the mechanical accessories was performed earlier in this project and subsequently enhanced from the experimental testing. The breakdown of mechanical accessories was accomplished by inference from component power curves, rather than actual measurement of mechanical torque and speed. The results of the component analysis are shown in Figure 2.

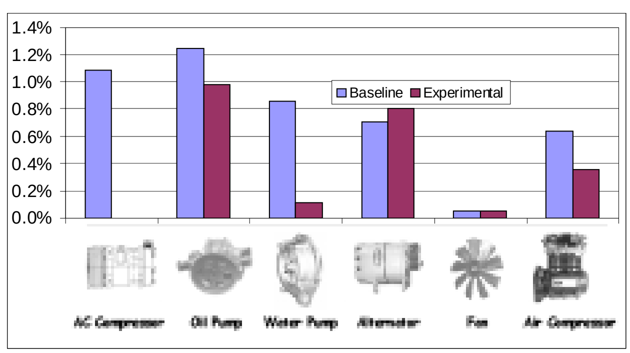

Figure 2. Test track component contribution to total fuel use.

The component analysis shows that the contribution of the mechanically driven, or belt-driven, AC compressor accounted for about 1.1% of test truck fuel consumption in the baseline segment. Assuming the contribution of the electrically driven HVAC system to fuel use is comparable to that of a belt-driven AC compressor, an additional 1.1% can be subtracted from the 2.4% improvement shown in Table 2 for the 9-24-03 segment, to give an overall on road fuel economy benefit from under test track conditions of 1.3%. This is probably the closest numeric figure that can be arrived at for MET electrification fuel economy benefit, on the basis of the data produced as a result of the track test portion of the MET fuel economy testing.

The component breakdown of fuel use for the baseline and experimental (MET), shown in Figure 2, reveals that the electric water pump was the largest, single contributor to diminished fuel use for the MET in the track tests. The control strategy for the water pump allowed for minimal coolant flow (and, thus, low power draw) at the relatively low engine torque demands (about 40%), as seen in the level cruising conditions of the track test. The combination of reduced flow mechanical and electric oil pump in parallel configuration provided a small (0.2%) benefit in power consumption. About a 0.3% benefit was seen from the electrically driven air compressor because of the elimination of parasitic compressor torque to the power train during unloaded conditions in the gear-driven, non-MET air compressor.

The summation of the fuel percentage from the electrically powered oil pump, water pump, down converter, air compressor, (0.32 + 0.11 + 0.80 + 0.35 = 1.58%) matches well with the 1.59% fuel improvement difference between the 9/24/03 and 9/25/03 tests, where the latter test had the APU providing power to the electrical accessories.

A small increase in power use was seen in the MET down converter, or 12-V power supply, versus the conventional alternator used in the baseline test. This was due to a significant increase in 12-V loads from the addition of an AC power inverter, extra power converters to MET power electronics, and a faulty (shorted) relay solenoid to the air compressor cooling fan. Subsequent static testing of the down converter revealed an operational efficiency of 85–90%, compared to the near 50% efficiency of a belt driven alternator. This would indicate that (1) an overall fuel economy benefit could be expected by implementing the MET down converter and (2) the results seen in the track test were an anomaly.

Also, from Figure 2, equally low energy consumption was seen from the cooling fan for both baseline and experimental tests because of low engine loading and high ram air available to the cooling system during the level cruising conditions of the track test. Also, as noted above, the MET modular HVAC system was temporarily non-functional during the track testing, and so a comparison of this component was not possible in this test. Finally, a summation of the component breakdown reveals an overall fuel benefit of 1.2% from the MET components versus the baseline, which is close to the 1.3% derived from the measured fuel use described above.

Test Results: Highway Testing

The over road test was conducted by Kenworth Labs, Renton, Washington, where one test segment consisted of three, 76.5-mi laps on Interstate 90 near Ellensburg Washington. The terrain was approximately one-third level or slightly sloping grade and two-thirds long, steep, mountainous terrain across the Columbia River Gorge. The topography of the route is shown in Figure 3.

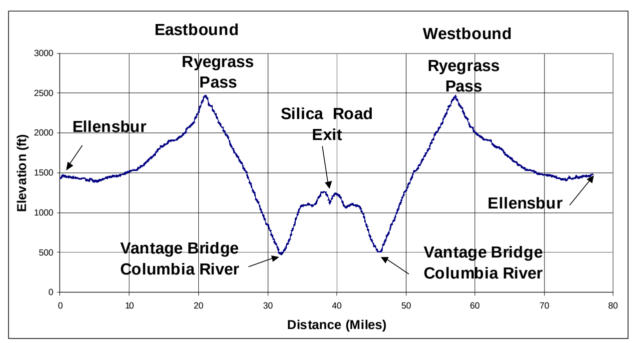

Figure 3. Vantage Grade I-90 route.

This route was chosen to provide extreme loading conditions for the truck and its cooling system. The westbound segment of the route includes an 11-mi uphill portion (the Vantage Grade), with an average slope of 3.5%; this grade, in combination with typically high ambient conditions, puts an extraordinary load on a truck's cooling system. In traveling up the Vantage Grade, a truck typically slows down to about 35 mph, decreasing ram air available to the aftercooler and radiator, which then necessitates the engagement of the cooling fan clutch, putting an additional 10–20-kW fan load on the engine.

The baseline Vantage Grade test was performed on September 11 and 12, 2002; again, the test involved combining the truck with a loaded trailer for GVW of 76,240 lb. The same control truck and loaded trailer were used as in the track tests. A summary of the Vantage testing results is shown in Table 3. The first data column shows and average of two test segments conducted on 9/11/02 and 9/12/02. The experimental test was performed on 10/14/03, again with the electric accessories (MET convention). Only one experimental test was conducted during the scheduled testing, since inclement weather made the highway wet on the remaining testing days. The fuel consumption for each truck in each run was measured by metered pumping to a demarcated level in the fuel tank after a test segment. All fuel use shown in the table has been normalized to the control truck fuel use from the Vantage baseline segment.

The corrected MET fuel use shows a decrease of 4.32% over the baseline test truck. The Vantage data were also analyzed for a component-by-component breakdown of fuel consumption contribution.

Table 3. Baseline and MET Vantage Grade test results, normalized to baseline control truck fuel use.

Date	Avg 9/11/02 and 9/12/02	10/14/03
Test	Baseline	Experimental
Temperature	81	60
Wind Speed	2.2	2.5
CT Fuel Use	1.000	0.964
TT Fuel Use	1.030	0.988
TT/CT Ratio	1.030	1.025
TT Fuel Use Change from BL (%)		-0.49
CT Change from BL (%)		-3.6
CT Comp. by 4 %	1.000	1.003
TT/CT Comp. Rat.	1.030	0.985
TT Fuel Use Change from Comp. BL (%)		-4.32

Similar to the findings from the track test, the control truck's fuel use also decreased between the Vantage baseline and experimental tests. A nominal decrease of 3.6% was observed. About a 3% increase in fuel could be attributed to the 21°F decrease in temperature, but this is offset by about 1.5% from the decreased load on the AC compressor and another 1.2% from the decreased fan-on time. The net of these, +0.3%, which is offset by a 4% expected decrease in fuel use of the control truck due to additional break-in miles, gives an expected decrease in fuel consumption for the control truck experimental versus the baseline of 3.7%, which is very close to the 3.6% decrease observed in the data. So, as in the test track results, the experimental data from the control truck were corrected by 4%, which yields a valid comparison of the MET electrification fuel benefit.

Correcting for the 4% decrease of the control truck, a fuel consumption decrease of 4.3% was observed for the MET versus the baseline. However, because of the 21°F decrease in ambient temperature for the experimental segment, the AC compressor and cooling fan contribution must be voided to give a valid comparison between the segments. Therefore, subtracting the 1.8% due to the AC compressor and 1.2% for the cooling fan leaves a 1.3% increase attributable to the MET electrification.

The results of the component breakdown analysis for the Vantage Grade test segment are shown in the bar chart of Figure 4. A summation of increases for the oil and water pumps, alternator, and air compressor gives a total component increase of 0.7%, which is somewhat less than the 1.3% from the total fuel analysis above. This difference may be attributable to the baseline breakdown of the mechanical components being understated, since the power input to these components was not measured but only estimated on the basis of component characterization curves. Also, since it was only possible to perform one experimental test segment, more variability may be present in the Vantage grade tests than in the track tests, which leads to lower confidence in these results.

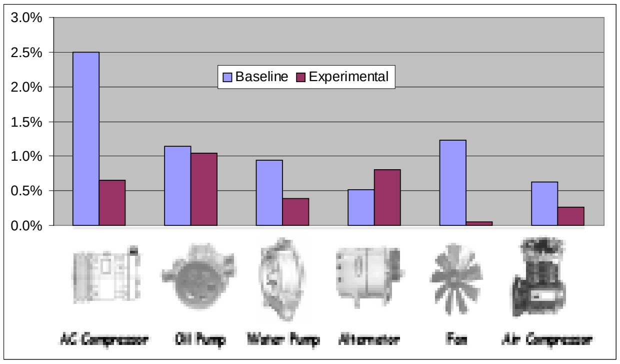

Figure 4. Vantage grade component contribution to total fuel use.

Also note that the power consumption of the electric water pump was more than in the track test because the topography forced the engine to operate under higher loading conditions, which required more coolant flow at higher pump speed. Again, the down converter of the MET consumed more energy than the alternator of the baseline as a result of increased 12-V loads, as mentioned in the track test above. Overall, the percentage of component energy consumption was lower in the Vantage Grade segment than in the track test, simply because a higher percentage of fuel was spent powering the truck over the steep terrain.

Advanced Power Management/Simulation

The Kenworth T-2000 Class-8 truck was modeled for simulation purposes by using Caterpillar's Dynasty dynamic-analysis software combined with the Simulink control-analysis package by Mathworks. The truck's inertial characteristics, power train, and cooling system were modeled with Dynasty, and the MEI components and controls were modeled with Simulink. The model was validated against measured data from the truck traveling the Vantage Grade I-90 route, which was described previously and depicted in Figure 3. For a course run at 16°C average ambient temperature, the simulation calculated that 54.51 L of fuel was required to complete the course, compared with the measured amount of 54.75 L, which is a difference of less than a half of a percent.

The baseline (non-MEI) truck was also modeled and simulated to compare performance with the MEI truck on the Vantage Grade route. The simulated fuel usage results with two different average ambient temperatures are shown in Table 4. In addition, an MEI truck with a controlled cab air-conditioning unit is also listed. In this case, the cab a/c was shut down whenever the engine load became greater than 80% of the maximum engine power of 350 kW. The simulation indicates that at higher temperatures, fuel savings could possibly be doubled by using such a control; however, how hot the cab might become if this control were actually employed in the real truck is unknown at present.

Table 4. Results of power management simulation.

Ambient Temperature (°C)	Baseline	MEI	MEI w/ Cab A/C Control
16	54.97	54.51 (-0.84%)	54.43 (-0.98%)
25	55.88	55.41 (-0.84%)	55.01 (-1.56%)

Investigation of further power-management control schemes is ongoing and will carry over into the Advanced Electric Systems program mentioned below in the Future Work section. Operating the MET in mild-hybrid mode, using regenerative braking and energy storage, and motoring the ISG when the engine is under heavy load are being explored through simulation with the high-fidelity models mentioned above. Preliminary simulation results of the truck operating in hybrid control mode over sinusoidal (hilly) terrain indicate a fuel savings potential of 2–4%.

Future Work

The MET, with electrified accessory components, will be maintained as a research platform for additional study in reduction of parasitic engine loads. A further proposal, "Advanced Electric Systems and Aerodynamics for Efficiency Improvements in Heavy Duty Trucks," has been accepted in response to DOE Solicitation DE-SC52-03NA68471. Four main areas of exploration for this project will include (1) a high-temperature-charge air cooler, for more heat rejection per unit area, and less pumping restriction; (2) an electrically driven engine cooling fan; (3) a more compact and efficient direct-drive scroll-type air compressor; (4) an electronic controlled engine coolant radiator by-pass valve, for elevated and more accurate engine coolant temperature regulation; and (5) advanced power management and hybrid traction use of the integrated starter generator.

The prototype modular HVAC component of the MET will be upgraded to a more production-intended second-generation design. This design will enable more compact, lightweight installation, as well as provide a higher-powered and more efficient blower to provide additional airflow to both cab and sleeper compartments.

The simulation work described in the previous section will continue as part of the Advanced Electric Systems project. Advanced power management strategies and hybrid configuration will be explored and implemented on the MET platform.

Summary and Conclusions

A prototype test vehicle, the More Electric Truck, (MET) was designed, built, tested, and demonstrated as the principal effort of this program (Figure 5). This Class-8 heavy-duty long-haul truck capitalizes on using variable-speed electric motors as prime movers for accessory engine systems to improve efficiency, power management, reliability, packaging flexibility, and customer value. Among the electrically driven accessory systems demonstrated in this program were the starter-generator, shore power converter, heating ventilation and air-conditioner, electronic battery charger (down converter), water pump, oil pump, service-brake air compressor, and auxiliary power unit. This truck configuration was tested and showed significant opportunity for reducing fuel consumption on long-haul Class 8 trucks.

Figure 5. MET with APU and power electronics box.

Reducing the main engine idle time will save fuel. An onboard APU may provide an important initial step toward reducing the fuel consumption of Class 8 trucks. A 75–80% reduction in fuel use was demonstrated on the test vehicle, with the APU providing cab-cooling power and main engine idling providing power to the belt-driven air conditioning compressor. The sound pressure levels inside the truck cab were also reduced by over 50% by using the APU instead of the main engine.

Another significant opportunity for reducing overall fuel consumption on long-haul trucks is to reduce over-the-road parasitic loads. SAE type II fuel consumption test procedures were used to document fuel savings of the MET test vehicle versus a baseline of the same vehicle configured with conventional engine accessories. For the MET with electric accessories versus the vehicle configured with conventional accessories, a fuel savings of 1.3% was observed under both level-cruising track test conditions and mountainous interstate highway conditions. The fuel savings were mostly attributable to the electric water pump and electric air compressor, with a small percentage decrease from the electric oil pump.

Advanced power management control strategies for MET accessory systems have been developed and simulated as part of the extension grant for this program. An improvement of up to 1.5% in fuel economy has been demonstrated in simulation. Simulation efforts aimed at using the MET starter generator in a mild-hybrid mode have shown a 2–4% improvement in fuel economy, depending on the type of terrain traveled, and the drive cycle.

This is the final annual report for this project; however, the MET test vehicle will be maintained as a research platform for additional study in reduction of parasitic engine loads. A further proposal, "Advanced Electric Systems and Aerodynamics for Efficiency Improvements in Heavy Duty Trucks," has been accepted in response to DOE Solicitation DE-SC52-03NA68471. Also, the modular HVAC prototype component will be upgraded to a more-production-oriented version with increased blower airflow.

References

1. Algrain, Marcelo, "Parasitic Energy Loss Reduction and Enabling Technologies for Class 7/8 Trucks," FY 2003 Annual Report, Caterpillar, Inc., 2003.
2. SAE J1321, Joint TMC/SAE Fuel Consumption Test Procedure – Type II, Surface Vehicle Recommended Practice, Society of Automotive Engineers, Inc., 1986.
3. Duffy, John, and Everett Chu, MEI-Engine Fuel Consumption Project, KW02-150, Kenworth Truck Company and Paccar, Inc., 2003.
4. Chu, Everett, "Effect of Factors Affecting Absolute Fuel Economy, Based on TMC RP 1111," Paccar, Inc., 2002.

XII. Ultralight Transit Bus System

Vehicle System Optimization of a Lightweight, Stainless-Steel Bus

Principal Investigator: J. Bruce Emmons
Autokinetics, Inc.
1711 West Hamlin Road
Rochester Hills, MI 48309-3368
(248) 852-4450, fax: (248) 852-7182, e-mail: jbemmons@autokinetics.com

Technology Development Area Specialist: Sidney Diamond
(202) 586-8032, fax: (202) 586-1600, e-mail: sid.diamond@ee.doe.gov
Field Technical Manager: Jules Routbort
(630) 252-5065, fax: (630) 252-4798, e-mail: routbort@anl.gov

Contractor: Argonne National Laboratory
Contract No.: 4F-02161

Objectives

- Perform the integration and optimization of a hybrid or battery/electric propulsion system and various vehicle subsystems into a lightweight bus body. Autokinetics will use as much off-the-shelf technology as possible. Optimization of the propulsion and vehicle systems will primarily be through careful selection of appropriately sized components. This project will result in a single proof-of-concept prototype bus, suitable for testing and evaluation of performance under controlled conditions.
- Identify one or more paths to rapid commercialization of the technology.

Approach

- Conduct computer simulations of a number of different types of propulsion systems to predict performance and energy efficiency.
- After identifying the most promising propulsion system architecture, use computer simulations to evaluate and select the individual components with the best combination of performance and affordability.
- Purchase and install the integrated propulsion system.
- Design or select optimized vehicle subsystems, such as seats, glass, and air conditioning.
- Purchase or fabricate and install all vehicle subsystems.
- Evaluate the performance and make modifications, if necessary.
- Perform initial testing.

Accomplishments

- Completed first project task — Propulsion System Modeling and Simulation.
- Initiated numerous ongoing discussions about commercialization and deployment in California, Tennessee, Michigan, and China.

Future Direction

- Complete the design of the propulsion system, including traction motor controller with regenerative braking, fuel converter and generator, vehicle controller, and energy storage system.

- Select specific propulsion components, including energy storage system, generator, low-voltage system, and vehicle controller.
- Design cooling system and hydraulic system.
- Purchase and/or fabricate the propulsion system.
- Design, fabricate, and install vehicle subsystems.
- Install and test the propulsion system.
- Perform FMEA (failure modes and effects analysis).
- Design, fabricate, and install the driver's station and controls.
- Perform limited testing and development of the complete vehicle.
- Continue efforts aimed at rapid commercialization.

Introduction

The intent of this project is to perform the integration and optimization of a hybrid or battery/electric propulsion system and various vehicle subsystems into a lightweight bus body. Off-the-shelf technology will be used wherever possible. Optimization of the propulsion and vehicle systems will primarily be through careful selection of appropriately sized components.

This project will result in a single proof-of-concept prototype bus, suitable for testing and evaluation of performance under controlled conditions. The design will not necessarily be ready for mass production, nor will it include trim and appearance items.

The completed prototype will include the primary body structure, suspension, glazing, driver's station, electric wheel motors, inverters, and energy storage system. It will also include regenerative braking, limited lighting, bumpers, and full seating. If a hybrid propulsion system is selected, an internal combustion engine with generator, fuel tank, and hybrid electronics or controls will be included.

Propulsion System Simulations

The lightweight stainless-steel body and chassis that has been developed by Autokinetics for the FreedomCar and Vehicle Technologies Program (under another project) is an important enabler for advanced technology propulsion systems of several types. The purpose of the initial task of this project was to use computer simulation tools to evaluate the performance of various candidate propulsion systems in order to select the most promising one for further development.

The ADVISOR (version 2002) program developed by NREL (National Renewable Energy Laboratory) for the development of hybrid and other fuel-efficient vehicles was used for this study.

ADVISOR includes a substantial database of vehicles and components, which allows comparisons to be made with certain existing vehicles. The approach taken by Autokinetics was to use existing ADVISOR models of a conventional diesel bus and a series hybrid bus as comparisons (the NovaBus RTS Conventional Diesel Bus and the Orion VI Low Floor Hybrid Bus). In addition, Autokinetics created four new models representing four different propulsion system architectures. These include diesel hybrid, fuel cell, battery-electric, and plug-in hybrid versions of the Autokinetics lightweight bus. Fuel consumption was evaluated by using the CBD 14 drive cycle. This represents a city business district bus route and is commonly used in the industry. For comparison purposes, the passenger load was standardized at 27 passengers for all vehicles (approximately one-half of the full seated capacity). The power required to run the air-conditioning system was not included, but it will be evaluated in a later task.

All fuel consumption results were compared by calculating the gasoline-equivalent miles per gallon. A comparison of the energy efficiencies of the various buses is presented in Figure 1. This chart does not include the energy required to produce and distribute the different types of fuels. This

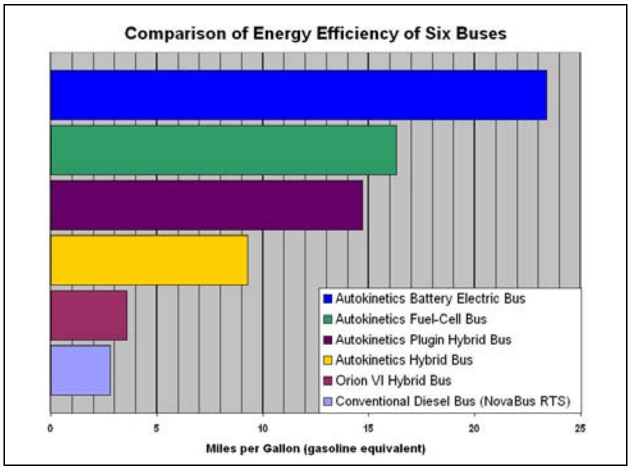

Figure 1. ADVISOR results showing comparative *vehicle-only* energy efficiency of six buses with 50% passenger load.

information is available from the GREET (Greenhouse Gases, Regulated Emissions, and Energy Use in Transportation) analysis model created by the Transportation Technology R&D Center of Argonne National Laboratory. The specific efficiency factors for diesel, hydrogen, and electricity were provided by Ye Wu by using version 1.6 of the GREET model. Figure 2 shows a comparison of the complete "well to wheels" energy efficiency of the six bus configurations.

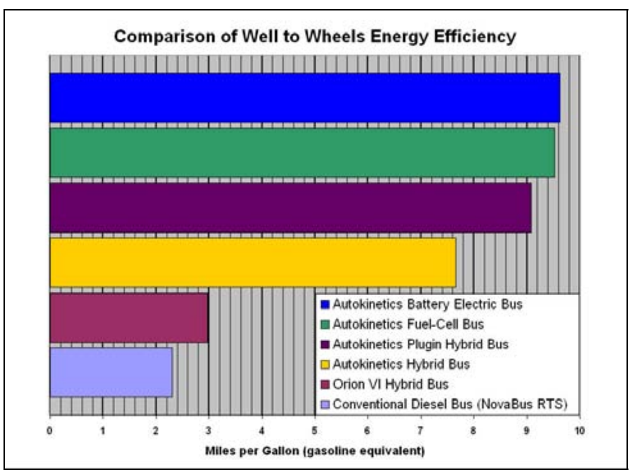

Figure 2. ADVISOR results showing comparative *well-to-wheels* energy efficiency of six buses with 50% passenger load.

Conclusions

The superior performance of a lightweight bus platform with a range of optimized propulsion systems is clearly shown in the results of this comparison study. The four versions of the Autokinetics bus outperform the more conventional buses by a wide margin. The best performance is achieved by the battery-electric version, with an improvement of over 300% compared to the Orion hybrid diesel. Since this configuration is relatively simple and straightforward to implement with off-the-shelf technology, it has been selected as the best choice of propulsion system for the prototype.

Printed on recycled paper

A Strong Energy Portfolio for a Strong America

Energy efficiency and clean, renewable energy will mean a stronger economy, a cleaner environment, and greater energy independence for America. Working with a wide array of state, community, industry, and university partners, the U.S. Department of Energy's Office of Energy Efficiency and Renewable Energy invests in a diverse portfolio of energy technologies.

For more information contact:
EERE Information Center
1-877-EERE-INF (1-877-337-3463)
www.eere.energy.gov